Targeting metabolic reprogramming in metastatic colorectal and prostate cancer cells to prevent therapeutic failure

Claudia Hernández Carro

TARGETING METABOLIC REPROGRAMMING IN METASTATIC COLORECTAL AND PROSTATE CANCER CELLS TO PREVENT THERAPEUTIC FAILURE

Claudia Hernández Carro

DOCTORAL THESIS | 2024

Targeting metabolic reprogramming in metastatic colorectal and prostate cancer cells to prevent therapeutic failure.

Claudia Hernández Carro

Doctoral Thesis

2024

UNIVERSITAT DE BARCELONA

PROGRAMA DE DOCTORAT EN BIOTECNOLOGIA

FACULTAT DE BIOLOGIA

TARGETING METABOLIC REPROGRAMMING IN METASTATIC COLORECTAL AND PROSTATE CANCER CELLS TO PREVENT THERAPEUTIC FAILURE

Memòria presentada per **Claudia Hernández Carro** per optar al grau de doctora per la Universitat de Barcelona. Programa de doctorat en Biotecnologia al Departament de Bioquímica i Biomedicina Molecular.

Claudia Hernández Carro
Doctoranda

Marta Cascante Serratosa
Codirectora i tutora

Míriam Neus Tarrado Castellarnau
Codirectora

ABSTRACT

Prostate and colorectal cancer are among the cancer types with the highest recurrence and mortality rates. The emergence of drug resistance poses a considerable challenge for effective treatment, especially in the advanced stages of the disease. Metabolic reprogramming is a crucial contributor to the adaptative process of drug resistance and a key hallmark of cancer that enables tumor cells to meet the metabolic and energetic requirements for tumor survival and progression. Then, targeting metabolic reprogramming represents a promising anti-cancer strategy, and understanding the metabolic alterations acquired after drug resistance can provide valuable insights for developing effective combination therapies.

In this work, we study metabolic alterations underlying Oxaliplatin, an alkylating agent that impairs DNA replication and transcription by promoting DNA damage through the generation of platinum crosslinks, and Palbociclib, a selective inhibitor of cyclin-dependent kinases 4 and 6 (CDK4/6) that arrests cells in the G1/G0 phase of the cell cycle. Both compounds are commonly employed in cancer therapies and have exhibited efficacy in several types of cancer. This work assesses the metabolic characterization of drug resistance acquisition after these treatments in advanced stages of colorectal and prostate cancer cells, focusing on the aggressive SW620 and PC-3 cell lines, respectively. Based on the metabolic characterization, transcriptomic, and respiratory data, or applying cell-line-specific metabolic reconstructions after data integration using Genome-Scale Metabolic Models (GSMM), our results identify metabolic vulnerabilities in drug-adapted phenotypes and reveal key metabolic pathways on which cancer cells rely to adapt and survive, serving as attractive targets for therapeutic interventions. These pathways include but are not limited to glycolysis, fatty acid metabolism, amino acid metabolism, and oxidative phosphorylation. Our strategy proposes rational therapeutic combinations with Oxaliplatin or Palbociclib to overcome drug resistance in advanced-stage prostate and colorectal cancers based on drug repurposing. These findings include the interaction between metabolic reprogramming and cell cycle regulation, promoting cell cycle arrest in the G1/G0 phase to address Oxaliplatin resistance, and targeting oxidative phosphorylation, mitochondrial metabolism, and reactive oxygen species (ROS) modulation to sensitize cells to Palbociclib. Notably, Palbociclib combination with a ROS modulator represents a successful approach that expands the potential of application across different colorectal models, showing efficacy in preclinical models, significantly compromising *in vivo* tumor progression in NOD/SCID mice with SW620 tumors and *in vitro* cell proliferation in both the metastatic SW620 and the primary colorectal cancer HCT116 cell lines.

Based on the metabolic reprogramming underlying Oxaliplatin and Palbociclib treatments, this work provides alternative combination therapies by targeting metabolic vulnerabilities that could be further explored to improve treatment outcomes and overcome drug resistance in advanced stages of prostate and colorectal cancers.

TABLE OF CONTENTS

TABLE OF CONTENTS

1.

INTRODUCTION

1. INTRODUCTION

1.1. Cancer: general insights

1.1.1. Cancer Overview

Cancer is a highly intricate disease involving the transformation of normal cells to malignant cells through aberrant cell growth, tumor development, and, ultimately, metastatic spread. It represents the second leading cause of death in the world, after cardiovascular diseases (Ferlay et al., 2020). Close to 19.3 million new cancer cases were diagnosed in 2020, and almost 10 million deaths were registered in the same year (Ferlay et al., 2020). Because of this, a significant portion of scientific research is dedicated to broadening the understanding of tumor initiation, progression and survival, flexibility and metastatic spread capacity, drug response, drug resistance mechanisms, genetic profile, cancer cell metabolism and signaling, tumor microenvironment, and cancer immunology. Besides, a renewed interest has emerged in utilizing genetic analysis of tumors to categorize patients (Fontana et al., 2019, Pal et al., 2018, Sveen et al., 2017) and to incorporate dietary interventions alongside metabolic-targeting therapies (Elia & Haigis, 2021, Martínez-Reyes & Chandel, 2021, Tajan & Vousden, 2020). The ultimate goal is to decrease mortality rates associated with cancer development by improving prevention and detection and expanding treatment options with more targeted, individualized, and efficient therapies.

In this thesis, targetable metabolic vulnerabilities are explored to improve drug response by identifying potential synergistic combinations with conventional therapy used nowadays.

1.1.2. Cancer Initiation, Progression, and Metastasis

Cancer initiation involves interaction in genetic mutations, epigenetics, and external sources contributing to tumor formation. Cancer origin is usually associated with a progenitor cancer cell that acquires a proliferating phenotype with continuous cell division, capable of avoiding programmed cell death and promoting tumor invasion and proliferation to other body parts.

Different cancer types are described and classified depending on the tissue of tumor initiation. Uncommon types are myelomas, which develop in the plasma cells of bone marrow; leukemia, which starts in the white cells of the blood; and lymphoma, which appears in the nodes of the lymphatic system. Sarcomas, the second type of cancer with more incidence, arise in supportive and connective tissues. The most frequent cancer type is carcinoma, which emerges in the epithelial tissue and can be initiated in organs and glands (adenocarcinomas) such as breast, lung, colorectal, bladder, and prostate cancer, (Cancer Research UK 2020, Siegel et al., 2023, Ferlay et al., 2020).

According to the risk assessments studied over the years, the external factors strongly associated with tumor development are age, obesity, environmental pollution exposition, substance abuse (e.g., tobacco, alcohol, opium), poor nutrition, or lack of physical activity. In this regard, cancer incidence correlates positively with the Human Development Index (HDI) due to the lifestyle of higher-income regions, whereas mortality

correlates negatively with HDI. Lower-income areas often face a lack of resources and higher carcinogens exposition, such as biological infections, which cause 30% of cancers diagnosed in these areas (Ferlay et al., 2020). Carcinogens are physical (e.g., ionizing and UV radiation), chemical (e.g., arsenic, formaldehyde, tobacco components, estrogen therapy or contraceptives), and biological agents (toxins or Hepatitis B, HPV, HIV, Epstein-Barr, or Helicobacter pylori infections) (IARC 2023) associated to mutagenesis, DNA damage, or hormone-like behavior, serving as ligands for specific receptors promoting favorable responses for tumorigenesis (IARC 2023, Chatterjee & Walker, 2017).

However, tumor development is also influenced by inherited factors such as the genetic predisposition to suffer hereditary cancer syndromes. Family history is linked to germline mutations, notably mutations affecting DNA damage response (DDR) pathways responsible for DNA repair and DNA genome stability maintenance. Deficiencies in DDR are accountable for the majority of these hereditary syndromes, such as hereditary breast-ovarian cancer (mutations in *BRCA1/2*), prostate cancer (mutations in *BRCA2* and *HOXB13*), or hereditary non-polyposis colorectal cancer also known as Lynch syndrome (HNPCC; mutations in *MLH1* and *MSH2*) (Chatterjee & Walker, 2017, Imyanitov et al., 2023).

Disease progression results from the sequential accumulation of genetic mutations affecting oncogenes, tumor suppressor genes (TSG), and DNA repair systems that alter tightly regulated processes within cells that control cell homeostasis. Cancer cells benefit from corrupted cell growth and division, adapted metabolic responses, and higher cellular stress tolerance, which are responsible for tumor progression and survival. In this context, the tumor microenvironment (TME), composed of cancer cells, stromal cells, and immune cells, could also influence tumor behavior through the interaction of signaling molecules, inflammatory responses, vessel formation, or nutrient and oxygen availability (Brunne & Finley, 2022, Elia & Haigis, 2021).

The metastatic spread is the ultimate consequence of disease progression when tumor cells acquire the ability to migrate and colonize other nearby tissues or distant organs until impairing normal organ functions. Mutations correlated with metastatic progress are usually expressed in primary tumors. The multistep process of metastasis is termed the metastatic cascade. Cancer cells usually alter epithelial cell-to-cell adhesion, promoting cell migration. In this regard, the epithelial-to-mesenchymal transition (EMT) mechanism plays an important role in metastatic dissemination. Cancer cells achieve local invasion and intravasation through the blood or lymphatic system, circulation until extravasation in distant tissues, successful stroma invasion, and micrometastasis formation, leading to tumor and vessel growth and resulting in distant organ colonization (Ganesh & Massagué, 2021). In this regard, metastatic mutations involving epigenetics, DNA methylation, and chromatin modification are usually found in most aggressive tumors. Frequently, drug resistance and cancer recurrence emerge due to intratumoral heterogeneity associated with specific mutations, genomic instability, or phenotypic plasticity acquired by cancer cells that present the most aggressive and adaptive phenotypes, such as cancer stem cells (Ganesh & Massagué, 2021). The complexity around cancer and, notably, metastasis and drug resistance represent the most challenging events. Metastatic disease is the major cause of death in cancer, responsible for more than 90% of cases (Ganesh & Massagué, 2021).

1.1.3. Cancer fundamentals: features, DNA damage and repair mechanisms, and cell cycle

1.1.3.1. The hallmarks of cancer

Tumor development, survival, and progression are complex processes entailing inherent and external factors; however, common features across a wide range of cancer types have been observed over the years and were described as the hallmarks of cancer by Hanahan and Weinberg (Hanahan & Weinberg, 2000). To this date, eight hallmarks of cancer are defined as acquired capabilities of pathogenic cancer cells and two enabling characteristics contributing to the acquisition of core hallmarks (Hanahan, 2022, Hanahan & Weinberg, 2011) (**Figure 1.1.1.**).

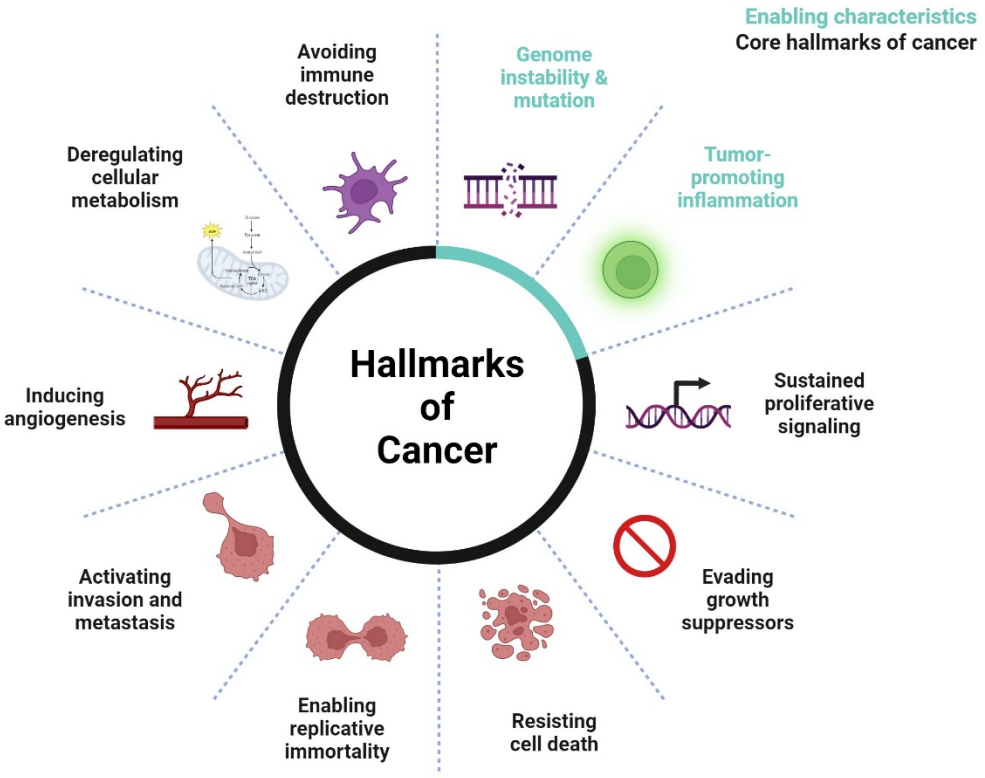

Figure 1.1.1. Hallmarks of cancer. The core hallmarks of cancer (black) and the enabling characteristics contributing to pathogenic acquisition (turquoise). Figure adapted from "Hallmarks of cancer: Circle" by https://www.biorender.com/ (2023) (Hanahan, 2022, Hanahan & Weinberg, 2011), and retrieved from https://app.biorender.com/biorender-templates.

Genome instability provides advantages to cancer cells supporting tumor proliferation through genomic alterations that could affect the expression of genes involved in cell division, DNA repair machinery, TSG, and oncogenes, contributing to core hallmarks acquisition. Also, cancer cells take advantage of the immune cells within TME for tumor-promoting inflammation, supporting tumor growth and survival. The inflammatory mediators secreted can suppress the immune system and prevent immune destruction, while the growth factors provided (such as EGF and VEGF, chemokines, cytokines, or matrix metalloproteinases) are used by cancer cells for tumor proliferation, angiogenesis, and metastatic spread.

Cancer cells sustain proliferative signaling by decreasing their dependence on mitogenic growth signals that tightly control cell growth, survival, and differentiation. There is a dysregulation of important signaling pathways such as the PI3K/AKT/mTOR and MAPK/ERK. Also, cancer cells can display mechanisms to evade growth suppressors by altering TSG to facilitate uninterrupted cell proliferation and overcome growth inhibition. The most frequently altered regulators of cell cycle or programmed cell death (apoptosis) in all cancer types are *RB* and *TP53*. In fact, the loss of *TP53*, which plays a crucial role in triggering apoptosis, is the most common mechanism for avoiding cell death (Aubrey et al., 2018).

Cell proliferation is limited in normal cells where telomerase expression is tightly regulated, leading to a finite replicative capacity and ultimate senescence. However, cancer cells achieve replicative immortality through telomerase overexpression and maintaining telomeres length, promoting an unlimited replicative process. Consequently, cancer cells continuously divide and increase the risk of DNA damage and genetic instability.

The activation of invasion and metastasis is another hallmark of cancer. Frequently, with disease progression, tumor cells can grow and survive beyond the tumor initiation site, promoting migration and invasive phenotypes. One of the most common mechanisms in this process is cell-cell adhesion impairment via altering E-cadherin expression (Janiszewska et al., 2020).

In the tumor niche, oxygen and nutrient supply are essential for cell growth. Hence, cancer cells activate vasculogenesis and angiogenesis to sprout new vessels across the tumor. This process is mainly regulated by the vascular endothelial growth factor-A (VEGF-A) and upregulated by hypoxia or oncogenic signaling promoted by disease progression, invasion, and metastasis.

Cancer cells reprogram their metabolism to fulfill the energetic and biosynthetic demands, providing metabolic precursors and macromolecules (e.g., membrane lipids, nucleic acids, or proteins) to sustain their aberrant proliferation and survival. Also, metabolic reprogramming is an essential mechanism to generate reducing equivalents and increase tolerance against cellular stress-associated events, such as redox imbalance, hypoxia, or nutrient deprivation. The most frequent metabolic alteration associated with malignant transformation is an increase in aerobic glycolysis, first described by Otto Warburg in 1920s (Warburg, 1924). The Warburg effect describes a metabolic shift in cancer cells characterized by increased reliance on glycolysis under normoxic conditions, providing ATP and metabolic intermediates required to meet the biosynthetic demand imposed by the uncontrolled tumor cell proliferation (DeBerardinis & Chandel, 2016). This hallmark, metabolic reprogramming, represents this thesis's main focus of attention since metabolic changes are crucial for enabling adaptive processes conferring drug resistance and promoting cancer recurrence.

Also, new emerging hallmarks of cancer have been proposed, including unlocking phenotypic plasticity to evade differentiation and inducing senescence by arresting cell cycle while stimulating morphological and metabolic changes, which activates a senescence-associated secretory phenotype (SASP) that contributes to cell signaling, cell survival, and drug resistance. In the same context, two enabling characteristics have been identified; the non-mutational epigenetic reprogramming considering the influence

of the environment, intratumor heterogeneity or TME on gene expression regulation, and the polymorphic microbiomes which may mediate immunological response and mutagenesis (Hanahan, 2022).

1.1.3.2. DNA damage and repair mechanisms

Correct transcription of DNA is essential for maintaining normal cell function and genomic stability. After DNA damage, normal cells activate specific DDR pathways that recognize and repair damage depending on the lesion type and origin (**Figure 1.1.2.**). Defective DDR causes alterations in cell cycle checkpoints and cell division, senescent state, and tolerance to programmed cell death. DNA damage leads to genomic instability, and mutagenesis acquisition contributes to cancer development and tumor progression (Chatterjee & Walker, 2017).

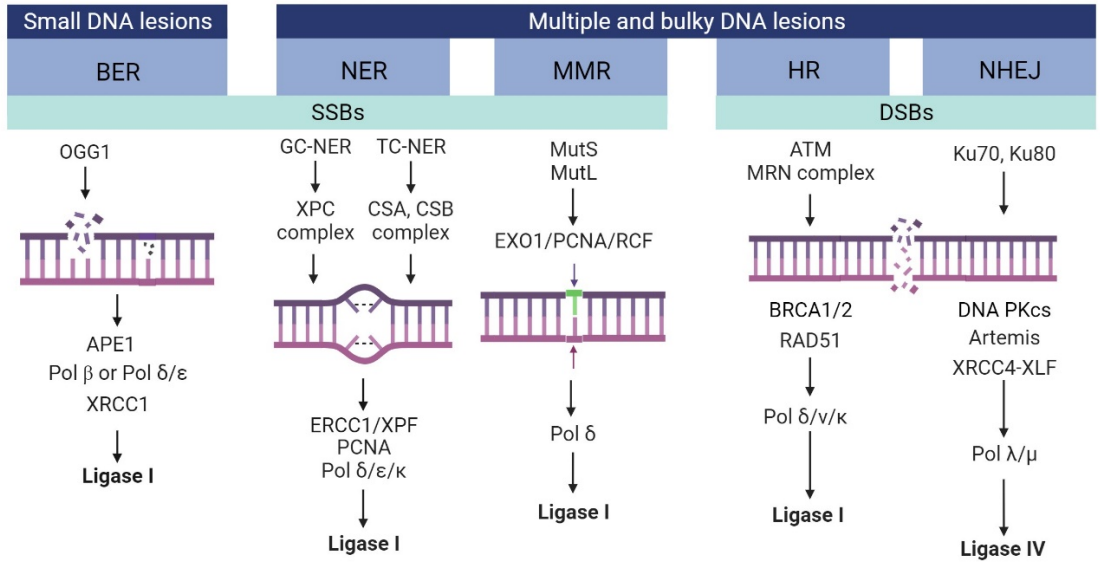

Figure 1.1.2. Major DNA damage response (DDR) mechanisms. Small DNA lesions in single-strand breaks (SSBs) activate the base excision repair (BER) mechanism. Multiple and bulky lesions generating SSBs activated the nucleotide excision repair (NER) during the replicative phase or mismatch excision repair (MMR). Double-strand breaks (DSBs) are addressed through homologous recombination (HR) using DNA templates during the replicative phase of the cell cycle or non-homologous end joining (NHEJ) in the absence of DNA templates. Interstrand crosslink repair (ICL) and translation synthesis (TLS) (not shown) are active in more specific lesions and are cooperative repair pathways using common machinery for NER or HR. Figure adapted from "DNA Repair mechanisms" by https://www.biorender.com/ (2023) (Bohen et al., 2018, Morgan & Lawrence, 2015) and retrieved from https://app.biorender.com/biorender-templates.

One source of DNA damage is endogenous processes such as replication errors, base DNA damage originates from endogenous processes like replication errors, base deamination, and excessive reactive oxygen species (ROS) production, which can lead to oxidative reactions affecting DNA, proteins, and lipids. Exogenously, DNA lesions can result from factors such as ionizing and UV radiation, which generate ROS-like damage and add alkyl groups to specific base ring nitrogen, creating dimers or DNA adducts, along with other electrophilic compounds, contributing to carcinogenic and mutagenic properties.

Small lesions such as O- and N-alkylated DNA are addressed through O6-methylguanine-DNA methyltransferase (*MGMT*) and α-ketoglutarate-dependent

dioxygenase (*ALKB*), respectively, which remove DNA adducts in a stoichiometric manner. For instance, cancer cells regulate MGMT expression to increase tolerance to DNA alkylating agents (Chatterjee & Walker, 2017, Sabharwal & Middleton, 2006). In case of oxidative, deamination, alkylation, and abasic sites affecting a single nucleotide base during the G1 phase of the cell cycle, cells activate the base excision repair (BER) mechanism. DNA glycosylases, like OGG1, recognize and excise damaged DNA, generating apurinic/apyrimidinic (AP) sites, subsequently repaired through AP endonuclease (APE1), base substitution, and ligation. Via DNA ligase. OGG1 downregulation has been linked to cancer progression (Baquero & Benítez-Buelga, et al., 2021, Chatterjee & Walker, 2017, Huang & Zhou, 2021).

Multiple and bulky base damage on single-strand breaks (SSBs) of DNA is tackled through more complex mechanisms, including nucleotide excision repair (NER) system, mismatch excision repair (MMR), interstrand crosslink repair (ICL), and translation synthesis (TLS):

- The nucleotide excision repair system repairs single-strand breaks promoted by UV radiation and bulky DNA adducts from chemotherapies, addressing covalent bonds that distort the DNA helix. NER involves two branches to recognize DNA lessons through the global genome NER (GG-NER), which uses the damage sensor complex XPC, and the transcription-coupled NER (TC-NER), through the CSA-CSB complex. The final NER steps imply enzymatic recruitment to promote transcription factor IIH (TFIIH) initiation for DNA repair, involving endonucleases XPF-ERCC1 and XPG, replication proteins PCNA and RFC, polymerases and ligases (Chatterjee & Walker, 2017, Huang & Zhou, 2021, Kusakabe et al., 2019). In this regard, overexpression of XPF-ERCC1 has been associated with Oxaliplatin resistance in several solid tumors (Yin et al., 2011, Hatch & Swift, 2014).
- Errors not detected during the replicative pathway are addressed by the mismatch repair (MMR) system. In MMR, the MutS and MutL homologs (commonly MutSα/β and MutLα) recognize and incise the DNA lesion. Exonuclease I (EXO1) removes damaged DNA for DNA repair depending on PCNA/RFC for subsequent synthesis and ligation (Chatterjee & Walker, 2017, Huang & Zhou, 2021).
- DNA interstrand crosslink repair (ICL) restores covalent bonds generated between DNA strands by crosslinking agents. Fanconi anemia (FA) proteins recognize and repair the ICL. Different FA proteins implicated are recruited and activated downstream through phosphorylation until other repair mechanisms, such as NER and homologous recombination (HR), get involved to accomplish ICL repair (Unno et al., 2016). Translation synthesis (TLS) is another cooperative repair pathway that recruits specialized TLS polymerases depending on the lesion type. TLS is recruited on the DNA damage site after an incomplete DNA repair process. They present specific structural properties that differ from DNA polymerases; however, the replication of DNA is achieved to the detriment of fidelity (Anand et al., 2023, Chatterjee & Walker, 2017).

SSBs also differ from the major pathways to repair double-strand breaks (DSBs), which are repaired through homologous recombination (HR) and non-homologous end joining (NHEJ) pathways:

- HR is active during the replicative phase of the cell cycle, specifically the late S or G2 phase, requiring an identical sister chromatid as a template. Initiated with MRN complex recognition of DSBs, ATM recruitment activates resection. RAD51, the key protein in HR, binds to the 3' overhangs generated through nucleotide degradation by EXO1 and DNA2 and performs homology DNA sequences search, D-loop formation, and DNA strand invasion, which involves association with BRCA1, BRCA2, and RAD54. Finally, DNA polymerase synthesizes the new DNA strands until DNA ligation. Holliday junction is resolved by cutting in a crossover or non-crossover manner for chromosome restoration (Chang 2017, Chatterjee & Walker, 2017, Huang & Zhou, 2021).
- On the other hand, the absence of genomic templates activates the NHEJ pathway. 53BP1 is a positive regulator for DSBs via the NHEJ can be recruited at any point of the cell cycle. In the NHEJ mechanism, DSBs are efficiently recognized and protected by Ku70/Ku80 heterodimer, which forms a high-affinity complex with DNA-PKcs. This complex recruits necessary nucleases, polymerases, and ligases for repair. This complex recruits the nucleases, polymerases, and ligases for strand formation. Ku or DNA ligase IV complex absence leads to mutation due to a less efficient repair involving microhomology and polymerase Pol θ-mediated end joining (Chang et al., 2017, Chatterjee & Walker 2017, Huang & Zhou, 2021).

Unrepaired DNA damage can induce a senescence or quiescent state by arresting the cell cycle to avoid further cell division or activate programmed cell death when DNA damage is overwhelming. Cancer cells frequently promote a deficient DDR, which increases DNA damage tolerance and favors the prevalence of advantageous mutations for tumor progression.

1.1.3.3. Cell cycle

Cell division is a tightly regulated process within normal cells where critical cellular events such as DNA replication, transcription, protein translation, and post-translational modifications occur in a coordinated manner and depending on the cell cycle stage to ensure their proper execution (Wang, 2022).

The mitotic cell cycle comprises two main events: DNA replication during interphase and cellular content repartition during the segregation phase, yielding two genetically identical cell daughters. The interphase is, at the same time, comprised of three sequential phases; first, the gap 1 (G1) pre-replicative phase, which provides a decision window for either initiating a new cell cycle after division or exiting the cell cycle; second, the replicative or DNA synthesis phase (S phase) and third, the gap 2 phase (G2) or post-replicative that flanks the S phase to provide a second decision window for mitotic entry. Once interphase is overcome, during mitosis (M phase), cells promote cellular content segregation and cell division. Subsequently, cells decide whether they promote cell cycle exit or continue in the proliferative state (Bretones et al., 2015, Matthews et al., 2022, Mughal et al., 2023) (**Figure 1.1.3.**).

Cell cycle initiation, progression, and completion until cell division are sequential events regulated by cyclin-dependent kinases (CDKs), a family of serine/threonine protein kinases whose activity depends on cyclin binding. Cyclins are the regulatory subunits of

CDKs-cyclin complexes that are consecutively synthesized to drive the cell cycle phase progression (Bretones et al., 2015, Matthews et al., 2022) (**Figure 1.1.3., B**).

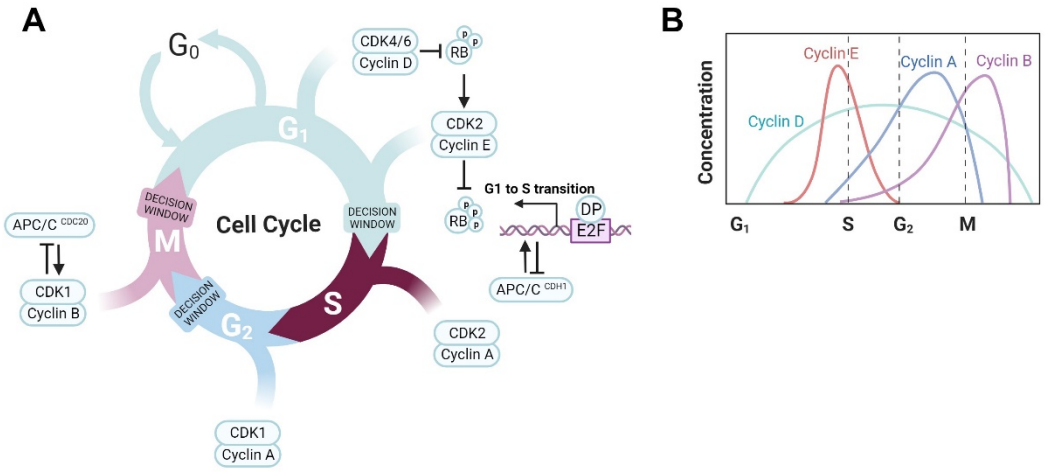

Figure 1.1.3. Cell cycle progression and checkpoints. A) Cell cycle is comprised of interphase (G1, S, and G2) for DNA replication and mitotic phase (M) for cellular content segregation. Different phases are limited upon the achievement of decision windows for cell cycle entry and DNA replication initiation (green), mitotic entry (blue), and mitotic exit (red). Active cyclins-dependent kinases – cyclins complexes involved in different phases are indicated. B) Cyclins, regulatory subunits of CDKs, accumulation, and degradation drive cell cycle progression through different phases. G; gap 1 phase. S; synthesis phase. G2; gap 2 phase. M; mitotic phase. Figure adapted from "Cyclins: Cell Cycle Regulators" by https://www.biorender.com/ (2023) (Cancer Research Product Guide; Tocris Bioscience 2016, Hochegger et al., 2008, Wagener et al., 2016) and retrieved from https://app.biorender.com/biorender-templates.

Normal cells usually are found in a non-proliferative but reversible state (quiescence, G0) until growth signals and mitogenic signaling activate cell division. For cell cycle induction, these signals involve the RAS/RAF/MAPK pathway for Cyclin D expression and the initiation of the pre-replication event upon binding to CDK4 and CDK6, which prevents cell cycle exit (Matthews et al., 2022). CDK4/6-Cyclin D complexes are required for retinoblastoma protein (RB) family inactivation by phosphorylation. RB remains attached to the transcriptional factor E2F upon partial phosphorylation by CDK4/6-Cyclin D that allows E2F release, Cyclin E-CDK2 expression, and increases CDKs activity until RB hyperphosphorylation. Then, Cyclin A expression allows the expression of genes required for DNA replication by the E2F-DP transcription factor. Cyclin E and Cyclin A-CDK2 complexes are essential for overcoming the mitogen-dependent restriction point. This restriction point defines the first decision window for the G1 to S phase transition. Cell cycle phase exit decision is accompanied by the inactivation of the E3 ubiquitin ligase anaphase-promoting complex/cyclosome (APC/C) with CDH1 (APC/C^{CDH1}), which is responsible for cyclin degradation, to prevent cyclin accumulation, and required to exit the G1 phase (Bretones et al., 2015, Matthews et al., 2022). The replicative phase (S) is initiated upon the accumulation of Cyclin A- and Cyclin B-CDK1 complexes, leading to mitotic entry after achieving a successful second decision window in the G2/M transition. APC/C and the activator protein CDC20 (APC/C^{CDC20}) are activated for cyclin degradation and cell cycle completion with cell division (Matthews et al., 2022). Also, in order to regulate cell cycle progression and kinase activity of CDKs, the transcription factors that trigger the expression of particular members from the INK4 ($P16^{INK4A}$, $P15^{INK4B}$, $P18^{INK4C}$, $P19^{INK4D}$) or KIP/CIP ($P21^{CIP1}$, $P27^{KIP1}$, $P57^{KIP2}$) families of the cyclin-dependent kinase inhibitors (CKIs), the negative regulators of the kinase activity of

CDKs, are activated controlling Cyclin A-E/CDK2, Cyclin D/CDK4-6 and Cyclin A-B/CDK1 functions(Bretones et al., 2015).

Cell cycle progression depends on specific checkpoints along the cell cycle phases. During the decision windows, these checkpoints should be successfully overcome to prevent the accumulation of mutations during cell division and allow cell cycle progression. DNA damage, replication stress, and deficient spindle assembly promote either cell cycle slowdown or arrest by CDKs and APC/C activity inhibition. Specifically, DSBs generated during interphase activate ATM and phosphorylate checkpoint kinase 2 (CHK2) and transcription factor P53, which, in turn, either activate P21 to prevent CDKs complex formation and progression to the S phase or degrade CDC25 phosphatases which have an important dephosphorylation role in CDK1 activation. DNA replication stress checkpoint during the S phase prevents mitotic entry as a response to address SSBs, activating ATR and sequentially CHK1 via CDC25 degradation or phosphorylation by WEE1 (Matthews et al., 2022). Functional mitotic checkpoint or spindle assembly checkpoint (SAC) is active during the M phase as a mechanism to ensure proper chromosome segregation. SAC forms the mitotic checkpoint complex (MCC) that inhibits APC/C^{CDC20} preventing further mitotic progression (Matthews et al., 2022) (**Figure 1.1.4.**).

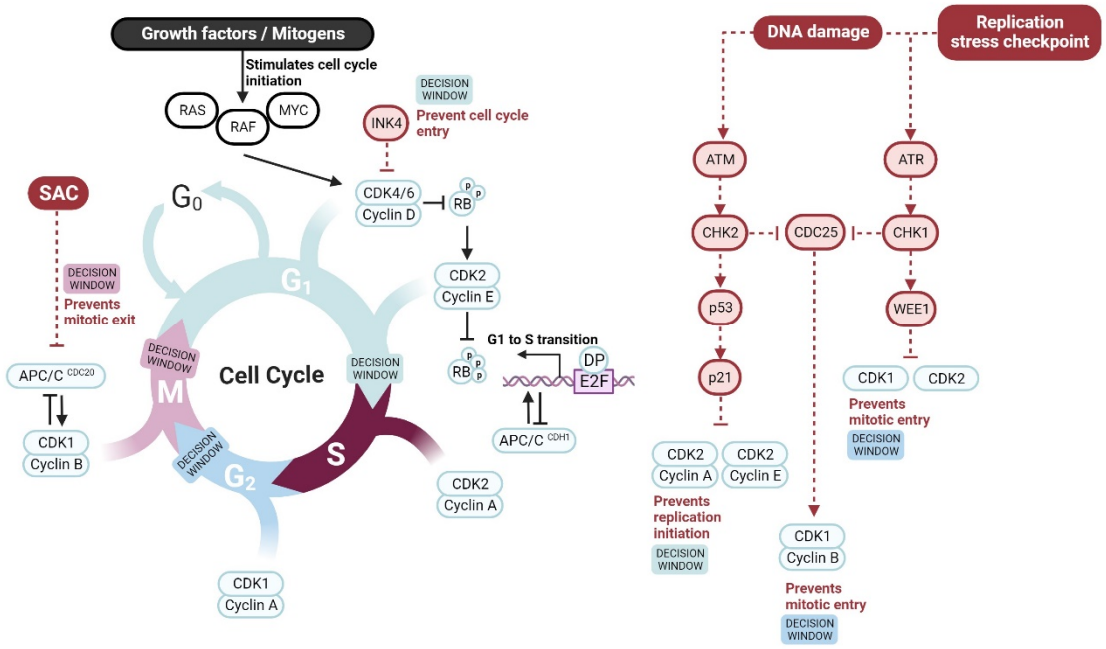

Figure 1.1.4. Cell cycle regulation. Mitogen-dependent responses, including the RAS/RAF/MAPK pathway and MYC expression, promote cell cycle entrance. Negative regulators limit cell cycle entry and replication initiation through INK4 and CIP/KIP family (only shown P21^{CIP1}). DNA damage prevents cell cycle progression via ATM and P53 or CDC25 during the interphase. The replication stress checkpoint prevents mitotic entry via ATR or CDC25 during the late S and G2 phases. The mitotic checkpoint slows mitotic progression until the SAC complex ensures proper DNA content separation prior to cell division. SAC; spindle assembly checkpoint. Figure created with https://www.biorender.com/ (2023), and adapted from Matthews et al., 2022.

Cell cycle arrest implies a non-proliferative reversible (quiescent) or irreversible (senescent) state, depending on the phase of the cell cycle and the DNA damage extent. Aberrant damage triggers programmed apoptosis through P53-dependent pathways (Chatterjee & Walker, 2017, Matthews et al., 2022,).

Concerning cell cycle regulation, c-MYC is an important transcription factor directly correlated with cell cycle progression. MYC upregulation exerts a critical role in quiescent cells for entering in cell cycle and is also involved in the expression of other important genes regarding the cell cycle control, such as CDK4, CDK6, Cyclin D, Cyclin E, Cyclin A, E2F, and CDC25, and represses CDK inhibitory kinase WEE1. MYC also affects apoptosis regulation and promotes cell proliferation antagonizing with growth suppressors P21 and P27 by expressing components of the ubiquitin ligase SCF complex for its degradation. MYC influences the cell cycle at mitogenic control by encoding for CDK1 and cyclins involved in the M phase and also mediates the expression of APC/C components for mitotic progression (Bretones et al., 2015).

1.1.3.3.1. Dysregulation of the cell cycle in cancer cells

The continued division supporting highly proliferative rates in cancer cells due to cell cycle dysregulation is a hallmark of cancer. Usually, mutations affect P53, DNA damage checkpoint, and E2F transcription factor, thus preventing apoptosis and compromising the cell cycle exit. On the other hand, DNA replication stress checkpoint and SAC functions are rarely mutated since they are essential, even for cancer cells, to avoid aberrant genomic instability that leads to cell death (Matthews et al., 2022).

The most common mutations stimulate G1 to S transition to provide autocrine production that affects the mitogen-dependent restriction point. Specifically, loss of RB, CDKs dysregulation, and c-MYC overexpression overcome mitogenic signaling that is usually limited in normal cells by growth inhibitory factors such as TGF-β and interferon-γ, which prevent RB phosphorylation by CDK inhibitors and c-MYC suppression (Bretones et al., 2015, Evan & Vousden, 2001).

Cancer mutations supporting aberrant cell proliferation represent therapeutic opportunities to explore drugs forcing cell cycle exit, inducing DNA damage or replication stress, or impairing SAC functions and causing mitotic defects. In this regard, Cyclin D-CKD4/6 complexes represent an important therapeutic target for cancer treatment in many cancer types and proved to be effective in several solid malignancies (Goel & Bergholz et al., 2022, Matthews et al., 2022, Mughal et al., 2023).

1.1.4. Types of cancer under study

More than a hundred types and subtypes of cancer types have been identified (ASCO 2023, National Cancer Institute 2023); among these, colorectal and prostate cancer are two of the most prevalent (Ferlay et al., 2020) and stand for the focus of this thesis.

1.1.4.1. Colorectal Cancer

To this date, available data collected by WHO reveals that colorectal cancer (CRC) is the third type of cancer in terms of the number of new cases emerging worldwide (Ferlay et al., 2020), meaning nearly two million people were diagnosed with CRC in 2020.

Although some CRC tumors detected at early stages can be addressed with surgery, approximately 20% of patients exhibit metastatic CRC (mCRC) once diagnosed for the first time (SEER Explorer 2023, Biller & Schrag, 2021, La Vecchia & Sebastián, 2020). Colorectal cancer presents one of the highest incidence values and also entails higher

mortality rates, responsible for around 9% of cancer patient deaths, only behind the 18% promoted by lung cancer (Ferlay et al., 2020). These dreadful data denote CRC aggressiveness, current treatment limitations, and the high recurrence imposed by the great heterogeneity associated with this type of cancer (Fontana et al., 2019, Pal et al., 2018, Sveen et al., 2017).

1.1.4.1.1. Colorectal cancer initiation and tumor progression

The cell origin of the colorectal tumor is the cycling crypt base columnar intestinal stem cells (ISCs) located in the bottom part of the intestinal crypts. The intestinal cells are subjected to constant exposure and abrasion. In this context, ISCs are highly self-renewing and present the potential to differentiate into all cell types; thus, they are the main contributor to normal intestinal epithelium regeneration. Therefore, mutations affecting ISCs impair their primary function and promote uncontrolled epithelium formation (Ganesh et al., 2020, La Vecchia & Sebastián, 2020). The most common mutation is *APC* (adenomatous polyposis coli) loss-of-function (LoF), promoting a constant activation of the WNT/β-catenin pathway required for epithelium formation and migration, which is highly expressed in regenerative tissues. *APC* LoF appears at the early stages of CRC and is present in 70% of colorectal adenomas (La Vecchia & Sebastián, 2020, Novellasdemunt et al., 2015, Zhan et al., 2017).

Upon WNT signaling activation during tumor initiation, important genetic alterations sequentially emerge affecting MAPK/ERK and PI3K/AKT/mTOR signaling cascades activated by Epidermal Growth Factor Receptor (EGFR), but also P53, and TGF-β pathways, involving cell proliferation, differentiation, migration, adhesion, cell cycle regulation, and apoptosis (Jung et al., 2017, Reya & Clevers, 2005). In this regard, *PIK3CA* overexpression, *SMAD4,* and *PTEN* LoF are commonly found in CRC (Eklöf et al., 2013, Jung et al., 2017).

Also, the starting point for carcinogenic cascade in some CRC tumors is genetic instability alterations such as microsatellite instability (MSI) or deficiency in MMR genes (i.e. *MLH1/2, MSH6, PMS2, EPCAM)* (Biller & Schrag, 2021, Singh et al., 2019), which are responsible for the most frequent hereditary form of CRC, the Lynch syndrome (Boland et al., 2018, Imyanitov et al., 2023). Moreover, tumors may achieve other genetic alterations such as chromosomal instability (CIN), which is the most frequent phenotype diagnosed, and CpG island methylator phenotype (CIMP) (Singh et al., 2019).

Notably, disease progression and more aggressive tumors affect the rat sarcoma viral oncogene (RAS) family of the MARPK/ERK pathways. The RAS family are small GTPase proteins that comprise three isoforms; KRAS (Kirsten-RAS), NRAS (Neuroblastoma-RAS), and HRAS (Harvey-RAS), which are involved in transcription factor activation of genes related to cell growth, differentiation, and survival. These are the predominant mutations in advanced CRC. Concretely, KRAS is considered a driver mutation in CRC accounting for 40% of cases diagnosed. KRAS mutation is present in around 25% of tumors and is particularly prevalent in the most lethal cancer types, including PDAC and NSCLC (Huang, 2021).

1.1.4.2. Prostate Cancer

Prostate cancer is one of the most common cancers in men arising worldwide, according to the World Health Organization (WHO). It is ranked fourth in the number of new cases diagnosed in 2020, followed by breast, lung, and colorectal cancer (Ferlay et al., 2020). It is reported that prostate cancer affects 7.3% of total new cases, meaning 1.41 million people are diagnosed every year (Ferlay et al., 2020). Its incidence is strongly associated with age, i.e., 65 to 74 years old being the most affected range (SEER Explorer 2023). However, other factors are also involved in tumor development, such as hormone balance, genetics, family history, ethnicity, or environmental context (Desai et al., 2021, Ferlay et al., 2020, Parker et al., 2020, Rebello & Oing et al., 2021).

Nevertheless, prostate cancer is not the most lethal type of cancer due to the early diagnoses in most patients with localized tumors when curative approaches can still be applied (SEER Explorer app 2023). However, a small percentage of patients are still diagnosed with regional and distant metastasis (SEER Explorer 2023). In these cases, advanced disease can only be addressed with palliative treatments. Disease progression is directly correlated with mortality cases, representing 7.7% of patients in 2020 (Ferlay et al., 2020).

1.1.4.2.1. Prostate cancer initiation and tumor progression

The prostate gland is part of the male reproductive organ whose function is to produce and secrete proteolytic enzymes into the seminal fluid to ensure sperm viability. Three zones could be anatomically differentiated in an adult prostate which is located below the bladder, being the central, transition, and peripheral zones (Rebello & Oing et al., 2021, Wang, 2018). The peripheral zone is the largest part of the prostate (around 70% of the total gland volume) and the primary area where tumors emerge, representing 80% of cases diagnosed (Rebello & Oing et al., 2021, Wang, 2018). The prostatic duct, through which seminal fluid is expelled, is most notably composed of three types of differentiated epithelial cells, i.e., luminal (expressing androgen receptor (AR), prostate-specific antigen (PSA), and cytokeratin 8 and 18 (CK8/18)), basal (expressing CK5, CK14, and P63), and neuroendocrine cells (expressing neuroendocrine markers such SYN, CGA, or NSE) (Rebello & Oing et al., 2021, Wang, 2018). Other cell types surrounding, such as smooth muscle or stroma cells, including fibroblast, play a role in the TME by supporting survival signaling (Rebello & Oing et al., 2021).

Hormones produced and regulated by the hypothalamic-pituitary-gonadal axis, such as testosterone and DHT (5α-dihydrotestosterone), bind to AR, promoting its transcriptional activation, which regulates genes involved in the development and maintenance of a normal prostate function. Therefore, non-tumorigenic epithelial cells in a prostate gland usually express high levels of *AR* (Rebello & Oing et al., 2021).

Current findings suggest that most of the prostate cancer diagnosed origin is usually associated with an accumulation of somatic mutations in the prostate gland's basal or luminal epithelial cells (Rebello & Oing et al., 2021). Initial abnormal cell growth is revealed as prostatic intraepithelial neoplasia (PIN), which could give rise to more advanced prostate adenocarcinoma. Prostate tumor progression is highly dependent on androgens and androgen receptor function (Desai et al., 2021, Gandaglia et al., 2014,

Germain & Lafront et al., 2023, Hugging & Hodges 1941, Parker et al., 2020, Rebello & Oing et al., 2021, Wang, 2018) since the androgen-induced transcriptional response of *AR* involves genes regulating cell growth (Desai et al., 2021, Rebello & Oing et al., 2021).

The genetic profile in prostate cancer is highly heterogeneous. Among the most notable genetic changes is the fusion of transmembrane serine protease 2 (*TMPRSS2*) gene and erythroblast transformation-specific (*ETS*) related transcription factor (*ERG*) or *TMPRSS2-ERG* fusion, through chromosomal translocation, which occurs in approximately 50% of tumors (Adamo & Ladomey, 2015, Rebello & Oing et al., 2021, Wang, 2018). This mutation involves the promoter region of the *AR* regulator *TMPRSS2* and the encoding region of *ERG*, a member of the ETS family, which promotes malignant transformation and metastasis by increasing cell migration and invasion. Additionally, *ERG* overexpression and deletions or mutations in tumor suppressor genes *PTEN*, *RB1*, and *TP53* lead to a high-risk carcinoma phenotype. *MYC* oncogene amplification is also frequently observed in prostate cancer, contributing to cell survival, invasion, androgen independence, and biochemical relapse (Adamo & Ladomey, 2015, Rebello & Oing et al., 2021, Wang, 2018).

Localized and primary prostate cancer cells do not depend on AR expression; however, the genomic state of AR is indicative of the disease's evolution to a metastatic state as a natural response to evade hormonal therapy. The genomic alteration most commonly found in AR is *AR* amplification or overexpression by improving the enhancer region of *AR*. Less frequent are *AR* mutations affecting the specificity of the receptor, providing gain-of-function mutations on the ligand-binding domain, dysregulating microRNAs, or increasing AR gene sensitivity in response to other steroid hormones or low testosterone and DHT levels. Also, post-transcriptional modifications increase the production of AR structural variants (SVs) by alternative splicing, which can also act as an active transcription factor. In some cases, AR is not expressed, which implies the evasion of AR dependence for metastatic spread. This phenotype is associated with the most aggressive metastatic castration-resistant prostate cancer (mCRPC) (Rebello & Oing et al., 2021).

1.2. Cancer Metabolism

Metabolic reprogramming is described as one of the hallmarks of cancer (Hanahan & Weinberg, 2011) which is crucial for cell survival, supporting uncontrolled tumor growth and progression. Metabolic changes provide cell adaptability, even in hostile environments, against cellular stress, nutrient depletion, or hypoxic conditions, and promote interactions with oncogenes, tumor suppressor genes, and tumor microenvironment (TME). Hence, it is not surprising that metabolic reprogramming contributes significantly to adaptative processes such as metastasis, tumor heterogeneity, and drug resistance acquisition (La Vecchia & Sebastián, 2020).

The most frequent metabolic distinctive traits described as hallmarks of cancer cells are related to bioenergetic, biosynthetic, and redox homeostasis pathways (Pavlova & Thompson, 2016, Pavlova & Thompson, 2022) (**Figure 1.2.1.**), and include:

- Dysregulated glucose and amino acids uptake to increase carbon sources and support ATP production. This increased uptake is frequently boosted by aberrant

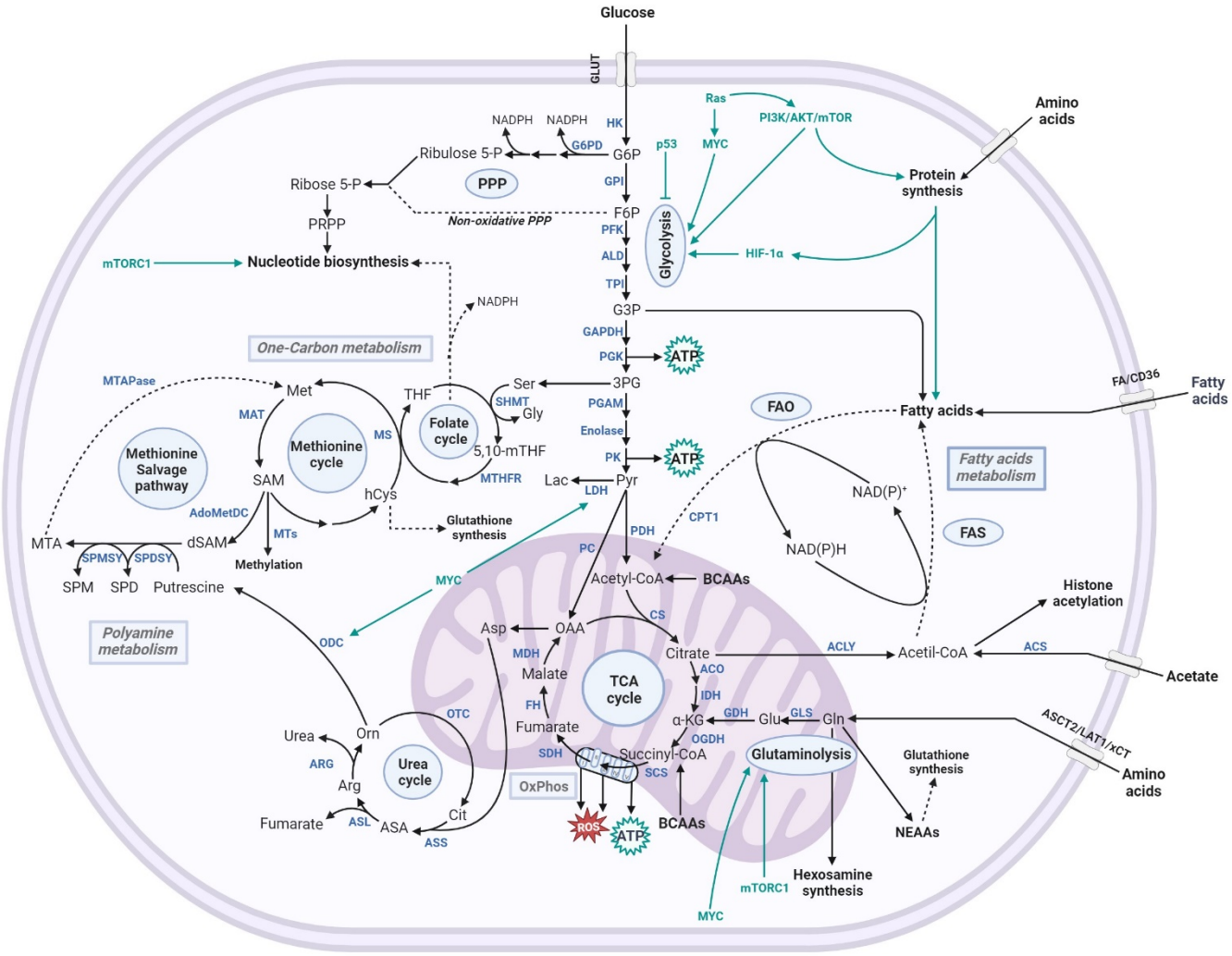

Figure 1.2.1. Metabolic and signaling pathways in cancer cells. Central metabolic pathways in cancer cells including glycolysis, serine biosynthesis, and one-carbon metabolism, comprised of the folate cycle, methionine and salvage pathways, polyamine synthesis, pentose phosphate pathway (PPP), urea cycle, the tricarboxylic acid (TCA) cycle, glutaminolysis, fatty acid oxidation (FAO) and fatty acid synthesis (FAS). Also, signaling pathways regulating metabolic genes (highlighted in green). **Enzymes** (highlighted in blue): ACLY; ATP citrate lyase, ACO; aconitase, ACS; acetyl-CoA synthetase, ALD; aldolase, AdoMetDC; adenosylmethionine decarboxylase, ARG; arginase, ASL; argininosuccinate lyase, ASS; argininosuccinate synthase, CPT1; carnitine palmitoyltransferase, CS; citrate Synthase, FH; fumarate hydratase, G6PD; glucose-6-phosphate dehydrogenase, GAPDH; glyceraldehyde-3-phosphate dehydrogenase, GDH; glutamate dehydrogenase, GLS; glutaminase, GPI; glucose-6-phosphate isomerase, HK; hexokinase, IDH; isocitrate dehydrogenase, LDH; lactate dehydrogenase, MAT; methionine adenosyltransferase, MDH; malate dehydrogenase, MTAPase; methylthioadenosine phosphorylase, MTHFR; methylenetetrahydrofolate reductase, MTs; Methyltransferases, MS; vitamin-B12 dependent methionine synthase, ODC; ornithine decarboxylase, OGDH; oxoglutarate dehydrogenase, OTC; ornithine transcarbamylase, PC; pyruvate carboxylase, PDH; pyruvate dehydrogenase, PFK; phosphofructokinase, PGAM; phosphoglycerate mutase, PGK; phosphoglycerate kinase, PK; pyruvate kinase, SCS; succinate-CoA ligase, SDH; succinate dehydrogenase, SHMT; serine hydroxymethyltransferase, SPDSY; spermidine synthase, SPMSY; spermine synthase, TPI; triosephosphate isomerase. **Abbreviations;** 5,10-mTHF; 5,10-metilentetrahydrofolate, ASA; argininosuccinate lyase, BCAAs; branched-chain amino acids, dSAM; decarboxylated SAM, F6P; fructose-6-phosphate, G3P; glyceraldehide-3-phosphate, G6P; glucose-6-phosphate, hCys; homocysteine, MTA; 5'-methylthioadenosine, NEAAs; non-essential amino acids, OAA; oxaloacetate, PRPP; phosphoribosyl diphosphate, SAH; S-adenosylhomocysteine, SAM; S-adenosylmethionine, SPD; spermine, SPM; spermidine, THF; tetrahydrofolate, α-KG; α-ketoglutarate. Figure created with https://www.biorender.com/ (2023), adapted from DeBerardinis & Chandel, 2016, Kerk et al., 2021, and Sanderson et al., 2019.

activation of signaling pathways such as PI3K/AKT/mTOR or *PTEN* and *INPP4B* loss.

- Use of central carbon metabolism, including glycolysis, tricarboxylic acid (TCA) cycle, and oxidative phosphorylation (OxPhos), for the biosynthesis of fatty acids, cholesterol, and non–essential amino acids.
- Use of autophagy and macromolecular lysosomal degradation via macropinocytosis as an alternative to nutrient acquisition, supported by PI3K/AKT/mTOR and RAS activation, independently of growth factor stimulation.
- Dependence on constant regeneration of electron acceptors (NAD+ and FAD) by increasing glycolysis and lactate production (Warburg effect) or electron transport chain (ETC) activity to generate protein and nucleic acid synthesis precursors.
- Increased cell defense mechanisms such as glutathione (GSH) and thioredoxin (TRX), or regulation through isocitrate dehydrogenase isoforms (IDHs) or pentose phosphate pathway (PPP) to increase ROS tolerance, NADPH regeneration, and to cope with cellular stress damage to prevent cell death.
- Increased demand for nitrogen sources, commonly increasing glutamine dependence, essential for macromolecules and non-essential amino acid synthesis to maintain the aberrant proliferation of cancer cells.

In this context, where cancer metabolism displays a specific phenotype, metabolic reprogramming is reported to contribute to cell malignant transformation and tumor initiation. However, whether metabolic alterations are a cause or a consequence of the malignant transformation is a debatable question (Seth Nanda et al., 2020).

On the other hand, cancer therapy promotes heterogenic genetic and epigenetic alterations whose downstream effects converge in metabolic pathway alterations. Therefore, increasing evidence suggests that targeting the metabolic reprogramming resulting from cell adaptation to chemotherapy represents an effective anti-cancer strategy (DeBerardinis & Chandel, 2016, Porporato et al., 2018, Seth Nanda et al., 2020, Stine et al., 2022).

1.2.1. Metabolic pathways altered in cancer cells

1.2.1.1. Glucose metabolism

Otto Warburg observed the altered energetic metabolism in cancer cells, describing the increased glucose uptake for lactate production despite oxygen presence as the Warburg effect or aerobic glycolysis (DeBerardinis & Chandel, 2016). Nowadays, it is reported that glycolysis is one of the most dysregulated pathways in cancer due to glucose being the primary energy and carbon source sustaining tumor proliferation (Hanahan & Weinberg, 2011, Martínez-Reyes & Chandel, 2021). It serves to derive intermediates to various biosynthetic pathways, such as serine biosynthesis or nucleotide metabolism, and also to produce reduced nicotinamide adenine dinucleotide phosphate (NADPH), which is an essential cofactor in cancer cells for FA, cholesterol synthesis, nucleic acids synthesis, and redox homeostasis (Shi et al., 2017, Stine et al., 2022) (**Figure 1.2.2.**).

Within this pathway, fructose-2,6-biphosphatase 3 (PFKFB3) is the most active among the PFKFB isoenzymes (PFKFB 1-4) and is considered a glycolytic orchestrator (Shi et

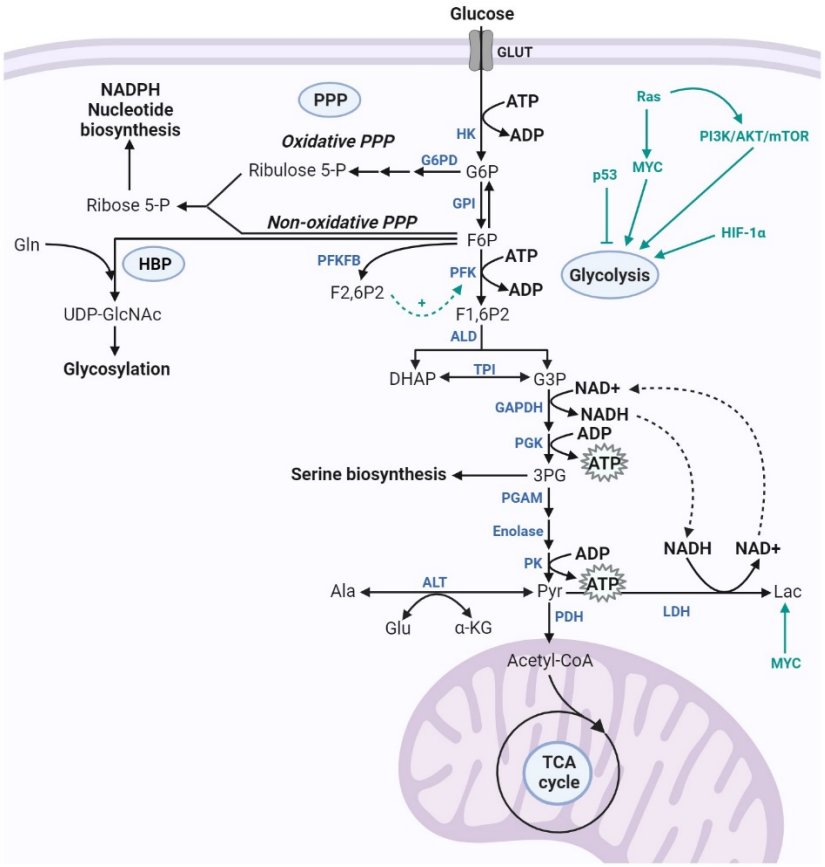

Figure 1.2.2. Glycolytic pathway in cancer cells. Glucose metabolic process upon complete oxidation generates ATP through Oxidative phosphorylation (OxPhos). Glycolytic intermediates serve for alternative biosynthetic pathways such as pentose phosphate pathway (PPP), hexosamine biosynthetic pathway (HBP), and serine biosynthesis. **Enzymes (highlighted in blue):** ALD; aldolase, ALT; alanine aminotransferase, G6PD; glucose-6-phosphate dehydrogenase, GAPDH; glyceraldehyde-3-phosphate dehydrogenase, GPI; glucose-6-phosphate isomerase., HK; hexokinase, LDH; lactate dehydrogenase, PDH; pyruvate dehydrogenase, PFK; phosphofructokinase, PFKFB; fructose-2,6-biphosphatase, PGAM; phosphoglycerate mutase, PGK; phosphoglycerate kinase, PK; pyruvate kinase, TPI; triosephosphate isomerase. **Abbreviations;** 3PG; 3-Phosphoglycerate, DHAP; dihydroxyacetone phosphate, F1,6P2; fructose-1,6-bisphosphate, F2,6P2; fructose-2,6-bisphosphate, F6P; Fructose-6-phosphate, G3P; Glyceraldehide-3-phosphate, G6P; Glucose-6-phosphate, PPP, Pentose phosphate pathway; α-KG; α-ketoglutarate. Figure created with https://www.biorender.com/ (2023), adapted from DeBerardinis & Chandel, 2016, and Kerk et al., 2021.

al., 2017). PFKFB3 is involved in both the synthesis and degradation of fructose-2,6-bisphosphate (F2,6P2), a regulatory molecule whose intracellular concentration activates phosphofructokinase-1 (PFK-1). This latter enzyme catalyzes the first rate-limiting step in the glycolytic process, fructose-6-phosphate (F6P) conversion to fructose-1,6-bisphosphate (F1,6P2) (Shi et al., 2017, Yi et al., 2019). The isoform PFKFB4 also regulates the glycolytic byproduct F2,6P2, and together with PFKFB3, are the most highly expressed PFKFB isoforms in cancer cells (Kotowski et al., 2021, Yi et al., 2019). These enzymes regulate the glycolytic flux and are required for cell cycle progression and apoptotic avoidance (Kotowski et al., 2021, Shi et al., 2017). Also, 3-phosphoglycerate (3PG) is an important intermediary that serves as an NADPH source while promoting serine biosynthesis, an essential amino acid for cell membranes, and is linked to folate and one-carbon metabolism for nucleotide synthesis, epigenetic modifications, and reductive metabolism (Ju & Lin et al., 2020, Stine et al., 2022).

The major contributor to NADPH generation is the flux deviation from the glucose pathway to the oxidative branch of the pentose phosphate pathway (PPP) (Ju & Lin et al., 2020). In this regard, glucose-6-phosphate dehydrogenase (G6PD) is one of the most important enzymes in PPP, contributing to ribose 5-P generation for nucleotide synthesis. G6PD activity is frequently increased in several cancer types, such as bladder, breast, prostate, or gastric cancer (Ju & Lin et al., 2020).

The last rate-limiting step in glycolysis is catalyzed by pyruvate kinase, producing pyruvate and ATP from phosphoenolpyruvate (PEP), and promoting the Warburg effect in cancer cells (Dong et al., 2020). The muscle form of pyruvate kinase isoform 2 (PKM2) is frequently found upregulated in cancer, in comparison with PKM1 isoform, and it is associated with increased glycolytic flux (Dong et al., 2020). Also, PKM2 promotes the use of glycolytic intermediates in alternative biosynthetic pathways such as PPP or serine synthesis (Dong et al., 2020, Taniguchi et al., 2016).

Pyruvate generated can enter the tricarboxylic acid (TCA) cycle and promote reducing equivalents generation by complete glucose oxidation through oxidative phosphorylation (OxPhos) by the electron transport chain (ETC) or through lactate production catalyzed by lactate dehydrogenase (LDH), which has a critical role in maintaining the NAD+/NADH ratio in cancer cells (Mullen et al., 2014, Stine et al., 2022). Glucose can also serve as an alanine precursor via the enzyme alanine aminotransferase (ALT), also known as glutamic-pyruvate transaminase (GPT), which has a significant function in the intermediate processing of glucose and amino acid metabolism (Stine et al., 2022). Also, a smaller glucose fraction enters the hexosamine biosynthesis pathway (HBP), which has a key role in protein glycosylation (Lam et al., 2021).

Increased glycolysis is associated with activated oncogenes such as *RAS*, *MYC*, *BRAF*, and PI3K/AKT signaling, which, alongside hypoxia and *TP53* depletion mutations, upregulate this pathway through glycolytic enzymes such as hexokinase 2 (HK2), the enzyme catalyzing the first step in glycolysis, or glucose transporters (GLUT) (Dong et al., 2020, Hanahan & Weinberg, 2011).

1.2.1.2. Mitochondrial metabolism

Mitochondrial metabolism is widely known for regulating programmed cell death, controlling mitochondrial outer membrane permeabilization, and preventing apoptotic events, but it also represents an essential contributor to tumor progression. The increased mitochondrial activity supports the rising bioenergetic demand and provides alternative carbon sources to glucose, such as acetate, lactate, serine, or glycine, as building blocks for cell proliferation while maintaining redox homeostasis (Porporato et al., 2018).

In this regard, the TCA cycle is the core cycle in the mitochondrial network, supporting OxPhos for electron donor generation (i.e., NADH or $FADH_2$) during GTP and ATP production (Yoo, Yu & Sung et al., 2020) (**Figure 1.2.3.**). Through the TCA cycle enzymes, which produce electron donors and direct them into the ETC complexes I through IV, OxPhos meets cells' bioenergetic needs. Complexes I, III, and IV pump protons out into the intermembrane gap while electrons travel through them. Oxygen serves as the final electron acceptor in the production of ATP, which is produced after protons flow back into the mitochondrial matrix through Complex V (ATP synthase)

(Greene et al., 2022). Alternatively, the TCA metabolic intermediates, citrate, isocitrate, α-ketoglutarate (α-KG), succinate, fumarate, malate, and oxaloacetate (OAA), are essential to fuel biosynthetic pathways to produce lipids, proteins, and nucleic acids. The reversibility of enzymatic reactions within the TCA cycle coupled to OxPhos, and the diverse anaplerotic sources, makes this pathway responsible for the major metabolic adaptation in response to TME interactions and drug presence (Mullen et al., 2014, Porporato et al., 2018). Therefore, the increased reliance on OxPhos has emerged in numerous aggressive cancer types and has become an attractive therapeutic target in cancer research (Ashton et al., 2018, El-Botty et al., 2023, Machado et al., 2023).

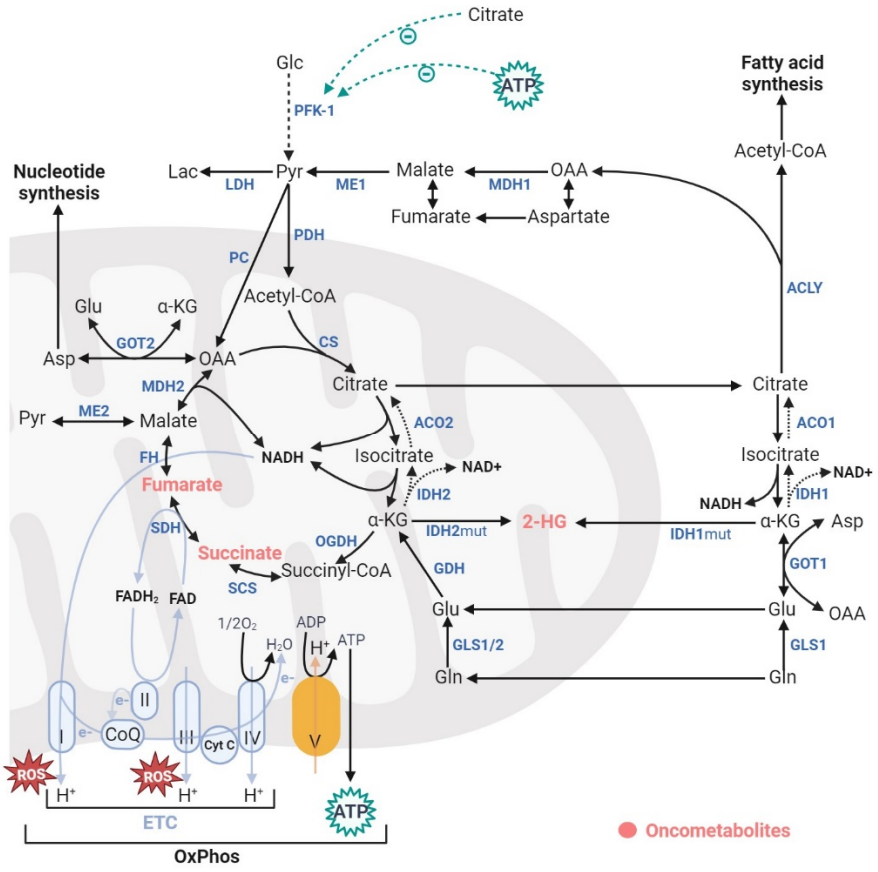

Figure 1.2.3. The tricarboxylic acid (TCA) cycle is coupled to oxidative phosphorylation (OxPhos). The TCA cycle follows the oxidative reaction, generating NADH and $FADH_2$ toward OxPhos (comprised by APTase (Complex V), and Complex I to IV of the electron transport chain (ETC)), for ATP and reactive oxygen species (ROS) production. Reversible reactions allow the reductive function of the TCA through the reductive carboxylation upon citrate. **Enzymes (highlighted in blue):** ACLY; ATP citrate lyase, ACO1/2; aconitase 1 and 2, CS; citrate Synthase, FH; fumarate hydratase., GDH; glutamate dehydrogenase, GLS1/2; glutaminase 1 and 2, GOT1/2; glutamic-oxaloacetic transaminase 1, IDH1/2; isocitrate dehydrogenase 1 and 2, IDH1/2mut; mutant isocitrate dehydrogenase 1 and 2, LDH; lactate dehydrogenase, ME1/2; malic enzyme 1 and 2, MDH1/2; malate dehydrogenase 1 and 2, OGDH; oxoglutarate dehydrogenase, PC; pyruvate carboxylase, PDH; pyruvate dehydrogenase, SCS; succinate-CoA ligase, SDH; succinate dehydrogenase subunits. **Abbreviations**; CoQ; Coenzyme Q, Cyt C; Cytochrome C, OAA; Oxaloacetate, α-KG; α-ketoglutarate. Figure created with https://www.biorender.com/ (2023), adapted from DeBerardinis & Chandel, 2016, Kerk et al., 2021, and Martínez-Reyes & Chandel, 2020.

The TCA cycle also serves as a significant provider of aspartate, essential for nucleotide metabolism, and represents an important source of citrate, the metabolite in the intersection between the anabolic and catabolic directions in the TCA cycle (Stine et al.,

2022). Citrate promotes the oxidative function for ATP production, OAA, and acetyl-CoA generation in the cytosol for fatty acid synthesis. On the other hand, citrate and ATP accumulation regulate the metabolic fluxes by increasing PPP deviation from glycolysis upon PFK-1 inhibition for NADPH production (Porporato et al., 2018).

Mutations affecting mitochondrial enzyme-related genes, such as *KRAS* and *APC*, but also drug presence or hypoxia, lead to mitochondrial function alteration to sustain aberrant proliferation. Also, mutations in succinate dehydrogenase (SDH) and fumarate hydratase (FH) causing loss-of-function are frequently found in cancer cells displaying defective mitochondrial activity and promote succinate and fumarate accumulation. On the other hand, isocitrate dehydrogenases IDH1 and IDH2 gain-of-function mutations trigger 2-hydroxyglutarate (2-HG) synthesis. All these metabolites are defined as oncometabolites since they lead to epigenetic modifications promoting cell transformation and altering cancer-driver mutations and protein expression (Porporato et al., 2018, Yoo, Yu & Sung et al., 2020).

Cancer cells overcome the mitochondrial impairment by increasing glutamine as a carbon source, promoting α-KG reductive carboxylation and conversion to isocitrate, taking advantage of the reversibility of NADPH-dependent isoforms of IDHs. Glutamine-dependent reductive carboxylation promotes citrate production for lipogenesis and OAA to supply other TCA cycle intermediates pool, thus enabling cells to maintain biosynthetic precursors despite the impairment of mitochondrial metabolism (Mullen et al., 2014, Yoo, Yu & Sung et al., 2020).

1.2.1.3. Amino acid metabolism

Amino acids maintain structure and function in non-transformed cells but also play an important role in cancer metabolism together with central carbon metabolism. Amino acids can be either metabolized for protein and non-nitrogenous molecules, such as glucose, glycogen, and fatty acids production, or oxidized to generate ATP, contributing to redox balance, and energetic and epigenetic regulation (Lieu et al., 2020, Stine et al., 2022).

The essential amino acids (EAAs) histidine, lysine, methionine, phenylalanine, threonine, tryptophan, and branched-chain amino acids (BCAAs; isoleucine, leucine, and valine) cannot be synthesized *de novo*, and they should be taken on diet instead. Together with non-essential amino acids (NEAAs) such as glutamine and asparagine, BCAAs serve as alternative fuels in nutrient deprivation conditions or hypoxia for tumor progression providing anaplerotic substrates for TCA cycle or generating succinyl-CoA and acetyl-CoA for further oxidation and lipogenesis (Lieu et al., 2020, Stine et al., 2022). These BCAAs are also implicated in epigenetics and post-transcriptional modifications promoting gene expression and cancer progression. Leucine, together with glutamine and arginine, mediates mTORC1 activation inducing amino acid transport for protein synthesis and ribosomal biogenesis, regulating growth signaling (Lieu et al., 2020, Ling et al., 2023, Stine et al., 2022).

On the other hand, non-essential amino acids (NEAAs) are essential precursors for one-carbon metabolism, nucleic acid, and protein synthesis (Stine et al., 2022). In this regard, aspartate, glycine, and glutamine are required for nucleobases in purine biosynthesis, which are conjugated to phosphoribosyl pyrophosphate (PRPP) yielding the

corresponding ribonucleotide in pyrimidine biosynthesis. Glycine, serine, and methionine provide one-carbon units through the methionine and folate cycles, comprising one-carbon metabolism, for *de novo* nucleotide biosynthesis, DNA methylation, and NADPH generation, representing an important source of reducing potential together with PPP (Lieu et al., 2020, Stine et al., 2022). In this regard, a relevant function of amino acids is cellular protection and redox homeostasis, due to the close connection with one-carbon metabolism, but also due to amino acids are essential precursors for glutathione tripeptide synthesis, which is comprised of glutamate, glycine, and cysteine and is an important endogenous antioxidant within cells (Hayes et al., 2020, Lieu et al., 2020, Stine et al., 2022).

Glutamine is a crucial non-essential amino acid in cancer cells, involved in many biosynthetic pathways supporting tumor growth and being their major carbon source (Lieu et al., 2020, Stine et al., 2022, Yoo, Yu & Sung et al., 2020). However, beyond glutamine, other NEAAs may also serve as alternative nitrogen and carbon donors, such as asparagine, which restores glutamine deprivation effects and protects cells from apoptosis upon mitochondrial impairment or hypoxia (Lieu et al., 2020, Pavlova et al., 2018), and proline, necessary for collagen synthesis and acting as an electron source for energy production (Pavlova & Thompson, 2022).

Considering the myriad of metabolic processes in which amino acids are involved, cancer cells frequently exhibit a high demand for amino acid uptake, promoting amino acid transporter upregulation (Lieu et al., 2020, Stine et al., 2022). This fact, also provides attractive therapeutic targets such as ASCT2 (*SLC1A5*), which is a neutral amino acid transporter essential for glutamine, alanine, serine, and cysteine transport, and cysteine/glutamate antiporter (xCT), indispensable for GSH synthesis (Lieu et al., 2020, Tarrago-Celada & Cascante, 2021). In this regard, transaminases are especially important in providing amino acids through interconversion reactions, encouraging the production of NEAAs such as phosphoserine, aspartate, and alanine, including glutamate–oxaloacetate transaminase (GOT1 and 2), phosphoserine aminotransferase 1 (PSAT1), glutamic-pyruvate transaminase (GPT1 and 2), and phosphoserine transaminase (PSAT) (Yang et al., 2017).

Catabolism of amino acids generates other intermediates that also interfere with tumor progression, such as polyamines (putrescine, spermine, and spermidine), derived from arginine conversion to ornithine mediated by arginase (ARG), playing an important role in epigenetics modifications, nitric oxide (NO) favoring angiogenesis for invasive processes, activating caspases and the tumor-suppressor *TP53*, kynurenine from tryptophan, which mediates immune responses, and 1-pyrroline-5-carboxylic acid (P5C) from proline, linking ornithine production toward urea cycle from glutamate and α-KG from TCA cycle (Stine et al., 2022).

1.2.1.3.1. Glutamine metabolism

Glutamine is involved in several metabolic processes representing the major nitrogen source for nucleotides, lipids, and NEAAs biosynthesis in cancer cells. This amino acid is an alternative carbon source providing metabolic intermediates, such as glutamate, aspartate, asparagine, alanine, arginine, or proline, nourishing the TCA cycle, also involved in nucleotide metabolism and redox homeostasis (Ju & Lin et al., 2020, Yoo, Yu

& Sung et al., 2020) (**Figure 1.2.4.**). Glutamine is indispensable for adaptative processes conferring drug resistance in many cancer types since it is involved in nutrient supply, antioxidant defense, hypoxia adaptation, cell signaling, epigenetic modifications, and, in turn, tumorigenesis. As a consequence, glutamine dependence is frequently observed in cancer cells (Ju & Lin et al., 2020, Yoo, Yu & Sung et al., 2020). In fact, glutamine deprivation impairs cell proliferation and is currently exploited as a therapeutic opportunity (Chen et al., 2021, Conroy et al., 2020 Hudson et al., 2016, Tarrado-Castellarnau et al., 2017, Wang et al., 2015).

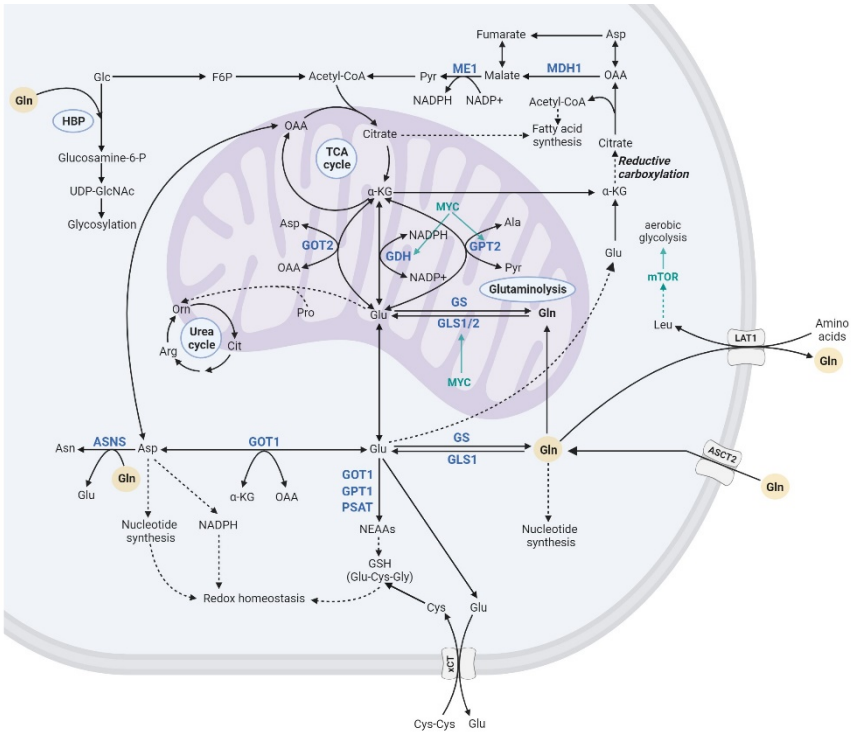

Figure 1.2.4. Glutamine metabolism in cancer cells. Glutamine takes part in several metabolic pathways serving as a carbon and nitrogen source fueling the TCA cycle, hexosamine biosynthetic pathway (HBP), and promoting non-essential amino acids (NEAAs), fatty acids, nucleotides, and glutathione synthesis. **Enzymes (highlighted in blue):** ASNS; asparagine synthetase, GDH; glutamate dehydrogenase, GLS1/2; glutaminase 1 and 2, GOT1/2; glutamic-oxaloacetic transaminase 1, GPT1/2; glutamic-pyruvate transaminase, 1 and 2, GS; glutamine synthetase, MDH1; malate dehydrogenase, ME1; malic enzyme, PSAT1; Phosphoserine Aminotransferase 1 (**Abbreviations**; OAA; Oxaloacetate, α-KG; α-ketoglutarate. Figure created with https://www.biorender.com/ (2023), adapted from Ju & Lin et al., 2020, Lieu et al., 2020 and Yoo, Yu & Sung et al., 2020.

Due to glutamine representing a pivotal role in cancer cells, increased glutamine uptake is normally observed by promoting glutamine transporters overexpression to enhance glutamine metabolism, notably the solute carrier ASCT2 (*SLC1A5*) (Stine et al., 2022, Zhang & Liu 2020). Cytosolic glutamine serves as nucleotide biosynthesis and NEAA precursor, required for highly proliferative cells, and also can be utilized in HBP, altering glycosylation and therefore affecting signaling transduction pathways, interfering in cell adhesion, migration, and invasion processes, and promoting cancer development and progression (Pinho & Reis 2015).

Glutaminases (isoforms GLS1 and GLS2) catalyze the first reaction toward TCA replenishment by glutamine deamination to glutamate. GLS1 activity is frequently found more active in cancer cells as a consequence of MYC overexpression (Stine et al., 2022, Zhang & Liu 2020, Yoo, Yu & Sung et al., 2020). Glutamate is a crucial glutamine-derived

metabolite essential for GSH biosynthesis in the cytosol, and a precursor for the divergent reactions supplying the TCA cycle (Forman et al., 2009). For mitochondrial glutaminolysis, cytosolic glutamine is internalized to the mitochondria through the SLC1A5 variant. Interestingly, even though glutamate is the primary by-product of glutamine, reduced mitochondrial respiration or impaired cell development cannot be restored by supplementing with glutamate during glutamine deprivation. Glutamate-derived glutamine is crucial for glutaminolysis (Yoo, Yu & Sung et al., 2020). Glutamate may be converted to α-KG supporting the TCA cycle but also can be exported to cytosol for GSH, NEAA, and nucleotides biosynthesis (Pavlova & Thompson, 2022, Stine et al., 2022, Yoo, Yu & Sung et al., 2020). During glutamate conversion to α-KG, the NADPH-dependent GDH represents an important source of reducing equivalents and generates glutamate-derived nitrogen as ammonia, that can be recycled by cancer cells for NEAA generation (Spinelli et al., 2017, Yoo, Yu & Sung et al., 2020). This α-KG conversion toward TCA replenishment is also performed through transaminases such as GOT2 and GPT2, producing NEAAs. α-KG generated to fuel the TCA cycle yields NADH or FADH2, GTP, and ATP, regulating histone and DNA methylation, and participating in fatty acid biosynthesis, or the reductive carboxylation pathway (Yoo, Yu & Sung et al., 2020). Glutamine-dependent reductive carboxylation supports cell proliferation inducing citrate production and lipogenesis, supporting cell proliferation, crucial under low-oxygen conditions or in cells presenting defective mitochondrial function (Metallo et al., 2011, Mullen et al., 2011).

Glutamine plays a pivotal role in maintaining redox homeostasis by glutaminolysis-derived NADPH generation, but also providing direct precursors for glutathione synthesis, being indirectly responsible for cystine uptake via the xCT antiporter for glutamate. Moreover, glutamine-derived aspartate is converted to OAA by GOT1, followed by transformation into malate, by malate dehydrogenase (MDH1) and is subsequently oxidized to pyruvate by malic enzyme (ME1), also contributing to NADPH generation (Ju & Lin et al., 2020, Yoo, Yu & Sung et al., 2020).

During metabolic reprogramming cancer cells orchestrate the metabolic pathways to increase demand for glucose and glutamine for cell survival. Notably, enhanced glutamine consumption, essential in cancer cells, is closely connected with the dysregulation of oncogenes such as MYC, PIK3CA, or mTOR. MYC-driven cancer cells increase glutamine uptake and glutaminolysis enzymes, inducing glutamine transporter SLC1A5, and GLS1/GLS2 and GDH for TCA cycle anaplerosis. With the same purpose, the oncogenic PIK3CA promotes the transamination reaction toward α-KG and alanine through upregulates of GPT2. Essential amino acids availability, and especially leucine, together with NEAAs derived from glutamine lead to mTORC1 activation, contributing to oncogenic growth (Yoo, Yu & Sung et al., 2020).

1.2.1.4. One-carbon metabolism

One-carbon metabolism comprises folate and methionine cycle, involved in*de novo* nucleotide biosynthesis, methylation, epigenetic regulation, and antioxidant defense (Affronti et al., 2020, Casero & Stewart et al., 2018, Lieu et al., 2020, Stine et al., 2022) (**Figure 1.2.5.**).

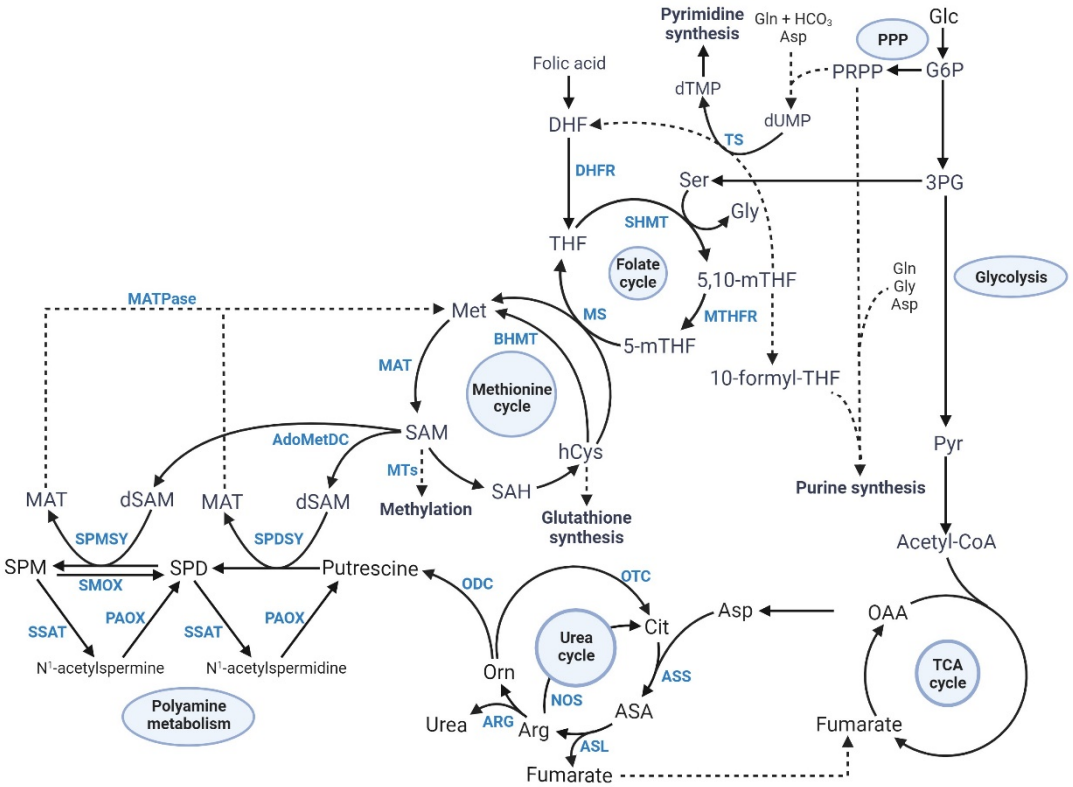

Figure 1.2.5. One-carbon metabolism, nucleotide synthesis, polyamine metabolism, and urea cycle. Metabolic pathways including one-carbon metabolism, comprised of folate and methionine cycles, nucleotide metabolism, methionine salvage pathway, polyamine synthesis, and urea cycle, indicating interconnected pathways and most important metabolic implications. **Enzymes** (highlighted in blue): AdoMetDC; adenosylmethionine decarboxylase, ARG; arginase, ASL; argininosuccinate lyase, ASS; argininosuccinate synthase, BHMT; betaine-homocysteine S-methyltransferase, DHFR; dihydrofolate reductase, MAT; methionine adenosyltransferase, MTAPase; methylthioadenosine phosphorylase, MTHFR; methylenetetrahydrofolate reductase, MTs; Methyltransferases, MS; vitamin-B12 dependent methionine synthase, NOS; nitric oxide synthase, ODC; ornithine decarboxylase, OTC; ornithine transcarbamylase, PAOX; polyamine oxidase, SHMT; serine hydroxymethyltransferase, SMOX; spermine oxidase, SPDSY; spermidine synthase, SPMSY; spermine synthase, SSAT; spermidine/spermine N1-acetyltransferase, TS; thymidylate synthetase. **Abbreviations;** 5-mTHF; 5-methyltetrahydrofolate, 5,10-mTHF; 5,10-metilentetrahydrofolate, ASA; argininosuccinate lyase, DHF; dihydrofolate, dSAM; decarboxylated SAM, dTMP; deoxythymidine monophosphate, dUMP; deoxyuridine monophosphate, F6P; fructose-6-phosphate, G6P; glucose-6-phosphate, MTA; 5'-methylthioadenosine, OAA; oxaloacetate, PRPP; phosphoribosyl diphosphate, SAH; S-adenosylhomocysteine, SAM; S-adenosylmethionine, SPD; spermine, SPM; spermidine, THF; tetrahydrofolate. Figure created with https://www.biorender.com/ (2023), adapted from Stine et al., 2022, Casero & Stewart et al., 2018 and Sanderson et al., 2019.

Serine conversion to glycine, catalyzed by serine hydroxymethyltransferases (SHMT1 and SHMT2), initiates one-carbon transfer to tetrahydrofolate (THF). The folate cycle is further completed by the NADP+-dependent methylenetetrahydrofolate dehydrogenases (MTHFD1/1L and MTHFD2/2L), entailing three sequential reactions. These reactions provide substrates for methionine and thymidylate, required for *de novo* synthesis of purines and serve as the primary source for NADPH regeneration, maintaining a high NADPH/NADP+ ratio which is crucial for the antioxidant defense molecules regeneration (Stine et al., 2022, Lieu et al., 2020). Both enzymes SHMT and MTHFD are usually found upregulated in several cancer types. Anti-folate treatment has a significant impact as an anti-cancer strategy in several cancer types such as different types of leukemia (ALL, CLL, CML), non-small-cell lung cancer (NSLCL), CRC, head and neck squamous cell carcinoma (HNSCC), gastric, pancreatic, breast, and ovarian cancers (Visentin et al., 2013, Stine et al., 2022).

Purine and pyrimidine nucleotide synthesis is essential for mRNA and DNA synthesis, highly required in rapid proliferative cells, and crucial for immune evasion, metastasis, and therapy resistance. In fact, nucleotide biosynthesis is frequently driven by oncogenic regulation including KRAS, PI3K, or MYC (Mullen & Singh, 2023). D*e novo* nucleotide synthesis requires amino acids and TCA intermediates, such as glutamine, glycine, glutamate, and aspartate to provide nitrogen and carbon atoms, glucose-derived ribose from PPP, and entails participation of different carbon oxidation states of tetrahydrofolate (THF) as the 1C carrier. *De novo* purine synthesis is a six-step process that requires formyl-THF (10-fomyl-TFH), while *de novo* pyrimidine synthesis is an eleven-step process requiring methylene-THF (5,10-mTHF) upon conversion of deoxyuridine monophosphate (dUMP) to deoxythymidine monophosphate (dTMP) mediated by thymidylate synthase (TS) (Stine et al., 2022).

The methionine cycle is crucial for methylation events by producing the universal methyl donor s-adenosylmethionine (SAM). Methylation in DNA, RNA, proteins, or phospholipids alters gene expression regulation, molecule stabilization, and protein interactions (Shen et al., 2020). Also, the methionine cycle is connected to the transsulfuration pathway for GSH synthesis after S-adenosylhomocysteine (SAH) hydrolyzation to homocysteine, which can be regenerated via the folate cycle, therefore comprising an important role in redox homeostasis (Hayes et al., 2020, Mota-Martorell et al., 2021). Furthermore, methionine metabolism is closely related to polyamine synthesis through the methionine salvage pathway. SAM serves as a polyamine precursor mediated by S-adenosylmethionine decarboxylase (AdoMetDC), and the 5-methylthioadenosine (MTA) generated is recycled through methionine salvage pathway, providing methionine and ATP catalyzed by 5′-methylthioadenosine phosphorylase (MTAPase) (Casero & Stewart et al., 2018).

1.2.1.5. The Urea cycle and polyamine metabolism

The urea cycle entails sequential biochemical reactions for the detoxification of the ammonia derived from proteins and amino acids, yielding urea for urinary secretion. The complete urea cycle only takes place in the liver; however, in other tissues, the urea cycle enzymes serve as source of endogenous arginine, citrulline, and ornithine, supporting anabolic reactions for carbon and nitrogen biosynthetic pathways in cancer cell metabolism (Keshet et al., 2018).

The citrulline-arginine cycle provides the arginine essential for cell survival and progression, serving as a precursor for polyamines, nitric oxide (NO), and proline. This cycle is also closely connected to the TCA cycle since argininosuccinate synthase (ASS) utilizes aspartate as a nitrogen donor and nourishes the TCA cycle with fumarate, a by-product from argininosuccinate lyase (ASL) (Keshet et al., 2018). ASS is the rate limiting enzyme in arginine biosynthesis, which encoding gene *ASS1* is frequently dysregulated in several cancer types, in fact *ASS1* is considered a tumor suppressor (Ding, et al., 2023, Zou & Hu et al., 2021).

Ornithine from the urea cycle is converted to putrescine by ornithine decarboxylase (ODC1), the rate-limiting enzyme for polyamine biosynthesis. In this regard, ODC1 and AdoMetDC activities are tightly regulated to preserve intracellular polyamine concentrations (Casero & Stewart et al., 2018) (**Figure 1.2.5.**). Polyamine metabolism

plays an important role in the normal prostate by secreting polyamines in the prostatic fluid and also participates in epigenetic regulation, cell signaling, antioxidant defense mechanism, apoptosis, and nucleotides synthesis, thus exerting advantageous functions to sustain rapid proliferation in cancer cells (Affronti et al., 2020, Casero & Stewart, 2018). Therefore, polyamine metabolism is frequently dysregulated in several cancer types, including prostate cancer, but also leukemias, lung, neural, and breast cancers (Affronti et al., 2020, Casero & Stewart et al., 2018, Seth Nanda et al., 2020).

Spermidine and spermine biosynthesis depends on SAM generated in the methionine pathway, which is converted into decarboxylated SAM (dSAM) by AdoMetDC and is the aminopropyl donor for spermidine synthase (SPDSY) and spermine synthase (SPMSY) (Casero & Stewart et al., 2018). MTA generated is recycled through the methionine salvage pathway by MTAPase, fueling one-carbon metabolism (Affronti et al., 2020, Casero & Stewart et al., 2018).

The intracellular polyamine concentration is controlled by spermidine/spermine N1-acetyltransferase (SSAT) activity, which catalyzes spermidine and spermine acetylation for back-conversion to putrescine by polyamine oxidase (PAOX) or secretion. Higher intracellular polyamines demand to sustain aberrant proliferation in cancer cells or polyamine deficit, induces SSAT activity, polyamine deacetylation by PAOX, or spermine oxidase (SMOX) for spermidine generation from spermine (Affronti et al., 2020, Babbar & Gerner, 2011, Casero & Stewart et al., 2018). Increased polyamine production implies additional pressure on other interconnected routes, such as one-carbon metabolism, and also is influenced by the interaction with important signaling pathways such as PI3K/AKT/mTOR, WNT, RAS, or MYC, which drives ODC transcription and has been reported as one of the major drivers of polyamine dysregulation on cancer cells (Casero & Stewart et al., 2018).

1.2.1.6. Lipid metabolism

Lipid metabolism is commonly found dysregulated in cancer because cells usually rely on either *de novo* fatty acid synthesis (FAS) or exogenous uptake to sustain rapid proliferation and provide energy under metabolic stress conditions through β-oxidation. Fatty acids play an essential role in cell membrane synthesis, homeostasis, and fluidity and serve as secondary messengers in signaling pathways such as PI3K/AKT/mTOR (Koundouros & Poulogiannis, 2020). In this regard, ceramides and sphingolipids are important bioactive lipids, such as the sphingosine-1-phosphate (S1P), regulating cancer cell signaling, taking part in both cancer cell death and survival, and in cellular stress response (Ogretmen, 2018).

As commented, fatty acids could be incorporated from exogenous sources by increasing fatty acids transporters such as fatty acid translocase (FAT/CD36), fatty acid transport protein (FATP) family, which is formed by the solute carriers family 27 (SLC27) members, and membrane fatty acid-binding proteins (FABPpm) (Koundouros & Poulogiannis, 2020). Once inside the cells, fatty acids could be either stored in droplets to provide reducing equivalents and ATP under cellular stress conditions or delivered for fatty acid oxidation (FAO), representing a major energy source. This process entails the participation of three connected metabolic pathways: the β-oxidation pathway, the TCA cycle, and the respiratory chain (Koundouros & Poulogiannis, 2020, Stine et al., 2022).

Then fatty acids are converted into acylcarnitines through carnitine palmitoyltransferase 1 (CPT1) for fatty acids internalization to the mitochondria, being the rate-limiting step for FAO, and acylcarnitines are reconverted to acyl-CoA by carnitine palmitoyltransferase 2 (CPT2) for further acetyl-CoA oxidation and catabolism (Koundouros & Poulogiannis 2020, Stine et al., 2022) (**Figure 1.2.6.**).

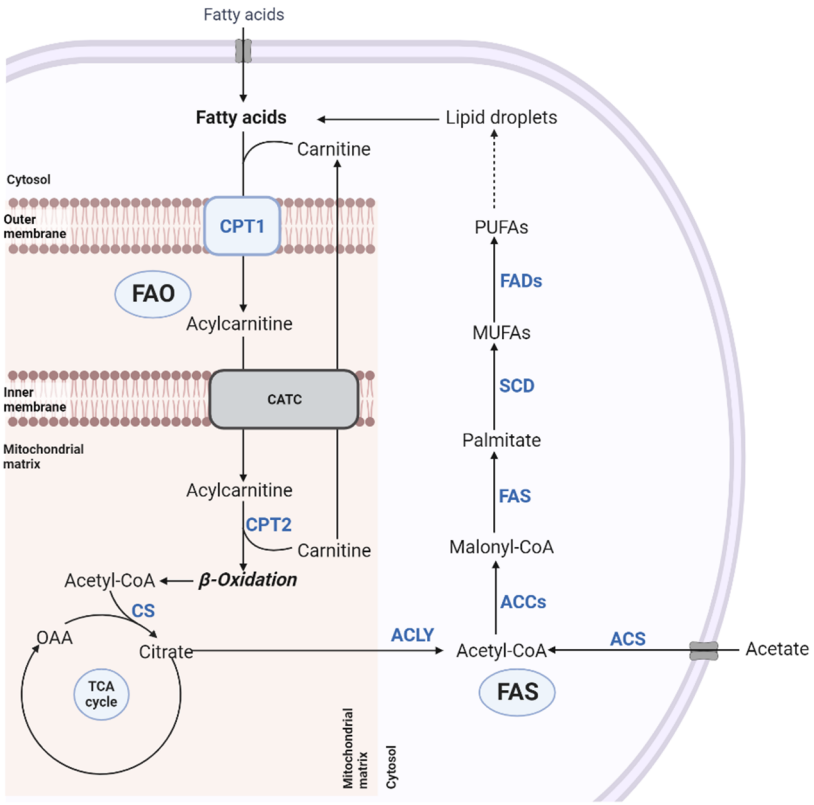

Figure 1.2.6. Fatty acid oxidation (FAO) and fatty acid synthesis (FAS) pathways. Fatty acids can be either de novo synthesized, internalized, and metabolized for energy and NAD(P)H production**. Enzymes**: ACCs; acetyl-CoA carboxylases, ACLY; ATP citrate lyase, ACS; acetyl-CoA synthetase, CPT1/2; carnitine palmitoyltransferase 1 and 2, respectively, CS; citrate synthase, FADs; fatty acid desaturases, FAS; fatty acid synthase, SCD; stearoyl-CoA desaturase. Figure created with https://www.biorender.com/ (2023), adapted from Melone et al., 2018, and Yoo, Yu & Sung et al., 2020.

Increased *de novo* lipogenesis in cancer cells provides all types of lipids necessary for cell proliferation utilizing glucose and amino acids, notably glutamine, as carbon sources. In this case, acetyl-CoA represents the major substrate for fatty acid synthesis (FAS), which can be obtained from citrate, or via acetyl-CoA synthetase (ACS) from acetate. Citrate is converted in acetyl-CoA by ATP citrate lyase (ACLY) as the first step reaction for fatty acids and cholesterol synthesis. Acetyl-CoA carboxylases (ACCs) generate malonyl-CoA for further chain elongation by fatty acid synthase enzyme (FAS), requiring NADPH cofactor for saturated 16-carbon palmitate (C16:0) generation. Palmitate can produce additional and more complex lipids through the activity of desaturases such as stearoyl-CoA desaturase (SCD) or fatty acid desaturase (FADs) and elongases (ELOVLs) (Koundouros & Poulogiannis, 2020, Stine et al., 2022).

1.2.2. Signaling pathways in cancer metabolism

Signaling pathways such as the serine/threonine-specific protein kinases and mitogen-activated protein kinase RAS/RAF/MAPK, phosphatidylinositol 3-kinase (PI3K) and its downstream components AKT and mammalian target of rapamycin (mTOR), and tumor

protein p53 (TP53) control the cell cycle, apoptosis, senescence, cell growth, and survival in normal cells, which activate transcriptional reprogramming by inducing MYC and other transcription factors stimulated by nutrients, oxygen, and amino acids availability (**Figure 1.2.1.**). Thus, these signaling pathways regulate metabolic, mitochondrial, and ribosomal genes as well as post-transcriptional modifications controlling the activity of metabolic enzymes. Therefore, signaling pathway dysregulation by aberrant activation independently of growth signals in cancer cells, e.g., PTEN loss, which is the major negative regulator of PI3K impairing AKT activation and consequent signaling cascade (Koundouros & Poulogiannis, 2020, Lee et al., 2018), or TP53 loss, leads to uncontrolled tumor proliferation and altered redox homeostasis (DeBerardinis & Chandel, 2016, Martínez-Reyes & Chandel, 2021, Seth Nanda et al., 2020, Stine et al., 2022).

In fact, PI3K/AKT/mTOR is the most dysregulated signaling pathway in cancer, controlling the biosynthesis of the three types of macromolecules essential for cancer metabolism: lipids, proteins, and nucleic acids (DeBerardinis & Chandel, 2016, Koundouros & Poulogiannis, 2020, Seth Nanda et al., 2020). AKT activation contributes to *de novo* lipogenesis by promoting anabolic reactions to provide carbon sources, increasing acetyl-CoA synthesis, and inducing the synthesis of reducing equivalents essential for redox homeostasis and fatty acid synthesis (Koundouros & Poulogiannis, 2020, Stine et al., 2022), by activation of nuclear factor erythroid 2-related factor 2 (NRF2) transcription factor driving the transcription of genes related to NADPH synthesis such as 6-phosphogluconate dehydrogenase (6PGD), glucose-6-phosphate dehydrogenase (G6PD) and malic enzyme 1 (ME1) (Koundouros & Poulogiannis, 2020). The mammalian target of rapamycin complex I (mTORC1) promotes amino acids, glucose, and fatty acids uptake mediated by MYC activation to drive lipogenesis and nucleotide and protein synthesis (DeBerardinis & Chandel, 2016, Stine et al., 2022). mTORC1, as well as oxygen depletion (hypoxia), activates the hypoxia-inducible factors (HIF1α and HIF2α), inducing the glycolytic flux and promoting lactate and serine production, therefore supporting one-carbon metabolism. MYC functions as a transcription factor exerting an important role in cell cycle progression and apoptosis but also induces glutamine catabolism, boosting the TCA cycle and providing precursors for fatty acids and nucleotide synthesis (Bretones et al., 2015, Stine et al., 2022).

1.2.3. Reactive oxygen species and redox homeostasis in cancer

Reactive oxygen species (ROS) are a group of compounds that comprises oxidant molecules, including superoxide radical ($\cdot O_2^-$), hydrogen peroxide (H_2O_2), peroxynitrite ($ONOO^-$), the hydrogen peroxide's product from the Fenton reaction which leads to the most oxidizing type of ROS, i.e., hydroxyl radical ($HO\cdot$), organic hydroperoxides (ROOH), also peroxyl ($ROO\cdot$) and alkoxyl ($RO\cdot$) radicals, which are intermediates and by-products from lipid peroxidation, and other non-radical ROS such as ozone (O_3) and singlet molecular oxygen ($^1O_2$) (Chatterjee & Walker, 2017, Sies & Jones, 2020). ROS is used as a general term that also encompasses the reactive nitrogen species (RNS), i.e., nitric oxide ($NO\cdot$), that similarly to oxygen species, are produced by normal cells in basal conditions as a consequence of cell metabolism (Hayes et al., 2020).

The most common ROS, superoxide radicals and oxygen peroxide, are mainly generated by the electron transport chain (ETC) at complexes I and III (Sies & Jones, 2020, Hayes et al., 2020) (**Figure 1.2.3.**). They are also produced by the reduction of O_2 by NADPH

oxidases, and there is a smaller contribution from cytochrome P450, cyclooxygenases (COX), and monoamine, xanthine, glycolate, hydroxy acid, aldehyde, and amino acid oxidases (Hayes et al., 2020). Increased ROS production is observed in cancer cells as a consequence of rapid cancer proliferation, allowing signaling pathways (PI3K and MAPK) and transcription factors (HIF and nuclear factor κβ (NF-κβ)) activation, regulating cell cycle progression, and supporting cell proliferation by promoting genetic instability, tumor growth, migration, and metastatic processes (Boonstra & Post, 2004, DeBerardinis & Chandel, 2016, Shah & Rogoff, 2015).

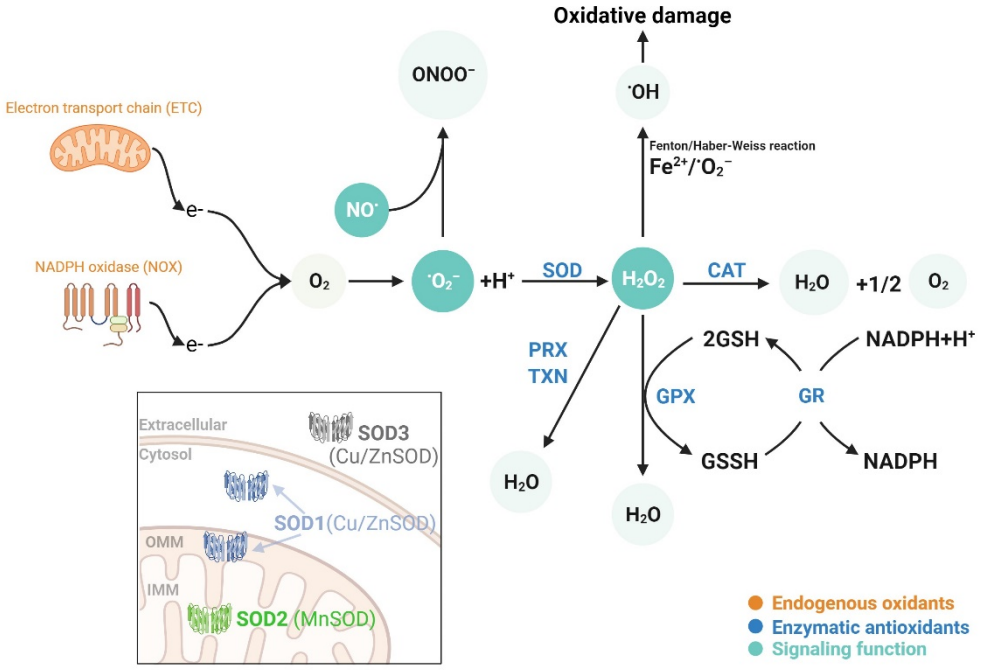

Figure 1.2.7. Enzymatic cell defense system for superoxide scavenging. Electron transport chain (ETC) and NADPH oxidase (NOX) represent the major superoxide (·O_2^-) sources. This superoxide reacts with nitric oxide (NO·) producing peroxynitrite ($ONOO^-$). Superoxide dismutase (SOD) catalyzes the ·O_2 dismutation to hydrogen peroxide (H_2O_2). H_2O_2 generates the hydroxy radical (OH·) through the Fenton/Haber-Weiss reaction, and can also be converted into water through catalysis by enzymes such as catalase (CAT), glutathione peroxidases (GPX), peroxiredoxins (PRX), or thioredoxin (TXN). Figure created with https://www.biorender.com/ (2023), adapted from Kitada et al., 2020, and Hamada et al., 2014.

ROS, notably H_2O_2, are indispensable for cellular signaling and used as secondary messengers by growth factors and oncogenes, modulating cell proliferation, migration, and survival (DeBerardinis & Chandel, 2016). ROS also play a pivotal role in cell cycle progression depending on their concentration. Low ROS levels promote protein oxidation in cysteine residues, leading to positive regulation of cell proliferation and protection against cellular stress (DeBerardinis & Chandel, 2016), and can also activate signal transduction pathways serving as mitogens, inducing cell proliferation, regulating protein expression of essential proteins for the G1 to S phase and cell cycle progression (Boonstra & Post, 2004, Menon et al., 2003). On the other hand, moderate or prolonged ROS levels promote cell cycle arrest in the G1 phase of the cell cycle and contribute to the expression of some of the cyclin D isoforms. Finally, high ROS levels and the presence of the most reactive compounds, such as superoxide and peroxynitrite radicals, promote oxidative damage in nucleic acids, proteins, and lipids. DNA damage induces P53 activity leading to growth suppressor P21 expression and, in turn, preventing CDKs

complex formation and cell cycle progression. This cell cycle arrest may be transient or permanent depending on the lesion and P21 activation (Boonstra & Post, 2004). Thus, redox balance is essential to control cell cycle progression but also to maintain a reduced state and cell homeostasis to support cell growth and evade oxidative stress, which is the molecular damage promoted by excessive ROS, leading to inflammation, senescence, apoptosis, or ferroptosis (Hayes et al., 2020, DeBerardinis & Chandel, 2016).

Therefore, cancer cells frequently develop counterbalance mechanisms to increase ROS tolerance, preventing oxidative damage events mediated by ROS activation by relying on several pathways involved in ROS homeostasis such as the glycolytic intermediates participating in connected metabolic pathways that contribute to generating reducing equivalents, for instance, the NADPH derived from PPP or through ME and IDH1 in the cytosol but also the NADH and $FADH_2$ generated from FAO during acetyl-CoA synthesis and ATP production. The folate cycle, the methionine cycle, and the transsulfuration pathway comprising one-carbon metabolism are also directly involved in ROS homeostasis by GSH synthesis and reducing potential generation (Lieu et al., 2020, Panieri & Santoro, 2023).

One of the principal mechanisms exerting antioxidant response in cancer cells is NRF2 activation, which induces the upregulation and transcription of many other antioxidant molecules and increases NADPH-producing metabolic pathways required to maintain the multiple antioxidant defense systems (Bansal & Simon, 2018, DeBerardinis & Chandel, 2016, Hayes et al., 2020). To overcome cellular stress damage, cells possess endogenous antioxidant cell defense mechanisms involving non-catalytic molecules, including α-lipoic acid, bilirubin, melanin, GSH, melatonin, and uric acid, and catalytic molecules that detoxify ROS to water (Hayes et al., 2020). The superoxide dismutase (SOD) family plays an important role in detoxifying the most common and damaging species that interfere with cell metabolism, i.e. $\cdot O_2^-$ and H_2O_2. SOD family comprises cytosolic copper/zinc superoxide dismutase (Cu/ZnSOD), also known as SOD1, mitochondrial manganese superoxide dismutase (MnSOD) or SOD2, and extracellular superoxide dismutase (Cu/ZnSOD) or SOD3 (Hayes et al., 2020). These enzymes scavenge specifically superoxide radicals to H_2O_2, which later are detoxified to O_2 and water by catalase (CAT) or by peroxiredoxins (PRX), thioredoxin (TXN), and glutathione reductase (GR), requiring NADPH cofactor for oxidized glutathione (GSSG) regeneration to GSH (Hayes et al., 2020, DeBerardinis & Chandel, 2016) (**Figure 1.2.7.**).

1.2.4. Tissue-specific metabolic profiling

Despite the common metabolic hallmarks found in cancer cells, there is growing evidence that metabolic reprogramming enabling tumor formation and progression differs depending on the tissue, therefore making it essential to acknowledge the metabolic features of the tissue-of-origin as direct influences to tumor metabolism (Bader & McGuire, 2020, Pavlova & Thompson, 2016, Pavlova & Thompson, 2022).

1.2.4.1. Colorectal cancer metabolism

CRC is strongly associated with family history; however, these cases do not represent the most common type diagnosed. Most CRCs arise because of disease progression

caused by sequential mutation accumulation (La Vecchia & Sebastián, 2020). Normal intestinal epithelium faces constant exposure to external harmful factors, requiring a high turnover rate to maintain the integrity of the gut lining. This tissue is comprised of Paneth cells and ISCs, neighboring cells that exhibit distinct metabolic profiles, particularly regarding lipid and glucose metabolism, and engage in constant interactions to sustain the self-renewal processes. It is believed that any metabolic alteration within this crosstalk is involved in tumor initiation (Barker et al., 2009, La Vecchia & Sebastián, 2020, Krausova & Korinek, 2014). In this regard, the enhancement of glycolysis, TCA, and cysteine and methionine metabolism observed in the early stages of CRC is mediated through WNT activating mutations, which regulate central carbohydrate metabolism, controlling glucose metabolism by transcriptional regulation of pyruvate dehydrogenase kinase 1 (PDK1) and the solute carrier transporter of pyruvate and lactate (MCT1), promoting angiogenesis, EMT, and cell migration (La Vecchia & Sebastián, 2020, Tarrago-Celada & Cascante, 2021). WNT activation, together with APC LoF mutation, is present in the majority of CRC and supports cell proliferation by contributing to ROS signaling modulation through TIGAR and RAC1 induction, which promote glutathione regeneration and increase ROS and apoptosis tolerance (Cheung et al., 2013, Myant et al., 2013, Zhang & Shay 2017).

Sequential mutations in many oncogenic signaling pathways, such as KRAS, WNT, MYC, PI3K/AKT, and TP53 pathways, play a major role in CRC progression (Brown et al., 2018). Other cases of CRC emerge through different mechanisms, including activating mutations in *BRAF* in serrated lesions or defective DDR-related genes in MSI tumors. Although these mutations can also lead to metabolic alterations, *KRAS* mutations are the most common in CRC and are considered drivers of metabolic reprogramming (Kerk et al., 2021). Indeed, KRAS activation increases glucose metabolism and regulates glutamine, amino acid, and lipid metabolism, improving metabolic adaptability and flexibility response against cellular stress promoted by increased ROS or nutritional depletion (La Vecchia & Sebastián, 2020, Kerk et al., 2021).

Altogether, the most common driver mutations described for CRC are also important metabolic regulators. This crosstalk promotes cancer stem cell phenotype, supporting cell survival, metabolic plasticity, tumor progression, and metastasis (La Vecchia & Sebastián, 2020). It has been reported that CRC metabolism is characterized by increased glycolysis, TCA cycle, and glutamine, amino acid, lipid, nucleotide, and steroid metabolisms, compared to benign tissue (Tarrago-Celada & Cascante, 2021). Increased aerobic glycolysis is associated with GLUT1, HIF-1α, hexokinase 1 and 2 (HK1/2), PKM2, and LDH upregulation. On the other hand, CRCs present an increased dependence on glutamine in anabolic and anaplerotic demands. In this regard, important core enzymes such as GLS1 and GDH are frequently upregulated, as well as the mitochondrial aspartate glutamate carrier (SLC25A13) (Tarrago-Celada & Cascante, 2021). The transsulfuration enzyme cystathionine-β-synthase (CBS) is also aberrantly enhanced in CRC, contributing to the increased glycolytic and PPP fluxes, lipogenesis, and glutathione metabolism, required for ROS scavenging (La Vecchia & Sebastián 2020 Phillips & Zatarain et al., 2017). Lipid metabolism is also commonly altered in CRC. Lipogenesis, elongation, and unsaturation of fatty acids are increased, as well as β-oxidation, by enhancing the rate-limiting enzyme CPT1A (Tarrago-Celada & Cascante, 2021, Wang et al., 2018). These events correlate with PPARγ, SREBP1/2, and FASN frequent upregulation in CRC, which, in turn, stimulates glycolysis and NADPH

production (La Vecchia & Sebastián, 2020). In fact, increased FAO in CRC has been associated with metastasis promotion in both the lymph node and the liver (Lee et al., 2019, Wang et al., 2018), being the latter the most common metastatic site in mCRC (Zhou et al., 2022).

Adaptation to hypoxic and oxidative damage conditions is essential for further metastatic progression and involves cystine import and folate metabolism for nucleotide and fatty acid synthesis and redox homeostasis (Tarrago-Celada & Foguet et al, 2021). Once in the metastatic site, the metabolic profile is also characteristic in mCRC. Hepatic cells increase lysine metabolism through the thrombopoietin (TPO) receptor CD110 to ultimately activate WNT signaling, fructose metabolism through aldolase B (ALDOB) to increase glycolysis, PPP, and gluconeogenesis fluxes, as well as phosphocreatine uptake through creatine kinase brain-type (CKB) induction to replenish the intracellular ATP pools (Bu et al., 2018, La Vecchia & Sebastián, 2020, Tarrago-Celada & Cascante, 2021).

Therefore, metabolic reprogramming plays a major role not only in tumor initiation and progression but also in metastatic adaptation in CRC. Hence, understanding CRC metabolism and identifying key players in metastatic development and drug resistance is crucial for improving CRC therapy (Bu et al., 2018, La Vecchia & Sebastián, 2020, Tarrago-Celada & Foguet et al., 2021).

1.2.4.2. Prostate cancer metabolism

Normal prostate function is controlled by the *AR* transcription factor, which is activated upon testosterone and DHT binding (Desai et al., 2021), expressing genes involved in cell survival, but also glycolysis, mitochondrial respiration, and lipid synthesis, as well as specific transporters such as zinc and aspartate solute carriers (i.e., SLC39A1 and SLC1A1, respectively) (Ahmad et al., 2021, Bader & McGuire, 2020). Aspartate, together with glucose, serves as a citrate precursor, and zinc acts as a mitochondrial aconitase (ACO2) specific inhibitor, preventing citrate entrance into the TCA cycle for further oxidation. Hence, citrate accumulation is a key component in the normal prostatic fluid, and the TCA cycle is found to be truncated in non-cancerogenic epithelial prostate cells. Due to this TCA depletion, prostate cells rely on glycolysis for ATP production to accomplish energy requirements (Ahmad et al., 2021, Bader & McGuire, 2020, Germain & Lafront et al., 2023).

Unlike other cancer types where the Warburg effect emerges with tumor initiation, in prostate cancer, the aerobic glycolysis overlaps with the higher glycolytic rate already promoted in the benign prostate gland. Therefore, conversely to other cancer types, the primary tumors of prostate cancer cells depend on oxidative phosphorylation and lipogenesis rather than glycolysis. Oxidative phosphorylation is essential for aspartate generation, which plays a pivotal role in nucleotide metabolism and lipogenesis, and is correlated with prostate cancer progression, being a hallmark of this cancer type (Bader & McGuire, 2020, Cutruzzolà et al., 2017). Increased lipid synthesis is controlled by AR signaling, upregulating biosynthetic enzymes such as FASN or ACACA, providing structural lipids for cellular membranes and cholesterol synthesis (steroid hormone precursor), serving as an energy source, or acting as a secondary messenger promoting post-transcriptional modifications (Giunchi et al., 2019). Disease progression is

accompanied by the TCA cycle restoration to support increased oxidative phosphorylation, demonstrating increased TCA activity in prostate cancer compared to benign prostatic hyperplasia (BPH) and benign tissues (Bader & McGuire, 2020). ZIP proteins, mainly responsible for zinc transport, are lost during AR-mediated tumor progression, avoiding ACO2 inhibition. Then, prostate cancer cells reduce zinc accumulation and citrate secretion, promoting lipogenesis and amino acid metabolism instead, which are required for cell proliferation (Ahmad et al., 2021, Bader & McGuire, 2020, Franklin et al., 2005). In fact, citrate and α-KG depletion in serum is associated with an increased risk of being diagnosed with aggressive prostate cancer, and these metabolites have been presented as metabolic biomarkers in a cancer prevention trial (Mondul et al., 2015).

More advanced prostate cancers present higher glycolytic rates since prostatic fluid secretion depends on AR activity, which is altered in mCRPC. Genes related to glycolysis and PPP pathways (i.e., *GLUT1*, *HK1/2, G6PD*) are also regulated by AR, promoting this glycolytic activity. Glycolysis in primary and advanced prostate cancer is also supported by the main mutations found in this cancer type, such as *PTEN* and *TP53* LoF, leading to PI3K/AKT/mTOR aberrant activation (Ahmad et al., 2021, Rebello & Oing et al., 2021). mTORC1, in turn, regulates polyamine synthesis pathways affecting AMD1 stability and promoting dcSAM (Casero & Stewart et al., 2018).

Polyamine secretion is elevated in normal prostatic fluid, contributing to sperm maturation and motility. Dysregulation of the polyamine pathway is correlated with anchorage-independent cell growth and highly associated with disease progression in prostate cancer (Affronti et al., 2020, Seth Nanda et al., 2020, Zabala-Letona et al., 2017). Polyamine secretion rate is intensified with disease progression due to AR regulating key enzymes involved in one-carbon metabolism. The methionine salvage pathway maintains the methionine pools essential for SAM replenishment and polyamine synthesis. Therefore, AR signaling alteration in advanced prostate cancer impacts not just polyamine synthesis but also one-carbon metabolic-related events such as nucleotide biosynthesis, redox homeostasis, and epigenetic alterations (Bistulfi et al., 2016, Corbin et al., 2016). In fact, prostate cancer is correlated with aberrant DNA methylation altering *AR* expression but also affecting DNA damage repair genes (e.g. *MGMT*), the antioxidant response (e.g. glutathione S-transferases encoding gene *GSTP1*), cell-cycle regulation genes (e.g. CKIs family members), tumor-suppressor genes (e.g. APC) or apoptosis, invasion and metastasis-related genes (e.g. death-associated protein kinase (*DAPK*), E-Cadherin, and metalloproteinases) (Majumdar et al., 2011).

1.3. Cancer therapy

To tackle this complex disease, there are different therapeutic strategies depending on cancer type, tissue, stage, family history, and genetic profile. Treatments include surgery, which implies tumor ablation from the body; radiotherapy, promoting localized DNA damage by external or internal beam; and chemotherapy, which entails systemic pharmacological therapy. Both radiotherapy and chemotherapy target highly proliferative cells based on the constant division of cancer cells as an effective anticancer strategy (National Cancer Institute 2023). Due to the mechanism of action, these approaches represent the most widespread strategies applied for many cancer types. Nevertheless,

hormone therapy, immunotherapy, and stem cell transplant are also used in specific scenarios (Ganesh & Massagué, 2021, National Cancer Institute 2023). Hormone therapy is effective in cancer types whose proliferation is supported by hormones, such as prostate or breast cancer, although hormone resistance development is its main limitation. Immunotherapy works to improve (via immune cell therapy, monoclonal antibodies, vaccines, or immune system modulators) or suppress (via immune checkpoint inhibitors) the immune system to increase its capacity to fight specifically against cancer cells (National Cancer Institute 2023). In this context, PD-1/PD-L1 blockade immunotherapy is more likely to respond in high mutational burden or MSI tumors (Goodman et al., 2019), although they represent a minority of cancers diagnosed. Stem cell transplants improve the ability to produce stem cells destroyed after chemotherapy or radiotherapy; however, their usage is limited to targeting cancer cells in liquid cancer types such as leukemia, lymphoma, neuroblastoma, and myeloma (National Cancer Institute 2023).

Chemotherapy is one of the main focuses of this work. It is based on cell division impairment and includes alkylating agents that directly target DNA, generating DNA adducts and crosslinks (i.e., Cisplatin, Carboplatin, or Oxaliplatin) promoting DNA damage, and ultimately, cell death (Di Francesco et al., 2002, Kang et al., 2015, Monneret, 2011). Despite its significant efficacy as an anticancer treatment, it is worth mentioning that chemotherapies do not target selectively cancer cells but rapidly dividing cells, thus leading to associated side effects upon treatment. To address this, targeted cancer therapies have been developed over the last decades, becoming a foundation of precision medicine.

Targeted therapies are small-molecule drugs and monoclonal antibodies (mAbs) that target specific proteins or receptors in cancer cells (Baudino, 2015). This selective mechanism of action blocks proteins and/or signals essential for cancer cell growth, cell cycle control, or apoptosis regulation, specifically affecting cancer cells or the tumor microenvironment. Small molecules include several types of inhibitors targeting different proteins or pathways altered in cancer, such as tyrosine kinase (e.g., Imatinib, Gefitinic, or Sorafenic), CDKs (e.g., Palbociclib, Abemaciclib, or Ribociclib), proteasome (e.g., Carfilzomib) and PARP (e.g., Rucaparib). mAbs target extracellular proteins to interact with cell signaling, directly binding to antigens or cell receptors, targeting effector cells or phagocytosis. The most extensively utilized mAbs include Trastuzumab (targeting hormone receptor HER2) and Bevacizumab (anti-VEGF) (Lee et al., 2018). This category also contains novel gene therapy, providing, among other applications, a tool to introduce siRNA or antisense oligonucleotide to silence specific genes by knockout or correct the mutated sequence by CRISPR-Cas9 utilization, a very specific strategy to manipulate oncogenes or tumor suppressor genes identified as disease promoters (Chen et al., 2022, Lee et al., 2018). Clinical trials targeting PD-1 in several solid malignancies are ongoing (e.g. NLM; NCT02793856, NLM; NCT03545815, NLM; NCT03747965), and other studies are exploring further applications, such as the insertion of the prodrug-converting enzyme herpes simplex virus type 1 thymidine kinase (HSV1-tk) into the fusion genes TMEM135–CCDC67 (official symbol DEUP1) and MAN2A1–FER in prostate and hepatocellular carcinoma cancer cells to provide a potential lethal gene specifically targeting cancer cells (Chen et al., 2017).

Despite these options, therapy failure often arises upon chemotherapy and targeted therapies application due to therapy resistance (Di Francesco et al., 2002, Kang et al., 2015, Lee et al., 2018, Matthews et al., 2022, Monneret, 2011, Otto & Sicinski, 2017, Zhu et al. 2022). However, understanding the mechanisms underlying therapeutic resistance allows for the design and application of combination therapies involving targeted therapy and chemotherapy, which have been reported to be more effective than single-drug treatments (Lee et al., 2018, Matthews et al., 2022, Otto & Sicinski, 2017).

1.3.1. Therapeutic strategies in colorectal cancer and prostate cancer

1.3.1.1. Colorectal cancer detection, tumor stages and treatment

Colonoscopy-guided biopsy is the most commonly used tool to detect the primary tumors on the colorectal site since most CRCs diagnosed are localized or regional tumors (SEER Explorer 2023). However, a large percentage of cases (around 20%-30%) are diagnosed once the tumor has led to distant metastasis (SEER Explorer 2023, Biller & Schrag, 2021), usually found in lymph nodes and liver but also lung and peritoneum (La Vecchia & Sebastián, 2020, Biller & Schrag, 2021).

To select the optimum treatment for CRC, due to its heterogeneity, it is necessary to consider the tumor stage based on the TNM staging system (**Table 1.3.1.**), the genetic instability status (MSI and deficient-MMR or microsatellite stable (MSS)), and the tumor-driver mutations (e.g., RAS family).

The consensus molecular subtypes (CMS) have been proposed as a new classification for CRC based on gene expression profiling and phenotype to address its high heterogeneity, aiming to predict disease biomarkers and personalized drug responses to improve treatment efficacy (Fontana et al., 2019, Linnekamp et al., 2017, Menter et al., 2019, Singh et al., 2019, Sveen et al., 2017). These CMSs comprise four groups for tumor stratification, including (1) CMS1, which presents immune activation, MSI^{+}, and CpG island methylator phenotype (CIMP)-positive, (2) CMS2 with canonical pathways upregulation i.e., WNT/MYC-driven mutations, $BRAF^{V600E}$, Chromosomal instability (CIN)-positive, and presenting epithelial phenotype, (3) CMS3, which presents metabolic pathways dysregulation, epithelial phenotype, and KRAS-driven mutations, and (4) CMS4, which displays a mesenchymal phenotype with high stromal density and active TGF-β and VEGF pathways, with CIN^{+} (Fontana 2019, Linnekamp et al,. 2017, Menter et al., 2019, Singh et al., 2019, Sveen et al., 2017).

Regarding treatment options, localized stage I tumors are usually addressed by surgery. Early stages of CRC presenting MSI^{+} and MMR deficiency correlated with better patient outcomes since they are more likely to respond to immune checkpoint blockade therapy that is not effective for the rest of CRC variants (Seidel et al., 2018). Indeed, the standard of care treatment for MSS patients entails fluoropyrimidines-based chemotherapies, such as 5-Fluorouracil (5-FU) (Vodenkova et al., 2020). The treatment for more advanced disease stages frequently combines adjuvant therapy with fluoropyrimidine treatment to increase effectivity, with FOLFOX being the most common regimen (Van Cutsem et al., 2016). FOLFOX is a combination of the antimetabolite 5-FU, which targets thymidylate synthetase; Folinic acid (LV, leucovorin), which potentiates 5-FU action; and Oxaliplatin, which directly targets DNA by crosslink formation. Altogether, targeting DNA synthesis

and replication leads to cell growth impairment and cell death (Biller & Schrag, 2021, Oki et al., 2018).

Table 1.3.1. Colorectal tumor stages. Tumor stages are classified as stages I, II (A, B, C), III (A, B, C), and IV (A, B, C), classified in relation to location and spread to other body parts according to TNM staging. TNM, tumor-node-metastasis. T represents the size and extent of the primary tumor: T0, cannot be found; T1 (a,b,c sub-stages), localized in the submucosa; T2, localized in muscularis propria; T3, tumor growth reaching subserosa or pericolorectal tissue; T4 (a, b), regional spread to nearby tissues/organs. N describes the spread to lymph nodes: N0, not spread to lymph nodes; N1, spread to lymph nodes, affecting one (N1a), 2 or 3 regional lymph nodes (N1b), or nodules in surrounding tissues such as mesenteric or pericolorectal (N1c); N2, affecting 4 to 6 regional lymph nodes (N2a), or more than 7 (N2b). M represents distant metastasis: M0, no distant spread to other body parts; M1, spread to other body parts, one distant site (M1a), 2 or more (M1b), distant metastasis and peritoneum (M1c) (Amin et al., 2017). TNM, tumor-node-metastasis.

Stage of disease		Location	Tumor extent (TNM Stage)
Stage I	Stage I	Muscularis propria	T1-T2, N0, M0
Stage II	Stage II A	Subserosa or pericolorectal tissue	T3, N0, M0
	Stage II B	Visceral peritoneum	T4, N0, M0
	Stage II C	Grown in nearby structures	
Stage III	Stage III A	Cross the inner lining or muscle layers. Affects lymph nearby lymph nodes (no more than three) or nodule in tissues surrounding colon and rectum.	T1-T2, N1-N1c, M0
			T1, N2a, M0
	Stage III B	Cross the bowel wall or surrounding organs. Affects nearby lymph nodes (no more than three) or nodule in tissues surrounding colon and rectum.	T3-T4a, N1-N1c, M0
			T2-T3, N2a, M0
			T1-T2, N2b, M0
	Stage III C	Nearby lymph nodes (more than 4)	T4a, N2s, M0
			T3-T4a, N2b, M0
			T4b,N1-N2, M0
Stage IV	Stage IV A	Distant metastasis (one site)	M1a
	Stage IV B	Distant metastasis (more than one part)	M1b
	Stage IV C	Peritoneum and distant metastasis	M1c

Adjuvant chemotherapy varies depending on clinical recommendations. Based on 5-FU plus LV, the combination with Irinotecan (FOLFIRI) is also frequently used, and even triple treatment FOLFOXIRI is applied. CAPOX, which substitutes 5-FU with its prodrug Capecitabine, is another common chemotherapeutic regimen (Biller & Schrag, 2021, Oki et al., 2018). Other targeted therapies are also considered for colorectal cancer treatment; concretely, mAB anti-VEGF, anti-angiogenic inhibitor, or anti-EGFR are administered together with FOLFOX/FOLFIRI to improve progression-free survival (Pal et al., 2018). However, their application is limited by the *KRAS* mutation presented since it determines treatment response. *KRAS* wild-type patients are usually treated with anti-

EGFR (upstream RAS GTPases) monoclonal antibodies (i.e., panitumumab and cetuximab), but they frequently develop drug resistance (Pal et al., 2018). On the contrary, the same treatment is inefficient for patients presenting *KRAS*$^{+}$. Also, depending on codon location and the amino acid substitution in *KRAS* mutation (being the most common in CRC G12D, G12V, G13D, G13C, and G12A), the binding affinity with important effectors such as RAS or the sensitivity to targeted therapy could be affected. As an example, the targeted therapy *KRAS*^{G12C} inhibitor (Sotorasib) was approved for stage IV for NSCL (CodeBreaK201 phase II clinical trial, NCT04933695) (Huang, 2021). However, despite the therapeutic efforts, only a small percentage of patients who reach stage IV of the disease (around 18%) achieve a 5-year survival rate (Oki et al., 2018). Tumors, at the most advanced stages of the disease, frequently develop resistance, becoming refractory and presenting an extremely challenging clinical scenario.

1.3.1.2. Prostate cancer detection, tumor stages, and treatment

Determination of tumor stage is also crucial for treating prostate cancer. Several measurement tools are considered to determine prostate tumor aggressiveness and risk depending on the histopathological phenotype, size, location, patient context, and genetic predisposition. The most used are the PSA value in blood tests that positively correlates with disease progression, the Gleason grading system that assigns five different patterns depending on tumor histological features categorized from groups 1 to 5 by the International Society of Urological Pathology (ISUP), and the tumor-node-metastasis (TNM) staging system, clinically determined, that describes tumor size, location, and spread. Considering all these factors, tumor stages in prostate cancer have been defined as low-risk (grade 1, PSA<10 ng/mL, T1-T2a), medium-risk (grade 2 or 3, PSA 10-20 ng/mL, T2b), and high-risk (grade > 3, PSA > 20 ng/mL, > T2b) (Cancer Research UK 2022, National Cancer Institute 2023, Rebello & Oing et al., 2021) (**Table 1.3.2.**).

Prostate tumor presence is detected by measuring PSA serum level and/or via digital rectal examinations (DRE) (Germain & Lafront 2023, Rebello & Oing et al., 2021). PSA levels increase with prostate cancer development but also with benign prostate hyperplasia (BPH) of the transition zone of the prostate gland. Despite overdiagnosis, these early detection methods significantly have improved life expectancy and decreased up to 20% in mortality cases (Rebello & Oing et al., 2021). Localized low- and medium-risk tumors are usually controlled by active surveillance or physically removed by radical prostatectomy or radiotherapy (Parker et al., 2020, Rebello & Oing et al., 2021). In spite of these therapeutic options, the high recurrence rates are still rising, and more than 25% of patients register recurrence after the first-line treatment (Germain & Lafront 2023).

The standard approach for locally advanced tumors involves androgen deprivation therapy (ADT) to reduce gonadal androgen production based on androgen dependency of prostate cancer cells. This hormonal depletion can be achieved through either surgical castration (orchiectomy) or medical castration, which interferes with the gonadotropin-releasing hormone (GnRH). The GnRH impairment includes the use of GnRH agonists, such as Leuprolide, Goserelin, Histrelin, and Triptorelin. Also, through the stimulation of GnRH receptors, thereby regulating negatively the GnRH (i.e., Degarelix, Relugolix), and

Table 1.3.2. Prostate tumor stages. Tumor stages are classified as stages I, II (A, B, C), III (A, B, C), and IV (A, B), defined as low-, medium-, or high-risk considering PSA levels (raging from <10 (low value), 10-20 (medium value), to >20 ng/mL (high value), detection on DRE (yes/no), the histological pattern through GS observations where the final GS is a sum of the first and second most prominent patterns, scoring from 2 to 10, being well-differentiated cells with GS ≤ 6 (ISUP grade 1), moderately differentiated cells GS 7 (ISUP grade 2-3), and poorly-differentiated cells GS 8 - 10 (ISUP grade 4-5), and TNM staging where T represents the size and extent of the primary tumor (T0, cannot be found; T1 (a,b,c sub-stages), cannot be detected by DRE; T2 (a,b,c), in situ located inside the prostate gland; T3 (a,b), localized; T4, regional spread to nearby tissues/organs), N describes the spread to lymph nodes (N0, not spread to lymph nodes; N1, spread to lymph nodes), and M distant metastasis (M0, no distant spread to other body parts; M1 (a,b,c), spread to other body parts) (Cancer Research UK 2022, National Cancer Institute 2023, Rebello & Oing et al., 2021). DRE, Digital rectal examination; PSA, Prostate-specific antigen; GS, Gleason Score; ISUP, International Society of Urological Pathology; TNM, tumor-node-metastasis.

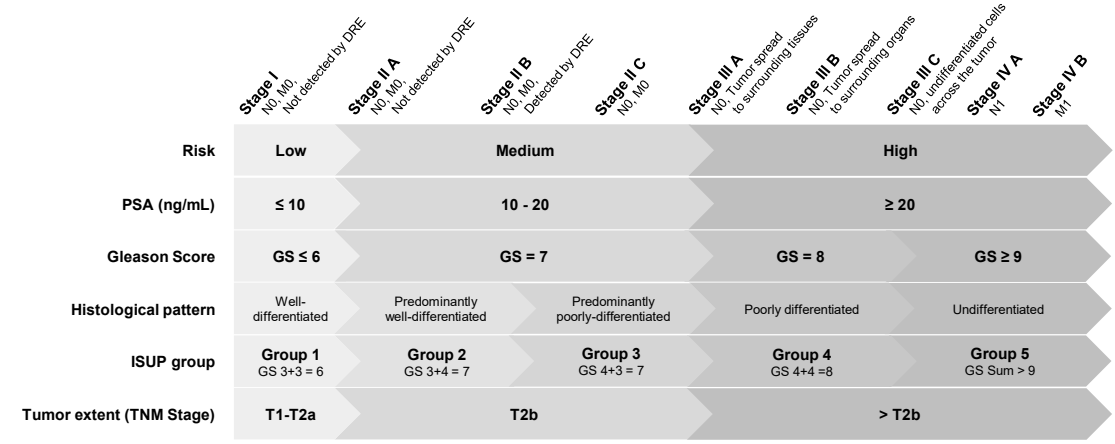

additionally, it involves the utilization of agents that inhibit GnRH receptors, like Degarelix and Relugolix, ultimately blocking testosterone production. Other current approaches impair extragonadal androgen production by inhibiting the CYP17A1 enzyme, a catalyzer for the synthesis of testosterone and DHT. This can be achieved using medications such as Abiraterone or Ketoconazole. Furthermore, there are next-generation AR antagonists, often referred to as androgen receptor signaling inhibitors (ARSIs), including Enzalutamide, Apalutamide, and Darolutamide. These ARSIs compete for the AR's ligand-binding domain, thereby impairing the attachment of testosterone or DHT to AR and downstream signaling processes (Desai et al., 2021).

More advanced and aggressive phenotypes of prostate cancer can affect several regions close to the prostate gland, such as regional metastasis in lymph nodes, or lead to distant metastasis, commonly appearing in bone (up to 85% of cases) but also in liver or thorax (Gandaglia et al., 2014, Rebello & Oing et al., 2021). The metastatic disease is usually treated with ADT for tumor burden reduction, followed by Docetaxel chemotherapy and prednisolone or ARSIs to increase treatment response. Second-line treatment includes Cabazitaxel plus Prednisolone, approved for tumors insensitive to Docetaxel, and radiotherapy is also applied depending on the metastasis extent. However, ADT usage frequently leads to therapy resistance promoting mCRPC, the most challenging event associated with prostate cancer (Rebello & Oing et al., 2021). At this point, only palliative approaches are alternative therapeutic options to increase overall survival (OV), such as the bone-targeted radionuclide Radium-223 chloride, effective specifically for bone-metastasis tumors, the ^{177}Lu-PSMA-617 targeted radiation therapy against PSMA-617-positive (prostate-specific membrane antigen) (VISION phase III trial, NCT03511664), or other targeted therapies such as Olaparib based on PARPi (poly(ADP-ribose) polymerase inhibition) for patients presenting deficient DDR, and monoclonal antibodies (Nivolumab (CheckMate 9KD phase II trial, NCT03338790) and Pembrolizumab),

effective for patients with MSI or MMR mutations in combination with PARPi (Parker et al., 2020, Rebello & Oing 2021).

In brief, the most advanced cancer disease requires the search for novel therapies, that may be performed by employing drug repositioning strategies to repurpose effective existing drugs for combination therapies (Pushpakom et al., 2019). The study of cancer metabolism is a pivotal component of this approach, as emerging evidence highlights the intricate relationship between metabolic pathways and drug resistance (La Vecchia & Sebastián, 2020). To validate alternative drugs and treatment strategies, it is crucial to consider their metabolic effects, given the established connection between metabolic reprogramming and adaptive responses.

1.3.2. Delving into Oxaliplatin and Palbociclib treatments

1.3.2.1. Oxaliplatin treatment in cancer

The first-generation platinum (Pt) II compound Cisplatin (Platinol®) was discovered serendipitously by Barnett Rosenberg in 1965 (Rosenberg et al., 1965) and exploited as a highly effective antitumor drug, which meant a significant improvement in chemotherapy efficiency, especially for bladder, testicular, and ovarian cancer. Despite platinum-based chemotherapy being widely used nowadays, the side effects and acquired resistance coexist with the highly effective cytotoxic effect on cancer cells (Monneret, 2011). To address this, the next generation of platinum agents has been developed over the years (Di Francesco et al., 2002, Kang et al., 2015, Monneret, 2011).

In this regard, Oxaliplatin (Eloxatin®), the third-generation compound derived from Cisplatin, was approved by the FDA in 2002 and authorized in the European Union for the treatment of colorectal cancer upon failure with primary treatment. Later, in 2004, it was approved for treating advanced colorectal cancer in combination with 5-Fluorouracil and folinic acid (Leucovorin; LV), known as FOLFOX (U.S. Food and Drug Administration 2015). Oxaliplatin differs from Cisplatin in the Pt atom complexed groups, oxalate, and the diaminocyclohexane (DACH) ring (**Figure 1.3.1.**).

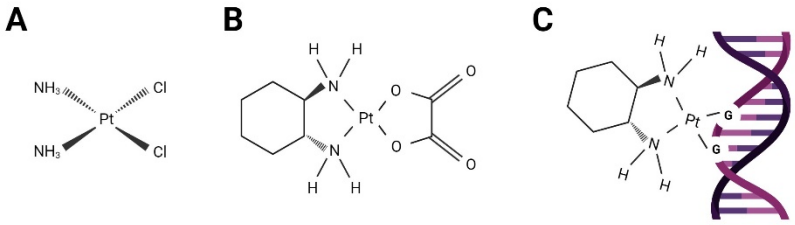

Figure 1.3.1. Platinum derivatives. Platinum compounds where the Platinum (II) atom is (A) tetracoordinate to four chloride anions in the Cisplatin molecule, (B) coordinated to oxalate and a diaminocyclohexane (DACH) ring in the Oxaliplatin molecule. (C) Schematic example of inter-crosslinks generated by Oxaliplatin covalent interaction with a DNA molecule between two adjacent guanines (GG). Figure created with https://www.biorender.com/ (2023).

Cell uptake mechanisms include passive diffusion but also facilitated and active transport. Once inside the cell, the Pt atom binds covalently to the N7 position of purine, generating DNA intra- and inter-crosslinks between two adjacent guanines (GG) or guanine-adenine bases (AG) (Di Francesco et al., 2002, Monneret, 2011). DNA damage triggers repairing and apoptotic pathways involving p38 MAPK, c6ABL, ERK, INK, and

p53 (Monneret, 2011). Cisplatin-DNA adducts promote DNA damage that is recognized by the MMR system, which enhances Cisplatin tolerance and resistance, while the bulky DACH ring in Oxaliplatin generates a hydrophobic and steric impediment that impairs MMR binding. Therefore, the toxic effects of Oxaliplatin do not depend on MMR, resulting in a lack of cross-resistance with Cisplatin (Di Francesco et al., 2002, Kline & El-Deiry, 2013).

Nowadays, Oxaliplatin is a high antitumor drug commonly applied in several solid tumors such as colorectal, gastric, and pancreatic cancer (National Cancer Institute 2023) and extensively studied in clinical trials for other cancer types, including prostate cancer (Droz et al., 2003, Marzo et al., 2022, Zhou et al., 2017).

1.3.2.1.1. Platinum drug resistance

Despite the high clinical efficacy of Oxaliplatin-based chemotherapy, it remains limited by the significant adverse reactions and its acquired resistance. The mechanisms involved in platinum drug resistance acquisition entail drug detoxification and increased tolerance against the effects promoted by the platinum compound presence. In particular, alterations in transport, defective DNA damage-induced repair, failure in apoptotic responses, and epigenetic marks constitute the platinum resistance mechanisms (Martinez-Balibrea et al., 2015, Monneret, 2011).

Cancer cells can develop several resistance strategies, such as decreasing drug uptake or increasing drug efflux by altering copper transporters like CRT1, involved in the accumulation of platinum drugs, p-type ATPases (ATP7A and ATP7B), responsible for copper transport and sequestration in Trans-Golgi network, or solute carriers (SLCs), notably SLC22 family, involved in detoxification of xenobiotics (Martinez-Balibrea et al., 2015, Zhou et al., 2020). In the case of platinum agents, the mechanism of action involves DNA adduct and crosslink generation (Monneret, 2011), therefore in response to this DNA damage, Oxaliplatin-resistant cells activate DDR by NER (Di Francesco et al., 2002), notably involving XPF-ERCC1 overexpression and leading to cell survival (Yin et al., 2011, Hatch & Swift, 2014). Once inside the cell, platinum compounds are hydrated, becoming active compounds, susceptible to react not just with DNA but other macromolecules (lipids and proteins) and thiol-containing molecules such as GSH, which is able to neutralize the electrophilic molecules generated (Martinez-Balibrea et al., 2015). Platinum-resistant cells display increased *GSTP1* levels, the gene encoding for glutathione S-transferases, which catalyze scavenging reactions involving GSH (Sawers et al., 2014). Thus, platinum detoxification (Cisplatin and Carboplatin) could be mediated by glutathione export. As a consequence of the electrophilic compound presence, ROS levels are increased within cells (Martinez-Balibrea et al., 2015). Of note, ROS play an important role in cell signaling but also promote DNA damage (DeBerardinis & Chandel, 2016). Accordingly, redox balance maintenance by increased ROS tolerance is also common in platinum-resistant cells (Martinez-Balibrea et al., 2015, Zhou et al., 2020).

Beyond these mechanisms, aberrant DNA damage affects the P53 signaling; thus, platinum-resistant cells suppress caspase activity and increase PI3K/AKT pathway activity, conferring the ability to avoid programmed cell death (Martinez-Balibrea et al., 2015). Central apoptotic regulator *TP53* is mutated in 50% of human tumors and has been suggested as a possible intrinsic mechanism of resistance (Martínez-Jiménez et

al., 2023). Moreover, platinum treatment also alters anti- and proapoptotic protein expression, such as BCL-2, BCL-XL, BAX and BAK, conferring platinum-resistance (Beale at al., 2000, Guo et al., 2021, Zhou et al., 2020). On the other hand, the extrinsic or death receptor apoptotic pathway is also affected by Oxaliplatin resistance mechanisms since cells acquire resistance by promoting mesenchymal characteristics triggered by *CD95* or *MMP7* overexpression, which play an important role in EMT (Martinez-Balibrea et al., 2015).

1.3.2.2. Palbociclib treatment in cancer

The alterations of cell cycle progression in cancer cells lead to continuous division and are supported by mutations of proteins involved in cell cycle regulation. The most common modifications include increased levels of cyclin D protein by *CCND1* (*cyclin D1*) amplification, usually found in several cancer types, and rarely *CCND2* (*cyclin D2*) and *CCND3* (*cyclin D3*). Also, activation of RAS/RAF/MAPK or PI3K/AKT pathways contributes to *CCND1* transcription, as well as amplification of CDK4 and CDK6 regulatory subunits that bind to cyclin D (Goel et al., 2017, Matthews et al., 2022, Otto & Sicinski, 2017). In addition, the loss of function of the CDK inhibitor $P16^{INK4A}$ by gene *CDKN2A* silencing through methylation or depletion is frequently found in cancer cells. All these alterations reflect that cell cycle dysregulation in the cancer cells promoting continuous division relies mainly on cell cycle initiation and G1/S checkpoint, providing a valuable therapeutic opportunity (Goel et al., 2017, Otto & Sicinski, 2017).

In this regard, the CDKs inhibitors Palbociclib, Ribociclib, and Abemaciclib are the targeted therapies for inhibiting D-type cyclin-CDK4/6 complexes. (Matthews et al., 2022). In particular, Palbociclib (IBRANCE®) was the first specific CDK4 and CDK6 inhibitor approved in 2015 by the FDA and in 2016 by the EMA as the first-line treatment of estrogen receptor (ER)-positive, human epidermal growth factor receptor 2 (HER2)-negative advanced breast cancer in combination with anti-estrogen therapy (European medicines agency 2021, U.S. Food and Drug Administration 2017). Mechanistically, Palbociclib alters continuous proliferation by promoting cell cycle arrest in the G1 phase by binding to and inhibiting cyclin-dependent kinases CDK4 and CDK6, thus impairing the canonical regulation for cell cycle progression. After Palbociclib binding to CDK4 and CDK6, cyclin D–CDK4 and cyclin D–CDK6 complexes cannot be activated, preventing RB family (RB1, RBL1, and RBL2) phosphorylation. Hence, E2F transcription factor activation is suppressed since RB remains attached until phosphorylation. Genes involved in the G1 to S phase transition, essential for replicative phase initiation, are no longer expressed, including E-type cyclins, which are necessary for CDK2 activation (Goel et al., 2017, Otto & Sicinski, 2017) (**Figure 1.3.2.**).

Therefore, Palbociclib plays a crucial role in impairing cell cycle initiation as a targeted therapy against CDKs activity, tackling continuous proliferation in breast cancer but also demonstrating promising results in other malignancies such as glioblastoma, neuroblastoma, NSCLC, HNSCC, melanoma (Goel et al., 2017, Otto & Sicinski, 2017), CRC (Sorah et al., 2022, Zhang et al., 2017, NLM; NCT03446157), and prostate cancer (NLM; NCT02905318, NLM: NCT02494921).

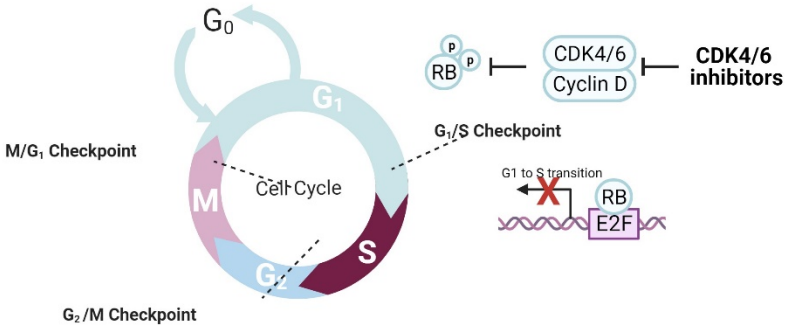

Figure 1.3.2. Palbociclib effect over cell cycle progression. CDK4 and CDK6 inhibition by Palbociclib impairs CDK4/6-Cyclin D complex activation, preventing the phosphorylation of RB family proteins. RB-E2F complex remains attached to DNA, impairing cell cycle progression by transcriptional repression of genes required for G1 to S phase transition. Figure adapted from "Cyclins: Cell Cycle Regulators" by https://www.biorender.com/ (2023) (Cancer Research Product Guide; Tocris Bioscience 2016, Hochegger et al., 2008, Wagener et al., 2016) and retrieved from https://app.biorender.com/biorender-templates.

1.3.2.2.1. Palbociclib drug resistance

Even though Palbociclib has shown efficacy in the treatment of breast cancer and promising results in other solid malignancies, drug resistance remains a significant challenge. In this regard, several mechanisms have been identified that contribute to the cancer cell response to Palbociclib treatment. Cells with mutations that stimulate cell cycle entrance and progression do not present the same antiproliferative effect and are associated with Palbociclib resistance. These mechanisms include alterations in the retinoblastoma tumor suppressor gene (*RB1*) pathway by loss of *RB1* function, *E2F2* overexpression, or hyperactivation of *Cyclin E1* (*CCNE1*) that can activate CDK2 and bypass the inhibitory effects of Palbociclib via *Cyclin E* overexpression or loss of function of $P21^{CIP1}$ and $P27^{KIP1}$ CDKs inhibitors (Matthews et al., 2022, Otto & Sicinski, 2017). On the other hand, resistance to CDK4/6 inhibitors also includes intrinsic mechanisms such as drug sequestration in the tumor cell lysosomal compartment and changes in chromatin modifiers that enable the reactivation of E2F target genes (Goel & Bergholz et al., 2022).

On the other hand, it is necessary to consider the complexity of CDK4/6 activity. Some studies suggest a compensatory function in CDKs, where the cell cycle progresses in the absence of D-type cyclins or CDK4 and 6 exhibiting redundancy and plasticity (Malumbres et al., 2004). Alternative cell cycle progression also proposes that CDK4/6-mediated phosphorylation of RB is not essential for CDK2 activation and that CDK2 and CDK1 could also be responsible for cell cycle progression under certain circumstances (Santamaría et al., 2007).

In summary, the mechanisms underlying Palbociclib-acquired resistance are poorly understood, and the responses of different tumors to CDK4/6 inhibition are heterogeneous. Further research is needed to explore additional pathways and identify novel therapeutic targets to address this limitation (Goel & Bergholz et al., 2022, Goel et al, 2017).

1.4. Metabolism in cancer therapy

Cell metabolism plays an essential role in cancer development and progression since cancer cells undergo metabolic reprogramming to support their proliferation and survival. Particularities in cancer cell metabolism also represent therapeutic opportunities and vulnerabilities for cancer diagnosis, biomarkers, and targeted therapies, alone or in combination with other chemotherapies to improve drug response.

Imaging techniques such as Positron Emission Tomography (PET) and Magnetic Resonance Imaging (MRI) are used to visualize highly metabolically active tissues by monitoring the radioactive molecules accumulation in specific locations and taking advantage of cancer cells' constant proliferation. The most widely used substrate in PET is [18F]fluoro-deoxyglucose ([18F]FDG), a glucose analog that is more metabolized in highly glycolytic cancer cells, hence providing valuable information for diagnosis or metastatic spread. On the other hand, MRI allows the detection of ^{1}H and ^{13}C-enriched metabolites (Di Gialleonardo et al., 2017), providing information about the distribution and metabolism of these molecules along the body.

Considering metabolism for targeted therapy, the first anti-folate developed was Aminopterin, reported by Farber & Diamond in 1948. This targeted therapy demonstrated significant remissions in childhood leukemia (ALL) patients, signifying an important change in the treatment of this disease and setting a precedent for antimetabolite usage in cancer therapy (Farber & Diamond, 1948). Targeting nucleotide metabolism (e.g., Pemetrexed, 5-Fluorouracil, Gemcitabine, or Methotrexate) has achieved successful results not just in liquid cancer but also in other solid cancer types such as NSLCL, CRC, HNSCC, gastric, pancreatic, breast, and ovarian cancers (Visentin et al., 2013, Stine et al., 2022). Some metabolic drugs have also been approved for non-cancer indications, such as targeting oxidative metabolism for type 2 diabetes (Metformin), pyrimidine metabolism or autophagy for chronic inflammatory disease rheumatoid arthritis (Leflunomide and Hydroxychlorquine), lipid synthesis for atherosclerotic cardiovascular disease (Bempedoic acid), or cysteine/glutamate exchange for ulcerative colitis (Sulfasalazine) (Zhao et al., 2022).

On the other hand, specific oncogenic mutations affecting metabolic adaptations and contributing to or driving tumor progression, such as RAS or PI3K, MYC, and mTOR in many cancer types, also provide metabolic vulnerabilities that can be therapeutically exploited, for instance, with tyrosine kinase inhibitors already approved as anticancer drugs (Zhao et al., 2022), or genetic synthetic lethal interactions using small interfering RNAs (siRNAS), short hairpin RNAs (shRNAs), or CRISPR–Cas9 technology (Stine et al., 2022).

Finally, short-term treatment exposition also induces cell metabolic reprogramming, promoting specific phenotypes that alter core metabolic pathways such as glycolysis, glutamine, or fatty acid metabolism. As described in the Hallmarks of Cancer section, these metabolic adaptations support cell survival for a specific population, conferring flexibility and advantages to overcome therapeutic effects by resistance acquisition, ultimately contributing to disease progression. A lot of clinical trials are focused on these metabolic vulnerabilities, targeting core metabolic alterations in cancer cells. For instance, exploring the tissue-specificity of metabolic particularities such as polyamine

dysregulation in prostate cancer can be addressed by inhibiting ODC and AdoMetDC using analog substrates such as DFMO or MGBF (Murray-Stewart et al., 2016). Metabolic adaptations are also important for the rational design of targeted therapy combinations. This consideration has already been exploited in approved drugs such as the double-hit on DNA synthesis in FOLFOX treatment, targeting nucleotide metabolism and promoting DNA damage (Van Cutsem et al., 2016, Xie et al., 2020). Other new therapeutic strategies under evaluation target glutamine metabolism, which is essential for cell survival in several cancer types, with glutaminase inhibitors such as CB-839 (GLS1 inhibitor), with limited success as a single drug (Gross et al., 2014). Exploring glutamine dependence in specific scenarios allows the designing of combination therapies, for instance, by impairing both GLS1 and glutathione synthesis required to protect cells from cellular stress in PDAC (Biancur et al., 2017, Seth Nanda et al., 2020) or by targeting GLS1 after CDK4/6 inhibition, which promotes MYC upregulation and increases glutamine and mTOR pathways to support cell survival in colorectal cells (Tarrado-Castellarnau et al., 2017). Likewise, the application of CDK4/6 inhibitors in prostate cancer, considering the similar behavior of AR in prostate and ER in breast cancer in driving *CCND1* transcription, displays promising results in both hormone-sensitive and CRPC (Goel et al., 2017).

Understanding metabolic reprogramming depending on cancer type, disease stage, and mutational burden allows for identifying targetable metabolic vulnerabilities and dependencies, which is crucial for developing effective therapies (Hanahan & Weinberg, 2011, Pavlova & Thompson, 2022).

1.4.1. System biology approach for metabolic-based therapy

Systems biology integrates multi-omics data (genomics, transcriptomics, proteomics, and metabolomics), combining multidisciplinary fields to construct complex networks of interactions that allow studying an organism in a given condition (Karakitsou & Foguet et al., 2019).

Advances in high-throughput technologies allow obtaining valuable information at the cellular level, such as whole genome sequencing to understand genetic mutations contributing to cancer development and progression, gene expression data through transcriptomic techniques such as microRNA (miRNA) and RNA sequencing (RNA-seq), which allow studying the differentially expressed genes and the gene enrichment considering a group of genes annotated in a predefined gene set using the Gene Set Enrichment Analysis (GSEA) (Subramanian et al., 2005). Characterization of proteins and metabolites has been an increasing interest in the last decades. Proteomics elucidates the interactions, function, composition, and structures of proteins and their cellular activities, while targeted metabolomics aims to the quantification of a known group of metabolites, providing information about reaction rates and allowing the construction of metabolic flux analysis. Metabolites can be measured through nuclear magnetic resonance (NMR) and mass spectrometry (MS) based techniques coupled to different separation instruments such as gas chromatography (GC-MS), capillary electrophoresis (CE-MS), or liquid chromatography (LC-MS), depending on the metabolism of interest (Heo et al., 2021, Zamboni et al 2015, Zhao et al., 2022).

All these data sets can be integrated into mathematical metabolic models to simulate the cell metabolic state and study the emerging properties or the response upon a perturbation in the system by predicting the metabolic fluxes. Constraint-based modeling assumes a metabolic steady-state flux distribution through stoichiometric linear equations to simplify the human metabolism reactions in the system. The Genome-Scale Metabolic Models (GSMM) are a collection of metabolic reactions, gene reaction associations, metabolites, and interactions translated to a single mathematical framework represented as a stoichiometric matrix. The reactions are a mass and charge balance, considering the subcellular location and transport and exchange reactions with the extracellular media (fluxomics). A unique solution for flux distribution is ultimately optimized by maximizing the biomass function, which is the objective function for cancer cells, through the Flux Balance Analysis (FBA) application. Human constraint-based GSMM reconstruction is obtained by Recon 3D. The integration of the available omic data to GSMM and the application of FBA leads to a condition-specific GSMM that provides valuable applications for drug discovery to explore metabolic capabilities, including essential genes and reactions for cell survival, also to identify synthetic lethal genes and simulate responses identifying putative biomarkers and drug targets (Heo et al., 2021, Karakitsou & Foguet et al., 2019).

Different conditions can be simulated for drug discovery to explore the metabolic changes occurring in the transition from the reference or control state to the treatment condition, generating the resulting flux distribution. The best potential target should accomplish both requirements: to impair the metabolic transition to the resulting state and to revert the transition to the reference state. For this purpose, the Metabolic Transformation Algorithm (MTA) alongside the Minimization of Metabolic Adjustment (MOMA) are applied to the specific GSMM simulation, leading to the identification of putative targets and metabolic vulnerabilities to explore with therapeutic combinations (Foguet et al., 2022, Segrè et al., 2002, and Valcárcel et al., 2019) considering drug repurposing annotated in external databases such as DrugBank (Knox et al., 2024) or Therapeutic Target Database (Chen et al., 2002).

2.

OBJECTIVES

2. OBJECTIVES

Metabolic reprogramming is a key hallmark of cancer that enables the tumor cells to accomplish the metabolic and energetic requirements for tumor survival and progression (Hanahan, 2022, Hanahan & Weinberg, 2011). It is a crucial contributor to adaptative events such as metastatic development and drug resistance. Thus, targeting metabolic reprogramming represents a promising antitumor strategy, and understanding the metabolic alterations acquired after drug resistance can provide valuable insights for developing effective combination therapies (DeBerardinis & Chandel, 2016, Seth Nanda et al., 2020, Stine et al., 2022, Porporato et al., 2018).

In this thesis, the metabolic reprogramming underlying drug resistance is studied in two types of cancer, metastatic colorectal cancer (mCRC) and metastatic castration-resistant prostate cancer (mCRPC), which both present high rates of incidence and recurrence (Ferlay et al., 2020). The study is assessed in two *in vitro* models representing the most advanced and aggressive types of mCRC and mCRPC, being SW620 and PC-3 cell lines, respectively (Luo & Song et al., 2022, Germain & Lafront et al., 2023). The metabolic fingerprints of both cell lines are evaluated after incubation with two different treatments used for cancer therapy: Palbociclib, which is a CDK4 and CDK6 selective inhibitor that arrests cells in the G1/G0 phase of the cell cycle, and Oxaliplatin, which impairs replication and transcription of DNA by promoting DNA damage. Metabolic, transcriptomic, and respiratory data are used to identify metabolic vulnerabilities in drug-adapted phenotypes to increase tumor sensitivity using combination therapies, which may improve treatment outcomes and overcome drug resistance (Lee et al., 2018, Matthews et al., 2022, Otto & Sicinski, 2017), also applying Genome-Scale Metabolic Models (GSMM) after data integration to generate cell-line-specific models and predict putative targets able to compromise cell proliferation in treatment-surviving cells (Tarragó-Celada & Foguet et al., 2021, Foguet et al., 2022). Therefore, the main objectives defined for this thesis are described below:

1. Study of the metabolic reprogramming underlying short-term treatment with Oxaliplatin chemotherapy to unveil combined drug targets to address Oxaliplatin treatment resistance.

2. Study of the metabolic reprogramming underlying short-term treatment with Palbociclib targeted therapy to unveil combined drug targets to address Palbociclib treatment resistance.

3. Validation of the most promising combinations based on the metabolic characterization, transcriptomic, and respiratory data, or the metabolic targets proposed by the specific GSMM reconstructions.

3.

RESULTS

3. RESULTS

3.1. Chapter 1. Metabolic profiling reveals new drug combinations to sensitize colon and prostate adenocarcinoma cells to oxaliplatin therapy.

3.1.1. Introduction.

Oxaliplatin is one of the most common platinum derivatives applied in standard chemotherapy (Monneret, 2011, Zhang & Xu et al., 2022) for the treatment of several solid malignancies, mainly colorectal and gastric cancer (Di Francesco et al., 2002, Kang et al., 2015, Kline & El-Deiry, 2013, Monneret, 2011, Huang et al., 2016). It targets highly proliferative cells by promoting DNA damage through DNA crosslink generation and impairing DNA replication and transcription. Upon first chemotherapy applications, the strategy of drug combination appeared to overcome drug resistance responsible for the therapeutic failure. This strategy resulted from increased knowledge about cancer features supporting cell survival upon drug response (Jin et al., 2023, Stordal et al., 2007). Oxaliplatin administrated together with 5-fluorouracil and folinic acid (a combination known as FOLFOX treatment), is one of the standard and most effective chemotherapies for metastatic colorectal cancer (mCRC) (Van Cutsem et al., 2016, Xie et al., 2020). This regimen was approved for targeting nucleotide metabolism while promoting DNA damage in colorectal cancer (CRC) (U.S. Food and Drug Administration 2015). Clinical studies demonstrated the antiproliferative effect of FOLFOX rather than single drugs alone, improving drug resistance and overall survival (André et al., 2009). However, despite oxaliplatin-based therapies demonstrating effective results in several solid malignancies (Conroy et al., 2011, Lee et al., 2014, Park et al., 2021), the emerging chemoresistance is a major cause of mortality in CRC, especially challenging in the advanced stage of cancer disease. Further research into the mechanisms involved in drug resistance is necessary for the development of more effective therapeutic strategies, ultimately improving patient outcomes (Chen & Gong et al., 2022, Monneret, 2011, Rottenberg et al., 2021). An increasing number of studies support an association between metabolic reprogramming and the acquisition of chemotherapy resistance (Tan & Li et al., 2022, Xu et al., 2020). Therefore, the determination of metabolic features specifically associated with cancer cell resistance upon Oxaliplatin treatment is critical for the development of new combined therapy strategies.

This chapter aims to unveil the metabolic reprogramming of cancer cells upon Oxaliplatin short-term exposition to identify targetable metabolic pathways and improve Oxaliplatin sensitivity using new combined treatments. This strategy implies a cell metabolic characterization of cancer cells, including metabolomic and transcriptomic profiles, upon Oxaliplatin exposition and a computational approach integrating multi-omic data into condition-specific genome-scale metabolic flux models (GSMM). Finally, using the GSMM and a drug repurposing strategy, we identify druggable targets and validate new putative Oxaliplatin-combined therapies to avoid metabolic reprogramming associated with Oxaliplatin resistance.

As a case study, this multidisciplinary strategy is applied to identify putative oxaliplatin-combined therapies for two common advanced cancer types, metastatic colorectal and prostate cancers, since they represent two of the most lethal and recurrent tumors

nowadays (Ferlay et al., 2020). With this purpose, the most aggressive preclinical models have been selected: the PC-3 cell line, a metastatic prostate cell line (grade IV) isolated from the lumbar vertebra of a 62-year-old white male patient presenting AR, PTEN, and P53 negative mutations (Germain & Lafront et al., 2023), and the SW620 cell line, a metastatic colorectal cell line (Dukes C type) isolated from the lymph node metastasis of the large intestine of a 51-year-old male patient presenting *KRAS* positive mutation (Luo & Song et al., 2022).

The study of metabolic reprogramming through this multidisciplinary strategy helps to understand the drug-acquired resistance to Oxaliplatin and propose alternative therapeutic approaches. Comparative analysis of Oxaliplatin adaptive responses in colon and prostate cancer cells reveals common mechanisms such as the reduction of the central carbon metabolism, mainly affecting glycolytic flux and amino acid dependence to maintain cell survival. However, Oxaliplatin treatment causes a different reprogramming of mitochondrial metabolism in both cancer types. The cancer type-specific GSMM reconstruction for the resistant phenotypes effectively identifies metabolic vulnerabilities as putative drug targets, leading to the discovery of the combined treatment of Oxaliplatin with Cladribine, a nucleotide metabolism inhibitor (Wu & Gong 2022), causing synergistic antiproliferative effects in colon cancer cells. In addition, the combination of Oxaliplatin and Palbociclib, a cyclin-dependent kinase 4 and 6 (CDK4/6) selective inhibitor that arrests cells in the G1/G0, is effective for both prostate and colon cancer cells. Altogether, the obtained results led to potential new therapeutic opportunities that need to be further explored in preclinical studies.

3.1.2. Results.

3.1.2.1. Oxaliplatin treatment impairs cell growth in metastatic colorectal and prostate cancer cell lines.

To study the metabolic reprogramming after short-term treatment with Oxaliplatin in both cancer types, first was determined the drug concentration required to reduce 50 % of cell proliferation (IC_{50}). With this aim, short-term resistance acquisition was assessed after 48 h of treatment with Oxaliplatin in both the metastatic colorectal (mCRC) SW620 cell line and the metastatic prostate (mCRPC) PC-3 cell line. The percentage of alive, early apoptotic, and late apoptotic/necrotic cells was also measured after 48 h of Oxaliplatin treatment in both cell lines.

Results determined 0.25 μM as the effective Oxaliplatin IC_{50} for SW620 (**Figure 3.1.1., A**), which notably differs from the concentration of 7 μM established for the PC-3 cell line (**Figure 3.1.1., B**). The difference in IC_{50} value exceeding one order of magnitude evidence that the metastatic colorectal cell line is more sensitive to the drug's effects. Short-term incubation with IC_{50} caused a progressive decrease in cell proliferation over time in both cell models, displaying a significant impairment of duplication time. Indeed, Oxaliplatin-treated cells proliferate 2.25 times slower compared to the non-treated condition in both cell lines. The doubling time increases from 16 h (non-treated) to 37.5 h (Oxaliplatin-treated) in the case of the SW620 cells (**Figure 3.1.1., C**) and from 21.5h to 48 h in the case of PC-3 cells (**Figure 3.1.1., D**).

Regarding the percentage of alive, early apoptotic, and late apoptotic/necrotic cells measured by flow cytometry after Oxaliplatin treatment, the results indicated a significant increase in the apoptotic response only in the prostate cell line (**Figure 3.1.1., E**). Although the percentages obtained in early apoptotic and late apoptotic/necrotic cells did

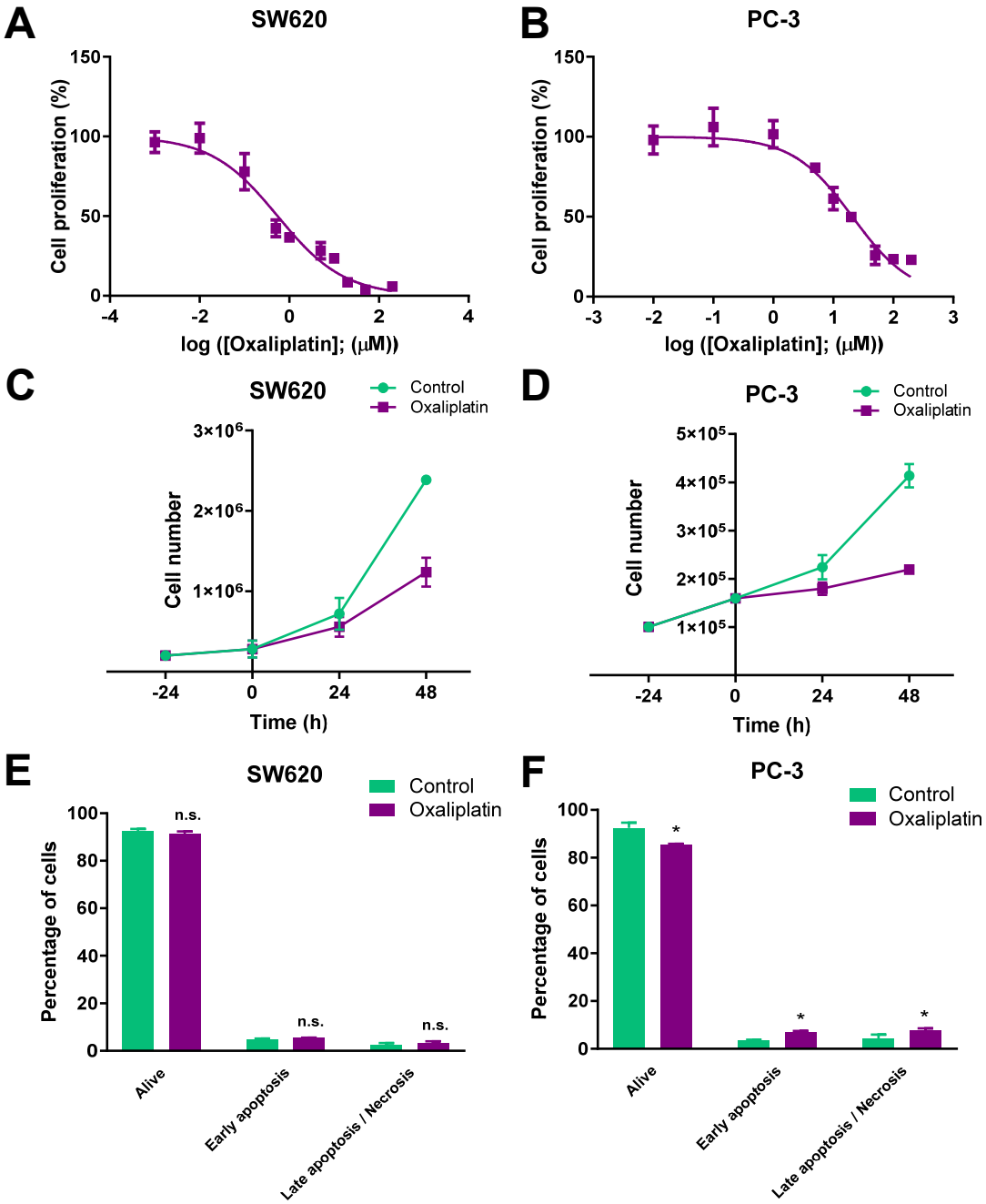

Figure 3.1.1. Oxaliplatin effect on cell proliferation and apoptosis in colorectal and prostate cancer cells. A, B. Representative graphs showing cell proliferation curves after 48 h of Oxaliplatin treatment at increasing concentrations in A) the metastatic colorectal SW620 cell line, and B) the metastatic prostate PC-3 cell line. C, D. Cell proliferation over time in non-treated and treated cells at fixed concentrations (IC_{50}) C) using 0.25 μM of Oxaliplatin in SW620 cells, and D) using 7 μM of Oxaliplatin in PC-3 cells. E, F. Apoptosis assay after Annexin V-FITC incubation discerning cells found alive, in early apoptosis and late apoptosis/necrosis after 48 h measured in non-treated and Oxaliplatin-treated E) SW620 cells (0.25 μM), and F) PC-3 cells (7 μM). An independent sample t-test was applied for relative comparison between the two groups, * indicates significant differences ($p < 0.05$).

not reach more than 10% of the cell population. In the case of the colorectal SW620 cell line, short-term treatment with Oxaliplatin did not promote apoptosis compared to the non-treated condition (**Figure 3.1.1., F**).

Therefore, Oxaliplatin treatment impairs cell proliferation in metastatic colorectal and prostate cancer cell lines, promoting a significant reduction in growth rate. Despite the increase in the apoptotic response upon Oxaliplatin treatment in the prostate cell line, the small percentage of cells displaying apoptosis in both cell lines suggests that apoptotic activation is not the primary mechanism responsible for the 50 % decrease in cell proliferation.

3.1.2.2. Oxaliplatin treatment depletes glycolysis and central carbon metabolism in metastatic colorectal and prostate cancer cells.

In order to evaluate Oxaliplatin's short-term treatment effect over the major metabolic pathways, the transcriptome differential expression (DE) analysis was performed using DEseq2 (Love et al., 2014). Transcriptomic data were analyzed based on the enrichment score of the genes distributed on gene set pathways employing the gene sets enrichment analysis (GSEA) (Subramanian et al., 2005) according to the metabolic individual pathways defined by the Kyoto Encyclopedia of Genes and Genomes (KEGG) database using a combination of 2-4 letter code and 5 digit number (the unique KEGG-pathways identifiers and the genes included in each pathway are described in detail in https://www.kegg.jp/) (**Figure 3.1.2.**).

DE analysis results showed significant downregulation of “hsa01200 Carbon metabolism” in both SW620 (**Figure 3.1.2., A**) and PC-3 cell lines (**Figure 3.1.2., B**). This metabolic network of central carbohydrate metabolism includes glycolysis/gluconeogenesis, PPP, TCA cycle, pyruvate oxidation, serine biosynthesis, glycine cleavage system, and propionyl CoA metabolism. Also, in the SW620 cell line, biosynthesis of amino acids is significantly decreased by Oxaliplatin treatment which includes several pathways such as three-carbon glycolytic intermediates, the first carbon oxidation of the TCA cycle, PPP, 5-phosphoribosyl-1-pyrophosphate (PRPP) biosynthesis, serine, cysteine, arginine and proline biosynthesis, and enzymes from the urea cycle.

Remarkably, no metabolic gene sets were positively enriched after Oxaliplatin treatment in any of the two cell lines. Therefore, these results indicate that cells treated with Oxaliplatin exhibit a downregulation in the cell metabolic pathways as an adaptation to this treatment.

Searching for a common trait on central metabolism affectation upon Oxaliplatin treatment, further gene expression comparisons between the two cell lines have been performed, attending to the individual gene expression level. Therefore, genes encoding for the major proteins involved in glycolysis and pentose phosphate central metabolic pathways were evaluated (**Figure 3.1.3.**). Downregulation of central carbon metabolism in both cell types is reflected by a significant decrease in the expression of the genes encoding for the most important glycolytic enzymes. Notably, the glycolytic orchestrator *6-Phosphofructo-2-Kinase/Fructose-2,6-Biphosphatase 3 (PFKFB3)* is downregulated in both cell types after 48 h of treatment with Oxaliplatin. Also, *transketolase (TKT)* or

transaldolase 1 (TALDO1), which are essential non-oxidative PPP genes, are found to be significantly downregulated in the two cancer models.

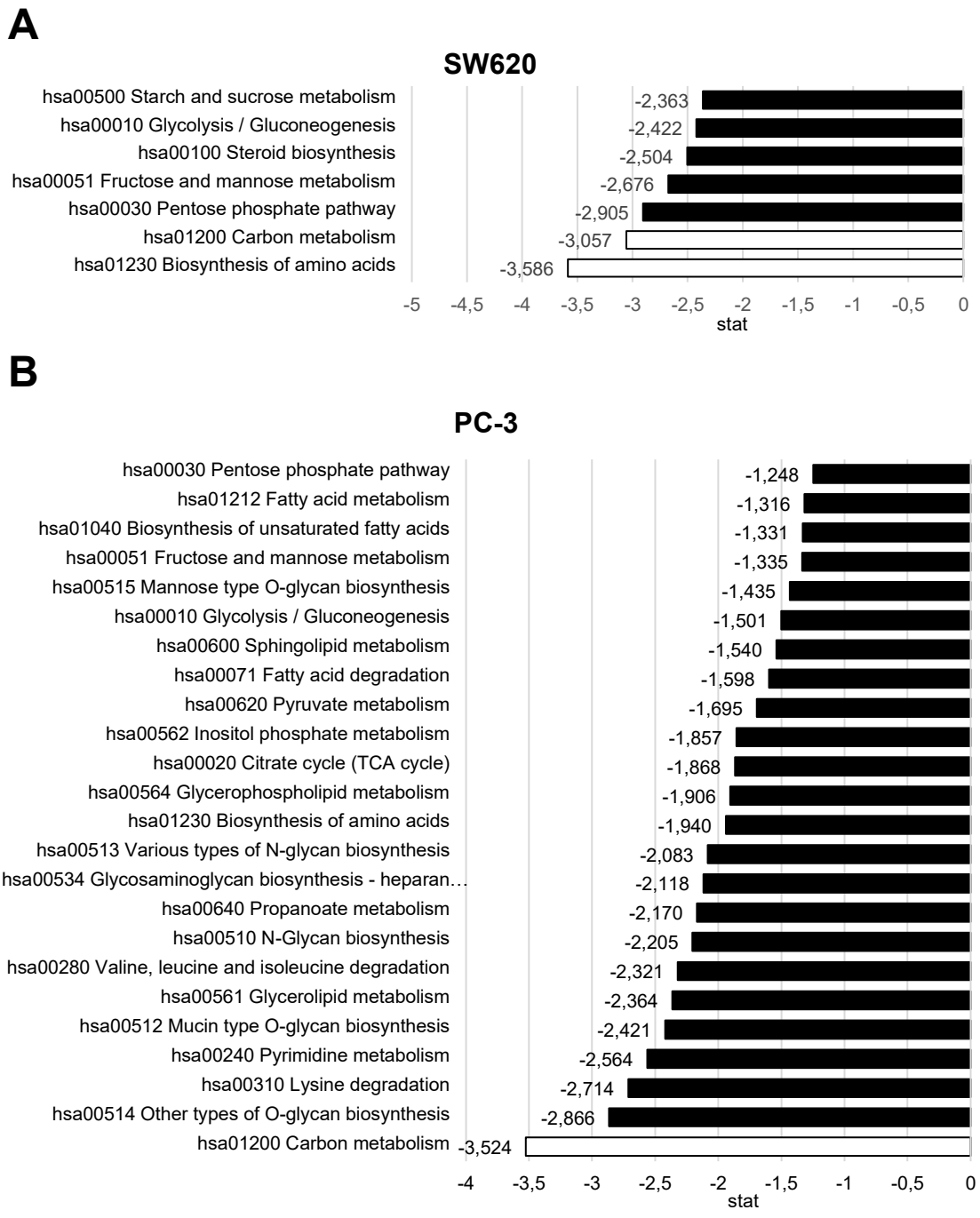

Figure 3.1.2. Gene set enrichment analysis (GSEA) according to metabolic individual KEGG pathways classification. A, B. Differential expression is analyzed after 48 h of treatment with Oxaliplatin in A) SW620 and B) PC-3 cells. Stat represents enrichment score, being positive when it increases or negative when it decreases. White-colored bars indicate significant differences with respect to non-treated cells (adjusted p-value < 0.05), and black-colored bars indicate patterns with adjusted p-value < 0.25.

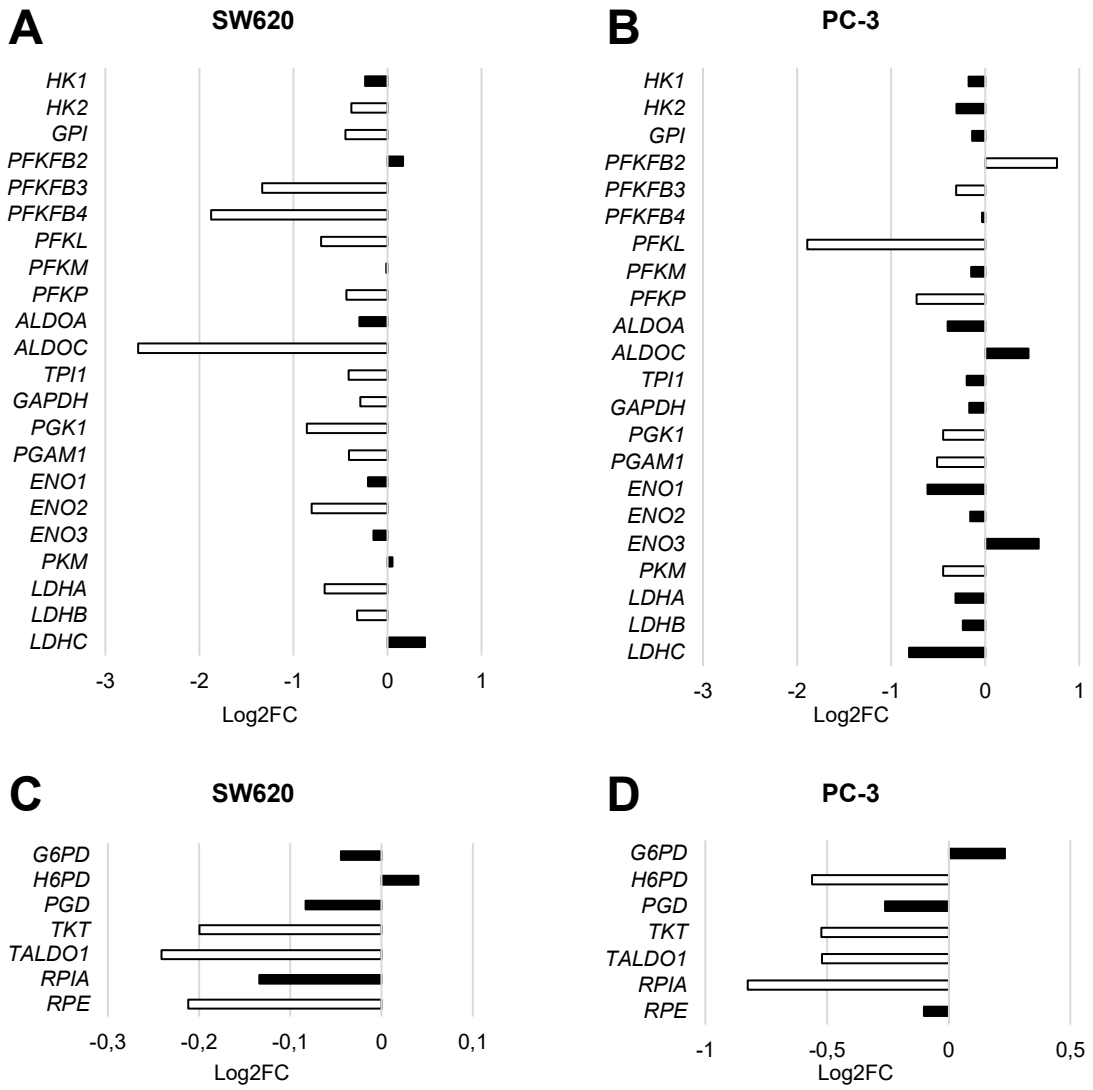

Figure 3.1.3. Differential gene expression of glycolytic and pentose phosphate pathway (PPP) enzymes after Oxaliplatin treatment. Differential gene expression in terms of Log 2 fold-change (Log2FC) after 48 h of treatment with Oxaliplatin regarding the principal encoding genes for glycolytic enzymes in A) SW620 cells, and B) PC-3 cells, and PPP enzymes in C) SW620 cells, and D) PC-3 cells. White-colored bars represent significant differences with respect to non-treated cells (adjusted p-value < 0.05). Glycolytic genes: *HK1, HK2; hexokinase 1, and 2, respectively. GPI; glucose-6-phosphate isomerase. PFKFB2, PFKFB3, and PFKFB4; 6-phosphofructo-2-kinase/fructose-2,6-biphosphatase 2, 3, and 4, respectively. PFKL, PFKM, PFKP; phosphofructokinase, liver type, muscle, and platelet, respectively. ALDOA, ALDOC; aldolase A, and C, respectively. TPI1; triosephosphate isomerase 1, GAPDH; glyceraldehyde-3-phosphate dehydrogenase. PGK1; phosphoglycerate kinase 1. PGAM1; phosphoglycerate mutase 1. ENO1, ENO2, ENO3; enolase 1, 2, and 3, respectively. PKM; pyruvate kinase M1/2. LDHA, LDHB; LDHC; lactate dehydrogenase A, B, and C respectively.* PPP genes: *G6PD; glucose-6-phosphate dehydrogenase. H6PD; hexose-6-phosphate dehydrogenase/glucose 1-dehydrogenase. PGD; phosphogluconate dehydrogenase. TKT; transketolase. TALDO1; transaldolase 1. RPIA; ribose 5-phosphate isomerase A. RPE; ribulose-5-phosphate-3-epimerase.*

Then, glucose and lactate, the most abundant metabolites in the extracellular media associated with the glycolytic pathway, were measured to confirm the metabolic pathway alteration observed with the transcriptomic analysis after Oxaliplatin treatment. The assessment of the consumption and production rates evidenced a decrease in glucose consumption and lactate production after 48 h of treatment with Oxaliplatin in both cell types (**Figure 3.1.4., A, B**). These results are in agreement with the gene set enrichment analysis results, demonstrating a decrease in central carbon metabolism (**Figure 3.1.2.**).

Also, the ratio of lactate/glucose, which indicates the lactate production derived from the Warburg effect, did not change with respect to the control condition in none of the cell types (**Figure 3.1.4., C, D**), suggesting an even decrease of the glycolytic pathway and lactate production.

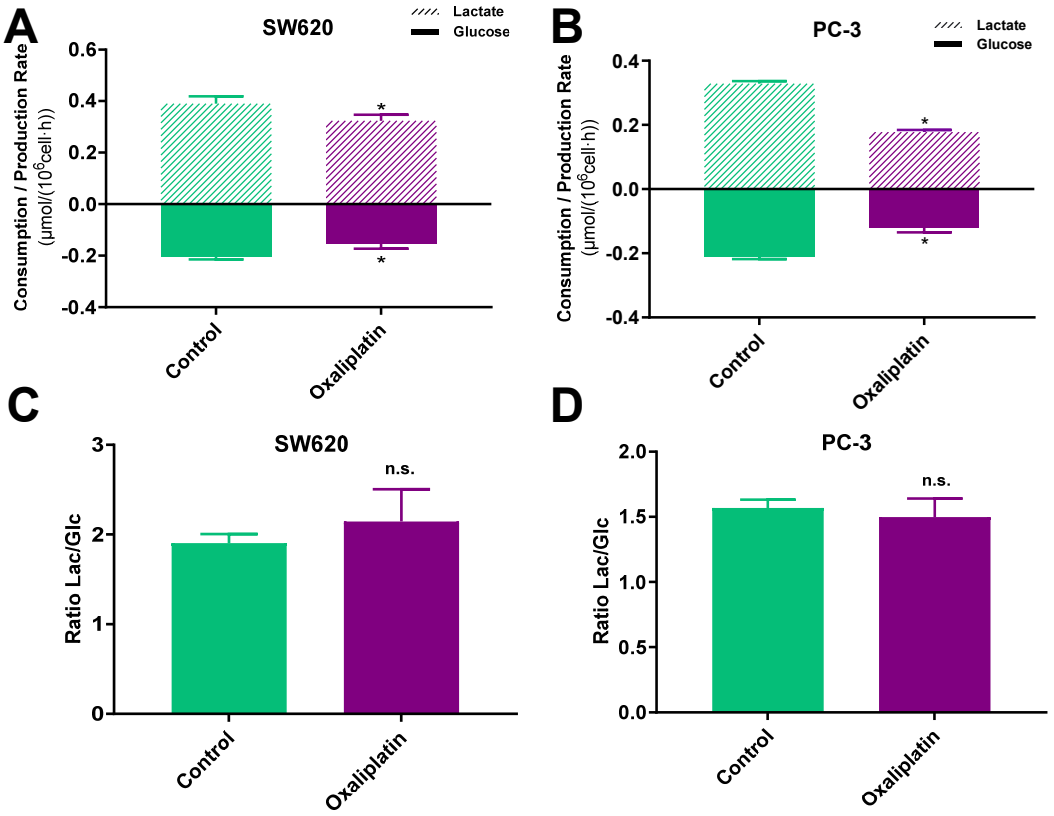

Figure 3.1.4. Reduction in glycolytic pathway and lactate production in Oxaliplatin-treated cells. A, B. Extracellular glucose consumption and lactate production rates measured after 48 h in A) control and Oxaliplatin-treated (0.25 µM) SW620 cells and B) control and Oxaliplatin-treated (7 µM) PC-3 cells. C, D. Ratio of lactate production to glucose consumption in C) SW620 cells and D) PC-3 cells. An independent sample t-test was applied for relative comparison between the two groups, * indicates significant differences ($p < 0.05$).

Therefore, short-term Oxaliplatin treatment alters central carbon metabolic pathways by significantly decreasing the glycolytic pathway in both the metastatic colorectal and the prostate cancer cell lines.

3.1.2.3. Oxaliplatin treatment induces a distinct effect on amino acid and polyamine metabolism in prostate and colorectal cancer cells.

As stated in the previous section, short-term Oxaliplatin treatment promoted a decrease in central carbon metabolism and impaired cell proliferation in metastatic prostate and colorectal cells. However, cells were able to survive by overcoming the Oxaliplatin cytotoxic effect and displaying a resistant phenotype. In order to identify other carbon and nitrogen sources that may be contributing to resistance acquisition and cell survival, we evaluated the metabolite fingerprint in both Oxaliplatin-resistant cancer cell lines.

First, we measured the extracellular glutamine consumption and glutamate production rates, since they are the most abundant metabolites after glucose and lactate and are closely related to tumor progression and resistance phenotype acquisition (Yoo, Yu &

Sung et al., 2020). Results showed an increase in glutamine consumption after Oxaliplatin treatment in the colorectal SW620 cell line (**Figure 3.1.5., A**), accompanied by a greater glutamine dependence (**Figure 3.1.5., B**). However, glutamate production was not significantly increased (**Figure 3.1.5., A**), and the ratio of glutamine consumption to glutamine not committed to glutamate production (estimated as Gln/(Gln-Glu)) was slightly decreased (**Figure 3.1.5., C**). These results suggest that glutamine consumption in Oxaliplatin-treated colorectal cells is increased for other purposes beyond glutamate production. On the other hand, in the PC-3 cell line, neither the extracellular glutamine consumption nor the glutamate production rate calculated after Oxaliplatin treatment displayed significant changes compared to the control condition (**Figure 3.1.5., D**). Likewise, the ratio of glutamine usage for glutamate production was not altered (**Figure 3.1.5., E**). However, since there were no significant changes in glutamine consumption and a reduction in glucose uptake after Oxaliplatin treatment, prostate cancer PC-3 cells exhibited an increase in glutamine dependence (**Figure 3.1.5., F**).

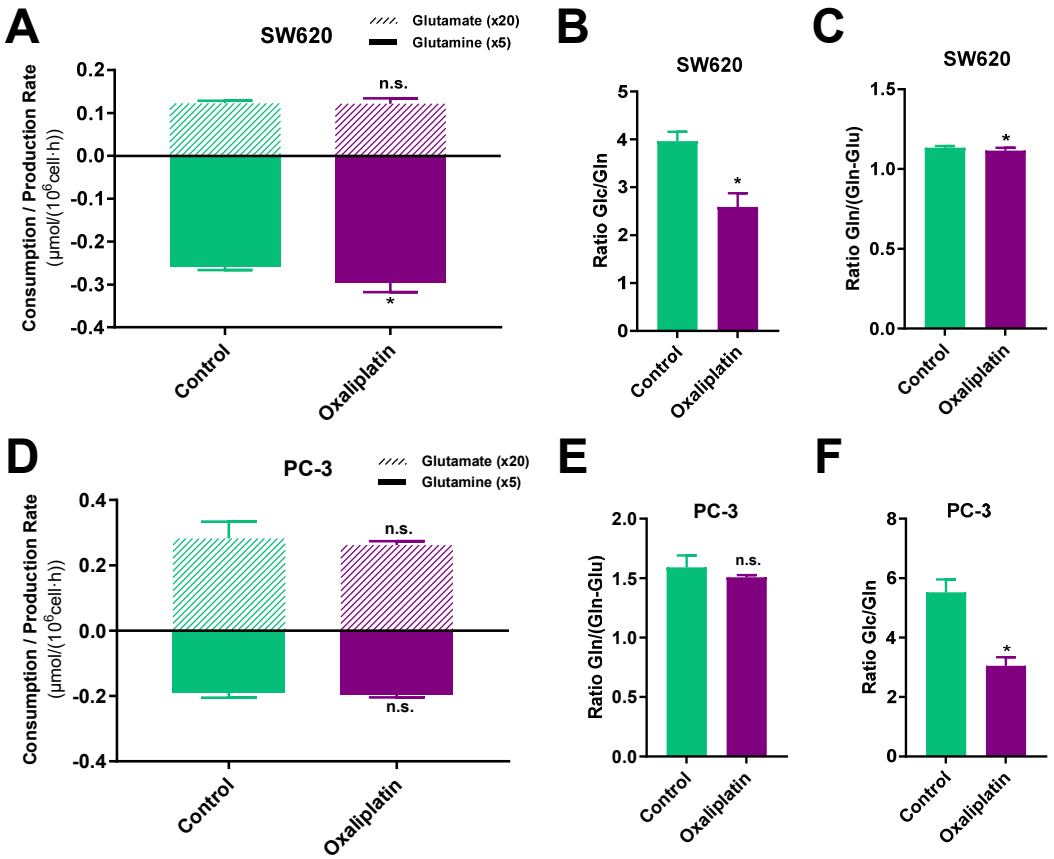

Figure 3.1.5. Effects of Oxaliplatin treatment in glutaminolysis. A, D. Extracellular glutamine consumption and glutamate production rates measured after 48 h in A) control and Oxaliplatin-treated (0.25 µM) SW620 cells and D) control and Oxaliplatin-treated (7 µM) PC-3 cells. B, F. Ratio of glucose with respect to glutamine utilization in B) SW620 cells and F) PC-3 cells. C, E. Ratio of glutamine consumption to glutamine not committed to glutamate production (estimated as Gln/(Gln-Glu)) in C) SW620 cells and E) PC-3 cells. An independent sample t-test was applied for relative comparison between the two groups, * indicates significant differences ($p < 0.05$).

These findings indicate that both cell lines display an increase in glutamine dependence as a common trait, which suggests that glutamine metabolism plays an important role in Oxaliplatin-resistant cells' metabolism, together with the glycolytic flux reduction observed in the previous results.

By analyzing the extracellular consumption and production rates of amino acids after 48 h of treatment with Oxaliplatin, we did not observe alterations in essential amino acids (EAAs) (results are displayed in **Appendix I, Section I.1.**) in the colorectal cancer SW620 cell line. However, our results showed a significant increase in asparagine, aspartate, glycine, and proline production rates (**Figure 3.1.6., A**). These increments indicate that these non-essential amino acids (NEAAs) were more produced and secreted to the extracellular medium after Oxaliplatin treatment. In contrast, we observed that both EAAs and NEAAs exhibited significant changes after Oxaliplatin treatment in the PC-3 cell line (**Figure 3.1.6., B**). Notably, serine, tyrosine, phenylalanine, tryptophan, and valine were significantly less consumed from the extracellular media after Oxaliplatin treatment, while there was an augmented asparagine, glycine, ornithine, and proline production rates.

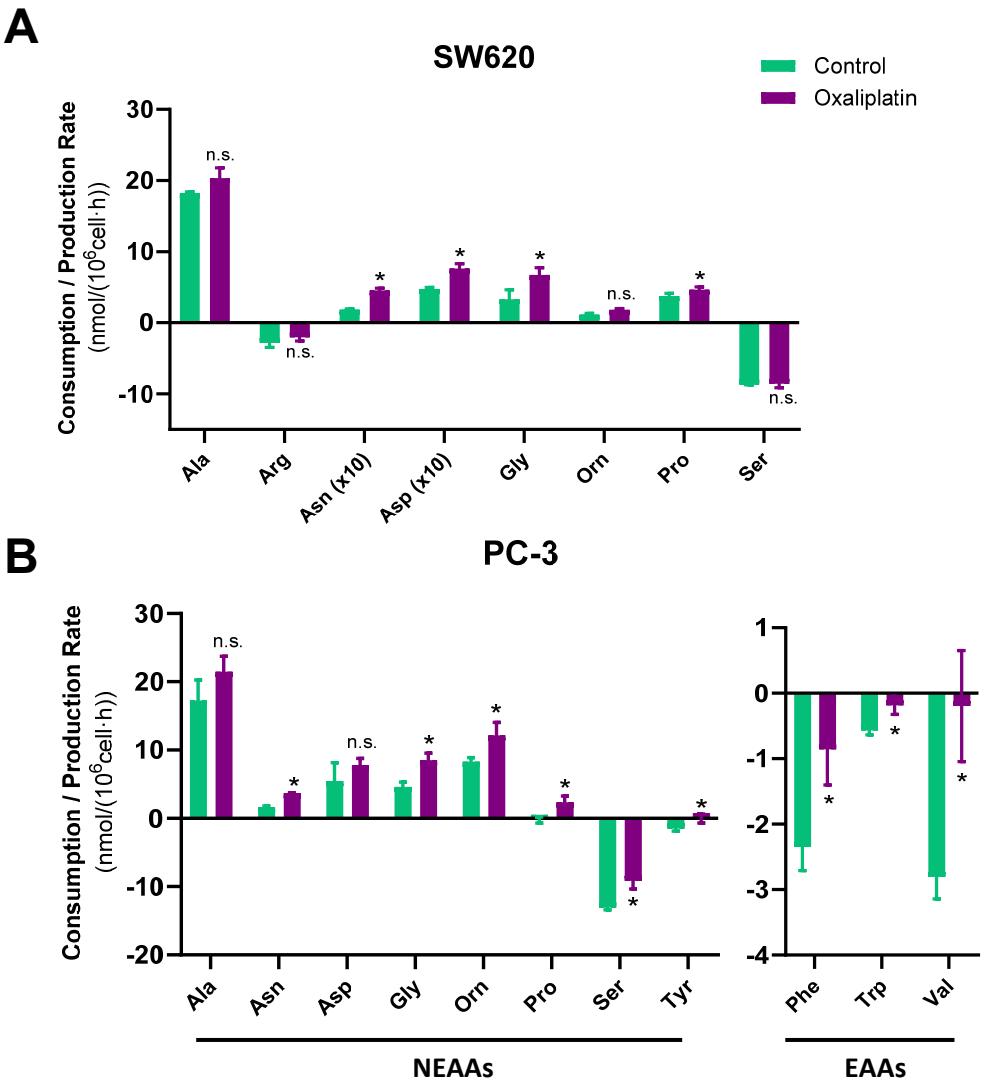

Figure 3.1.6. Extracellular consumption and production rates of amino acids after Oxaliplatin treatment. A) Extracellular consumption and production rates of NEAAs measured after 48 h in control and Oxaliplatin-treated (0.25 μM) SW620 cells. B) Extracellular consumption and production rates of NEAAs and EAAs measured after 48 h in control and Oxaliplatin-treated (7 μM) PC-3 cells. NEAAs. Non-essential amino acids. EAAs: Essential amino acids. Only amino acids that were significantly produced or consumed from the medium are shown. An independent sample t-test was applied for relative comparison between the two groups, * indicates significant differences ($p < 0.05$).

These results indicate the importance of amino acid metabolism in Oxaliplatin-resistant cells, in which glutamine plays a central role. Notably, this amino acid is correlated with non-essential amino acid biosynthesis, one-carbon metabolism for nucleotide biosynthesis, epigenetic regulation, or urea cycle for ammonium detoxification, which, in turn, is linked to polyamine metabolism (Ju & Lin et al., 2020, Yoo, Yu & Sung et al., 2020), which plays an important role in prostate cancer and seminal fluid (Affronti et al., 2020, Casero & Stewart et al., 2018). Therefore, we explored one-carbon, urea cycle, and polyamine metabolisms in order to determine the contribution of these pathways to cell survival after Oxaliplatin treatment in both cell lines.

To this end, we evaluated the differential gene expression of the most important enzymes belonging to the folate cycle, methionine cycle, methionine salvage pathway, polyamine metabolism, and urea cycle after 48 h of Oxaliplatin treatment in colorectal and prostate cell lines (**Figure 3.1.7.**). In SW620 cells, the most significant gene expression increments after Oxaliplatin treatment were found in *methylenetetrahydrofolate dehydrogenase* (*MTHFD1*), together with *adenosylmethionine decarboxylase 1* (*AMD1*) and *ornithine decarboxylase 1* (*ODC1*) (gene expression values are specified in **Appendix I**, **Table I.1.**). Also, there was a remarkable overall decrease in the expression of genes encoding for the mitochondrial isoforms of one-carbon (folate) metabolism (*MTHFD1L, MTHFD2*, and in *serine hydroxymethyltransferase 2* (*SHMT2*)). In agreement with the overexpression of polyamine metabolism rate-limiting enzymes *AMD1* and *ODC1*, the putrescine production rate was also increased after treatment (**Figure 3.1.8., A**). Also, downregulation of *spermidine/spermine N1-acetyltransferase 1* (*SAT1*) might impair polyamine catabolism due to the increased polyamine synthesis induced by Oxaliplatin treatment. Regarding the prostate cell line, we observed a significant overexpression of *MTHFD2L,* and in the catabolic genes *SAT1* and *spermine oxidase (SMOX)*. At the same time, there was a substantial decrease in the expression of genes involved in methionine salvage pathway (*methylthioadenosine phosphorylase (MTAP)*), methionine cycle (*5-methyltetrahydrofolate-homocysteine methyltransferase (MTR)*, and *adenosylhomocysteinase (ACHY)*), and notably, in polyamine synthesis including downregulation of *spermidine* and *spermine synthase* (*SRM* and *SMS*, respectively), and *ODC1* (**Figure 3.1.7.**). The tendency observed in the reduction of putrescine extracellular secretion in Oxaliplatin-resistant prostate cells was also in line with the observed downregulation of polyamine synthesis (**Figure 3.1.8., B**). Despite the downregulation in polyamine synthesis, we observed an increase in ornithine secretion to the extracellular media by Oxaliplatin treatment in prostate cancer cells which is in accordance with the decrease in *ODC1*, the enzyme that catalyzes the conversion of ornithine into putrescine (**Figure 3.1.6., B**). Furthermore, in agreement with the glycolytic impairment after Oxaliplatin treatment, there is a notable inhibition of genes encoding for enzymes of serine biosynthesis from 3-phosphoglycerate (3PG). This inhibition does not hinder the maintenance of the cytosolic folate cycle, either through an increase in serine consumption, resulting in augmented glycine production in the prostate cell line, or the overexpression of the *MTHFD1* gene in the colon cell line.

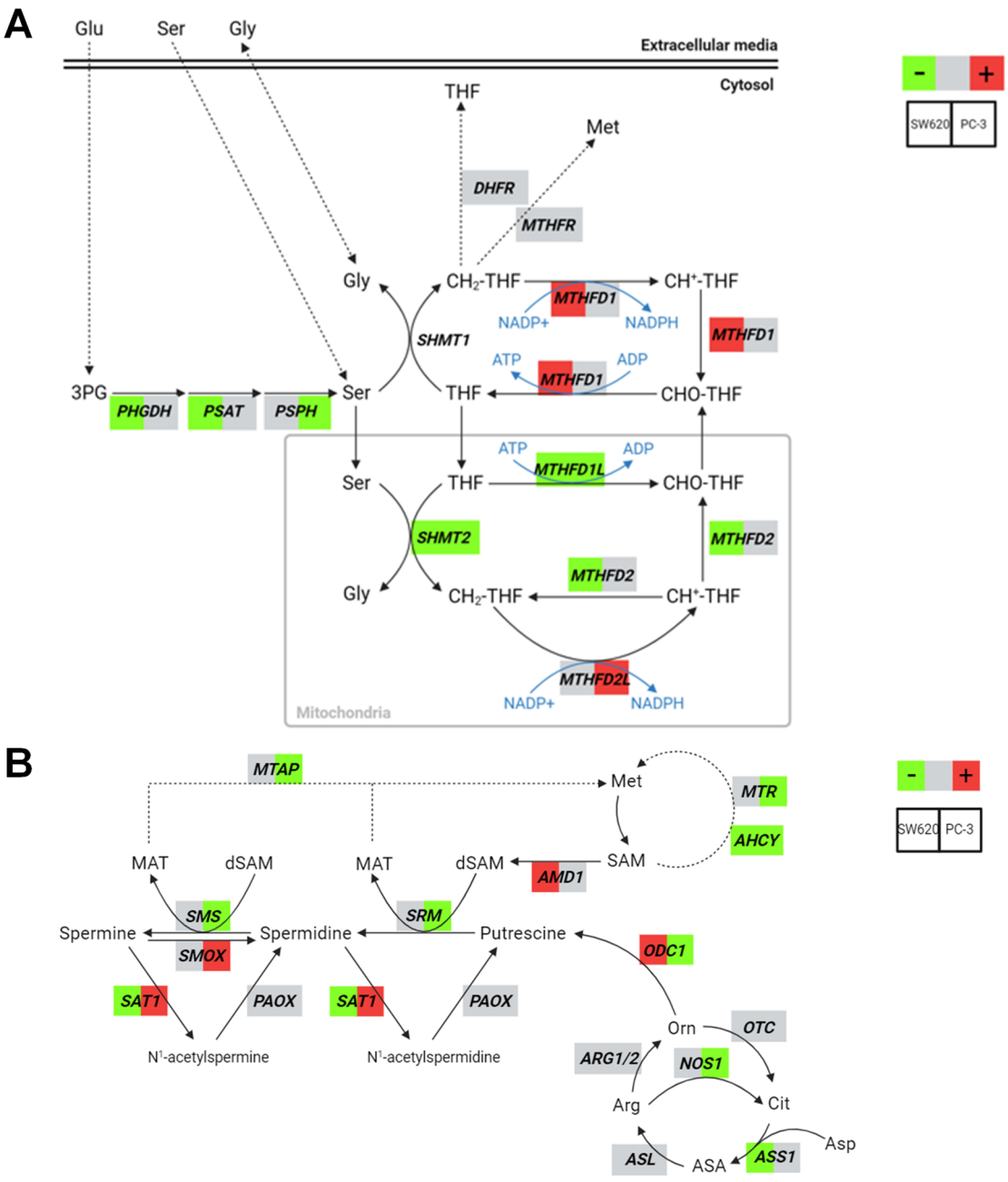

Figure 3.1.7. Genes encoding for key enzymes involved in once-carbon (methionine and folate) metabolism, polyamine metabolism, and urea cycle. Significantly differentially expressed genes after Oxaliplatin treatment in SW620 and PC-3 for enzymes in A) the serine biosynthesis and folate cycle, and B) the methionine cycle, methionine salvage pathway, polyamine metabolism, and urea cycle. Colors refer to gene expression changes compared to control; green is downregulated, red is upregulated and grey indicates no significant differences (adjusted p-value > 0.05). Genes: *AHCY; adenosylhomocysteinase, AMD1; adenosylmethionine decarboxylase 1, ARG2; arginase 2, ASL; argininosuccinate lyase, ASS1; argininosuccinate synthase 1, DHFR; dihydrofolate reductase, MTAP; methylthioadenosine phosphorylase, MTHFD1; methylenetetrahydrofolate dehydrogenase, MTHFD1L; methylenetetrahydrofolate dehydrogenase (NADP+ dependent) 1 like, MTHFD2; methylenetetrahydrofolate dehydrogenase (NADP+ dependent) 2, MTHFD2L; methylenetetrahydrofolate dehydrogenase (NADP+ dependent) 2 like, MTHFR; methylenetetrahydrofolate reductase, MTR; 5-methyltetrahydrofolate-homocysteine methyltransferase, NOS1; nitric oxide synthase 1, ODC1; ornithine decarboxylase 1, OTC; ornithine transcarbamylase, PAOX; polyamine oxidase, PHGDH; phosphoglycerate dehydrogenase, PSAT1; phosphoserine aminotransferase 1, PSPH; phosphoserine phosphatase, SAT1; spermidine/spermine N1-acetyltransferase 1, SHMT1; serine hydroxymethyltransferase 1, SHMT2; serine hydroxymethyltransferase 2, SMOX; spermine oxidase, SMS; spermine synthase, SRM; spermidine synthase*. Figure adapted from Tedeschi et al., 2013, and Casero & Stewart et al., 2018, and created with https://www.biorender.com/ (2023).

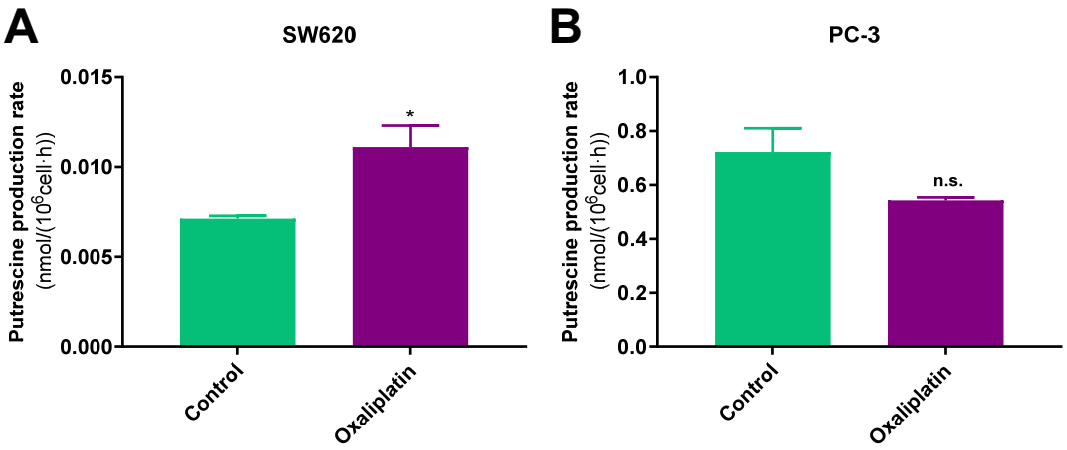

Figure 3.1.8. Putrescine production in control and Oxaliplatin-treated cells. Extracellular putrescine production rate measured after 48 h in A) control and Oxaliplatin-treated (0.25 µM) SW620 cells and B) control and Oxaliplatin-treated (7 µM) PC-3 cells. An independent sample t-test was applied for relative comparison between the two groups, * indicates significant differences ($p < 0.05$).

In brief, Oxaliplatin treatment promoted a distinct effect on amino acid metabolism, and causing a greater glutamine reliance in both cancer types. Oxaliplatin treatment also altered polyamine metabolism in opposite directions. These results indicate that Oxaliplatin treatment may impact mitochondrial metabolism, therefore prompting us to investigate the impact on cellular respiration and alternative energy sources such as fatty acids.

3.1.2.4. Different impact on mitochondrial and fatty acid metabolism after Oxaliplatin treatment in prostate and colorectal cancer cells.

To evaluate the impact on mitochondrial respiration capacity, energy production, and ability to respond to an energetic demand after Oxaliplatin treatment, we used the Mito Stress Test to calculate the mitochondrial function-related parameters by measuring the Oxygen Consumption Rate (OCR) and the glycolytic function through the Extracellular Acidification Rate (ECAR). These responses evidence the different behavior of the Oxaliplatin-resistant cells in comparison with the non-treated cells against the acute injection of glucose and different electron transport chain (ETC) inhibitors.

The extracellular acidification is measured in the complete medium after glucose acute injection to obtain the basal ECAR (**Figure 3.1.9., A**, **Figure 3.1.10., A**). This parameter accounts for the protons produced from lactic acid through LDH activity and mitochondrial-derived CO_2 (Romero et al., 2018, Romero et al., 2021). Therefore, a more direct correlation with the glycolytic function is given by the Proton Efflux Rate (PER) (glycoPER), which eliminates the additional acidification of the extracellular medium resulting from the mitochondrial activity. Our results, focusing on glycoPER, displayed significantly lower values in both Oxaliplatin-surviving cells in comparison with the non-treated condition (**Figure 3.1.9., B**, **Figure 3.1.10., B**). These results correlate with the glycolytic depletion observed after Oxaliplatin treatment in both cell lines.

On the other hand, mitochondrial respiration given by the OCR measured after Oxaliplatin treatment displays different patterns in both cell lines. First, the colorectal cell line did not show any significant alteration in basal respiration in comparison with the

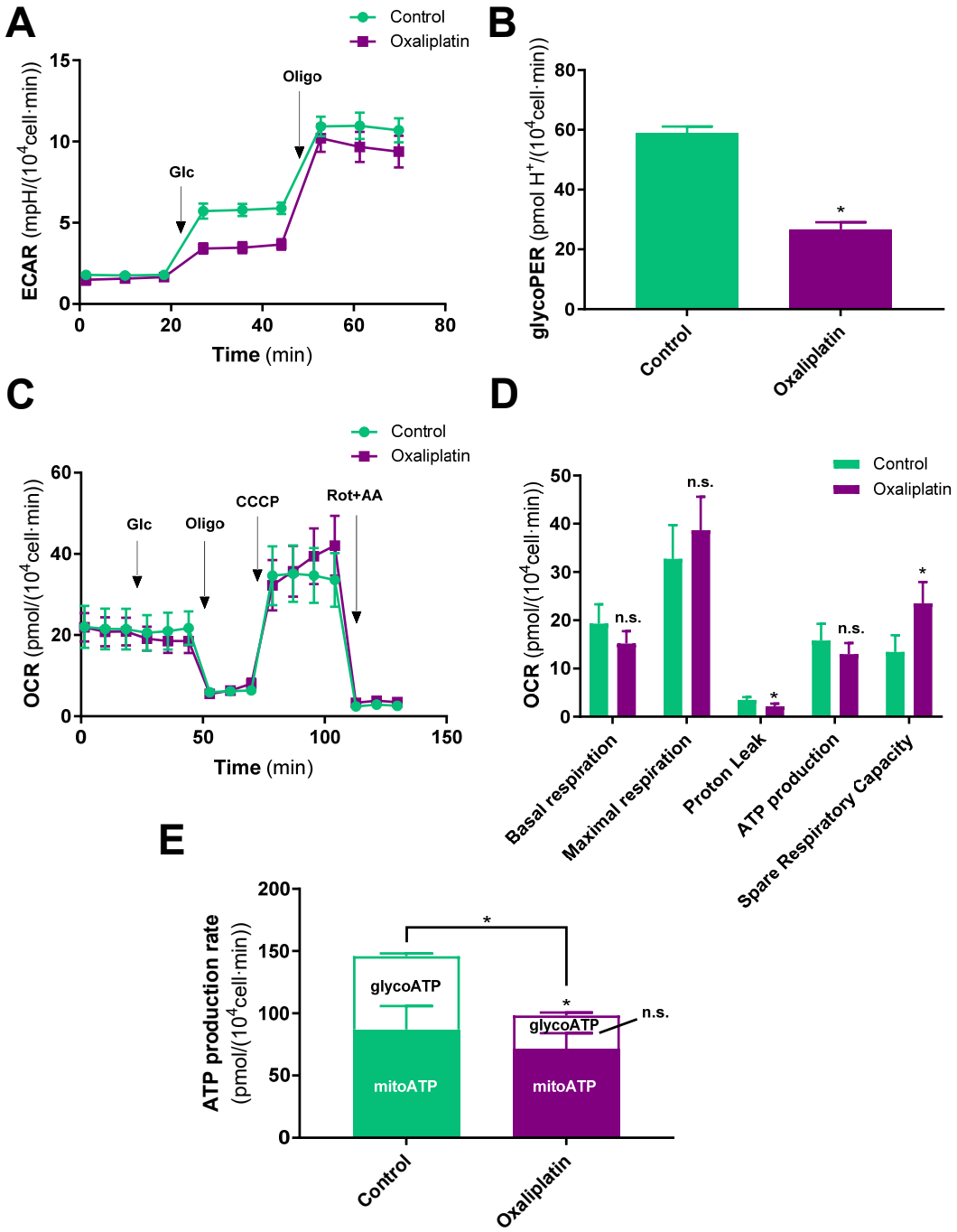

Figure 3.1.9. Respiratory response in SW620 cells treated with Oxaliplatin. Characterization of the mitochondrial function in SW620 cells after 48 h in control and Oxaliplatin-treated (0.25 μM) SW620 cells. A) Normalized monitored values of Extracellular Acidification Rate (ECAR) over time. B) Glycolytic Proton Efflux Rate (glycoPER). C) Normalized monitored values of Oxygen Consumption Rate (OCR) over time. D) Quantification of OCR-related parameters, including basal respiration, maximal respiration, non-ATP linked oxygen consumption (proton leak), ATP production-associated respiration, and spare respiratory capacity. E) ATP production rate discerning mitochondrial ATP (mitoATP) and glycolytic ATP (glycoATP) production. Mito Stress test was performed in Seahorse XFe medium supplemented with glutamine (4mM), with and without Oxaliplatin (depending on the condition) prior to the sequential injection of glucose (Glc, 12.5 mM), Oligomycin (1.5 μM), CCCP (600 nM), and Rotenone (Rot, 2 μM) + Antimycin (AA, 2 μM). An independent sample t-test was applied for relative comparison between the two groups, * indicates significant differences ($p < 0.05$).

control (**Figure 3.1.9., C, D**). Equally, some other OCR-related parameters, such as maximal respiration and respiration associated with ATP production, did not display

differences. However, the oxygen consumption not coupled to ATP production, also known as proton leak, was decreased after Oxaliplatin treatment. In addition, the spare respiratory capacity, which indicates the cells' ability to respond to an energetic demand, was increased. Despite there were no differences in ATP production-related respiration, the total ATP production rate was found to decrease upon Oxaliplatin treatment (**Figure 3.1.9., E**). This parameter comprises the ATP production rate from glycolysis (glycoATP) and mitochondrial oxidative phosphorylation (mitoATP). We determined that the decrease in total ATP production rate was only associated with less ATP production from glycolysis (glycoATP), in accordance with the significant decrease in glucose consumption. In contrast, the ATP production derived from mitochondria (mitoATP) was not altered after Oxaliplatin treatment. Therefore, the metabolic reprogramming arising from Oxaliplatin treatment in colorectal cells maintains the mitochondrial function, conferring metabolic flexibility against cellular stress and preventing a decrease in OCR and ATP production.

In contrast, OCR-related parameters measured after Oxaliplatin response in prostate cancer cells indicated a significant increase in basal respiration, maximal respiration, respiration linked to ATP production, and spare respiratory capacity, with the only exception of proton leak that did not display changes with respect to the control condition (**Figure 3.1.10., C, D**). Even though the total ATP production rate did not reflect differences, there was an increase in mitoATP balanced with a decrease in glycoATP (**Figure 3.1.10., E**), which agreed with the glycolytic reduction promoted by Oxaliplatin treatment in the prostate cell line. Thus, results in Oxaliplatin-resistant PC-3 cells suggest the existence of carbon sources other than glucose fueling respiration, mitochondrial function, and cell flexibility.

To sum up, mitochondrial function was maintained in the colorectal cell line and augmented in the prostate cell line despite the glycolytic depletion promoted by the Oxaliplatin treatment. Our findings in the previous section suggest that amino acid metabolism, notably glutamine, might be the major supporter of mitochondrial metabolism in both cell lines. Considering the increase in glutamine usage as opposed to glucose displayed in colorectal and prostate Oxaliplatin-resistant cells, we explored the main central pathways contributing to resistance linked to glutamine metabolism and oxidative phosphorylation (OxPhos) and, in turn, mitochondrial metabolism. Therefore, we evaluated the differential expression of individual genes regarding the TCA cycle in both cell types (**Figure 3.1.11.**).

In the colorectal SW620 cell line, Oxaliplatin treatment caused a significant overexpression of *pyruvate carboxylase* (*PC*), and *citrate synthase* (*CS*) (**Figure 3.1.11., A**). In the case of prostate cancer PC-3 cells, a decrease is observed in the expression of the genes encoding for the enzymes related to the TCA cycle such as *PC, CS,* but also *OGDH*; the *A subunit of succinate dehydrogenase (SDHA)* and *GTP-specific succinate-CoA ligase (SUCLG2),* encoding for succinate dehydrogenase (SDH) and succinate-CoA ligase (SCS), respectively (**Figure 3.1.11., B**). Hence, TCA cycle enzyme regulation after Oxaliplatin treatment depends on the cancer tissue, and gene expression of TCA cycle enzymes is more affected in the prostate cancer cell line.

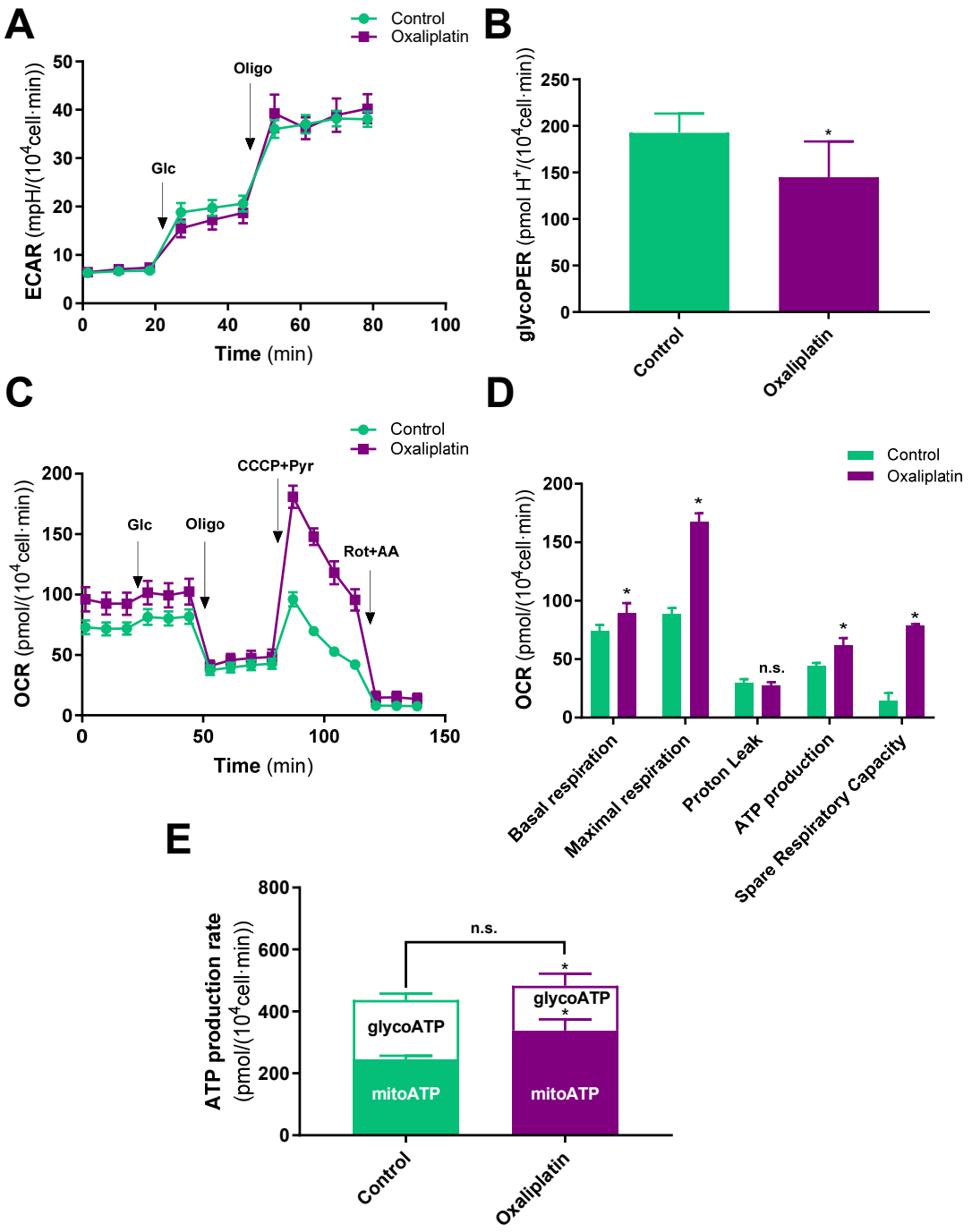

Figure 3.1.10. Respiratory response in PC-3 cells treated with Oxaliplatin. Characterization of the mitochondrial function in PC-3 cells after 48 h in control and Oxaliplatin-treated (7 μM) PC-3 cells. A) Normalized monitored values of Extracellular Acidification Rate (ECAR) over time. B) Glycolytic Proton Efflux Rate (glycoPER). C) Normalized monitored values of Oxygen Consumption Rate (OCR) over time. D) Quantification of OCR-related parameters, including basal respiration, maximal respiration, non-ATP linked oxygen consumption (proton leak), ATP production-associated respiration, and spare respiratory capacity. E) ATP production rate discerning mitochondrial ATP (mitoATP) and glycolytic ATP (glycoATP) production. Mito Stress test was performed in Seahorse XFe medium supplemented with glutamine (2 mM), with and without Oxaliplatin (depending on the condition) prior to the sequential injection of glucose (Glc, 10 mM), Oligomycin (1.5 μM), CCCP (600 nM) + Pyruvate (Pyr, 2 mM), and Rotenone (Rot, 2 μM) + Antimycin (AA, 2 μM). An independent sample t-test was applied for relative comparison between the two groups, * indicates significant differences ($p < 0.05$).

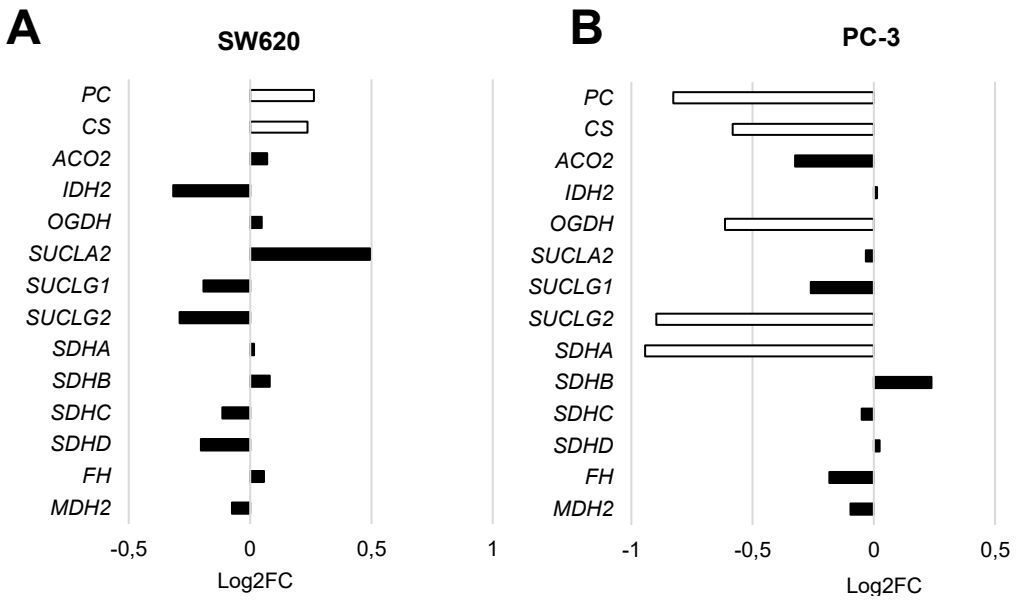

Figure 3.1.11. Differential gene expression of mitochondrial TCA cycle enzymes after Oxaliplatin treatment. Differential gene expression in terms of Log 2 fold-change (Log2FC) after 48 h of treatment with Oxaliplatin regarding the principal encoding genes for TCA cycle enzymes in A) the colorectal SW620 cell line and B) the prostate PC-3 cell line. White-colored bars depict significant differences with respect to non-treated cells (adjusted p-value < 0.05). *ACO2;* aconitase 2. *CS*; citrate synthase. *FH*; fumarate hydratase. *IDH2;* isocitrate dehydrogenases 2. *MDH2*; malate dehydrogenase 2. *OGDH*; oxoglutarate dehydrogenase. *PC*; pyruvate carboxylase. *SDHA, SDHB*, *SDHC*, and *SDHD*; succinate dehydrogenase essential subunits A, B, C, and D. *SUCLA2*, *SUCLG1*, *SUCLG2*; succinate-CoA ligase invariant subunit (G1), and substrate-specific subunits ATP- specific (A2) and GTP-specific (G2).

Together, our results indicate that Oxaliplatin promotes different mitochondrial function responses in both cancer cell lines. Since differential expression results suggest a depletion of the TCA cycle entrance from glycolysis due to the *PC* and *CS* decreased gene expression after Oxaliplatin treatment in the prostate cell line, we explored the gene expression associated with key enzymes controlling fatty acid metabolism to understand whether glutamine is the unique carbon source maintain the mitochondrial function. In this regard, the gene encoding for the isoform C of the CPT1 enzyme, responsible for long-chain amino acids internalization in the mitochondria for further β-oxidation (Li et al., 2019, Wang et al., 2020), was found to be significantly overexpressed (log2FC (*CPT1C*)=1.1±0.2, adjusted p-value $2.85 \cdot 10^{-8}$). Moreover, transcriptomic data integration in the Pathview web server (Luo et al., 2017, Luo et al., 2013) indicated that fatty acid degradation was altered after Oxaliplatin treatment in PC-3 cells (**Figure 3.1.12.**), suggesting that fatty acid oxidation (FAO) plays a pivotal role in generating ATP and reducing potential after Oxaliplatin treatment in the prostate cell line.

On the other hand, differential expression analysis in SW620 cells treated with Oxaliplatin suggested a greater entrance in the TCA cycle from pyruvate to oxaloacetate and toward an increased citrate production through *PC* and *CS* overexpression. Usually, citrate production is correlated to increased lipogenesis (Williams & O'Neill, 2018), and in this case, only ACLY encoding gene (*ACLY;* log2FC=0.17±0.06, adjusted p-value 0.03) was slightly overexpressed after Oxaliplatin treatment in SW620 cells. Hence, we assessed the lipid metabolomic profile by measuring the intracellular concentration of sphingolipids, glycerophospholipids, and acylcarnitines after 48 h in control and

Oxaliplatin-treated SW620 cells. We used heatmaps to distribute the concentration of lipid metabolites based on non-supervised clusterization.

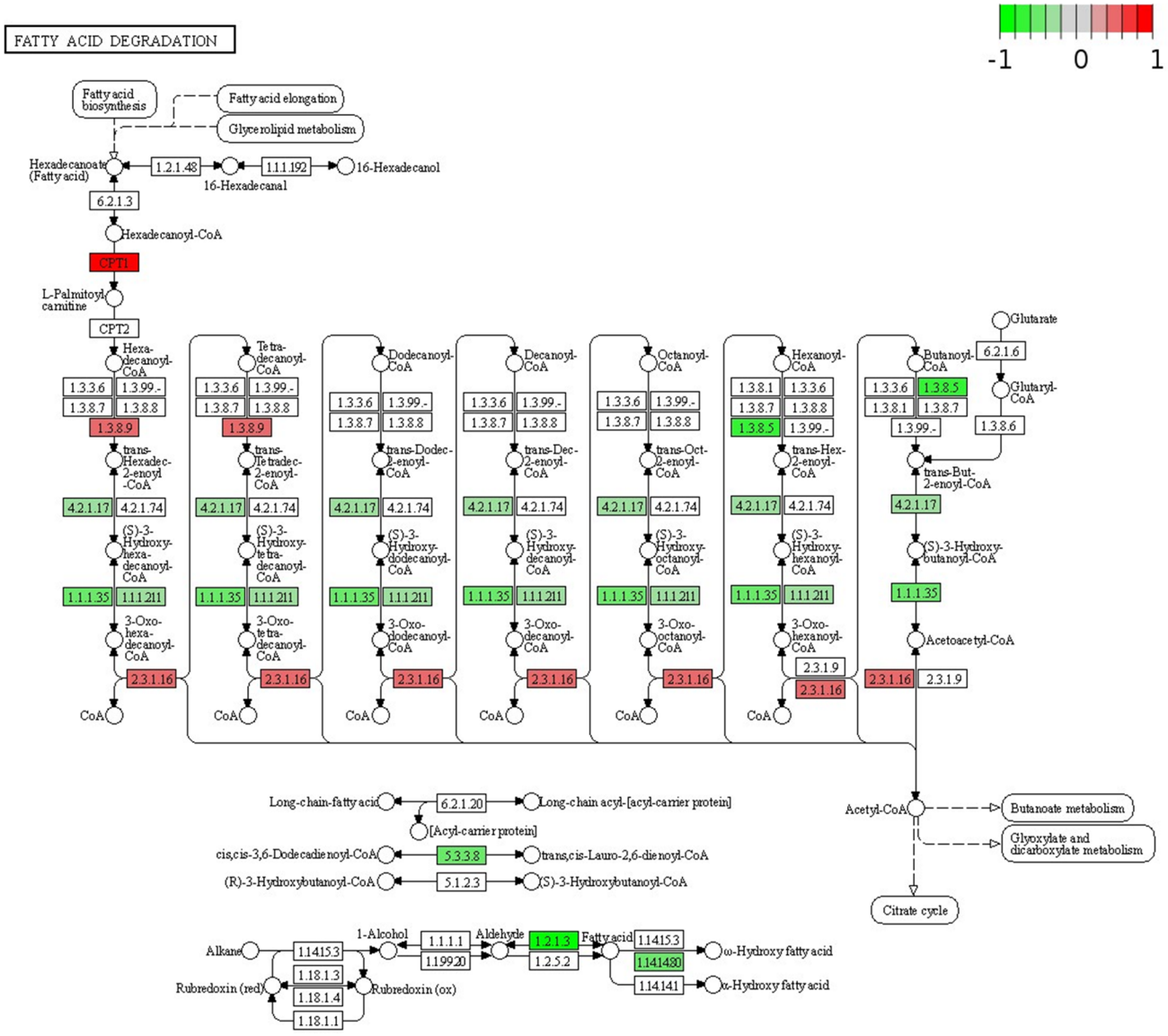

Figure 3.1.12. KEGG Pathview analysis of Oxaliplatin treatment effect on Fatty acid degradation pathway. Pathview map displays the differential expression of genes involved in the 'fatty acid degradation' (KEGG) after 48 h of treatment with Oxaliplatin in PC-3 cells. Colors refer to the expression level; green is downregulated and red is upregulated after Oxaliplatin treatment compared to control (Gene names associated with each reaction are available at https://www.genome.jp/kegg-bin/show_pathway?hsa00071). The figure was downloaded from the Pathview web server (www.pathview.uncc.edu).

Results discerned Oxaliplatin-resistant condition from the control in acylcarnitines (**Figure 3.1.13., A**) and glycerophospholipids (**Figure 3.1.14.**), indicating a lipid profile alteration correlated with the Oxaliplatin treatment. However, these changes were not observed in the intracellular concentration of sphingolipids (**Figure 3.1.15.**).

After Oxaliplatin treatment, there was a notable decrease in the concentrations of short- and long-chain acylcarnitines, according to ratios of (C2+C3) / C0 (**Figure 3.1.13., B**), and (C16+C18) / C0 (**Figure 3.1.13., C**), respectively. These ratios indicated a reduction of fatty acid uptake and subsequent β-oxidation (Koundouros & Poulogiannis 2020, Stine et al., 2022), and a decrease in carnitine palmitoyl transferase 1 (CPT1) activity (Dossus

& Kouloura et al., 2021), indicating a drop in FAO. On the other hand, Oxaliplatin-treated cells displayed an increase in the overall intracellular glycerophospholipid concentrations, suggesting an enhanced synthesis of glycerophospholipids (**Figure 3.1.14.**).

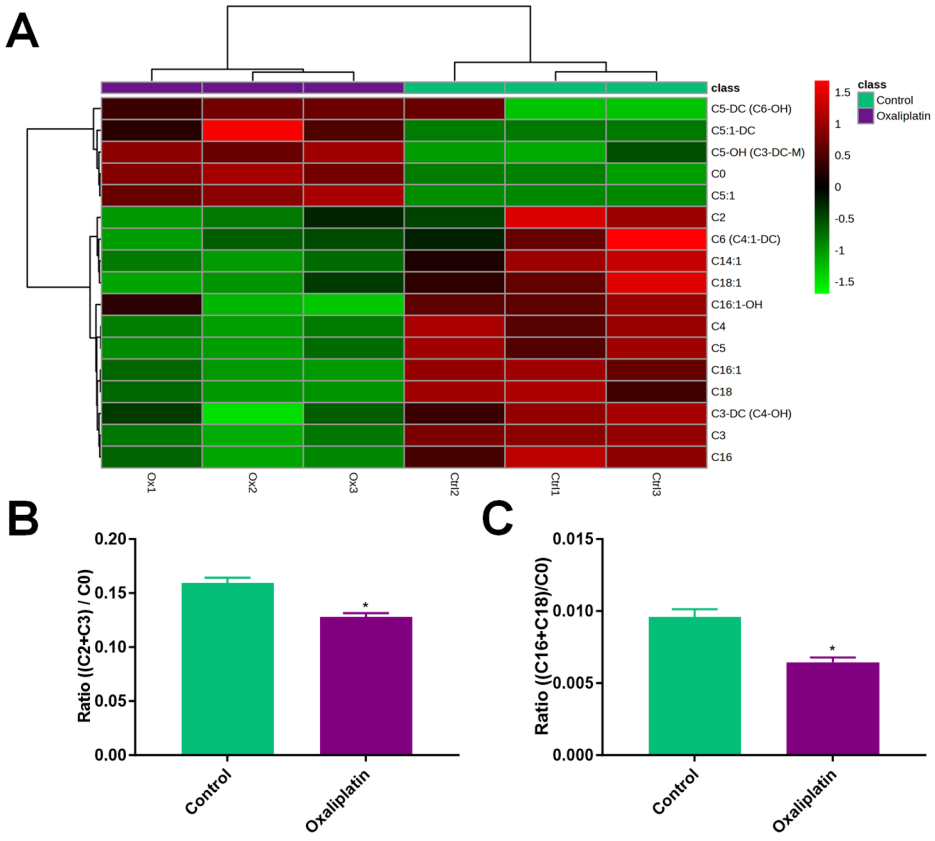

Figure 3.1.13. Acylcarnitines profile in control and Oxaliplatin-treated colorectal cancer SW620 cells. A) Heatmap distribution after non-supervised clusterization of the intracellular acylcarnitines measured after 48 h in control and Oxaliplatin-treated (0.25 μM) SW620 cells. Results expressed in nmol/μg protein were normalized by sum applying Pareto data scaling using Metaboanalyst 5.0 software. B) Ratio of short-chain acylcarnitines to free carnitine ((C2+C3)/C0), which is a measure of overall β-oxidation activity. C) Ratio of long-chain acylcarnitines to free carnitine ((C16+C18)/C0), which is correlated with the activity of carnitine palmitoyl transferase 1 (CPT1). An independent sample t-test was applied for relative comparison between the two groups, * indicates significant differences ($p < 0.05$).

In brief, the metabolic and respiratory results in the PC-3 cell line and the observed differential gene expression in the fatty acid oxidation pathway, indicate that Oxaliplatin treatment caused increased respiration, ATP production, and metabolic flexibility, fueled by increased fatty acid oxidation together with enhanced amino acid metabolism. Thus, there is an increment in the mitochondrial function for cell survival to the detriment of the glycolytic response triggered by Oxaliplatin in the prostate cancer PC-3 cells. In the SW620 cells, Oxaliplatin treatment increases the entrance of pyruvate to the TCA cycle and induces lipogenesis rather than lipid oxidation toward energy production. In this case, glutamine and non-essential amino acids are the major supporters of mitochondrial metabolism, maintaining respiration and redox cell homeostasis through one-carbon metabolism despite the glycolytic depletion promoted by Oxaliplatin.

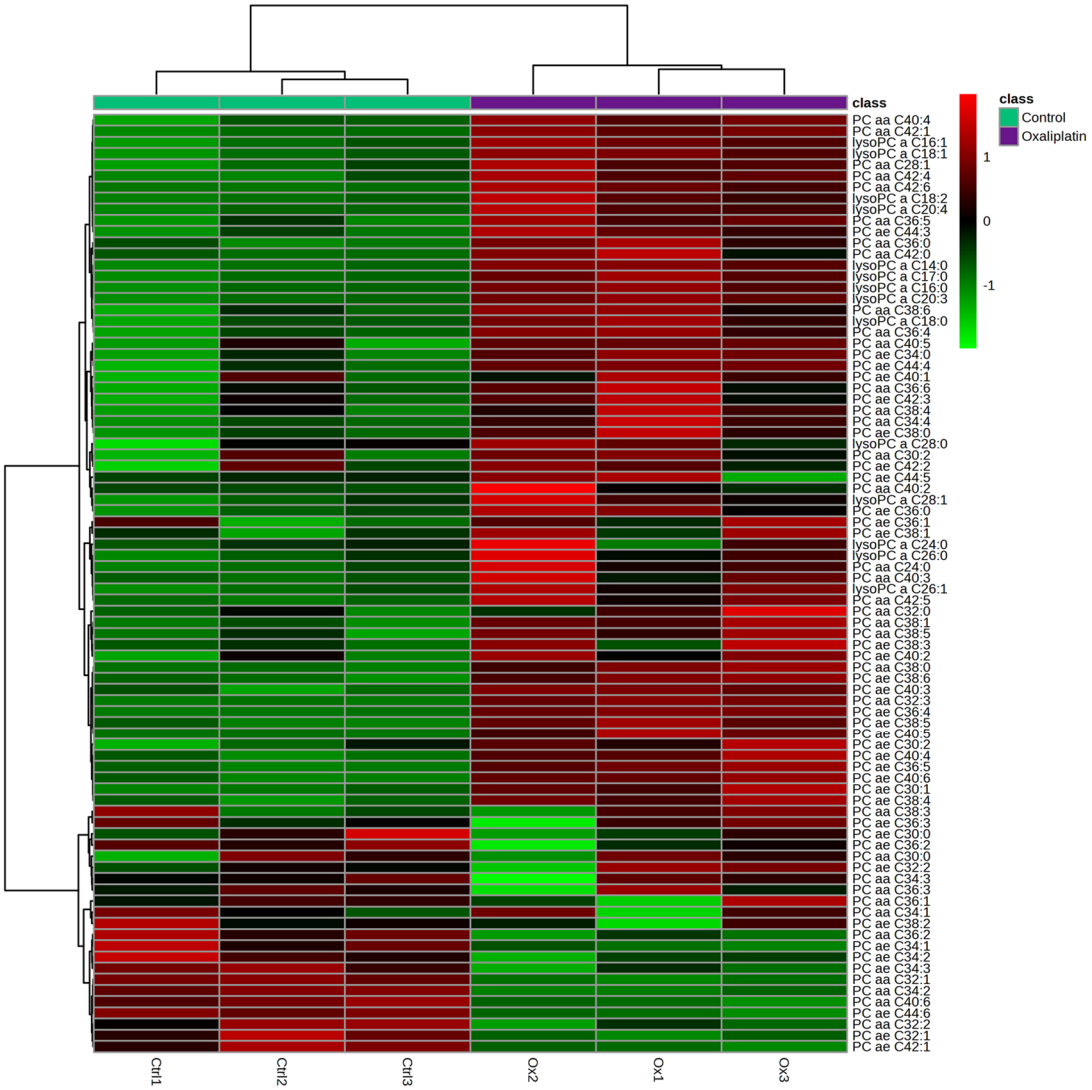

Figure 3.1.14. Glycerophospholipids profile in control and Oxaliplatin-treated colorectal cancer SW620 cells. Heatmap distribution after non-supervised clusterization of the intracellular glycerophospholipids measured after 48 h in control and Oxaliplatin-treated (0.25 μM) SW620 cells. Results expressed in nmol/μg protein were normalized by sum applying Pareto data scaling using Metaboanalyst 5.0 software.

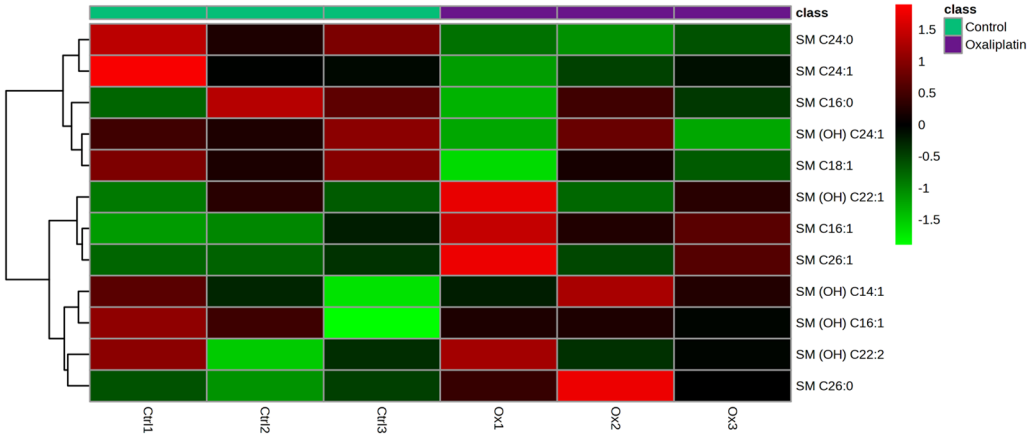

Figure 3.1.15. Sphingolipids profile in control and Oxaliplatin-treated colorectal cancer SW620 cells. Heatmap distribution after non-supervised clusterization of the intracellular sphingomyelins (SM) measured after 48 h in control and Oxaliplatin-treated (0.25 μM) SW620 cells. Results expressed in nmol/μg protein were normalized by sum applying Pareto data scaling using Metaboanalyst 5.0 software.

3.1.2.5. Metabolic vulnerabilities and combinatory treatments predicted by GSMM in colorectal and prostate cancer cells after Oxaliplatin treatment.

We integrated the transcriptomics and metabolomics data to construct a specific genome-scale metabolic model (GSMM) for Oxaliplatin-resistant cells in each cell line, SW620 and PC3 (see **Appendix II** for details). These simulations provided valuable information for flux balance analysis and estimated the final flux distribution after treatment. Flux distribution analysis identified the major fluxes upon Oxaliplatin treatment expressed in terms of Log2FC (**Figure 3.1.16., A**, **Figure 3.1.17., A**), and the final pathway-flux variation contribution to the resistant phenotype was defined in terms of μmol/(10^6cell·h) (**Figure 3.1.16., B**, **Figure 3.1.17., B**). This methodology was applied to evaluate the final contribution of the pathways with significantly altered flux after treatment.

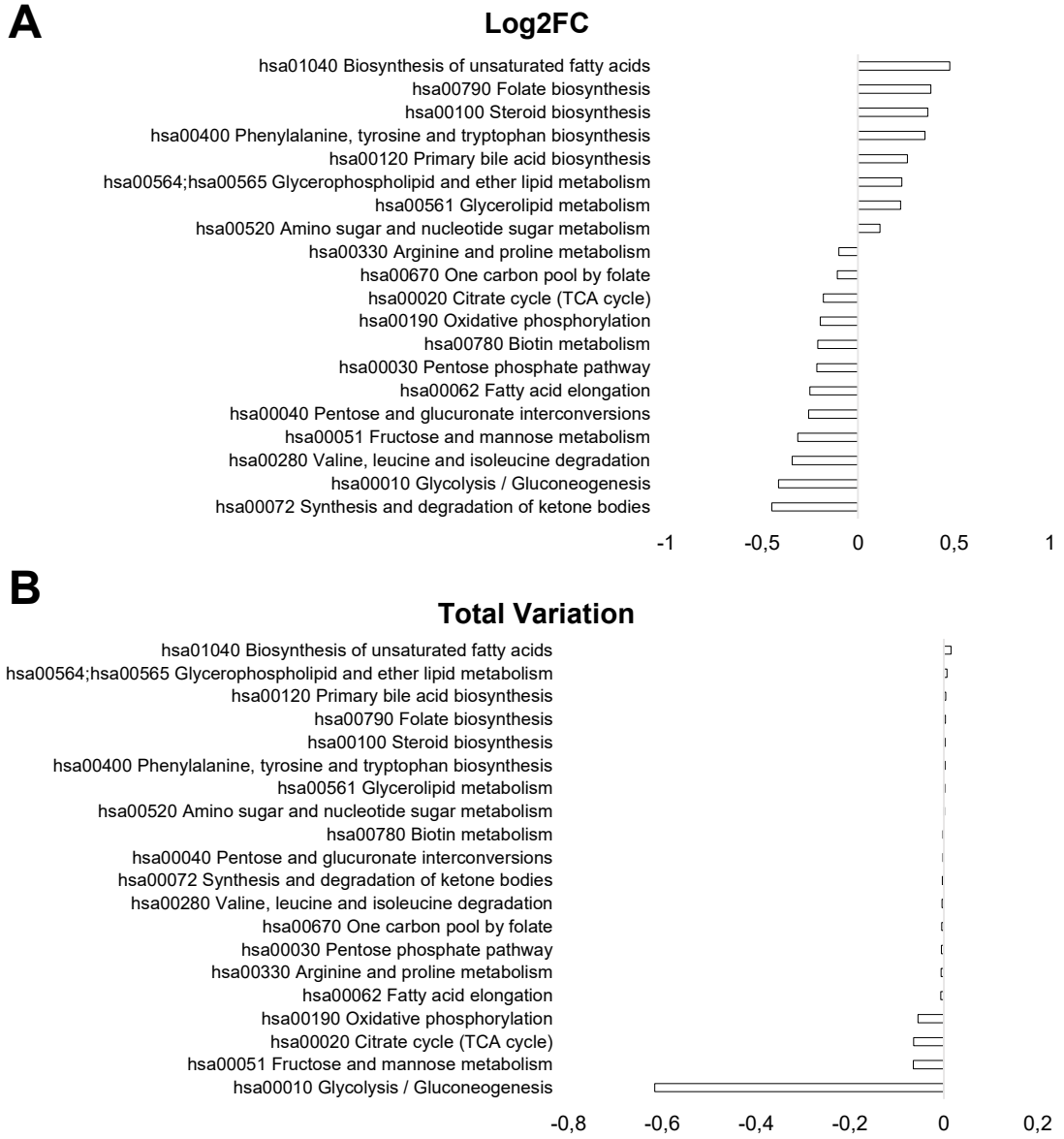

Figure 3.1.16. Flux variations of metabolic KEGG pathways after Oxaliplatin treatment in SW620 cells. Significant changes in Log2FC (Treated / Non-treated) and Total variation μmol/(10^6cell·h) (Treatment – Non-treated) have been considered (total_flux_vres ≥ 0.01) and filtered by fluxes with differences Log2FC ≥ 0.1.

Results indicated an increased flux of biosynthesis of unsaturated fatty acids and folate biosynthesis as significant contributors to metabolic reprogramming promoted by Oxaliplatin treatment in the SW620 cell line (**Figure 3.1.16., A**). However, the contribution of these flux variations to the total flux variation had a minor impact in comparison to the remarkable decrease in glycolysis (**Figure 3.1.16., B**). On the other hand, metabolic fluxes promoted by Oxaliplatin treatment in PC-3 cells had a greater contribution to the total variation than in SW620 cells. Notably, the TCA cycle, OxPhos, and fatty acid metabolism and degradation were the major cell survival supporters in Oxaliplatin-treated cells, presenting the highest increased fluxes and total variation. Also, GSMM in PC-3 described a great decrease in glycolysis, having the most notable total variation in this cell type after Oxaliplatin treatment (**Figure 3.1.17., A**, **Figure 3.1.17., B**).

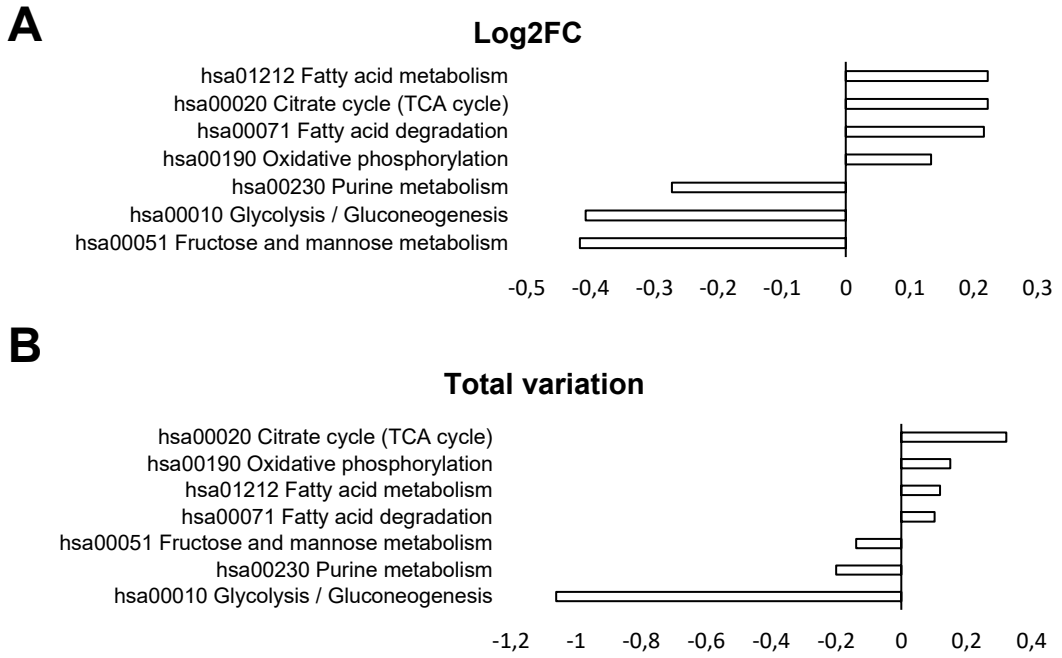

Figure 3.1.17. Flux variations of metabolic KEGG pathways after Oxaliplatin treatment in PC-3 cells. Significant changes in Log2FC (Treated / Non-treated) and Total variation μmol/(10^6cell·h) (Treatment – Non-treated) have been considered (total_flux_vres ≥ 0.01) and filtered by fluxes with differences Log2FC ≥ 0.1.

Therefore, the GSMM reconstruction identifies the glycolytic decrease as the main metabolic pathway variation, in accordance with the experimental results obtained in both cell types.

The GSMM reconstruction also revealed the metabolic vulnerabilities underlying Oxaliplatin adaptation and provided putative metabolic inhibitors able to revert and prevent the transition to the Oxaliplatin resistant phenotype. GSMM strategy involves drug repurposing to propose metabolic inhibitors whose mechanism of action and genes encoding for their target enzymes (denoted as target genes) are annotated in DrugBank (Knox et al., 2024) and Therapeutic Target (Chen et al., 2002) databases. In this regard, our results are filtered by a positive aggregate score, as indicated in **Table 3.1.1.** and **Table 3.1.2.**, which denotes the potential capability to hinder the transition, where the highest values indicate a greater capacity to prevent or reverse drug resistance.

Table 3.1.1. Target genes and drug candidates predicted by GSMM for reverting Oxaliplatin resistance in SW620 cells. Target genes (NCBI number) and drugs proposed by GSMM, applying the quadratic metabolic transformation algorithm (qMTA) and the minimization of metabolic adjustment (MOMA) to revert or prevent Oxaliplatin-resistant phenotype in SW620 are filtered by positive aggregate score. Only drugs annotated in DrugBank (Knox et al., 2024) and Therapeutic Target (Chen et al., 2002) databases are shown. The metabolic inhibitors with positive aggregate scores are arranged in descending order based on their values up to the metabolic inhibitor with an aggregate score value closest to 50% of the highest aggregate score value. **Gene IDs:** 526, *ATP6V1B2 ATPase H+ transporting V1 subunit B2*. 1633, *DCK deoxycytidine kinase*. 4860*, PNP purine nucleoside phosphorylase. 6240*, *RRM1* ribonucleotide reductase catalytic subunit M1. 6241, *RRM2 ribonucleotide reductase regulatory subunit M2*. 7296, *TXNRD1 thioredoxin reductase* 1. 7298, *TYMS thymidylate synthetase*. 10587*, TXNRD2 thioredoxin reductase 2*. 50484, *RRM2B ribonucleotide reductase regulatory TP53 inducible subunit M2B.*

Drug	Gene target	Aggregate Score	Target
Motexafin gadolinium	10587, 6241, 7296	0.81383788	Nucleotide metabolism
Cladribine	4860, 50484, 6240, 6241	0.75997523	
Clofarabine	50484, 6240, 6241	0.756686089	
Gemcitabine	6240, 7298	0.54335894	
Fludarabine	1633, 6240	0.54335728	
Hydroxyurea, Gallium maltolate, Clofarabine	6240	0.54334603	
Gemcitabine, Gallium maltolate	6241	0.54334603	
Gallium nitrate	526, 6241	0.54334603	

After Oxaliplatin treatment, GSMM reconstruction for the colorectal cancer cells identified nucleotide metabolism as the major metabolic vulnerability targetable by several metabolic inhibitors detailed in **Table 3.1.1.**. Cladribine, approved for multiple sclerosis (Pfeuffer et al., 2022) and effective in hematological disorders, is one of the metabolic inhibitors with the highest aggregate score. It is a prodrug that inhibits the adenosine-deaminase (ADA) enzyme and also the ribonucleotide reductase isoforms (RRM1/2/2B), DNA Polymerase catalytic subunits (POLA1, POLE, POLE2/3/4), and purine nucleoside phosphorylase (PNP), which, in turn, interferes with DNA synthesis (Knox et al., 2024, Warnke et al., 2010). Indeed, the combination of Cladribine and Oxaliplatin in colorectal cancer SW620 cells for 48 h of treatment yielded synergistic antiproliferative results in a low concentration range (**Figure 3.1.18.**).

Cladribine is a very similar drug to Fludarabine, listed in **Table 3.1.1.** with a lower aggregate score than Cladribine. Fludarabine is reported to inhibit DNA synthesis by targeting RRM1, POLA1, and deoxycytidine kinase (DCK) (Knox et al., 2024), which is also involved in nucleotide metabolism (Wu & Gong 2022). This drug has also displayed effective results in hematological disorders; however, depending on the features of the disease, the different combinations of Cladribine and Fludarabine lead to distinct survival outcomes (Park et al., 2016). Therefore, we tested the combination of Fludarabine and Oxaliplatin to evaluate the impact on cell proliferation. Our results for this combination showed no synergism after 48h of treatment (**Figure 3.1.19.**).

Gemcitabine is a nucleoside analog that targets RRM1, thymidylate synthetase (TYMS), and cytidine/uridine monophosphate kinase 1 (CMPK1), hence, DNA synthesis. This drug is extensively utilized as an anticancer treatment in several cancer types, such as pancreatic, ovarian, bladder, NSCL, and breast cancers (Pandit & Royzen, 2022). In fact, gemcitabine has already been suggested as an alternative treatment in combination with Oxaliplatin (GEMOX) for advanced CRC (Chocry et al., 2022, Kim et al., 2012, Ziras et al., 2006), being also effective across several solid tumors (Meriggi et al., 2010), validating the GSMM prediction. These findings depicted that nucleotide metabolism

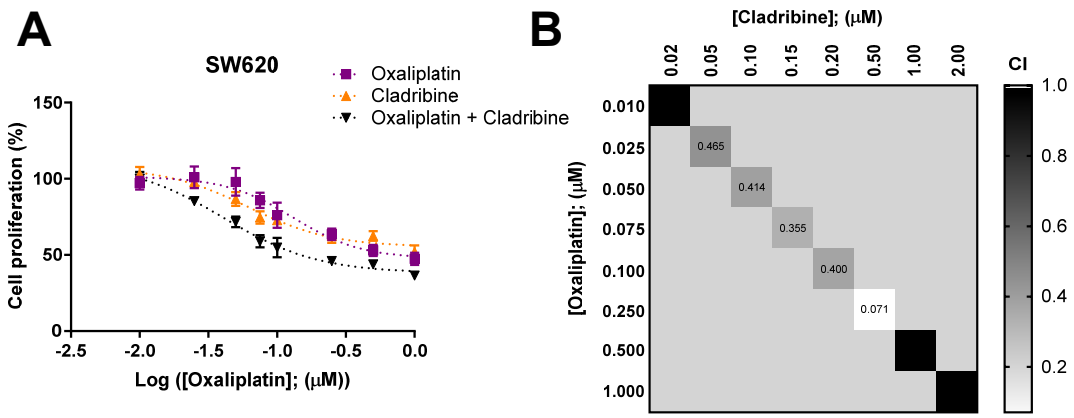

Figure 3.1.18. Synergistic antiproliferative effects of Oxaliplatin and Cladribine combined treatment in SW620 cells. A) Cell proliferation curves at increasing concentrations in the metastatic colorectal SW620 cell line after 48h of treatment with Oxaliplatin and Cladribine alone or in combination with a constant concentration ratio [Oxaliplatin: Cladribine] (1:2), B) Combination index (CI) value calculated with Compusyn software and Chou-Talalay method (black squares represent CI values > 1).

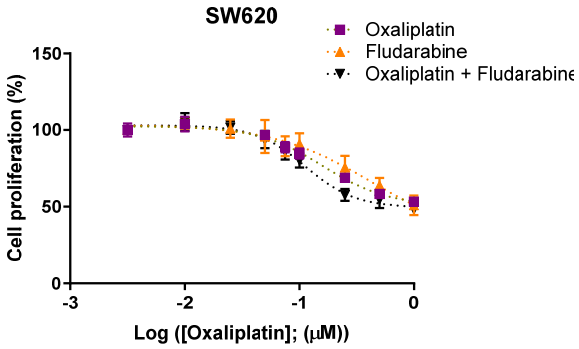

Figure 3.1.19. Antiproliferative effects of Oxaliplatin and Fludarabine combined treatment in SW620 cells. Representative cell proliferation curves at increasing concentrations in the metastatic colorectal SW620 cell line after 48h of treatment with Oxaliplatin and Fludarabine alone or in combination with a constant concentration ratio [Oxaliplatin: Fludarabine] (1:50).

is the main metabolic vulnerability identified through the specific GSMM reconstruction in SW620 Oxaliplatin-resistant cells, demonstrating compelling drug combination predictions to sensitize cells to Oxaliplatin treatment.

On the other hand, GSMM reconstruction for the Oxaliplatin-resistant prostate cancer cells (**Table 3.1.2.**) predicted genes are related to L-type amino acids transporter, including L-cystine/L-glutamate exchanger the solute carrier family 7 member 11 (SLC7A11). This prediction correlates with amino acids metabolism's pivotal role in cell survival and reprogramming after Oxaliplatin treatment, as observed in the previous section. Also, the reconstruction predicted the antioxidant defense mechanisms as targets, including the transsulfuration pathway for glutathione synthesis, thioredoxin reductase, and folate cycle, all of which are essential for reducing potential generation. These results indicated that the antioxidant defense systems are enhanced and critical after Oxaliplatin treatment in PC-3 cells. Finally, GSMM-based analysis also identified the metabolic inhibitors of carnitine palmitoyltransferase (CPTs), whose functions are internalizing L-cystine and fatty acids for maintaining the redox balance and long-chain fatty acids for β-oxidation and energetic supply.

Table 3.1.2. Target genes and drug candidates predicted by GSMM for reverting Oxaliplatin resistance in PC-3 cells. Target genes (NCBI number) and drugs proposed by the GSMM, applying the quadratic metabolic transformation algorithm (qMTA) and the minimization of metabolic adjustment (MOMA) to revert or prevent the Oxaliplatin-resistant phenotype in PC-3. Only drugs annotated in DrugBank (Knox et al., 2024) and Therapeutic Target (Chen et al., 2002) Databases are shown. The metabolic inhibitors with positive aggregate scores are arranged in descending order based on their values up to the metabolic inhibitor with an aggregate score value closest to 1% of the highest aggregate score value. 38, *ACAT1 acetyl-CoA acetyltransferase 1*. 240, *ALOX5 arachidonate 5-lipoxygenase*. 1374, *CPT1A carnitine palmitoyltransferase 1*. 1376, *CPT2 carnitine palmitoyltransferase 2*. 1491, *CTH cystathionine gamma-lyase.* 2936, GSR *glutathione-disulfide reductase.* 3158, *HMGCS2 3-hydroxy-3-methylglutaryl-CoA synthase 2.* 5319, *PLA2G1B phospholipase A2 group IB*. 5742, *PTGS1 prostaglandin-endoperoxide synthase 1*. 5743, *PTGS2 prostaglandin-endoperoxide synthase 2*. 6520, *SLC3A2 solute carrier family 3 member 2*. 6652, *SORD sorbitol dehydrogenase*. 6916, *TBXAS1 thromboxane A synthase 1.* 7296, TXNRD1 *thioredoxin reductase 1.* 113235; *SLC46A1 solute carrier family 46 member 1.* 23657, *SLC7A11 solute carrier family 7 member 11.*

Drug	Gene target	Aggregate Score	Target
AKOS003197197, 5-Hydrazino-1H-tetrazole, Hydrazinoacetic acid, propargylglycine	1491	1.44948	transsulfuration pathway
IGN523	I6520	0.92349	L-type amino acids transporter, including L-cystine/L-glutamate exchanger. L-cystine/L-glutamate exchanger
Riluzole	23657	0.90803	
Sulfasalazine	23657, 240, 38, 5319, 5742, 5743, 6916	0.90796	
3-Sulfinoalanine	2936, 3158	0.90065	Antioxidant defense system, glutathione, and thioredoxin
2,4,6 trinitrobenzene sulfonate 1,3-bis (2-chlorethyl)-1-nitrosourea, Oxidized glutathione, 3,6-Dihydroxy-Xanthene-9-Propionic Acid, 4-nitrobenzoc1,2,5thiadiazole, Trans-(1S(R),2S(R))-2-Hydroxycyclooctyl nitrate, N-6060, N-6547, 3-(Prop-2-Ene-1-Sulfinyl)-Propene-1-Thiol, Meta-Nitro-Tyrosine, uGlutathionylspermidine Disulfide, Trans-(R(S))-2-Hydroxy-1-phenylethyl nitrate, N-9xxx, 1-(2-chlorophenyl)penta-1,4-dien-3-one	2936	0.90065	
Golden phosphorous acetyletic compound 1, Golden phosphorous acetyletic compound 2, Acyl oxymethyl acrylamide ester derivative 1, Terpyridineplatinum(II) complexe 4, Terpyridineplatinum(II) complexe 3	2936, 7296	0.86365	
CP-470,711	6652	0.56103	Sorbitol pathway
HN5-methylfolate, Pemetrexed, 3Hfolinic acid	113235	0.17095	Folate cycle
Perhexiline	1374, 1376	0.11494	Fatty acid metabolism

Overall, targeting the metabolic reprogramming associated with Oxaliplatin short-term treatment based on GSMM-predicted targets was successful in colorectal cancer cells. Despite promising metabolic inhibitors provided by GSMM, further validation is needed in PC-3 cell line. Regarding this, Riluzole, the metabolic inhibitor presenting the highest aggregate score value (**Table 3.1.2.**), has been successfully administered in prostate cancer (Akamatsu et al., 2009, Wadosky et al., 2019) and showed promising results in combination with Oxaliplatin in colorectal cancer cells (Poupon et al., 2018), as well as Pemetrexed in combination with Oxaliplatin, which displayed effective results in castration-resistant prostate cancer (Dorff et al., 2013). Therefore, the computational GSMM predictions provide promising metabolic inhibitors to sensitize cells to Oxaliplatin in PC-3 cells since these combinations have demonstrated satisfactory outcomes in other models.

Then, we wanted to explore the mechanism behind the promising results arising from Cladribine and Oxaliplatin combination in colorectal cancer since they were not

replicated when combining Oxaliplatin with Fludarabine, despite the similarities between Cladribine and Fludarabine. It is reported that Cladribine induces cell cycle arrest in the phase G1/G0 in leukemia cells (Ma et al., 2011, Xu & Jiao et al., 2020), while Fludarabine induces a cell cycle arrest in the G2 phase in animal models (Grégoire et al., 1994, Zhang et al., 1998). This observed distinction in cell cycle responses between Cladribine and Fludarabine suggests a possible mechanism of action related to the effectiveness exhibited in our results. Therefore, cell cycle phase distribution after treatment with Oxaliplatin was evaluated to explore a different strategy to target Oxaliplatin-resistant cells. The experiments were carried out in comparison with Palbociclib, a canonical inhibitor that is known to promote cell cycle arrest in G1/G0 (Huang et al., 2012, Cetrella et al., 2019, Whittaker et al., 2017, Tarrado-Castellarnau et al., 2017, Goel & Bergholz et al., 2022) (**Figure 3.1.20.**).

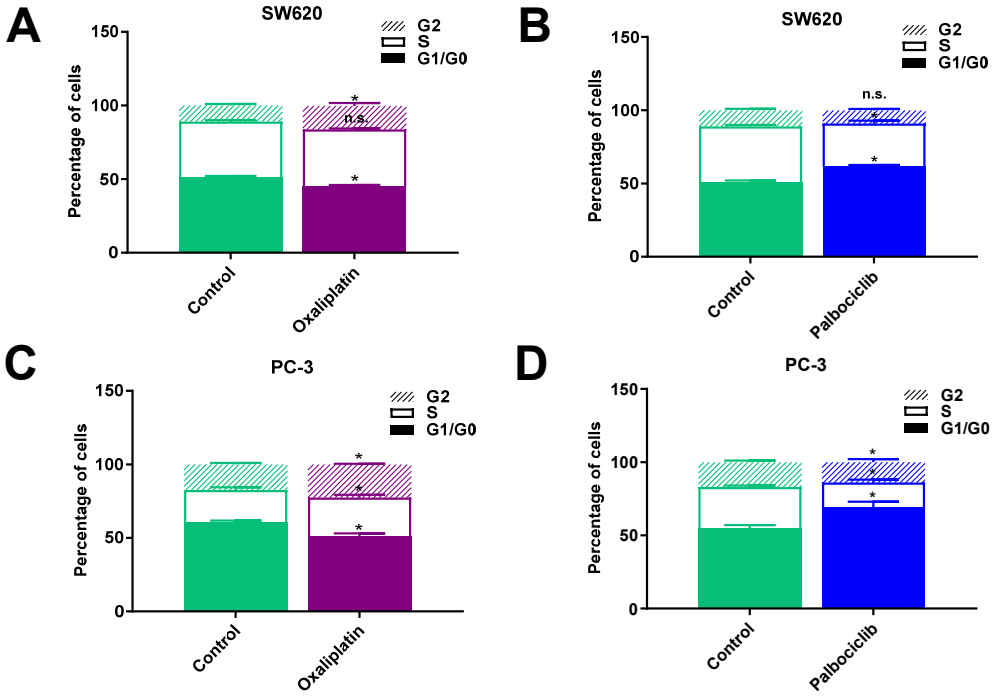

Figure 3.1.20. Oxaliplatin causes G2 cell cycle arrest. Cell cycle analysis after DNA staining with propidium iodide (PI) indicating percentage distributed among the cell cycle phases, pre-replicative (G1/G0), synthesis (S), and post-replicative (G2) phases, after 96h of treatment in SW620 cells with A) Oxaliplatin and B) Palbociclib, and in PC-3 cells with C) Oxaliplatin and D) Palbociclib. An independent sample t-test was applied for relative comparison between the two groups, * indicates significant differences ($p < 0.05$).

Results displayed a significant change in the distribution among the different phases of the cell cycle; Palbociclib promoted cell cycle arrest in G1/G0 similar to Cladribine (Ma et al., 2011, Xu & Jiao et al., 2020), while Oxaliplatin caused arrest in the G2 phase in both cell lines.

Upon this observation, we evaluated the combination of Palbociclib with Oxaliplatin since they promote opposite effects in cell cycle arrest in both cell lines. In concordance with Cladribine and Oxaliplatin combined therapy, short-term treatment with the Palbociclib and Oxaliplatin combination caused a significant decrease in cell proliferation in both SW620 and PC-3 cell lines, with Combination Index (CI) values smaller than 1 (CI<1), indicating a synergistic antiproliferative effect in both cancer types (**Figure 3.1.21.**).

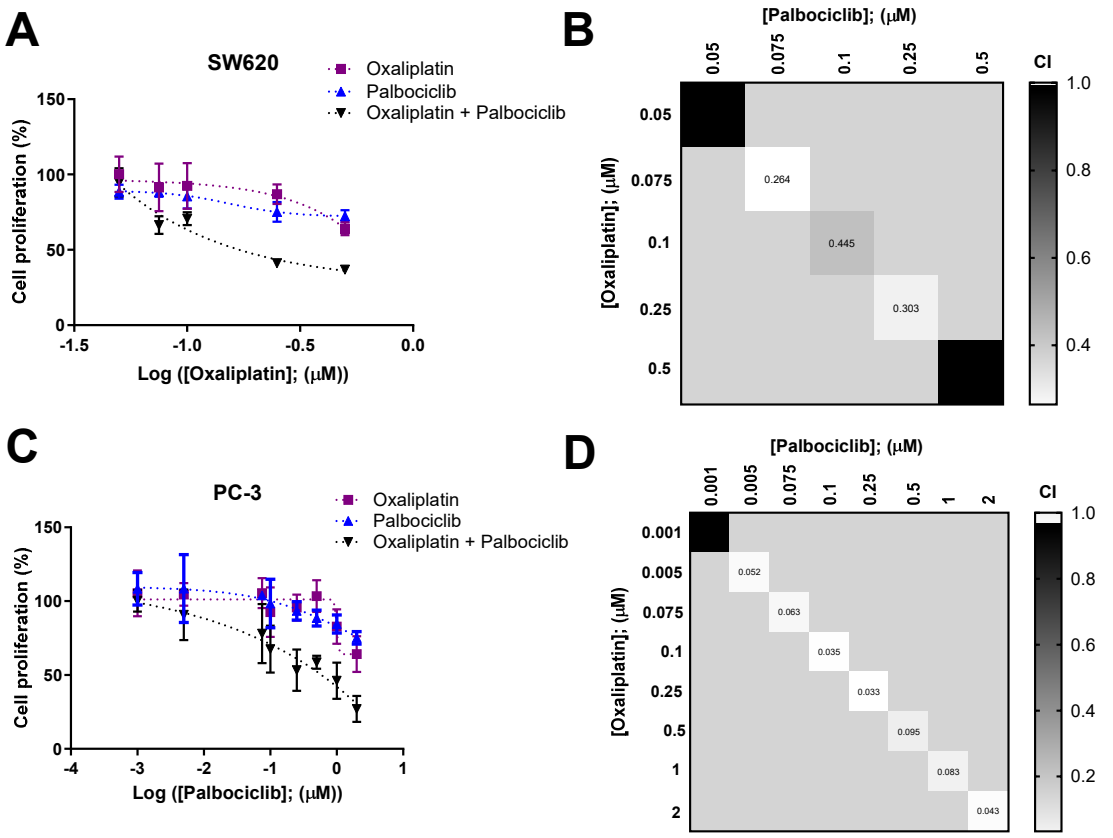

Figure 3.1.21. Oxaliplatin and Palbociclib combined treatment synergic inhibitory effects in SW620 and PC-3 cell proliferation. A, C. Representative graphs of cell proliferation curves at increasing concentrations after 48h of treatment with Oxaliplatin and Palbociclib alone and in combination with a constant concentration ratio [Oxaliplatin: Palbociclib] (1:1) in A) SW620 cells and B) PC-3 cells. B,D. Combination index (CI) value calculated with Compusyn software and Chou-Talalay method (black squares represent CI values > 1) in B) SW620 cells, and D) PC-3 cells.

Therefore, the short-term combined treatment of Palbociclib and Oxaliplatin displays synergism in both cell lines, providing an alternative strategy for combination therapy to overcome and forestall cancer cells' resistance to Oxaliplatin chemotherapy.

3.1.3. Discussion.

Oxaliplatin treatment impairs cell proliferation in advanced colorectal and prostate cancer cells, even after short-term drug exposition. Its effect is in agreement with the great efficacy demonstrated as an anticancer agent widely reported in several cancer types (Di Francesco et al., 2002, Kang et al., 2015, Monneret, 2011, Stordal et al., 2007). In this work, the mCRC SW620 cell line shows greater sensitivity to Oxaliplatin and, therefore, lower concentrations are effective in inhibiting cell proliferation in comparison with treated mCRPC PC-3 cells, in agreement with the Genomics of Drug Sensitivity in Cancer (GDSC) database (Yang et al., 2013).

The treatment with Oxaliplatin leads to significant perturbations in the whole cellular metabolism in both cancer cell types, as observed in other platinum-resistant cancer cells (Cruz-Bermúdez et al., 2019, Tan & Li et al., 2022, Sriramkumar et al., 2022), causing a marked downregulation of multiple metabolic pathways. Metabolic reprogramming after Oxaliplatin treatment is characterized by the notable impairment of

glycolytic function, a common trait in colorectal and prostate cell lines. There is an evident experimental correlation between the extracellular rates of glucose consumption and lactate production, the respiratory results associated with the glycolytic function, such as glycoPER, and the differential expression and gene set enrichment analysis (GSEA), which altogether evidence the impairment in the glycolytic function in Oxaliplatin-treated cells. This glycolytic decrease is also displayed by other cancer cell lines resistant to platinum compounds, including ovarian cancer and NSCLC (Cruz-Bermúdez et al. 2019, Tan & Li et al., 2022). Concerning this, the glycolytic orchestrator *PFKFB3* is found to be downregulated in both cancer cell lines after Oxaliplatin treatment. Indeed, *PFKFB3* depletion has been reported to promote a glycolytic impairment in breast, and endometrial cancer, leukemia, and carcinoma (Clem et al., 2008, O'Neal et al., 2016, Xiao et al., 2021), suggesting that this gene may mediate the glycolytic decrease in Oxaliplatin-surviving cells.

Cell survival upon Oxaliplatin treatment is still possible even with the glycolytic impairment and the decrease in central metabolism. Despite this common response in SW620 and PC-3, the metabolic reprogramming relies on distinct metabolic pathways to support cell survival according to the cell type. The glycolytic impairment triggered by Oxaliplatin induces a metabolic switch to OxPhos or lipid metabolism as reported in other platinum-resistant cancer cells (Sriramkumar et al., 2022, Tan & Li et al., 2022). Our transcriptomic data revealed that genes *PC*, related to TCA cycle entrance, and *CS*, associated with citrate production, displayed significant alterations in both cell lines after Oxaliplatin treatment. Within the TCA cycle, citrate represents an intersection between anabolic and catabolic pathways. Once citrate is produced from oxaloacetate (OAA) and acetyl-CoA by CS, the citrate levels in the mitochondria and cytosol serve as regulators of important metabolic pathways including the TCA cycle, glycolysis, and fatty acid metabolism, representing a key intermediate for metabolic flexibility (Iacobazzi & Infantino, 2014, Porporato et al., 2018, Williams & O'Neill, 2018). These findings suggest that citrate might play a pivotal role underlying the metabolic reprogramming observed in these cell lines subjected to short-term Oxaliplatin treatment.

Normal prostate cells exhibit a specific metabolic profile characterized by increased citrate secretion. Alterations in citrate usage are associated with a metabolic shift towards increased OxPhos reliance and lipogenesis, and correlate with disease initiation and progression in prostate cancer (Bader & McGuire, 2020). In this regard, prostate cancer cells treated with Oxaliplatin displayed *CS* and *PC* downregulation as well as *CPT1C* overexpression, which has been associated with glucose deprivation, FAO induction and ATP production for cell survival and cellular stress protection (Zaugg et al., 2011). This isoform is a regulator of lipid metabolism reprogramming in cancer cells and mediates β-oxidation, exhibiting similar functions to canonical CPT1 isoforms, which includes fueling the TCA cycle (Fadó et al., 2023, Li et al., 2023, Qu et al., 2016). Therefore, these findings suggest an increment in FAO after Oxaliplatin treatment in the PC-3 cell line, which can increase the production of acetyl-CoA, $FADH_2$ and NADH for TCA cycle entrance and ATP generation via ETC and induce citrate oxidation rather than promote lipogenesis, correlating with the observed increment in respiration and mitochondrial ATP production despite the glycolytic drop. Therefore, we hypothesized that Oxaliplatin alters TCA cycle regulation and funnels citrate toward oxidation through the TCA cycle to meet the energetic requirements in this model. In agreement, the induction of fatty acid catabolism has been also revealed as a metabolic vulnerability

observed upon *CPTB1*, and *CPT2* upregulation in gastrointestinal cancers treated with Oxaliplatin (Wang et al., 2020).

Our results also indicate that genes involved in polyamine biosynthesis such as *ODC*, *SMS,* and *SRM* are downregulated after Oxaliplatin treatment in the prostate cell line, promoting a decrease in the putrescine secretion and inducing the expression of the catabolic genes *SAT1* and *SMOX*, which might face the polyamine deficit. The gene encoding for MTAP, which plays an important role in maintaining methionine pools in cells that require greater polyamine synthesis, such as prostate cancer cells (Bistulfi et al., 2016), was also found downregulated after Oxaliplatin treatment in PC-3 cells. Hence, these results indicate that both the methionine salvage pathway and methionine cycle directly correlate with the polyamine depletion observed in prostate cancer cells after Oxaliplatin treatment, which, in turn, might be altering the epigenetic modifications and cell signaling.

In contrast, *PC* and *CS* were found to be overexpressed after Oxaliplatin treatment in SW620 cancer cells. Increased citrate levels secreted to the cytosol activate acetyl-CoA carboxylases (ACCs), stimulating lipogenesis and inhibiting fatty acids uptake for subsequent β-oxidation (Iacobazzi & Infantino, 2014, Williams & O'Neill, 2018). In correlation, we observed a decrease in CPT1 activity and β-oxidation after Oxaliplatin treatment in the colorectal cell line, suggesting the induction of lipogenesis following citrate production. Also, *ACLY*, the gene encoding for the first rate-limiting enzyme for lipogenesis, is found to be slightly but significantly upregulated in Oxaliplatin-resistant SW620 cells. This enzyme is also associated with chemoresistance acquisition in CRC (Zhou et al., 2013). Its gene overexpression is accompanied by an altered lipid profile concerning glycerophospholipids, which play major roles in the cell membrane, cell signaling, and energy metabolism (van der Veen et al., 2017), and acylcarnitines, which provide metabolic flexibility able to switch between glucose and fatty acid metabolism in cancer cells (Melone et al, 2018), thus contributing to the metabolic reprogramming after Oxaliplatin treatment.

Differential expression analysis, targeted metabolomics, and metabolites consumption and production rates after Oxaliplatin treatment in the colorectal cell line suggest an increase in the TCA cycle entrance and lipogenesis, while OxPhos and mitochondrial metabolism are maintained by non-essential amino acids metabolism, notably, glutamine. Increased glutamine reliance is a frequent metabolic response associated with adaptative processes conferring drug resistance in many cancer types (Chen et al., 2021, Hudson et al., 2016, Tarrado-Castellarnau et al., 2017, Wang et al., 2015, Conroy et al., 2020) since glutamine serves as a carbon source for TCA cycle and a nitrogen source for amino acid, nucleotide, and fatty acid synthesis (Yoo, Yu & Sung et al., 2020). Our findings indicate that glutamine provides metabolic intermediates, such as aspartate, asparagine, and proline, mainly involved in TCA replenishment, and nucleotide metabolism (Yoo, Yu & Sung et al., 2020). Greater glutamine utilization might be also involved in maintaining NADPH levels in the colorectal cancer cell line, through glutamate conversion to α-KG performed by NADPH-dependent glutamate dehydrogenases (GDH). Furthermore, glutamine-derived aspartate is converted to OAA by GOT1, followed by transformation into malate by malate dehydrogenase (MDH1), and subsequent oxidation to pyruvate by malic enzyme (ME1), also contributing to NADPH generation (Ju & Lin et al., 2020). *MTHFD1* upregulation stimulates the cytosolic folate

cycle for purine and ATP synthesis and might serve also to regulate NADPH homeostasis (Fan et al., 2016, Ju & Lin et al., 2020, Tedeschi et al., 2013). This pathway also supports the salvage methionine pathway, for methionine usage in polyamine synthesis (Stine et al., 2022, Lieu et al., 2020), which is found dysregulated after Oxaliplatin treatment in this CRC model. In this regard, *AMD1* and *ODC1* overexpression observed in SW620 cells is associated with increased polyamine synthesis and drug resistance through MYC metabolic reprogramming and apoptosis evasion mediated by mitochondrial dysfunction (Sato et al., 2020, Zhu et al., 2022). These findings suggest that MYC may have a role in the metabolic reprogramming of SW620 cells after Oxaliplatin treatment, correlating with the increase in polyamine synthesis for cell survival and in agreement with the observed increased glutamine consumption (Gao et al., 2009). Altogether, we found that the metabolic reprogramming after Oxaliplatin treatment in the metastatic colorectal SW620 cell line promotes nucleotide metabolism and antioxidant defense to support cell survival upon central carbon metabolism depletion.

We identified the principal contributors to metabolic reprogramming and cell survival in both cell types by reconstructing GSMM for the Oxaliplatin-resistant cells. The flux distribution analysis indicates increased fluxes of biosynthesis of unsaturated fatty acids and folate in SW620 cells, and TCA cycle, OxPhos (**Figure 3.1.21., A**), fatty acid metabolism and degradation in PC-3 cells (**Figure 3.1.21., B**). However, these fluxes represent a minor impact on the total fluxes variation since the major contribution is determined by the significant decrease in the glycolytic flux in both cell lines. Genes involved in these pathways responsible for cell survival are also identified as metabolic vulnerabilities and essential genes. Target genes comprising the nucleotide metabolism are the main putative targets in combination with Oxaliplatin in the SW620 cell line. In fact, the combination of Oxaliplatin treatment with Cladribine, a nucleoside analog described commercially as an adenosine deaminase inhibitor used for the treatment of various types of leukemia, multiple sclerosis and other cancer types such as breast cancer in combination with Tyrosine Kinase Inhibitors (Qasrawi et al., 2019, Moser et al., 2022, Wu et al., 2017), display a synergistic effect in a low concentration range. Accordingly, a similar metabolic pathway is targeted by the FOLFOX regimen, comprised of Oxaliplatin, the antimetabolite 5-Fluouracil, and Folinic Acid, which affects DNA synthesis, impairing nucleotide metabolism (Ser et al., 2016) and is widely used in chemotherapy (André et al., 2009, Van Cutsem et al., 2016). Whether Cladribine could be proposed as an alternative to FOLFOX therapy should be further studied. The synergic antiproliferative results obtained by targeting nucleotide metabolism to revert or prevent Oxaliplatin resistance acquisition, as proposed by the GSMM reconstruction, demonstrate this computational strategy's success in identifying metabolic vulnerabilities and predicting putative targets for combination therapies in SW620.

On the other hand, GSMM reconstruction in the prostate cell line identified metabolic vulnerabilities in amino acid uptake, antioxidant defense systems, and fatty acid internalization for subsequent FAO, representing the major cell survival supporters after Oxaliplatin treatment. However, despite having predicted the metabolic inhibitors to sensitize cells to Oxaliplatin in the PC-3 model, further experimental validation is needed to determine conclusive effective combinations.

The *in-silico* analysis of the drug effect over cell proliferation (simulated as biomass production) allows predicting which metabolic reactions must be inhibited to prevent cell

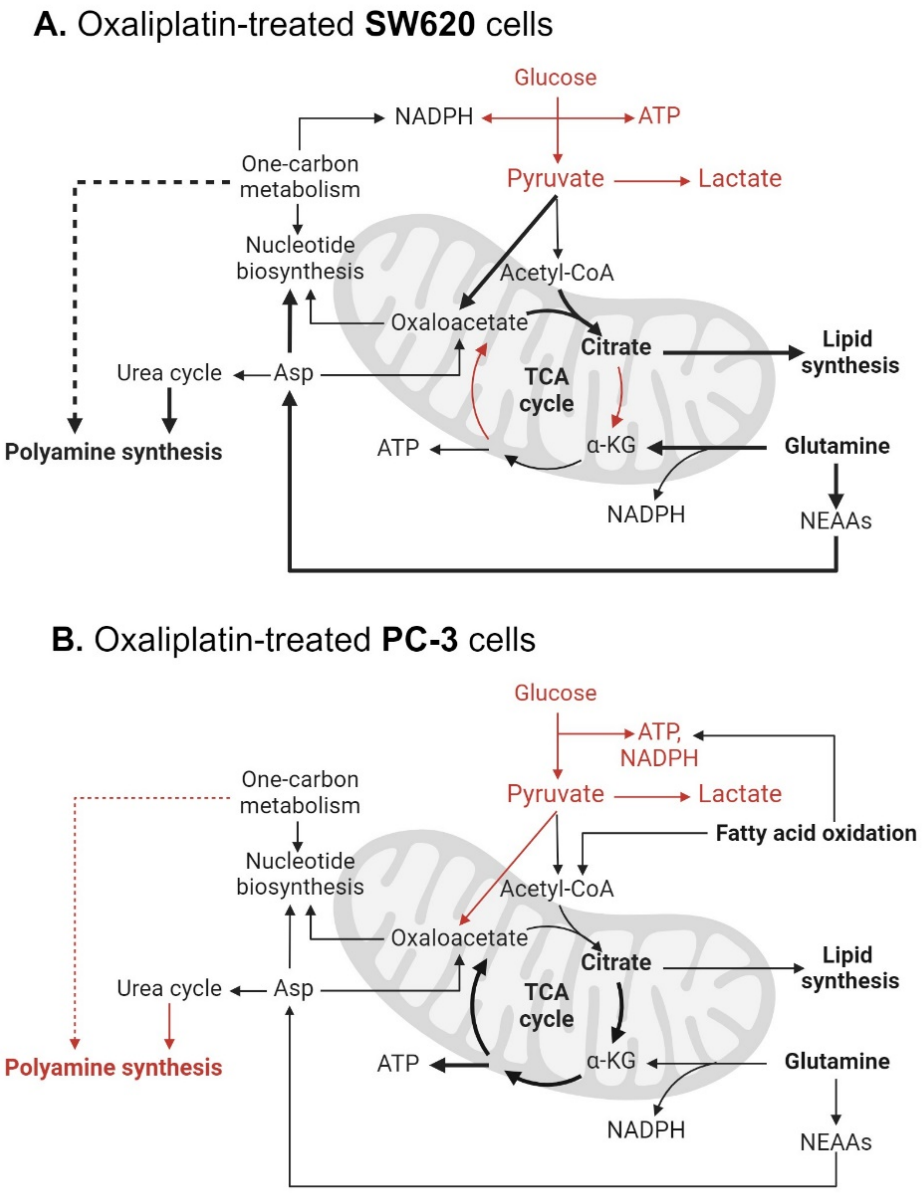

Figure 3.1.21. Graphical abstract of metabolic reprogramming following Oxaliplatin short-term treatment. Metabolic reprogramming underlying 48 h of Oxaliplatin treatment in A) SW620 cells and B) PC-3 cells. Red color indicates a decrease in the pathway after treatment and wider arrows indicate increased metabolic pathway fluxes. Figure adapted from "cancer cell metabolism (nutrient-deprived)" and created with https://www.biorender.com/ (2023).

proliferation. This procedure is carried out by simulating knock-downs (KD) after drug's metabolic reprogramming, comparing treated with non-treated cells, to identify metabolic inhibitors able to revert or prevent this transition. In this case, Oxaliplatin induces gene downregulation. Therefore, we hypothesize that the GSMM approach for putative target prediction is more precise when the drug-induced metabolic reprogramming does not entail a pronounced downregulation in the entire metabolic landscape, as the exhibited by Oxaliplatin-treated cells.

Regarding the most promising therapeutic combinations found to sensitize cells to Oxaliplatin treatment, including Cladribine and Oxaliplatin, which displayed promising results in SW620, and Oxaliplatin and Palbociclib, effective in both cancer types, our findings reveal that the observed synergisms are related to the distinct effects over

proliferation impairment and cell cycle progression. Oxaliplatin treatment may promote the activation of DNA damage response (DDR) mechanisms (Chatterjee & Walker, 2017). We found that cells promote the cell cycle arrest in the G2 phase upon Oxaliplatin treatment, blocking the G2 to M transition. This effect of Oxaliplatin over the cell cycle has also been reported in colon HCT116 and HT29, breast MCF7, uterine cervix HeLa, and lung A549 cancer cell lines (Voland et al., 2006, William-Faltaos et al., 2007), as well as in NSCLC cells after short-term Cisplatin treatment (Cruz-Bermúdez et al., 2019). Remarkably, the combination of Oxaliplatin in both cell lines with Palbociclib, a CDK4/6 inhibitor that exerts the opposite effect on the cell cycle by promoting arrest in the G1/G0 phases, and with Cladribine in the colorectal cell line, which is also reported to impair cell cycle progression by arresting cells in G1/G0 (Ma et al., 2011, Xu & Jiao et al., 2020), presented synergic antiproliferative effects. The combination of chemotherapy with the targeted therapy Palbociclib attending to the cell cycle response is a novel application that has demonstrated efficacy in several preclinical studies in different cancer types (Goel & Bergholz et al., 2022, NLM; NCT01522989, Suppramote et al., 2022).

Although the mechanism underlying the synergism displayed in the combination of Oxaliplatin with Palbociclib in the metastatic colorectal and prostate cancer cell lines is not explored in this work, we hypothesized that *PFKFB3* downregulation by Oxaliplatin treatment might not just mediate the glycolytic flux but could also improve the therapeutic effect of Palbociclib, since it has been reported that FPKFB3 protein is required for cell cycle progression upon interaction with CDK4, controlling the G1 to S phase transition in breast cancer (Jia et al., 2018).

3.1.4. Materials and methods.

3.1.4.1. Cell culture.

The human metastatic colorectal SW620 (ATCC, Rockville, MD, USA) cell line isolated from the large intestine of a 51-year-old male Dukes C colorectal cancer patient, was cultured in Dulbecco's Modified Eagle Medium (DMEM) (Gibco, Thermo Fisher Scientific, MA, USA) containing 4 mM L-glutamine and supplemented with 12.5 mM D-glucose (Merck Life Sciences, Germany), 5% Fetal Bovine Serum (FBS, 10270-106, Lot. 2058474, Gibco), and 1% Penicillin-Streptomycin (10.000 U/ml, Gibco). The human metastatic prostate PC-3 (ATCC, Rockville, MD, USA) cell line isolated from a vertebra metastasis of a 62-year-old male with a castration-resistant adenocarcinoma, grade IV, was cultured in Roswell Park Memorial Institute (RPMI) 1640 medium (Avantor, PA, USA) containing 10 mM D-glucose and supplemented with 2 mM L-glutamine (Gibco, Thermo Fisher Scientific, MA, USA), 10% FBS (10270-106, Lot. 2058474, Gibco), and 1% Penicillin-Streptomycin (Gibco). Cultures were maintained at 37 ºC in a humidified atmosphere with 5 % CO_2.

3.1.4.2. Cell proliferation.

SW620 cells were plated in 96- or 6-well plates (seeding 7×10^3/well and 2×10^5/well, respectively), and PC-3 cells were plated in 96- or 6-well plates (seeding 5×10^3/well and 1.5×10^5/well, respectively) and treated for 48 h with the specific treatments. Cell proliferation tests were assessed through manual counting using 0.2% Trypan Blue staining (Merck Life Sciences) and a Neubauer Chamber (Thermo Fisher Scientific) or

automated counting using Countess II FL (Thermo Fisher Scientific). Additionally, indirect proliferation techniques were utilized, the staining colorimetric MTT assay, where the thiazolyl blue tetrazolium (3-(4,5-dimethylthiazol-2-yl)-2,5-diphenyltetrazolium) bromide dye (MTT) (PanReac AppliCHem, Spain) was dissolved at 1 mg/ml in PBS and incubated 1:1 with serum-free medium for 1 h at 37 ºC 5% CO_2, avoiding light exposure. The colored formazan generated was dissolved in 100 µL of dimethyl sulfoxide (DMSO) and measured on an ELISA plate reader (Tecan Sunrise MR20-301, TECAN, Austria) at 550nm.

Data were analyzed through dose-response curves with GraphPad Prism 9 (GraphPad Software, San Diego, CA, USA). Synergy analysis and quantification was performed using the CompuSyn software (Version 1.0) (ComboSyn, Inc., NJ, USA) and the Chou-Talalay method (Chou, 2010), based on the combination index (CI) where the combination displays synergistic (CI < 1), additive (CI = 1), or antagonist effect (CI > 1). The duplication time was determined by assessing the cell growth at different time points and applying the exponential growth equation:

$$Ln\left(\frac{N_f}{N_0}\right) = \mu \cdot t$$

where,

N_f is the number of final cells (million cells)
N_0 is the number of initial cells (million cells)
μ is the growth rate (h^{-1})
t is the time (h)

Assuming active proliferation, where cells undergo division, holding the following assumption $N_f = 2N_0$. The duplication time was calculated from the final equation:

$$\frac{Ln2}{\mu} = t$$

3.1.4.3. Chemicals and reagents.

Oxaliplatin, Cladribine, and Fludarabine were purchased from MedChemExpress (Monmouth Junction, NJ, USA). Palbociclib was purchased from Selleckchem (Houston, TX, USA).

3.1.4.4. Apoptosis analysis.

Adherent and floating cells in the medium were collected and incubated with Annexin V coupled with FITC, following the kit's instructions (Bender System MedSystem, Viena, Austria) for 30 minutes in binding buffer (10 mM Hepes/NaOH, pH 7.4, 140 mM NaCl, 2.5 mM $CaCl_2$). Propidium Iodide (PI) (MilliporeSigma, MA, USA) was added at the final concentration of 20 µg/ml minutes for the analysis in flow cytometry. The samples were measured by flow cytometry using Gallios™ Flow Cytometer (Beckman Coulter, CA, USA), and the results were analyzed using FlowJo version 7.6.1. This analysis revealed percentages of alive cells, cells presenting early apoptosis, and late apoptosis or necrosis.

3.1.4.5. Protein extraction.

Protein extracts were obtained after 30 minutes of incubation with RIPA buffer (50mM Tris-HCl pH 8, 150mM NaCl, 1% Triton-X-100, 0.5% sodium deoxycholate, 0.1% SDS) supplemented with 1% phosphatase and protease cocktail inhibitors (MilliporeSigma), following the kit's instructions. Subsequently, cells were scraped and collected for quantification using the Pierce BCA Protein Assay Kit (Thermo Fisher Scientific).

3.1.4.6. Metabolic experiments.

3.1.4.6.1. Quantification of extracellular metabolites using spectrophotometric enzymatic assays.

The consumption and production rates of glucose, glutamine, lactate, and glutamate were determined by assessing their concentrations in the extracellular media at different time points and comparing the final to the initial concentrations. Concentrations in the extracellular media were measured using a COBAS Mira Plus (Horiba ABX, France) automated spectrophotometric analyzer based on the measurable concentration of coenzyme NADH at 340 nm. For D-glucose, measurements involved two consecutive reactions: hexokinase, followed by D-glucose-6-phosphate dehydrogenase (G6PD), producing 6-phosphogluconate and NADH. Lactate concentrations were determined by employing lactate dehydrogenase (LDH). Measurements were conducted under pH=9 conditions in the presence of hydrazine to shift the reaction toward pyruvate and NADH formation, effectively preventing the reversible reaction. Glutamate concentrations were measured after α-ketoglutarate conversion and NADH production by glutamate dehydrogenase (GLUD1), while glutamine was indirectly measured using the same method after glutamate conversion through glutaminase (GLS) reaction.

The calculation of the consumption/production rate for each metabolite was based on assuming exponential growth for control condition, with a constant growth rate during the incubation period. The results were subsequently normalized by the number of cells and expressed as a rate (μmol/(10^6 cell·h)).

$$Consumption/production\ rate\ = \left(\frac{\Delta M}{\Delta N}\right) \cdot \mu$$

where,

$\Delta M = M_f - M_0$ is the consumed/produced amount of each metabolite (μmol).

$\Delta N = N_f - N_0$ is the cell growth during the incubation time (million cells).

$\mu = Ln(N_f/N_0)/t$ is the growth rate constant (h^{-1}) for exponential growth.

Linear growth is applied in Oxaliplatin-treated cells:

$$Consumption/production\ rate\ = \left(\frac{\Delta M}{a}\right)$$

where,

$\Delta M = M_f - M_0$ is the consumed/produced amount of each metabolite (μmol).

$a = ((N_f + N_0)/2) \cdot t$ is the growth rate constant (h^{-1}) for linear growth.

3.1.4.6.2. Mass spectrometry-based targeted metabolomics.

The metabolite profile was quantified using the Absolute IDQ p180 kit (20714, Biocrates Life Sciences AG, Innsbruck, Austria). This kit measures 180 endogenous metabolites across seven compound classes, including acylcarnitines, amino acids, biogenic amines, monosaccharides, phosphatidylcholines, and sphingolipids. The analysis of these small molecules and lipids was carried out using tandem mass spectrometry coupled with liquid chromatography (LC/MS/MS) on the MS/MS Sciex Triple Quad 6500 instrument (AB Sciex, Framingham, MA, USA). After quantification, extracellular concentrations were normalized and expressed as consumption/production rate (calculations detailed in section 3.1.4.6.1.), while intracellular concentrations were normalized based on cell protein content.

The obtained results were analyzed using the MetaboAnalyst 5.0 software (Pang et al., 2022), a comprehensive platform used for the statistical analysis of metabolomics data. This software offers a wide range of functions and tools, including the statistical methods employed in this study, such as heatmap analysis.

3.1.4.7. RNA extraction.

RNA purification was carried out using the Qiagen RNeasy kit (Qiagen, Hilden, Germany). Each sample provided 200 ng of total RNA in 50 µL of RNase–free water. Global transcriptomic profiling was accomplished through next-generation sequencing (NGS) of total RNA (see **Appendix II, Section II.1.** for further details of NGS experiments).

3.1.4.8. Transcriptomic pathway visualization.

Differentially expressed genes identified based on adjusted p-values < 0.05 following treatment were integrated and visualized in specific metabolic pathways using the Pathview software tool (Luo et al., 2017, Luo et al., 2013). This approach allowed the effective mapping and interpretation of the significant changes in gene expression within the context of metabolic pathways.

3.1.4.9. Respiratory assays.

After 24 hours of treatment, SW620 and PC-3 cells were plated in XFe24-well plates (seeding 1×10^5/well and 3×10^4/well, respectively) and incubated with the treatment for 24 hours to perform a total treatment of 48 hours. The Agilent Seahorse XF Cell Mito Stress Test was assessed following protocol instructions, measuring Oxygen Consumption and Extracellular Acidification Rates (OCR/ECAR) using a Seahorse XFe24 Analyzer (Agilent, Seahorse Bioscience, North Billerica, MA, USA) in the presence of metabolic substrates targeting different Electron Transport Chain (ETC) components at the following final concentrations; 1.5 µM of Oligomycin (ATP synthase (complex V)), 600 nM of CCCP (Inner mitochondrial membrane) for SW620 cell line or Pyruvate (2 mM) added to 600 nM CCCP for PC-3 cell line, and 2 µM of Rotenone + 2 µM of Antimycin A (Complex I and III, respectively) (Mito Stress test parameters are detailed in **Appendix III**). The final values were normalized by cell count, determined

through automated counting using the Countess II FL Cell Counter (Thermo Fisher Scientific).

3.1.4.10. Cell cycle analysis.

Cells were collected, fixed in cold 70% ethanol, and kept overnight at 4 °C. Cellular suspension was incubated for 1 h at 37 ºC with 0.2 mg/ml RNase (Roche Holding AG, Switzerland) in PBS. Propidium Iodide (PI) (MilliporeSigma) was added in a final concentration of 40 µg/ml minutes before the analysis in flow cytometry. The samples were measured by flow cytometry using Gallios™ Flow Cytometer (Beckman Coulter), and the results were analyzed using FlowJo version 7.6.1. and Mycycle software histograms were utilized to discern cell cycle phases by segregating populations based on their DNA content, where 2n and 4n represent G1/G0 and G2/M, respectively.

3.1.4.11. Statistical analysis.

Statistical analysis was performed using jamovi software (Version 2.2) (The jamovi project, 2021). Group comparisons were evaluated using independent t-tests for pairwise comparisons, ensuring that the data met the assumptions of normality. The homogeneity of variances was assessed through Levene's test. When the assumption of homogeneity of variances was violated, Welch's correction was applied. Additionally, when the data did not meet the assumption of normality, the Mann-Whitney U test was employed. A significance level of $p < 0.05$ was used to determine statistical significance. Standard deviation was employed as a measure of dispersion in all statistical analyses.

3.2. Chapter 2. Study of metabolic reprogramming in metastatic prostate cancer cells after short-term treatment with Palbociclib.

3.2.1. Introduction.

Palbociclib is a specific CDK4/6 inhibitor approved for the treatment of estrogen receptor-positive and human epidermal growth factor receptor 2-negative (ER+/HER2)- advanced breast cancer in postmenopausal women (European medicines agency 2021, U.S. Food and Drug Administration 2017). This targeted therapy has shown promising results in several cancer types, including prostate cancer (NLM; NCT02905318, NLM: NCT02494921). Steroid hormone signaling has been described to alter CDK4/6 activity through the estrogen receptor (ER) in breast cancer and the androgen receptor (AR) in prostate cancer (Goel & Bergholz et al., 2022). Due to this influence on CDK4/6 activity, Palbociclib application in AR+ prostate cancer has gained attention (Tien & Sadar, 2022). However, concerns about Palbociclib resistance and high prostate cancer recurrence persist (Knudsen & Witkiewicz, 2017; Ferlay et al., 2020). Facing this challenge, our study adopts a novel approach focused on the application of Palbociclib in AR- prostate cancer to address potential Palbociclib resistance in the highly aggressive form of prostate cancer, represented by the AR- metastatic PC-3 cell line.

The hypothesis is based on (1) targeting the cell cycle, which represents a promising anticancer strategy since cell cycle dysregulation is frequently found in several cancer types to support continuous division and cell proliferation (Goel & Bergholz et al., 2022, Matthews et al., 2022, Mughal et al., 2023), (2) cell cycle impairment with Palbociclib is accompanied by metabolic changes that are responsible for the cell survival (Tarrado-Castellarnau et al., 2017, Franco et al., 2016), and (3) cell cycle inhibition opens new therapeutic opportunities, e.g., the metabolic vulnerabilities, that can be addressed through combination therapy (Jin et al., 2023, Stordal et al., 2007).

Results presented in the previous chapter (**Section 3.1. Chapter 1**) showed that Palbociclib treatment is effective in combination with Oxaliplatin chemotherapy. These results, together with other reported studies, support that the design of combination therapies improves drug effectiveness, overcomes drug resistance (Lee et al., 2018, Matthews et al., 2022, Otto & Sicinski, 2017), and enhances its durable response in comparison to single-targeted therapies (Jin et al.,2023). Considering this, the present work aims to identify the metabolic vulnerabilities contributing to tumor growth and chemotherapy resistance in metastatic prostate cells by studying the metabolic reprogramming upon short-term Palbociclib treatment and integrating -omics data for Genome-Scale Metabolic Models (GSMM) reconstruction. Based on previous studies in colon cancer (Tarrado-Castellarnau et al., 2017) and in other solid malignancies such as pancreatic cancer (Franco et al., 2016), we hypothesize that both the identification of metabolic pathways altered after Palbociclib treatment and the prediction of putative targets able to increase Palbociclib's anticancer effect through the GSMM reconstruction will lead to therapeutic alternatives to target castration-resistant prostate cancer cells resistant to Palbociclib.

Our results demonstrate that Palbociclib effectively inhibits cell proliferation in metastatic prostate cancer cells by blocking the cell cycle in the G1/G0 phase, and promotes a substantial metabolic reprogramming increasing oxidative phosphorylation (OxPhos),

glycolysis, and reductive carboxylation. These metabolic pathways provide TCA intermediates and supply the energetic demands and the reducing potential required to adapt to Palbociclib treatment. Furthermore, the use of GSMM to identify metabolic vulnerabilities proves to be a successful strategy for the rational design of combination therapies after an enhancement of the metabolic landscape caused by chemotherapy. This strategy effectively addresses Palbociclib resistance through OxPhos and cytochrome P450 inhibitors, demonstrating promising results by combining Palbociclib treatment with the polyphenol Piceatannol, or the antifungal Miconazole and the antibiotic Tigecycline, respectively.

3.2.2. Results.

3.2.2.1. Palbociclib impairs cell proliferation in metastatic prostate cancer cells by arresting the cell cycle in G1/G0.

To study the metabolic reprogramming caused by Palbociclib short-term treatment in the metastatic prostate PC-3 cell line, we first optimized the experimental conditions to evaluate the response of Palbociclib over cell proliferation and cell cycle, which is the principal mechanism of this drug. In order to establish the concentration required to reduce 50% of cell proliferation (IC_{50}), increased concentrations of Palbociclib were evaluated over cell proliferation after 96 h of treatment (**Figure 3.2.1., A**).

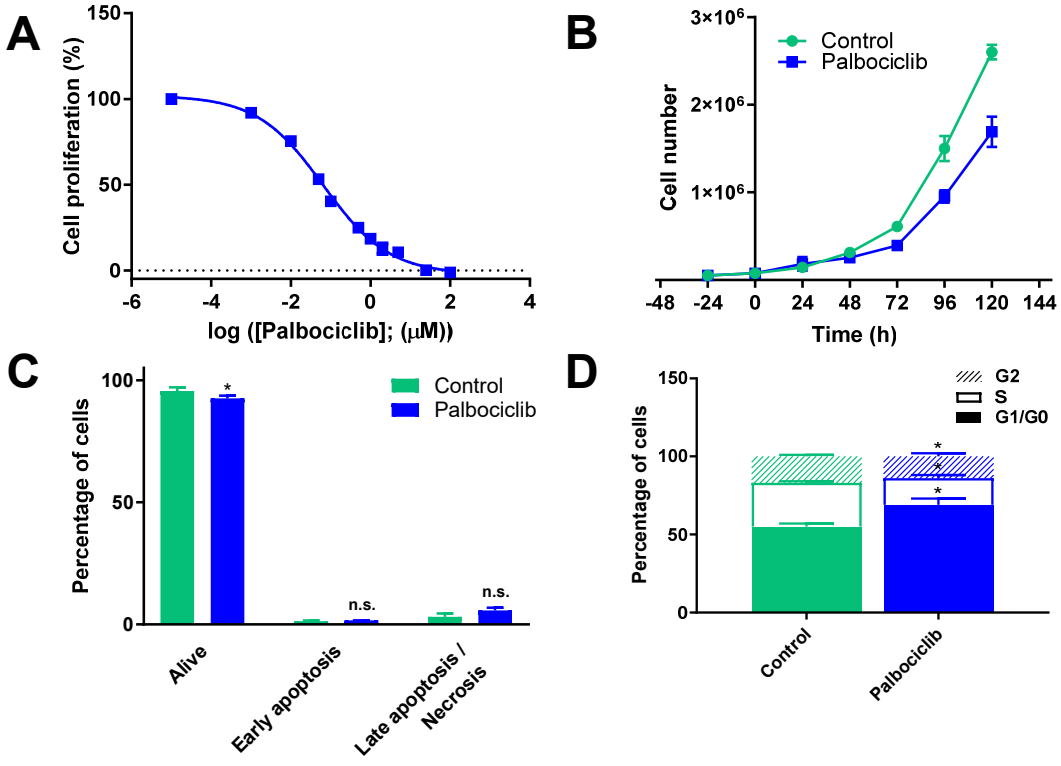

Figure 3.2.1. Palbociclib reduces PC-3 cell proliferation by arresting the cell cycle in the G1/G0 phase. Representative graphs of A) Cell proliferation curve at increasing concentrations of Palbociclib to determine the IC_{50} at 96 h, B) Cell proliferation over time at a fixed Palbociclib concentration (65 nM). C) Apoptosis assay after Annexin V-FITC incubation discerning cells found alive, in early apoptosis and late apoptosis/necrosis in control and 96 h Palbociclib-treated (65 nM) cells. D) Cell cycle analysis after DNA staining with propidium iodide (PI) indicating percentage distributed along the cell cycle phases, pre-replicative (G1/G0), synthesis (S), and post-replicative (G2) in control and 96 h Palbociclib-treated (65 nM) cells. An independent sample t-test was applied for relative comparison between the two groups, * indicates significant differences ($p < 0.05$).

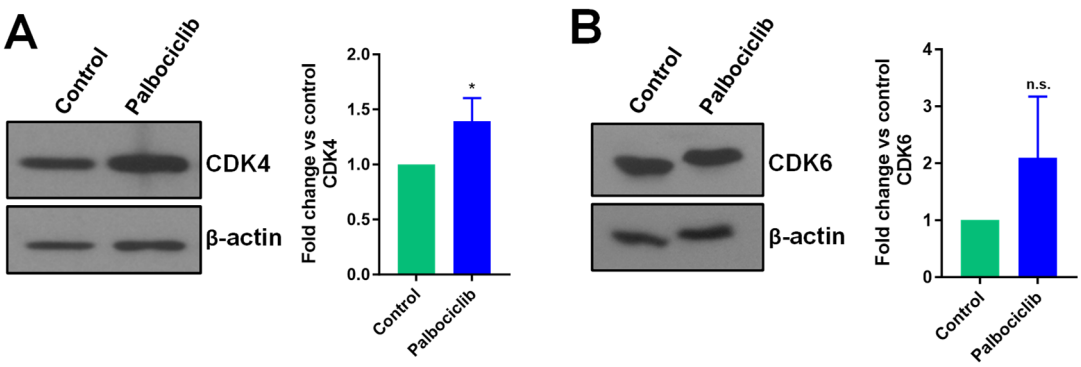

Figure 3.2.2. Effect on CDK4 and 6 protein levels by Palbociclib treatment in PC-3 cells. CDK4 (A) and CDK6 (B) total protein fractions tested in control and Palbociclib-treated PC-3 cells by western blotting. Both blots are accompanied by the quantification by densitometry analysis of protein levels using ImageJ software, representing the mean band intensity (n=3) normalized to β-actin and relative to untreated control. An independent sample t-test was applied for relative comparison between the two groups, * indicates significant differences ($p < 0.05$).

Therefore, the inhibition of cell proliferation after Palbociclib treatment is caused by cell cycle arrest in the G1/G0 phase rather than an apoptotic response. However, despite the increase in the percentage of cells arrested either in G1 or the quiescent state, the rest of the cells are able to overcome this arrest and progress through the cell cycle with a lower proliferation rate.

3.2.2.2. Short-term Palbociclib treatment increases oxidative phosphorylation and mitochondrial activity in prostate cancer cells.

In order to evaluate the major metabolic pathways involved in the metabolic reprogramming underlying survival of the Palbociclib-treated cells, we evaluated the transcriptomic data after 96 h of treatment with Palbociclib in PC-3 cells. We applied gene set enrichment analysis (GSEA) (Subramanian et al., 2005) to analyze the gene set enrichment score after treatment depending on the differential expression of the genes comprising the metabolic pathway gene sets defined by the Kyoto Encyclopedia of Genes and Genomes (KEGG) database, which use a combination of 2-4 letter code and 5 digit number (the unique KEGG-pathways identifiers and the genes included in each pathway are described in detail in https://www.kegg.jp/). Results, shown in **Figure 3.2.3.**, indicated that oxidative phosphorylation (OxPhos) was the most significant metabolic gene set positively enriched (adjusted p-value < 0.05) after short-term Palbociclib treatment in the metastatic prostate cell line.

In consequence, the respiratory capacity was measured to evaluate the gene set enrichment effect beyond the differential expression analysis through the Mito Stress Test after 96 h in control and Palbociclib-treated PC-3 cells. The Mito Stress Test allows the calculation of the mitochondrial function-related parameters by measuring the Oxygen Consumption Rate (OCR), including basal and maximal respiration, non-ATP linked respiration (proton leak), ATP production-associated respiration, and spare respiratory capacity. Also, the proton exchange was measured to obtain information related to the glycolytic function through the Extracellular Acidification Rate (ECAR). In line with the transcriptomic data, the respiratory analysis revealed a significant augment in OCR after Palbociclib treatment that was reflected in all OCR-related parameters

calculated (**Figure 3.2.4., A, B**), suggesting that Palbociclib triggers a higher response to energetic demands by augmenting flexibility and mitochondrial function.

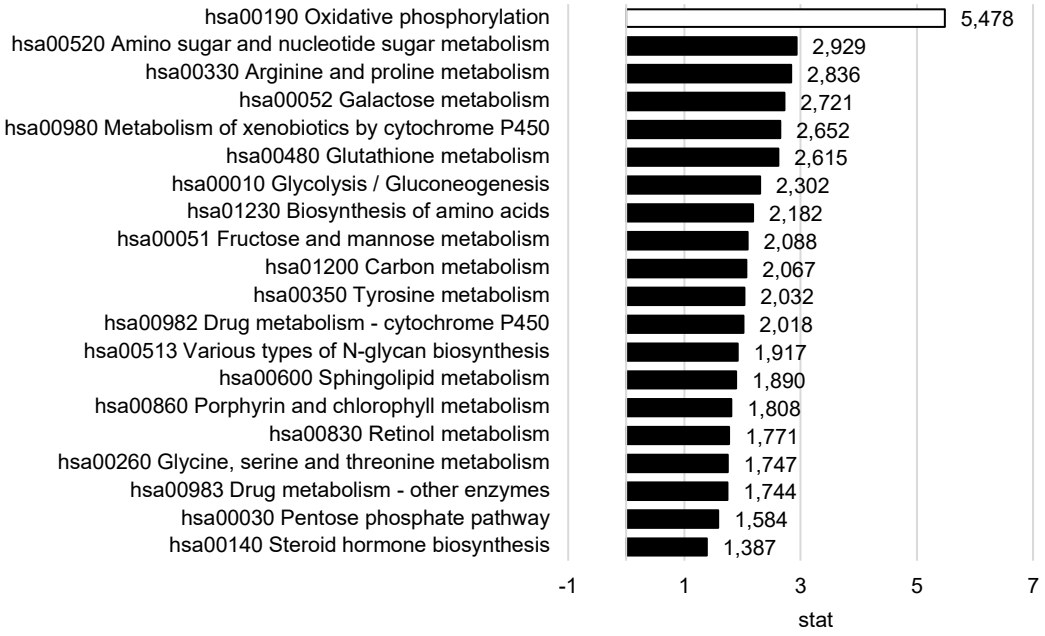

Figure 3.2.3. Gene set enrichment analysis (GSEA) according to KEGG pathways classification. Differential expression is analyzed after 96 h of treatment with Palbociclib in PC-3 cells. Stat represents enrichment score, being positive when it increases or negative when it decreases. White-colored bars indicate significant differences with respect to non-treated cells (adjusted p-value < 0.05), and black-colored bars indicate patterns with adjusted p-value < 0.25.

On the other hand, the glycolytic function measured by ECAR displayed an increase in both basal ECAR (**Figure 3.2.4., C**), corresponding to the cell's response after glucose injection and prior to oligomycin injection, and the glycolytic proton efflux rate (glycoPER) (**Figure 3.2.4., D**), which is directly correlated with glycolysis (Romero et al., 2018, Romero et al., 2021). In agreement with OCR, ECAR, and glycoPER, PC-3 cells also displayed an increase in the total ATP production rate, resulting from an increment in the ATP produced from glycolysis (glycoATP) and mitochondria (mitoATP) (**Figure 3.2.4., E**), both remarkably contributing to meeting the energetic needs to adapt to Palbociclib treatment.

In correlation with the significant increment observed in OxPhos and OCR, we evaluated the mitochondrial activity and the reactive oxygen species (ROS), which are the major by-products resulting from OxPhos upregulation (Sies & Jones, 2020, Hayes et al., 2020). The mitochondrial activity was estimated by measuring the mitochondrial dehydrogenase activity and normalizing it by the number of cells, revealing an increase of 35% after Palbociclib treatment (**Figure 3.2.5.**). In this line, we reported a significant increase in the intracellular ROS measured in the Palbociclib-treated condition (**Figure 3.2.6.**).

These results are in agreement with the augment in OxPhos but also explain the positive enrichment of cellular protective mechanisms preventing apoptotic activation caused by increased cellular stress, such as drug metabolism via cytochrome P450 or glutathione metabolism (**Figure 3.2.3.**).

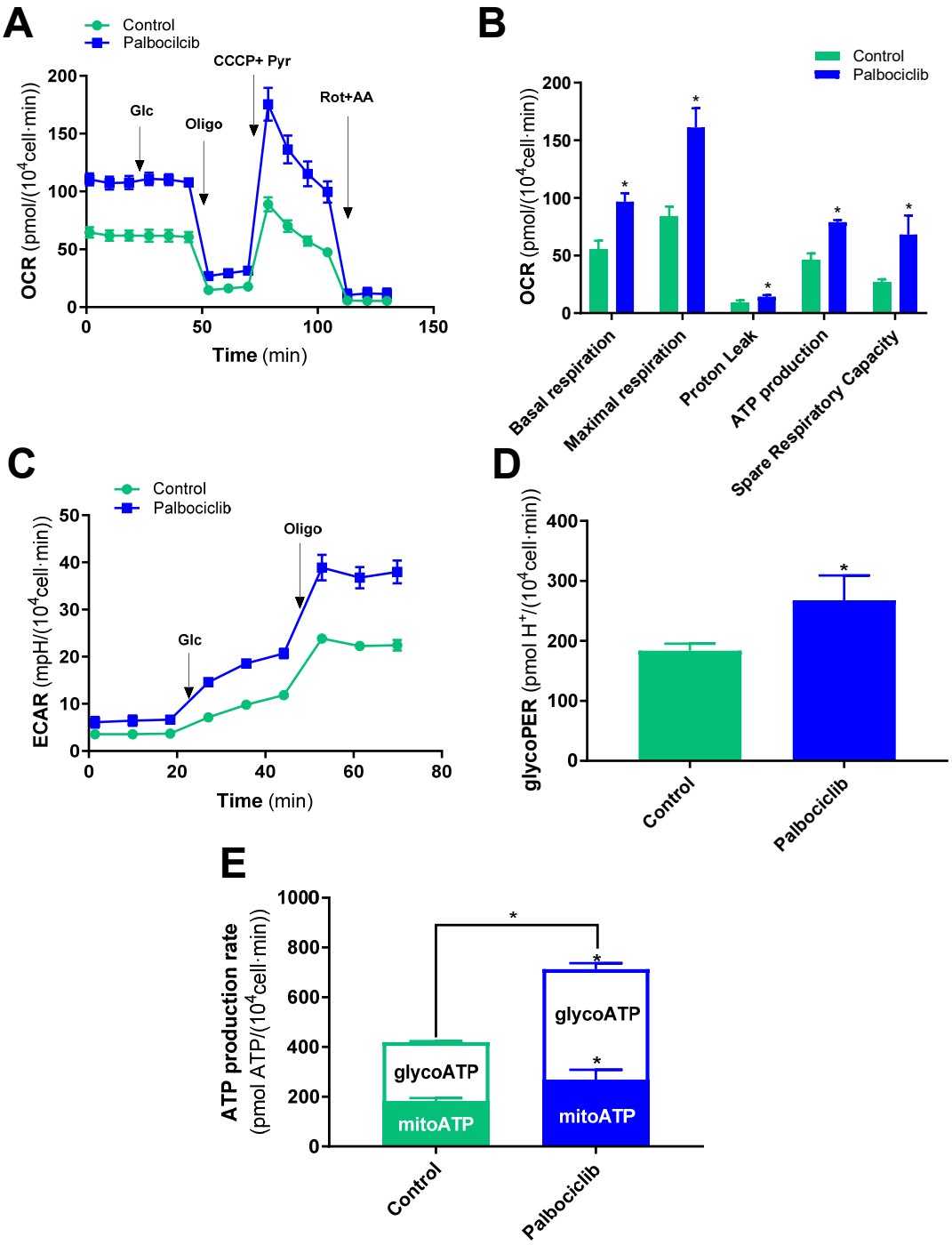

Figure 3.2.4. Respiratory response in PC-3 cells treated with Palbociclib. Mito Stress Test performed in PC-3 cells after 96 h with and without Palbociclib treatment (65 nM). A) Normalized monitored values of Oxygen Consumption Rate (OCR) over time. B) OCR-related parameters, including OCR basal respiration, maximal respiration, non-ATP linked respiration (proton leak), ATP production-associated respiration, and spare respiratory capacity. C) Normalized monitored values of Extracellular Acidification Rate (ECAR) over time. D) Glycolytic Proton Efflux Rate (glycoPER). E) ATP production rate discerning mitochondrial ATP production (mitoATP) and glycolytic ATP production (glycoATP). Mito Stress test was performed in Seahorse XFe medium supplemented with glutamine (2 mM), with and without Palbociclib (depending on the condition) prior to the sequential injection of glucose (Glc, 10 mM), Oligomycin (1.5 µM), CCCP (600 nM) and Pyruvate (Pyr, 2 mM), Rotenone (Rot, 2 µM) and Antimycin (AA, 2 µM). An independent sample t-test was applied for relative comparison between the two groups, * indicates significant differences ($p < 0.05$).

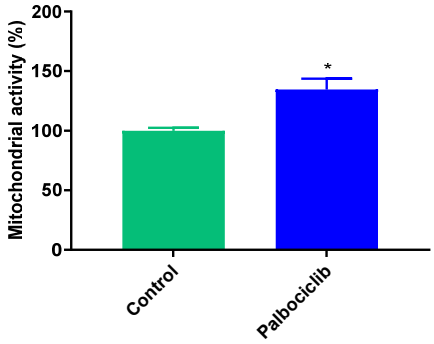

Figure 3.2.5. Palbociclib treatment enhances mitochondrial activity in PC-3 cells. Mitochondrial activity was measured after MTT assay and normalized by direct cell counting and 96 h of incubation with and without Palbociclib (65 nM) in the PC-3 cell line. An independent sample t-test was applied for relative comparison between the two groups, * indicates significant differences ($p < 0.05$).

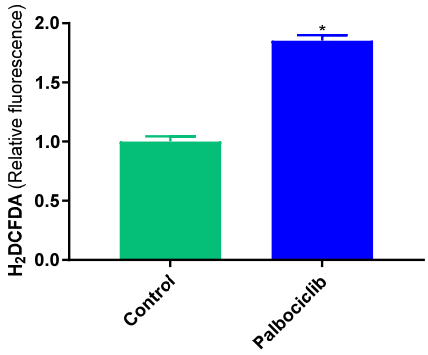

Figure 3.2.6. Palbociclib treatment causes an accumulation of reactive oxygen species (ROS) in PC-3 cells. Intracellular ROS were measured upon incubation with the H_2DCFDA probe (5 μM) after 96 h of treatment with and without 65 nM of Palbociclib in PC-3 cells. Fluorescence intensity values have been normalized with respect to the control condition. An independent sample t-test was applied for relative comparison between the two groups, * indicates significant differences ($p < 0.05$).

In brief, the short-term Palbociclib treatment promotes a significant increase in OxPhos in PC-3 cancer cells, representing the major metabolic change. The gene set analysis and experimental evidence support increased OCR, ATP production rate, ROS generation, and mitochondrial activity in accordance with the reported increment in OxPhos.

3.2.2.3. Metabolic pathways supporting increased oxidative phosphorylation in Palbociclib-resistant cells.

To further study the metabolic pathways contributing to the increased OxPhos and mitochondrial activity sustaining cell proliferation in the metastatic prostate Palbociclib-resistant cells, we evaluated the changes in the expression of genes associated with the central carbon metabolism pathways, and in the consumption/production rates of the main carbon, nitrogen, and energy sources, after 96 h of Palbociclib treatment in PC-3 cells.

First, we performed a differential expression analysis of the genes encoding for the most important enzymes comprising core metabolic pathways such as glycolysis, pentose phosphate pathway (PPP), and TCA cycle (**Figure 3.2.7.**). Palbociclib treatment induced significant overexpression affecting glycolytic genes such as *aldolase C* (*ALDOC*) and

enolase 3 (*ENO3*), and the PPP-related gene *transaldolase 1* (*TALDO1*), suggesting an increment in glycolysis and the non-oxidative PPP branch, and also in the *malate dehydrogenase 2* (*MDH2*), which encodes for the enzyme catalyzing the reversible oxidation of malate to oxaloacetate using the NAD/NADH cofactor in the TCA cycle.

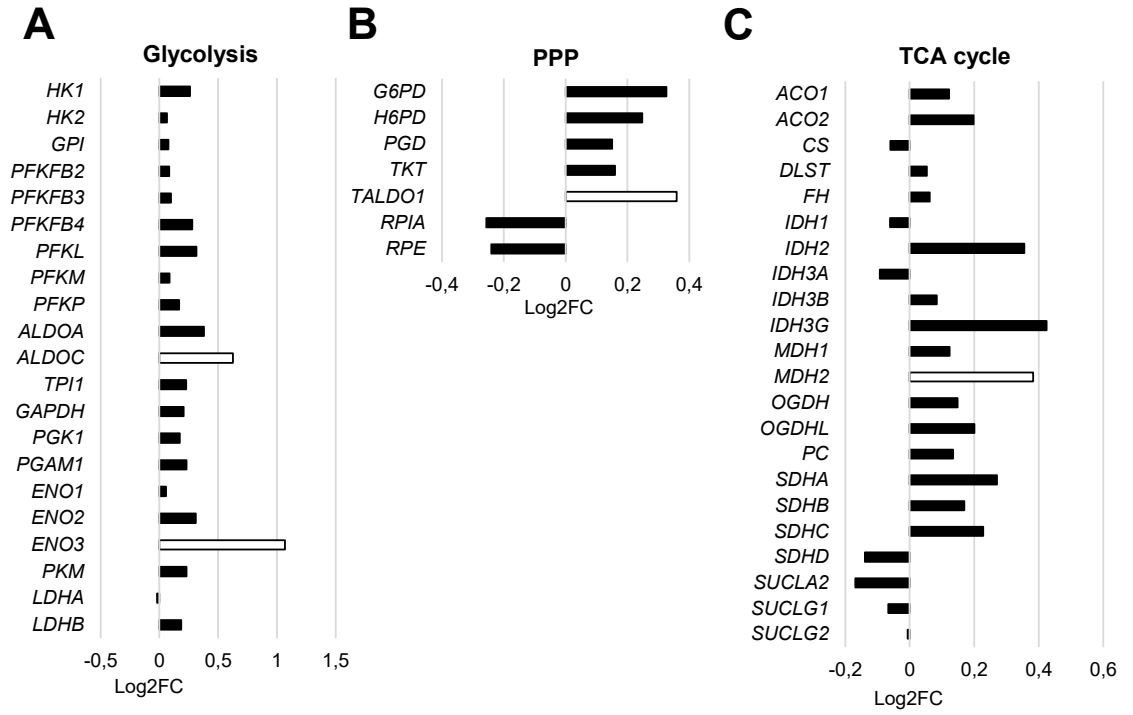

Figure 3.2.7. Differential gene expression of central metabolic pathways after Palbociclib treatment in PC-3 cells. Differential gene expression in terms of Log 2 fold-change (Log2FC) after 96 h of treatment with Palbociclib regarding the principal encoding genes for (A) glycolytic, (B) PPP, and (C) TCA cycle enzymes. White-colored bars represent significant differences with respect to non-treated cells (adjusted p-value < 0.05). **Glycolytic genes:** *HK1, HK2; hexokinase 1, and 2, respectively. GPI; glucose-6-phosphate isomerase. PFKFB2, PFKFB3, and PFKFB4; 6-phosphofructo-2-kinase/fructose-2,6-biphosphatase 2, 3, and 4, respectively. PFKL, PFKM, PFKP; phosphofructokinase, liver type, muscle, and platelet, respectively. ALDOA, ALDOC; aldolase A, and C, respectively. TPI1; triosephosphate isomerase 1, GAPDH; glyceraldehyde-3-phosphate dehydrogenase. PGK1; phosphoglycerate kinase 1. PGAM1; phosphoglycerate mutase 1. ENO1, ENO2, ENO3; enolase 1, 2, and 3, respectively. PKM; pyruvate kinase M1/2. LDHA, LDHB; lactate dehydrogenase A, and B, respectively.* **TCA cycle genes:** *ACO1, ACO2; aconitase 1, and 2. CS; citrate synthase. DLST; dihydrolipoamide S-succinyltransferase. FH; fumarate hydratase. IDH1, IDH2, IDH3A, IDH3B, IDH3G; isocitrate dehydrogenases (NADP(+)) dependent 1, 2, and the catalytic subunits 3 alpha, 3 beta, and 3 gamma, respectively. MDH1, MDH2; malate dehydrogenase 1, and 2. OGDH, OGDHL; oxoglutarate dehydrogenase, and OGDH-like. PC; pyruvate carboxylase. SDHA, SDHB, SDHC, and SDHD; succinate dehydrogenase subunits A, B, C, and D. SUCLA2; succinate-CoA ligase ADP-forming subunits beta. SUCLG1; succinate-CoA ligase GDP/ADP-forming subunit alpha. SUCLG2; succinate-CoA ligase GDP-forming subunit beta.* **PPP genes:** *G6PD; glucose-6-phosphate dehydrogenase. H6PD; hexose-6-phosphate dehydrogenase/glucose 1-dehydrogenase. PGD; phosphogluconate dehydrogenase. TKT; transketolase. TALDO1; transaldolase 1. RPIA; ribose 5-phosphate isomerase A. RPE; ribulose-5-phosphate-3-epimerase.*

The significant increment in ECAR, glycoPER, and ATP production rate from the glycolytic fraction after Palbociclib treatment did not translate into a substantial overall impact on the differential expression of genes related to glycolytic metabolism (**Figure 3.2.7., A**). Therefore, we assessed how Palbociclib affected the extracellular glucose consumption and lactate production rates after 96 h in PC-3 cells. Normalized values showed a significant increase in glucose consumption and lactate production rates after Palbociclib treatment (**Figure 3.2.8., A**). At the same time, the ratio of lactate/glucose, an indicator of the glycolytic capacity and Warburg effect, was significantly decreased

(**Figure 3.2.8., B**). These findings indicate that Palbociclib-resistant cells exhibit reduced lactate production, maintaining an increased glycolytic function, thus suggesting a greater glucose catabolism. These results are in correlation with the increased glycolytic function and ATP production rate observed after Palbociclib treatment.

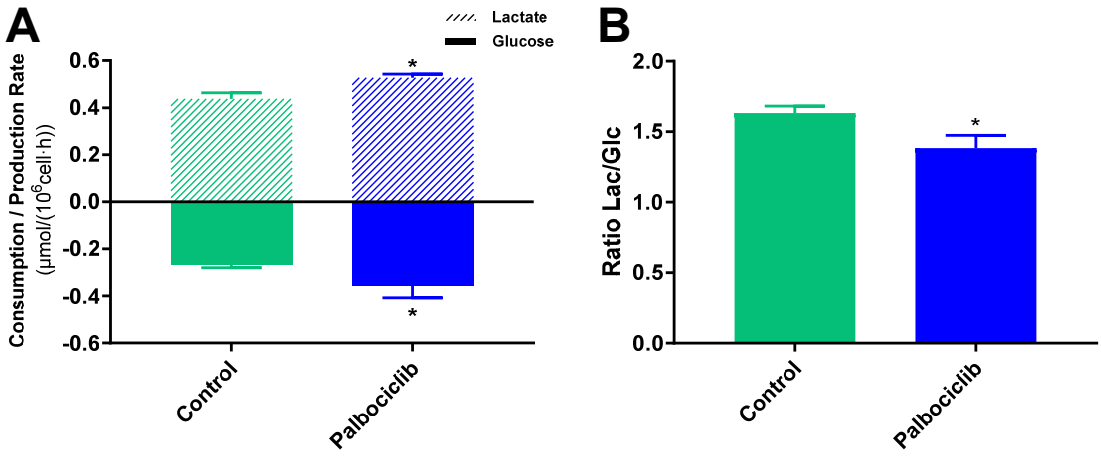

Figure 3.2.8. Augment in glycolytic function after Palbociclib treatment in PC-3 cells. A) Extracellular glucose consumption and lactate production rates, and B) the ratio of lactate production with respect to glucose consumption calculated in control and 96 h Palbociclib-treated (65 nM) PC-3 cells. An independent sample t-test was applied for relative comparison between the two groups, * indicates significant differences ($p < 0.05$).

The reduced lactate/glucose ratio despite the increase in glucose consumption might involve a dysregulation in lactate transporters, or higher glucose utilization in other biosynthetic routes such as PPP, serine biosynthesis, pyruvate production, and/or complete oxidation in the TCA cycle. In order to investigate pyruvate production after Palbociclib treatment in this prostate cell line, which represents a crucial intersection between glycolysis and the TCA cycle, we measured the extracellular pyruvate concentration in both conditions. Normalized values displayed a significant increment of pyruvate production rate in Palbociclib-treated cells (**Figure 3.2.9.**).

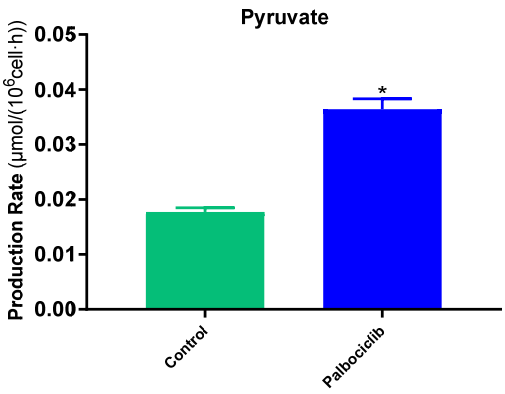

Figure 3.2.9. Palbociclib treatment increases pyruvate production rate in PC-3 cells. Extracellular pyruvate production rate in control and 96 h Palbociclib-treated (65 nM) PC-3 cells. An independent sample t-test was applied for relative comparison between the two groups, * indicates significant differences ($p < 0.05$).

These results demonstrated that Palbociclib treatment in prostate cancer cells induced pyruvate production, in correlation with the augmented glucose consumption.

Alternatively, transcriptomic data revealed a significant upregulation of *monocarboxylate transporter 4* (*MCT4*) after Palbociclib treatment (*SLC16A3*; log2FC=(+)0.8±0.1; adjusted p-value $3.61 \cdot 10^{-6}$). MCT4 is a proton (H^+)-coupled transporter of pyruvate and lactate across the membrane, whose transport direction depends on H^+ and lactate availability, although it is more associated with secretion rather than uptake (Felmlee et al., 2020). Indeed, our findings suggest a greater pyruvate production correlating with a greater extracellular secretion through MCT4 after Palbociclib treatment in the prostate cancer cells.

Glutamine is the major carbon source alternative to glucose contributing to increasing mitochondrial function in cancer cells (Yoo, Yu & Sung et al., 2020). Therefore, glutamine metabolism was also evaluated by measuring the extracellular glutamine consumption and glutamate production rates in PC-3 after 96 h with Palbociclib treatment. Results displayed a significant increase in glutamine catabolism in Palbociclib-treated cells (**Figure 3.2.10., A**), and greater glutamine utilization in comparison to glucose despite the increased glycolytic function (**Figure 3.2.10., B**), whereas glutamine consumption with respect to glutamine not committed to glutamate production remained constant (**Figure 3.2.10., C**). These results indicated that despite Palbociclib treatment significantly increased glutamine consumption, its usage was similar to that observed in the control condition. Increased glutamine dependence suggests that glutaminolysis may support an augment in oxidative phosphorylation and TCA cycle.

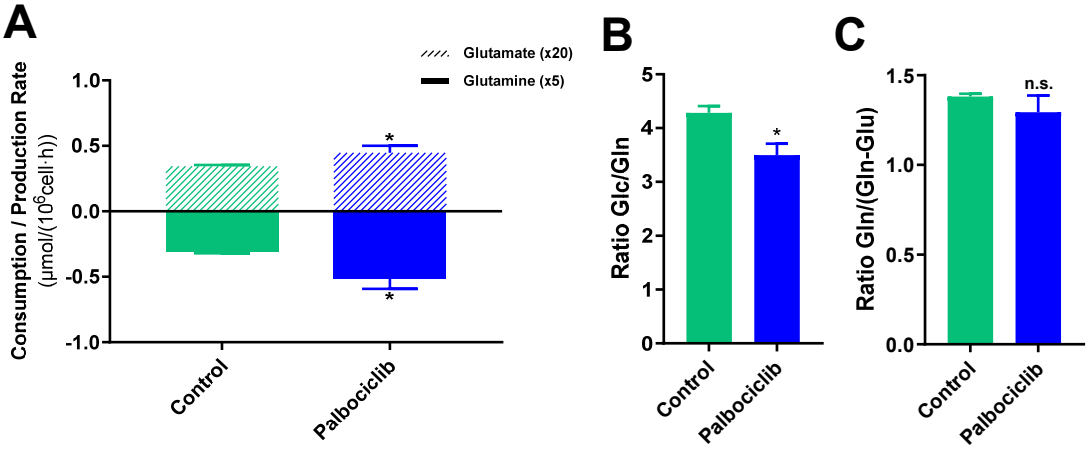

Figure 3.2.10. Palbociclib induces glutamine catabolism and dependence in PC-3 cells. A) Extracellular glutamine consumption and glutamate production rates in control and 96 h Palbociclib-treated (65 nM) PC-3 cells. B) Ratio of glucose with respect to glutamine utilization. C) Ratio of glutamine consumption with respect to glutamine not committed to glutamate production. An independent sample t-test was applied for relative comparison between the two groups, * indicates significant differences ($p < 0.05$).

Then, we used targeted metabolomics to evaluate the metabolic impact of other amino acids after Palbociclib treatment, analyzing the metabolic fingerprint regarding the intracellular content and the extracellular consumption and production rates. The overall intracellular concentrations of essential amino acids (EAAs) were not altered after Palbociclib treatment in PC-3, except for a decrease in lysine intracellular concentration (**Figure 3.2.11., A**). Palbociclib-treated cells presented an increased general pattern in EAA consumption rates, however, only tryptophan exhibited significantly increased uptake (**Figure 3.2.11., B**).

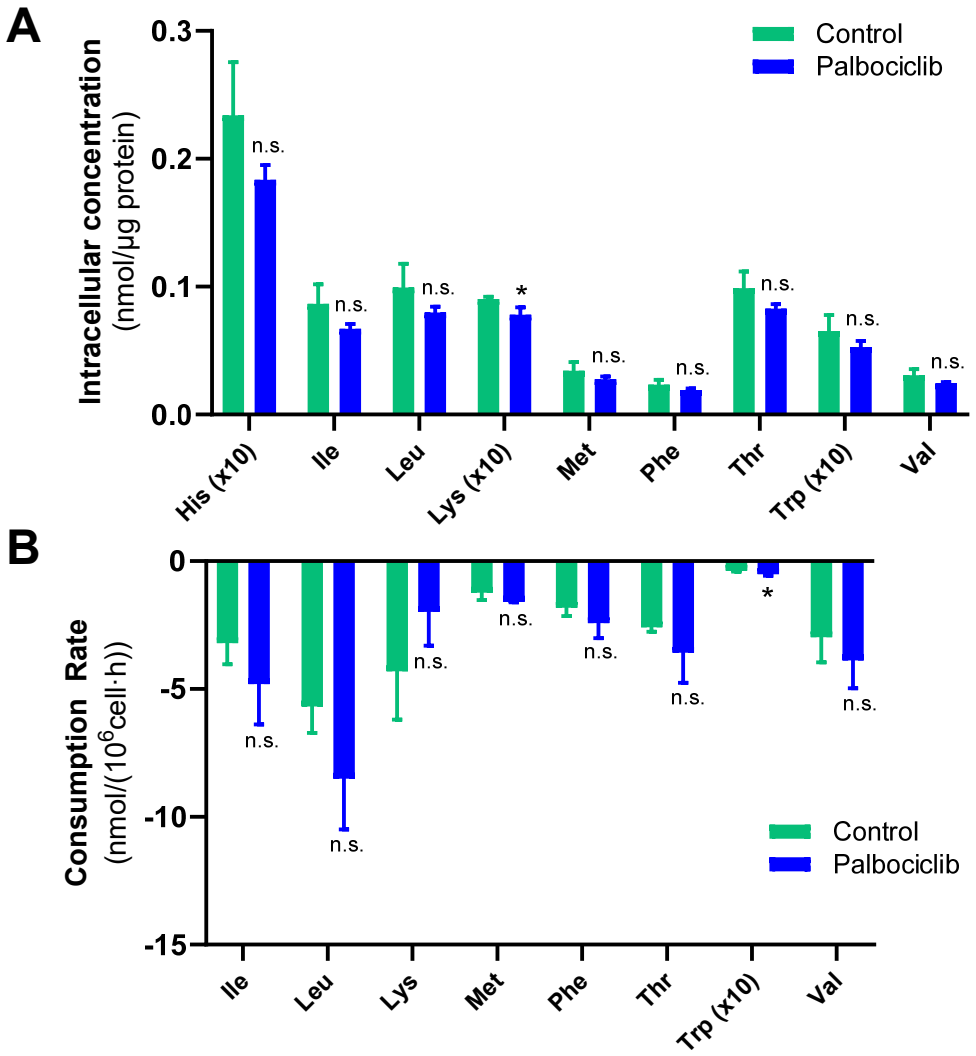

Figure 3.2.11. Essential amino acids (EAAs) profile after Palbociclib treatment in PC-3 cells. A) Intracellular EAAs concentration, and B) extracellular EAAs consumption rates in control and 96 h Palbociclib-treated (65 nM) PC-3 cells. Only amino acids that were significantly produced or consumed from the medium are shown. An independent sample t-test was applied for relative comparison between the two groups, * indicates significant differences ($p < 0.05$).

Results of intracellular and extracellular content of non-essential amino acids (NEAAs) showed that Palbociclib treatment caused a significant decrease in the intracellular concentration of glycine, ornithine, arginine, and glutamine (**Figure 3.2.12., A**). Regarding the extracellular media consumption and production rates, only alanine exhibited a significant release to the extracellular media in Palbociclib-treated cells in comparison with the control condition (**Figure 3.2.12., B**). Alanine represents an important intersection of glucose and glutamine metabolism, correlating with the augmented glycolytic rate, glutamine metabolism, and pyruvate production.

After Palbociclib treatment, we also found a depletion of ornithine intracellular concentration, which is involved in the urea cycle. Therefore, we calculated the ratios proposed by Dossus & Kouloura et al. (Dossus & Kouloura et al., 2021), regarding the activity of important urea cycle enzymes, such as nitric oxide synthase (NOS), ornithine transcarbamylase (OTC), or arginase (ARG). The results showed no changes in NOS activity, increased activity in OTC, and a non-significant decrease tendency in ARG activity (**Figure 3.2.13.**).

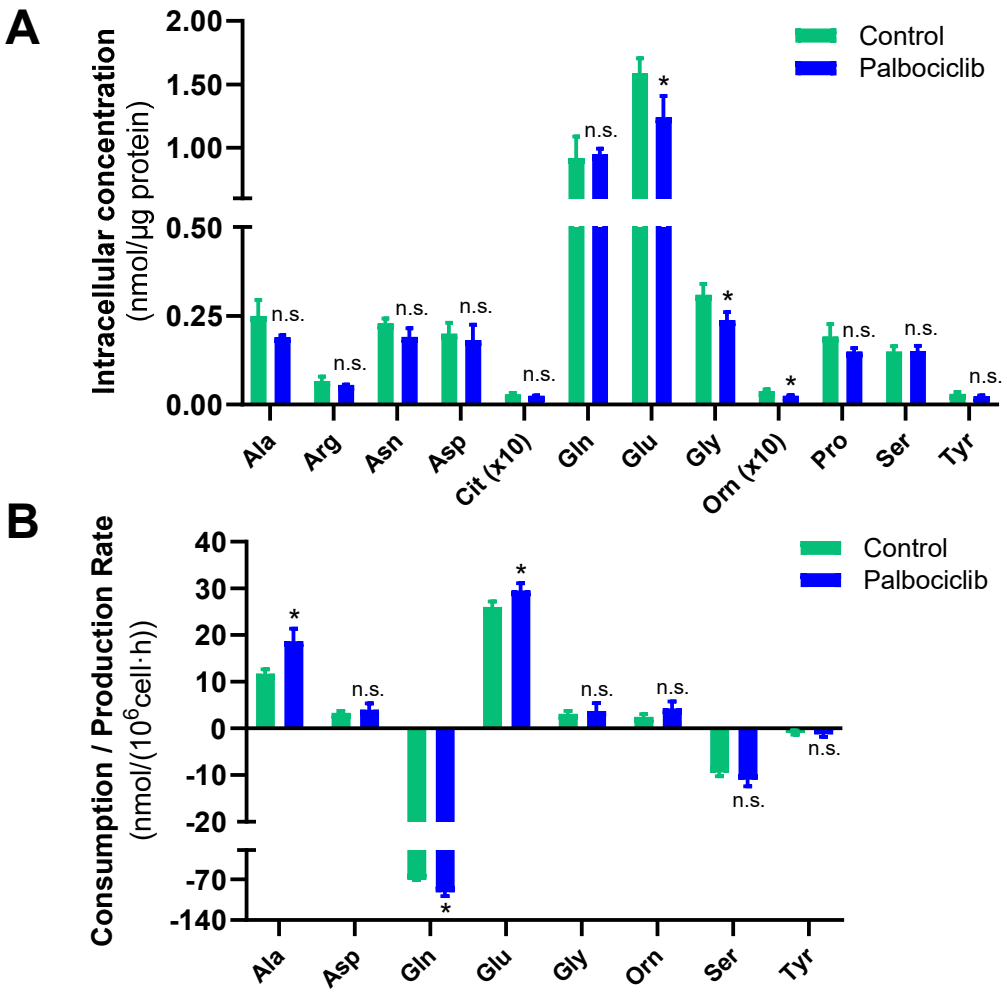

Figure 3.2.12. Non-essential amino acids (EAAs) profile after Palbociclib treatment in PC-3 cells. A) Intracellular NEAAs concentration, and B) extracellular NEAAs consumption and production rates in control and 96 h Palbociclib-treated (65 nM) PC-3 cells. Only amino acids that were significantly produced or consumed from the medium are shown. An independent sample t-test was applied for relative comparison between the two groups, * indicates significant differences ($p < 0.05$).

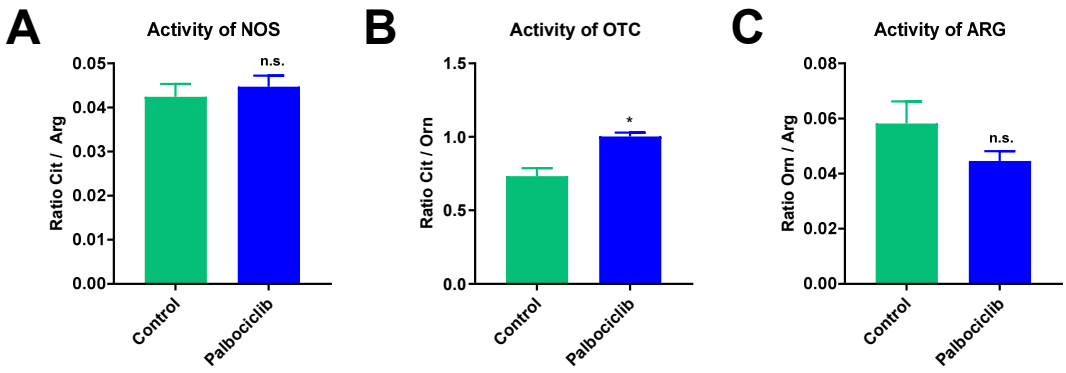

Figure 3.2.13. Activity indicators of key urea cycle enzymes after Palbociclib treatment Ratios calculated from the intracellular amino acid concentration. A) Activity of nitric oxide synthase (NOS) calculated from the ornithine/arginine ratio. B) Activity of ornithine transcarbamylase (OTC) calculated from the citrulline/ornithine ratio. C) Activity of arginase (ARG) calculated from the ornithine/arginine ratio. An independent sample t-test was applied for relative comparison between the two groups, * indicates significant differences ($p < 0.05$).

In addition, we examined the differential expression of the genes encoding for the most important enzymes related to the urea cycle, and polyamine metabolism (**Figure 3.2.14.**) (gene expression values are specified in **Appendix IV Table IV.1.**), considering the importance of these pathways in prostate cancer (see **section 1.2.4.2.**). In correlation with OTC increased activity, we found the urea cycle gene *argininosuccinate lyase* (*ASL*) significantly overexpressed. This gene encodes for the enzyme catalyzing the hydrolytic cleavage of argininosuccinate (ASA) into arginine and fumarate, boosting the TCA cycle and nourishing the TCA cycle. On the other hand, differential expression results also indicated an overexpression in the polyamine metabolism genes encoding for the enzymes *ornithine decarboxylase 1* (*ODC1*), suggesting an increased polyamine production from ornithine, and *spermidine/spermine N1-acetyltransferase 1* (*SAT1*), encoding for SSAT which controls the intracellular polyamine concentration by catalyzing polyamine acetylation and providing substrates for spermidine or putrescine back-conversion or secretion (Babbar & Gerner, 2011).

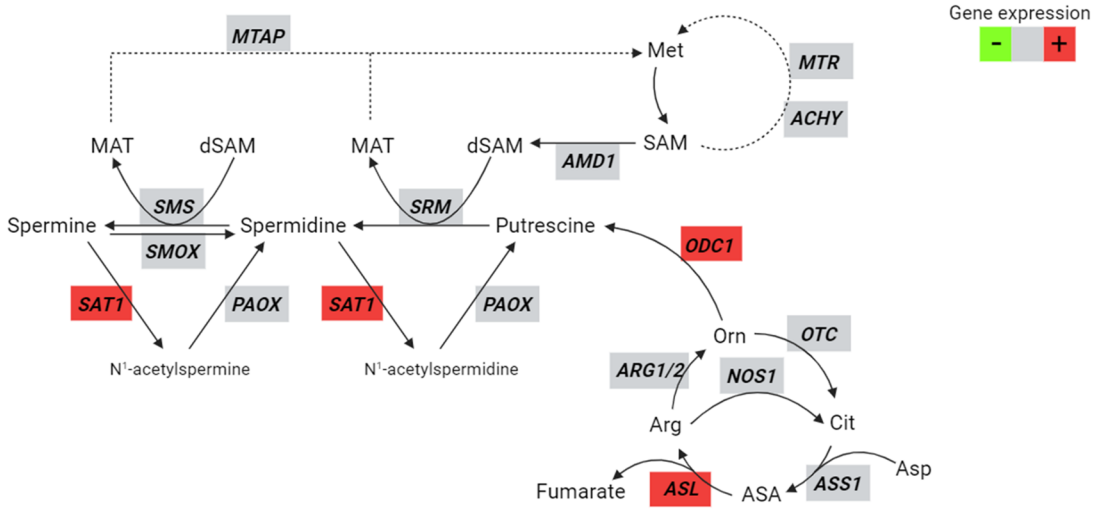

Figure 3.2.14. Genes encoding for key enzymes involved in polyamine metabolism and the urea cycle. Genes differentially expressed after Palbociclib treatment in PC-3 encoding for enzymes of methionine cycle, methionine salvage pathway, polyamine metabolism, and urea cycle. Colors refer to the expression; green is downregulated, red is upregulated and grey indicates no significant differences (adjusted p-value > 0.05). **Genes:** AHCY; adenosylhomocysteinase, AMD1; adenosylmethionine decarboxylase 1, ARG2; arginase 2, ASL; argininosuccinate lyase, ASS1; argininosuccinate synthase 1, MTAP; methylthioadenosine phosphorylase, MTR; 5-methyltetrahydrofolate-homocysteine methyltransferase, NOS1; nitric oxide synthase 1, ODC1; ornithine decarboxylase 1, OTC; ornithine transcarbamylase, PAOX; polyamine oxidase, SAT1; spermidine/spermine N1-acetyltransferase 1, SMOX; spermine oxidase, SMS; spermine synthase, SRM; spermidine synthase. Figure adapted from Casero & Stewart et al., 2018, and created with https://www.biorender.com/ (2023).

In agreement with *ODC1* and *SAT1* overexpression, the polyamine extracellular production rates measured after 96 h of Palbociclib treatment displayed increased putrescine production, indicating that prostate-resistant cells promote putrescine secretion to the extracellular media (**Figure 3.2.15.**).

Upon the greater glucose and glutamine utilization observed after Palbociclib treatment in this cell line, we analyzed the effects on lipid metabolism by evaluating the intracellular lipid profile. We measured the intracellular lipid concentration of acylcarnitines (**Figure 3.2.16.**), sphingolipids (**Figure 3.2.17.**) and glycerophospholipids (**Figure 3.2.18.**) after 96h of treatment in PC-3 cells by targeted metabolomics. The intracellular lipid concentrations were distributed in heatmaps based on non-supervised clusterization. In this regard, acylcarnitines clustered in two groups corresponding with the control and

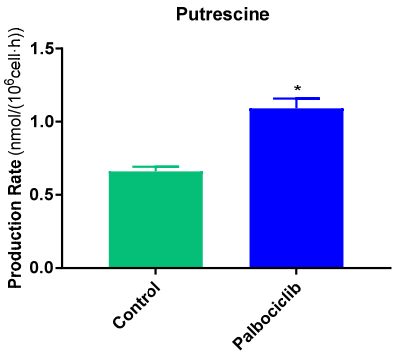

Figure 3.2.15. Putrescine production in PC-3 control and Palbociclib-treated cells. Extracellular putrescine production rate measured in control and 96 h Palbociclib-treated (65 nM) PC-3 cells. An independent sample t-test was applied for relative comparison between the two groups, * indicates significant differences ($p < 0.05$).

Palbociclib condition (**Figure 3.2.16., A**). Palbociclib-treated cells displayed significantly lower concentrations of short-chain acylcarnitines, and a reduced ratio of short-chain acylcarnitines to free carnitine (estimated by ((C2+C3)/C0)), which is associated with the overall ß-oxidation activity and branched-chain amino acid (BCAA) synthesis (Dossus & Kouloura et al., 2021) (**Figure 3.2.16., B**). Also, we found no significant differences in the long-chain acylcarnitines to free carnitine ratio, which correlates with the activity of carnitine palmitoyl transferase 1 (CPT1) (Dossus & Kouloura et al., 2021). CPT1 is the rate-limiting step in the uptake of fatty acids into the mitochondria (**Figure 3.2.16., C**), therefore, these results indicate that there were no significant changes in the fatty acids uptake for mitochondrial internalization and subsequent β-oxidation after Palbociclib treatment.

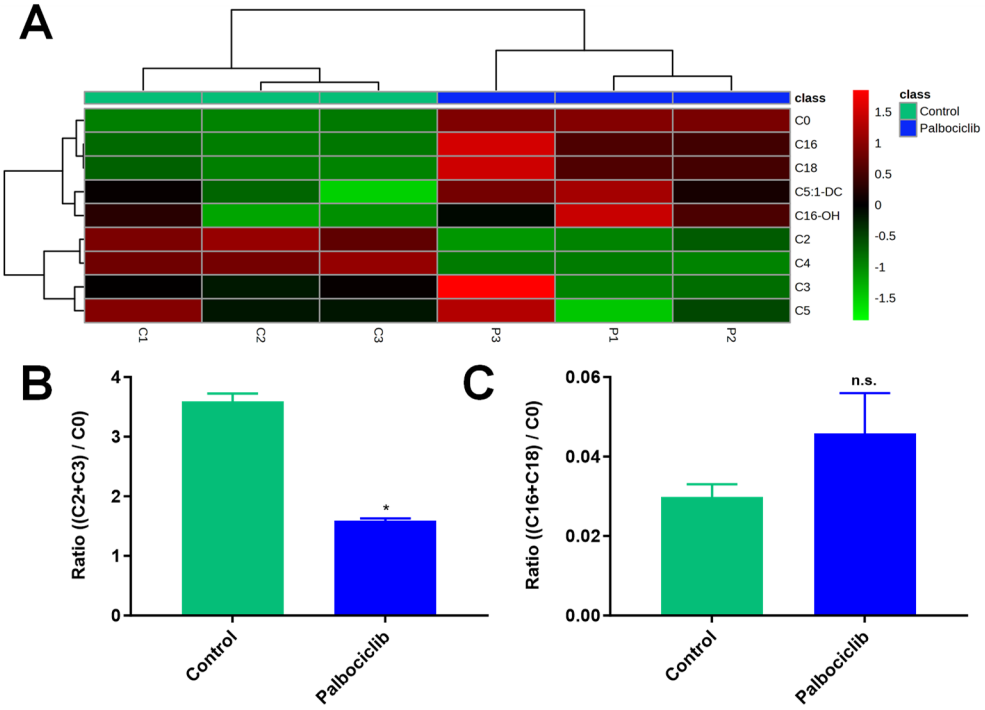

Figure 3.2.16. Acylcarnitines profile in control and Palbociclib-treated PC-3 cells. A) Heatmap distribution after non-supervised clusterization of the intracellular acylcarnitines measured in control and 96 h Palbociclib-treated (65 nM) PC-3 cells. Results expressed in nmol/µg protein were normalized by sum applying Pareto data scaling using Metaboanalyst 5.0 software. B) Ratio of short-chain acylcarnitines to free carnitine ((C2+C3)/C0), which is a measure of overall β-oxidation activity C) Ratio of long-chain acylcarnitines to free carnitine ((C16+C18)/C0), which is correlated with the activity of carnitine palmitoyl transferase 1 (CPT1). An independent sample t-test was applied for relative comparison between the two groups, * indicates significant differences ($p < 0.05$).

Heatmaps displaying sphingolipids (**Figure 3.2.17.**) and glycerophospholipids (**Figure 3.2.18.**) concentrations also clustered into Control and Palbociclib-treated conditions. Altogether, there was a clear alteration in the lipid profile of these two types of lipids after treatment, with a greater concentration in the Palbociclib-resistant cells. Therefore, these results suggest an increment in lipogenesis in the prostate Palbociclib-resistant cells.

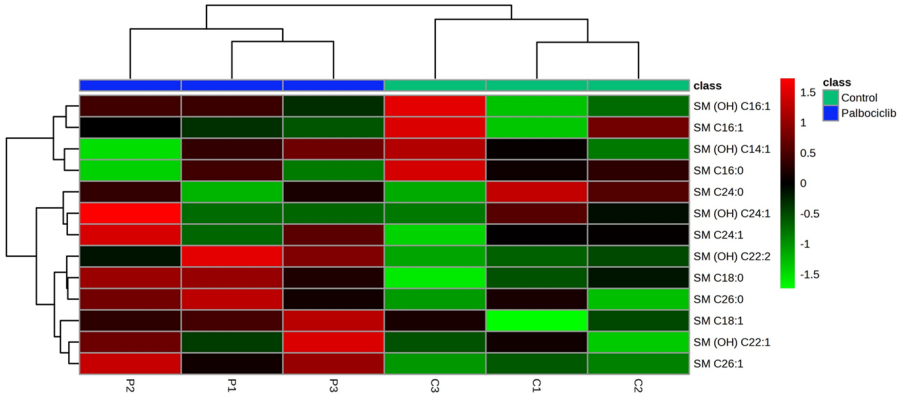

Figure 3.2.17. Sphingolipids profile in control and Palbociclib-treated PC-3 cells. Heatmap distribution after non-supervised clusterization of the intracellular sphingomyelins (SM) in control and 96 h Palbociclib-treated (65 nM) PC-3 cells. Results expressed in nmol/µg protein were normalized by sum applying Pareto data scaling using Metaboanalyst 5.0 software.

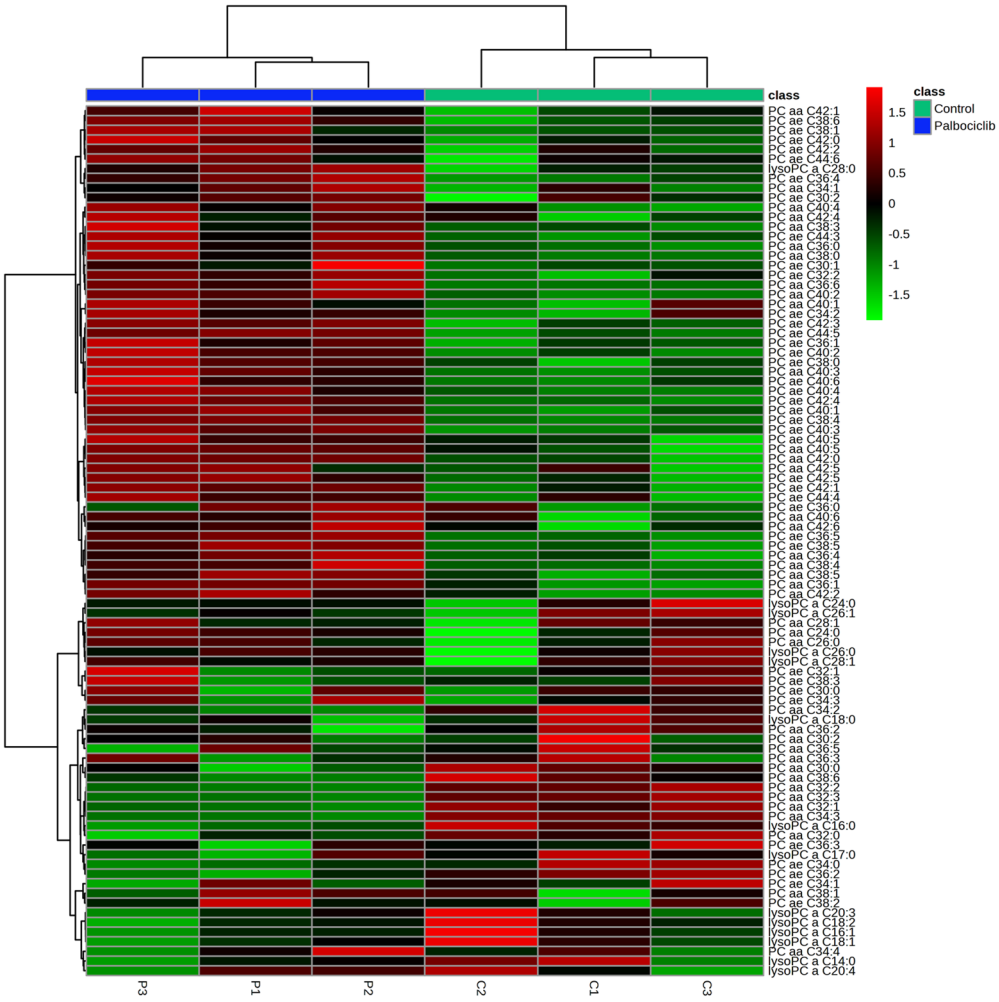

Figure 3.2.18. Glycerophospholipids profile in control and Palbociclib-treated PC-3 cells. Heatmap distribution after non-supervised clusterization of the intracellular phosphatidylcholines in control and 96 h Palbociclib-treated (65 nM) PC-3 cells. Results expressed in nmol/µg protein were normalized by sum applying Pareto data scaling using Metaboanalyst 5.0 software.

Overall, our results indicate that glutamine plays a pivotal role in the Palbociclib adaptive resistance of PC-3 cells. Glutamine is essential for NEAAs synthesis, inducing alanine and glutamate production, contributing to enhanced cellular metabolism, which might be involved in several biosynthetic routes, by inducing the activity of some urea cycle enzymes, and promoting greater polyamine synthesis after Palbociclib treatment. The increment in these metabolic pathways coexists with augmented glycolytic activity and glycolytic ATP production rate, as well as greater pyruvate production and lipogenesis. In order to understand the contribution of both carbon sources to the remarkable enhancement observed in the mitochondrial activity, we explored the mitochondrial metabolism using isotope-based metabolic analysis with ^{13}C enriched substrates.

We incubated with [1,2-$^{13}C_2$]-glucose or uniformly labeled [U-$^{13}C_5$]-glutamine for the last 24 h of the 96 h treatment of control and Palbociclib-treated PC-3 cells. Glucose contribution to the complete oxidation in the TCA cycle was determined after analyzing the mass isotopomer distribution of the intracellular metabolites displaying m2 labeled citrate and malate, which are the most abundant mass isotopomers derived from [1,2-$^{13}C_2$]-glucose (**Figure 3.2.19., A**). Results indicated no alteration in [1,2-$^{13}C_2$]-glucose contribution towards either citrate or malate, suggesting that Palbociclib induced higher glycolytic flux but not greater glucose contribution to the TCA cycle in comparison to the control condition (**Figure 3.2.19., B**). On the other hand, [U-$^{13}C_5$]-glutamine can be either

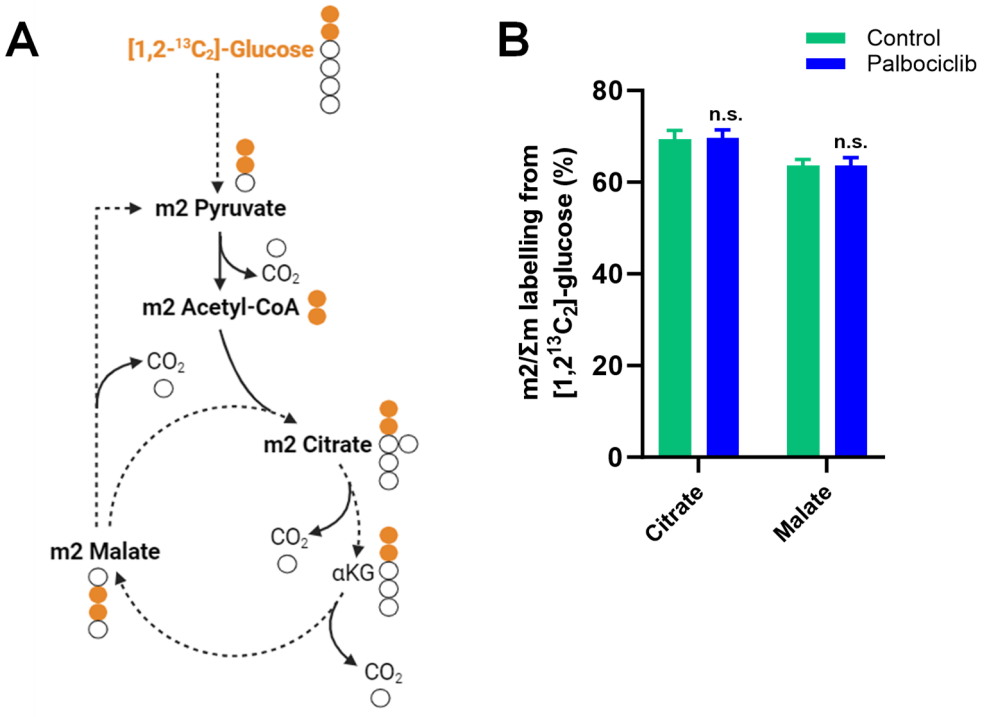

Figure 3.2.19. Glucose contribution to the TCA cycle in Palbociclib-treated PC-3 cells. Control and Palbociclib-treated (65 nM) PC-3 cells were incubated for the last 24 h of the 96 h treatment with 10 mM of [1,2-$^{13}C_2$]-glucose. A) Schematic representation of ^{13}C atoms (orange) distribution from [1,2-$^{13}C_2$]-glucose in the TCA intermediates in the first turn of the TCA cycle. B) Mass isotopomer distribution analysis of the intermediates of the TCA cycle labeled with m2 citrate and m2 malate displaying the major [1,2-$^{13}C_2$]-glucose contribution (complete isotopologue distribution is detailed in **Appendix IV**, **Table IV.2.**). An independent sample t-test was applied for relative comparison between the two groups, **n.s.** indicates no significant differences ($p > 0.05$).

oxidized via TCA cycle, which can be evaluated by monitoring glutamate (m5), malate (m4), and citrate (m4), or produce citrate via the reductive carboxylation from α-ketoglutarate (α-KG) (m5), yielding citrate (m4) through NADPH-dependent isocitrate dehydrogenases (IDHs) and ultimately malate (m3) and aspartate (m3) (**Figure 3.2.20., A**). These results revealed a slight but statistically significant decrease in [U-$^{13}C_5$]-glutamine contribution to the oxidative TCA cycle, together with a significant enrichment in ^{13}C incorporation in the reductive carboxylation to citrate (m5) and malate (m3) (**Figure 3.2.20., B**).

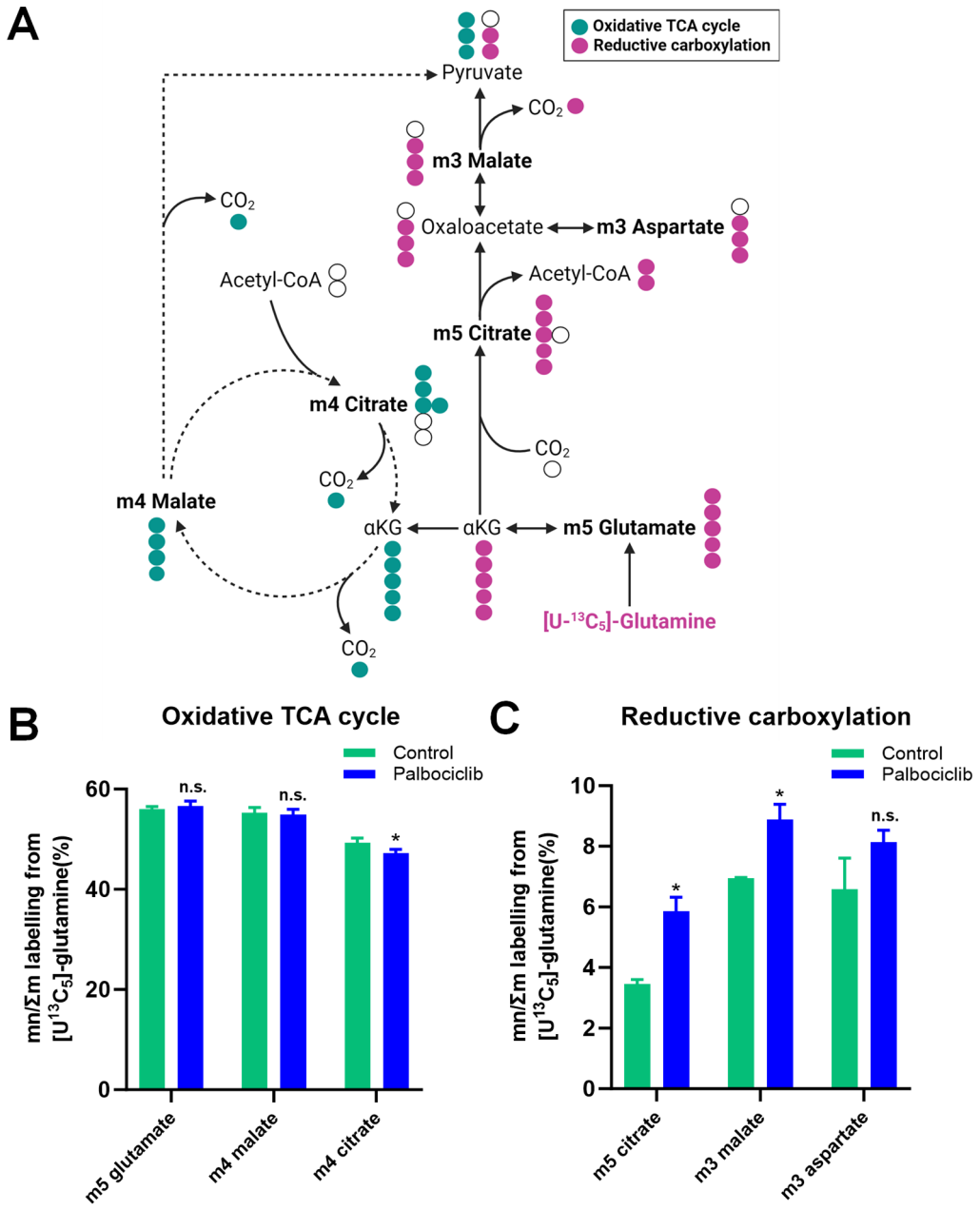

Figure 3.2.20. Glutamine contribution to the oxidative TCA cycle and the reductive carboxylation in Palbociclib-treated PC-3 cells. Control and Palbociclib-treated (65 nM) PC-3 cells were incubated for the last 24 h of the 96 h treatment with 2 mM of [U-$^{13}C_5$]-glutamine. A) Schematic representation of ^{13}C atoms distribution from uniformly labeled [U-$^{13}C_5$]-glutamine in the intermediates of the oxidative TCA cycle (green) and reductive carboxylation (pink) first turn. B, C. Mass isotopomer distribution analysis B) in the intermediates labeled with m5 glutamate, m4 malate, and m4 citrate displaying the major [U-$^{13}C_5$]-glutamine contribution to the Oxidative TCA cycle, and C) in the intermediates labeled with m5 citrate, m3 malate, and m3 aspartate displaying the major [U-$^{13}C_5$]-glutamine contribution to the reductive carboxylation (complete isotopologue distribution is detailed in **Table IV.3. Appendix IV**). An independent sample t-test was applied for relative comparison between the two groups, * indicates significant differences ($p < 0.05$).

It is reported that cancer cells with defective mitochondrial respiration sustain cell proliferation by augmenting glutamine-dependent reductive carboxylation to support increased citrate production (Mullen et al., 2011). Citrate mediates the metabolic shift from increased glycolytic rate to greater reliance on oxidative phosphorylation and lipogenesis described in normal prostate cells upon tumorigenic transformation. A mitochondrial impairment is observed in normal prostate as a consequence of greater glycolytic rates destinated to increase citrate production and secretion toward the seminal fluid (Ahmad et al., 2021, Bader & McGuire, 2020, Germain & Lafront et al., 2023). The augmented citrate production is boosted by zinc transporters (also known as ZIP proteins), promoting zinc accumulation, which serves, together with aspartate, as citrate precursors while acting as a mitochondrial aconitase (ACO2) inhibitor, and in turn, preventing citrate oxidation in the TCA cycle (Bader & McGuire, 2020). Hence, we evaluated the differential expression of genes encoding for ZIP proteins, belonging to the SLC39 family of transporters (Jeong & Eide et al., 2014), to examine a possible contribution to a truncated TCA cycle in Palbociclib-treated cells that may induce the glutamine-dependent reductive carboxylation. Our transcriptomic data showed that genes such as *SLC39A7* (log2FC=(+)0.4±0.1 with adjusted p-value $8.13 \cdot 10^{-4}$) and *SLC39A13* (log2FC=(+)1.0±0.2 with adjusted p-value 0.002) were upregulated after Palbociclib treatment in PC-3 cells. These results indicated that Palbociclib induced zinc transport, suggesting a potential enzymatic inhibition of ACO2, and altering the mitochondrial function. In agreement with these observations, our results also displayed an increased citrate and malate production (**Figure 3.2.21.**), correlating with the increased lipogenesis observed after Palbociclib treatment.

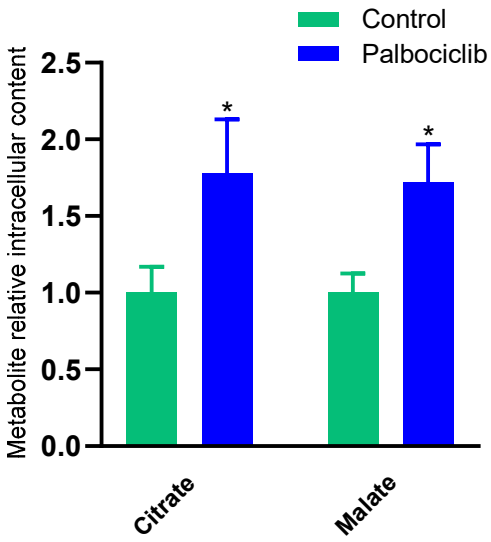

Figure 3.2.21. Increment in the citrate and malate content after Palbociclib treatment in PC-3 cells. Quantification of the intracellular citrate and malate relative to norvaline internal standard after 96 h of incubation with and without Palbociclib (65 nM) in the PC-3 cell line. Data were normalized by direct cell counting and represented relative to control cells.

Together, these results reveal that the reported greater glutamine utilization after Palbociclib treatment is associated with an increased reductive carboxylation upon mitochondrial impairment. Our results also elucidate an increased citrate synthesis as a response to Palbociclib treatment, boosted by reductive carboxylation and higher glycolytic flux, contributing to the enhancement of TCA cycle activity and lipogenesis.

3.2.2.4. Glycolysis, TCA, and OxPhos are the major metabolic reprogramming contributors identified by GSMM in Palbociclib-resistant PC-3 cells.

Based on transcriptomics and metabolomic data integration, GSMM-specific reconstruction for Palbociclib-resistant prostate cells provides the flux analysis distribution after treatment (see **Appendix II** for details). The major fluxes variation were expressed in terms of Log2FC (**Figure 3.2.22., A**) and fluxes contribution to the final variation in terms of μmol/(10^6cell·h) (**Figure 3.2.22., B**).

Results indicated a notable number of fluxes significantly altered after short-term Palbociclib treatment in prostate cancer cells (**Figure 3.2.22., A**). Core metabolic pathways significantly increased after treatment, including the central carbon pathways,

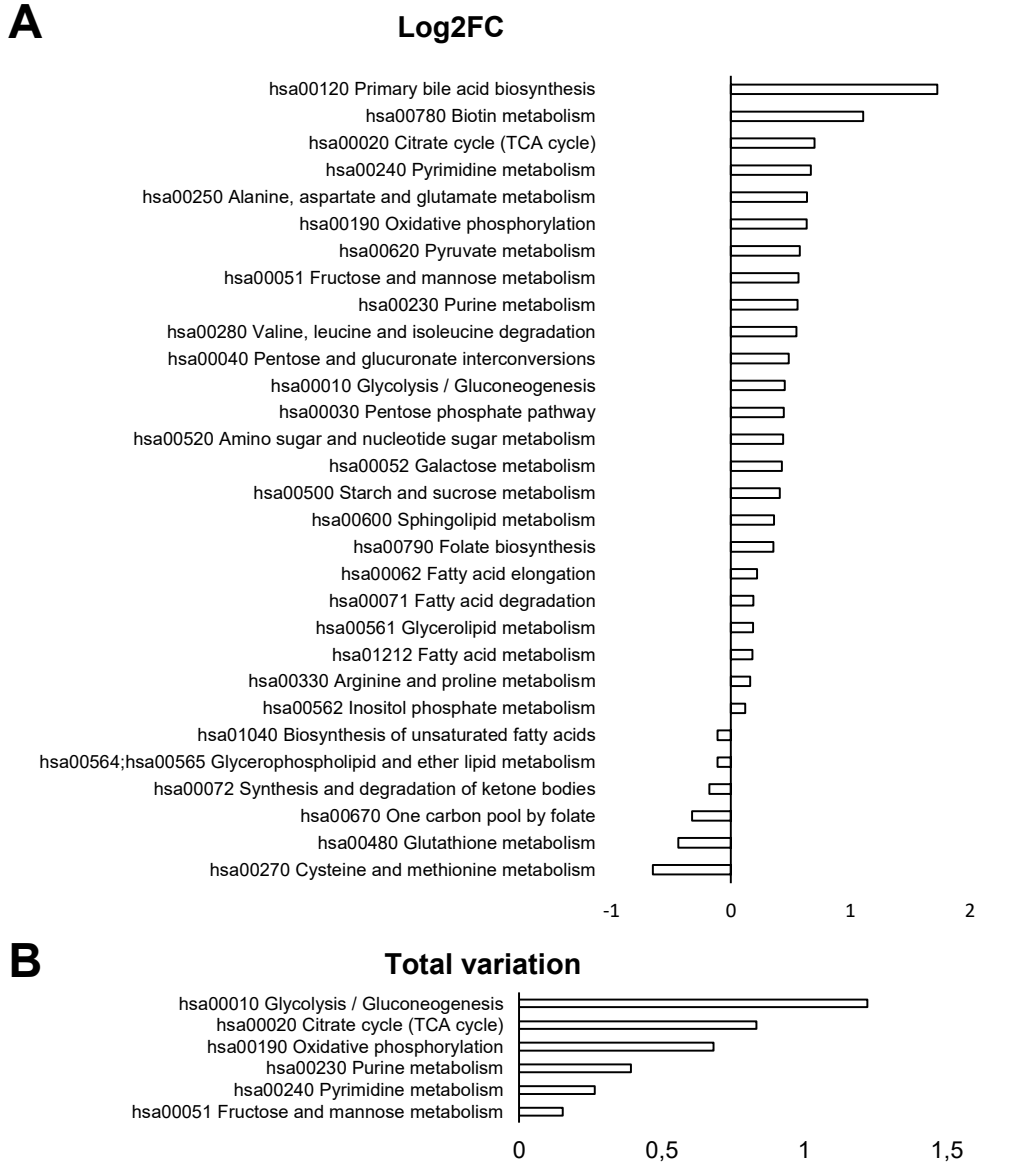

Figure 3.2.22. Metabolic flux variations analyzed by the GSMM simulation according to the KEGG pathways. Significant changes in Log2FC (Treated / Non-treated) and Total variation (μmol/(10^6 cell·h) (Treated / Non-treated) have been considered (total_flux_vres ≥ 0.01) and filtered by fluxes with differences Log2FC ≥ 0.1.

such as glycolysis, PPP, pyruvate metabolism, TCA cycle, OxPhos, purine and pyrimidine metabolism, and amino acids metabolism. Also, Palbociclib treatment promoted a reduction in the fluxes of one carbon pool by folate, glutathione metabolism, and cysteine and methionine metabolism. The overall variation was governed by pathways increasing the metabolic fluxes rather than decreasing them. The most important contributions to total flux variation were attributed to glycolysis, TCA cycle, OxPhos, and purine and pyrimidine metabolism (**Figure 3.2.22., B**).

The major flux variations analyzed by the GSMM simulation were in agreement with the experimental results depicting an increase of the core central metabolic pathways to satisfy the augmented mitochondrial function and oxidative phosphorylation.

3.2.2.5. The impairment of mitochondrial respiration synergizes with Palbociclib treatment in prostate cancer cells.

From the reconstructed GSMMs, using qMTA and MOMA algorithms, we simulated the effect of metabolic inhibitors annotated in DrugBank (Knox et al., 2024) and Therapeutic Target (Chen et al., 2002) databases on metabolic fluxes (see **Appendix II** for details). The five best-scored drugs, according to their efficiency in reverting/preventing the transition to the Palbociclib-resistant phenotype, listed in **Table 3.2.1.**, were drugs targeting reactions of mitochondrial respiration complex IV or complex V, in accordance with the observed enhanced mitochondrial respiration and ATP production in response to Palbociclib treatment.

Table 3.2.1. Target genes and drugs proposed by GSMM. The metabolic inhibitors and target genes (NCBI number) after quadratic metabolic transformation algorithm (qMTA) and the minimization of metabolic adjustment (MOMA) application to revert or prevent Palbociclib-resistant phenotype in PC-3. Only drugs annotated in DrugBank (Knox et al., 2024) and Therapeutic Target (Chen et al., 2002) databases are shown. The metabolic inhibitors with positive aggregate scores are arranged in descending order based on their values up to the metabolic inhibitor with an aggregate score value closest to 50% of the highest aggregate score value. **Gene IDs**: 126; *ADH1C alcohol dehydrogenase 1C* 498; *ATP5F1A, ATP synthase F1 subunit alpha*, 506; *ATP5F1B ATP synthase F1 subunit alpha,* 509; *ATP5F1C ATP synthase F1 subunit gamma*, 873; *CBR1 carbonyl reductase 1*, 1066; *CES1 carboxylesterase 1*, 1327; *COX4I1 - cytochrome c oxidase subunit 4I1,* 1329; *COX5B cytochrome c oxidase subunit 5B,* 1339; *COX6A2 cytochrome c oxidase subunit 6A2*, 1340; *COX6B1 cytochrome c oxidase subunit 6B1,* 1345; *COX6C cytochrome c oxidase subunit 6C,* 1346; *COX7A1 cytochrome c oxidase subunit 7A1,* 1349; *COX7B cytochrome c oxidase subunit 7B,* 1350; *COX7C cytochrome c oxidase subunit 7C,* 1351; *COX8A cytochrome c oxidase subunit 8A,* 1545; *CYP1B1 cytochrome P450 family 1 subfamily B member 1, 2172; FABP6 fatty acid binding protein 6,* 2235; *FECH ferrochelatase,* 4512; *MT-CO1 mitochondrially encoded cytochrome c oxidase I,* 4513; *MT-CO2 mitochondrially encoded cytochrome c oxidase II,* 4514; *MT-CO3 mitochondrially encoded cytochrome c oxidase III,* 4535*; MT-ND1 mitochondrially encoded NADH dehydrogenase 1,* 5294; *PIK3CG phosphatidylinositol-4,5-bisphosphate 3-kinase catalytic subunit gamma,* 5319; *PLA2G1B phospholipase A2 group IB,* 9377; *COX5A cytochrome c oxidase subunit 5A*, 26275*; HIBCH 3-hydroxyisobutyryl-CoA hydrolase*.

Drug	Gene target	Aggregate Score
N-Formylmethionine	1327, 1329, 1339, 1340, 1345, 1346, 1349, 1350, 1351, 4512, 4513, 4514, 4535, 9377	594.46876
Cholic Acid	1066, 1066, 126, 1327, 1329, 1339, 1340, 1345, 1346, 1349, 1350, 1351, 2172, 2235, 4512, 4513, 4514, 5319, 9377	542.18066
Talmapimod	4513	506.52385
Piceatannol	498, 506, 509	345.82539
Quercetin	1545, 26275, 498, 506, 509, 5294, 873	345.35401

Among these inhibitors proposed by GSMM, we assessed the effect of Piceatannol in combination with Palbociclib. Piceatannol is a natural polyphenol that exhibits a promising therapeutic potential in various cancer types (Banik et al., 2020) and is reported to inhibit ATP synthase activity (Zheng et al., 1999). The measure of cell confluency over time evidenced that the maximum inhibitory effect over PC-3 proliferation was achieved after combining Palbociclib and Piceatannol at 50 nM and 25 µM fixed concentrations, respectively (**Figure 3.2.23.**).

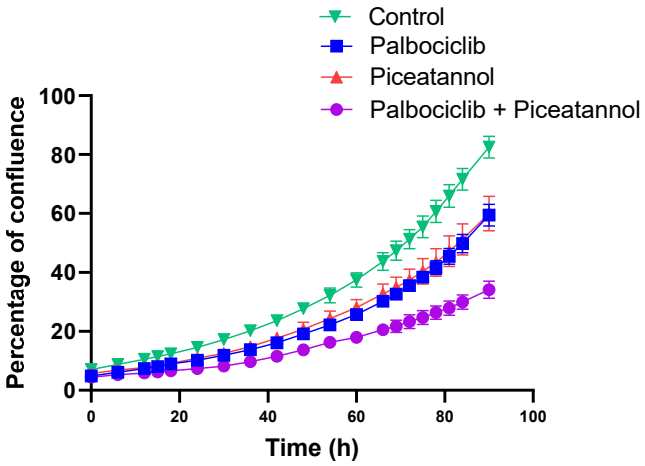

Figure 3.2.23. Effects of the combination of Palbociclib with Piceatannol in PC-3 cells. Proliferation curve from confluence life-quantification measured over time in the PC-3 cells showing control condition, single treatments Palbociclib at 50 nM, and Piceatannol at 25 µM, and their combination.

Next, taking into account that complex IV and complex V comprise OxPhos which exhibited the highest enrichment score according to GSEA analysis after Palbociclib treatment (**Figure 3.2.3.**), we decided to target this pathway using Tigecycline, an FDA-approved antibiotic used to treat microbial infections and described as a promising drug for cancer treatment due to its capacity to inhibit mitochondrial oxidative respiration and induce oxidative stress and cell cycle arrest (Dong et al., 2019). Moreover, as cytochrome P450 metabolism had a high enrichment score according to GSEA analysis (**Figure 3.2.3.**), we assessed the effect of Miconazole, an antifungal that has been reported as a potent pan-inhibitor of cytochrome P450 (Niwa et al., 2014, Piérard et al., 2012), in combination with Palbociclib. Miconazole has also been described to induce mitochondrial-mediated apoptosis and G1/G0 cell cycle arrest in bladder cancer cells (Yuan et al., 2017), autophagic cell death by inducing an ROS-dependent endoplasmic reticulum stress response in glioblastoma cells (Jung et al., 2021), and exhibited *in-vitro* ATPase inhibition (Lax et al., 2002). Noteworthy, the use of antifungal or antibiotics as anticancer therapy may offer the advantage of affecting multiple cell pathways, which can hinder the utilization of other routes involved in cell survival and drug resistance (Karp & Lyakhovich, 2022, Weng et al., 2023).

Results evaluating the cell proliferation curves at increasing drug concentrations showed that both Miconazole and Tigecycline treatments display synergistic antiproliferative results when combined with Palbociclib according to the combination index calculated through Compusyn software and the Chou-Talalay method (Chou, 2010) (**Figure 3.2.24.**).

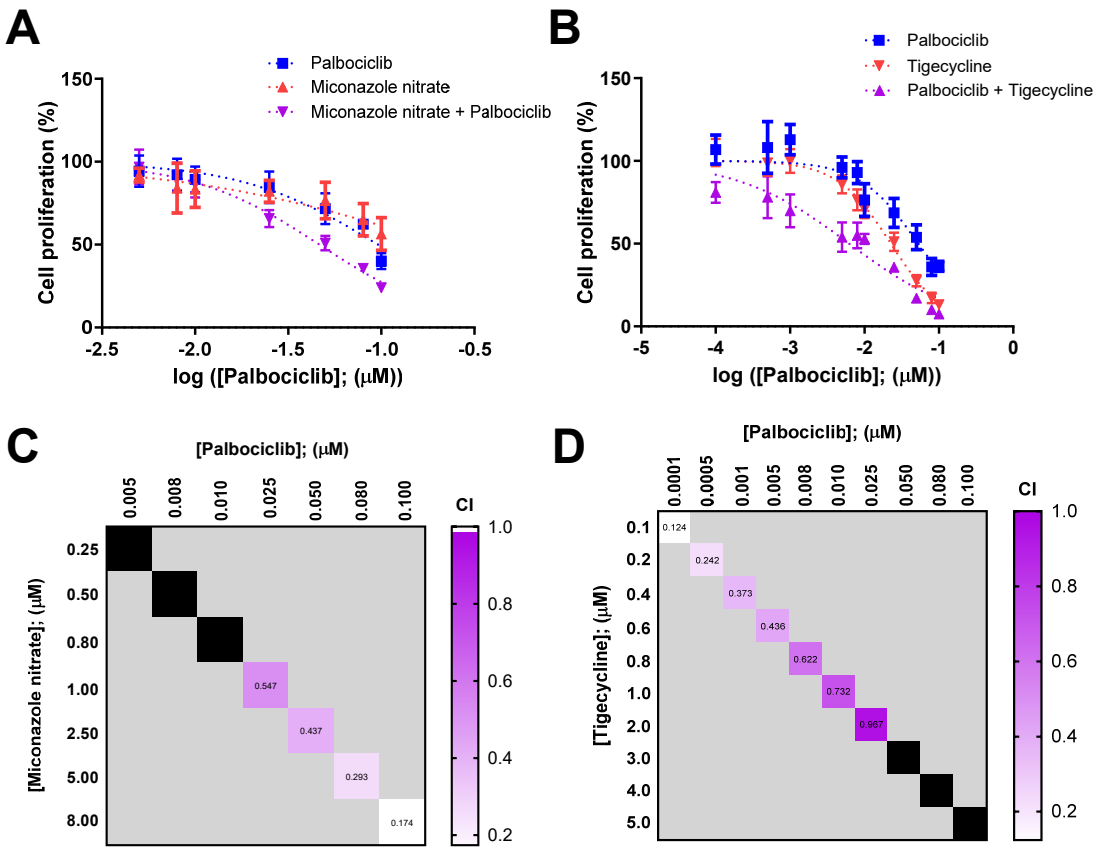

Figure 3.2.24. Synergistic effect by targeting oxidative phosphorylation (OxPhos) and cytochrome P450 in Palbociclib-resistant PC-3 cells. A, B. Representative graphs of cell proliferation curves in the metastatic prostate PC-3 cell line after 96 h of treatment at increasing drug concentrations with (A) Palbociclib (0.005, 0.008, 0.010, 0.025, 0.050, 0.080, and 0.100 μM) and Miconazole nitrate (0.25, 0.50, 0.80, 1.00, 2.50, 5.00, and 8.00 μM) alone or in combination with a non-constant ratio, (B) Palbociclib (0.0001, 0.0005, 0.001, 0.005, 0.008, 0.010, 0.025, 0.050, 0.080, and 0.100 μM) and Tigecycline (0.1, 0.2, 0.4, 0.6, 0.8, 1.0, 2.0, 3.0, 4.0, and 5.0 μM) alone or in combination with a non-constant ratio. C, D. Combination index (CI) value calculated with Compusyn software and Chou-Talalay method (black squares represent CI values > 1) for the combination of Palbociclib and Miconazole nitrate (C) and Palbociclib and Tigecycline (D).

Altogether, these results highlight the efficacy of targeting OxPhos and cytochrome P450 proteins in Palbociclib-resistant cells. The decrease in cell proliferation when the combinatory treatment is applied demonstrates the importance of oxidative phosphorylation in Palbociclib-resistant cells for cell survival and resistance acquisition, representing the major metabolic vulnerability in prostate cancer cells resistant to Palbociclib. These findings have promising implications for potential combination therapies to enhance Palbociclib's effectiveness and point out the potential of GSMM for target prediction.

3.2.3. Discussion.

Prostate cancer is frequently addressed through surgery and androgen deprivation therapy (ADT) (Desai et al., 2021, Germain & Lafront et al., 2023, Rebello & Oing et al., 2021). However, it is one of the most recurrent cancer types described (Ferlay et al., 2020), eventually progressing to the metastatic stage. Our work focuses on studying the metabolic reprogramming underlying drug resistance to Palbociclib treatment in the most

aggressive stage of prostate cancer disease, employing androgen-independent PC-3 cells. Palbociclib treatment is an emerging strategy for prostate cancer (Tien & Sadar, 2022) and also for rapidly proliferating cancer cells by blocking the cell cycle (Goel & Bergholz et al., 2022, Otto & Sicinski, 2017). Our findings indicate that Palbociclib treatment is able to impair cell proliferation by arresting the cell cycle in G1/G0 in PC-3 cells. The absence of AR signaling may facilitate Palbociclib cell cycle impairment, as AR blockade has been reported to overcome Palbociclib resistance in breast cancer cells (Ji et al., 2019). This effect in the cell cycle is consistent with reported studies in response to Palbociclib in other types of cancer where the percentage of cells arrested varies from 10 to 30% in G1/G0, depending on drug concentration, cell line, and cancer type (Cretella et al., 2018, Franco et al., 2016, Goel & Bergholz et al., 2022, Tarrado-Castellarnanu et al., 2017). It is known and extensively reviewed that CDK4 and CDK6 synthesis, accumulation, and degradation depend on the cyclin patterns that regulate their activity (Knudsen & Witkiewicz 2017). In this regard, due to CDK4 accumulation, our results suggest a decrease in cyclin D synthesis or impairment of its activity that prevents the formation of CDK4/6-Cyclin D complexes for the G1 to S phase transition, promoting cell cycle arrest and leading to a senescent or quiescent state.

Nevertheless, Palbociclib-acquired resistance emerges upon short-term drug exposition promoting metabolic reprogramming for cell survival. Cell cycle arrest after Palbociclib treatment leads to a decrease in cell proliferation and elevated ROS production without apoptosis activation, suggesting that other mechanisms must be involved in cell proliferation reduction and apoptosis evasion after Palbociclib treatment, such as xenobiotic metabolism via Cytochrome P450 and glutathione, both pathways observed to be activated in GSEA, and also in agreement with the decrease observed in the intracellular concentrations of glutamate and glycine, which might be used for glutathione synthesis. In fact, the induction of antioxidant enzymes is one of the most important mechanisms to cope with increased ROS levels in cancer cells (Nakamura & Takada, 2021). This correlation is evident in other studies where CDK4/6 inhibitors deplete the antioxidant response after glycolytic flux inhibition, decreasing NADPH and glutathione levels, and leading to apoptotic activation (Wang et al., 2017). Then, by increasing the glycolytic function, other connected fluxes related to other biosynthetic routes might contribute to NADPH production, such as serine biosynthesis boosting one-carbon metabolism and PPP.

In the context of metabolic reprogramming, Palbociclib treatment causes an increment in the mitochondrial activity and all the OCR-related parameters, including basal OCR, ATP production-associated respiration, spare respiratory capacity, and maximum respiration, indicating an increased metabolic flexibility and pointing to the significant increment in OxPhos as the major contributor to the Palbociclib-resistant phenotype. In agreement, GSEA also identified OxPhos as the key process for metabolic reprogramming in the PC-3 metastatic prostate cancer cell line.

Alternatively, our results reveal an increased glycolytic flux after Palbociclib treatment, reflected in greater glucose consumption and glycolysis-associated ATP production rate. In this regard, *ENO3* overexpression is associated with glycolysis induction and sustaining tumor progression in colorectal cancer (Chen & Zhang et al., 2022). In this study performed by Chen & Zhang et al., they also report an increase in *ENO3* expression in prostate cancer. Therefore, these findings suggest that *ENO3* might play

an important role in mediating the glycolytic response for cell survival after Palbociclib treatment in PC-3 cells.

The increase in glycolytic flux is the major contributor to total flux variation along with the TCA cycle, OxPhos, and nucleotide metabolism, aligned with the experimental findings indicating that increased core metabolic pathways fulfill increased mitochondrial activity and OxPhos. Together with the increased glycolytic function displayed after Palbociclib treatment, our study also reports an augment in glutamine utilization. Glutamine is the major carbon alternative source in cancer cells to fuel the mitochondrial function when glucose is funneled to lactate production rather than complete oxidation in the TCA cycle (Yoo, Yu & Sung et al., 2020). An increased glutamine dependence supporting the mitochondrial function after Palbociclib treatment has also been observed in other types of cancer (Conroy et al., 2020, Franco et al., 2016, Lorito et al., 2020, Tarrado-Castellarnau et al., 2017). Our findings show that after Palbociclib treatment glutamine also contributes to non-essential amino acid biosynthesis by promoting higher alanine and glutamate production, and reveal the induction of reductive carboxylation toward citrate generation instead of glutamine oxidation in the TCA cycle.

Glutamine-dependent reductive carboxylation supports cell proliferation in cancer cells presenting defective mitochondrial function (Mullen et al., 2011). Mullent et al., observed how this pathway enables osteosarcoma and renal cancer cells' proliferation despite mitochondrial metabolism impairment. Also, they reported that the mitochondrial defective cells promoted higher glucose consumption and lactate production in response to defective OxPhos, and induced glutamine-dependent reductive carboxylation to generate 4-carbon TCA intermediates and greater citrate production to enhance lipogenesis, supporting cell growth. In our work, we observed that Palbociclib-treated cells respond in correlation to cells with a defective mitochondrial function as reported by Mullen et al., inducing glutamine-dependent reductive carboxylation and displaying higher glucose consumption and lactate production, together with increased citrate production toward lipogenesis, which is associated with a truncated TCA cycle in normal prostate cells that present a distinctive metabolic profile, mainly glycolytic (Bader et al., 2019). In this regard, our investigations demonstrated an increased glycolytic flux supporting the enhanced TCA, and greater glutamine consumption, both converging in augmented citrate production, in agreement with the significant increase in the relative intracellular citrate content displayed after Palbociclib treatment. At the same time, increased lipogenesis is evidenced by the significant alteration in the intracellular lipid profile after Palbociclib treatment, displaying an increase in the concentration of intracellular sphingolipids and phosphatidylcholines, and a decrease in the estimation of the overall ß-oxidation activity.

On the other hand, advanced prostate cancer cells rely on OxPhos and lipogenesis, whereas normal prostate cells present a truncated TCA cycle for citrate secretion to the prostatic fluid and a higher glycolytic rate under basal conditions. This metabolic shift is prompted after the overexpression of AR and aberrant activation of PI3K/AKT/mTOR, promoting the loss of zinc transporters and restoring truncated TCA by avoiding the inhibition of ACO2 (Ahmad et al., 2021, Bader & McGuire, 2020, Germain & Lafront et al., 2023, Rebello & Oing et al., 2021). The PC-3 prostate cancer model presents AR-and, surprisingly, our results indicate the overexpression of certain zinc transporters (*SLC39A7* and *SLC39A13*) after Palbociclib treatment, accompanied by increased

glycolytic rate, and responses according to cells with impaired mitochondrial metabolism (Mullen et al., 2011). Despite the metabolic similarities with cells with mitochondrial inhibition, Palbociclib-treated PC-3 cells displayed enhanced mitochondrial activity. Palbociclib treatment has been reported to increase mTOR signaling in other types of cancer such as breast, colon, pancreatic, and pleura (Bonelli et al., 2017, Cretella et al., 2018, Franco et al., 2016, Tarrado-Castellarnau et al., 2017), which may also explain the boost in central metabolism after treatment in PC-3 cells, promoting glycolysis, glutaminolysis, and also mitochondrial function and OxPhos.

Therefore, we hypothesized that Palbociclib-treated cells sustain mitochondrial function by increasing glycolytic flux and other anaplerotic routes, such as augmented fumarate entrance from the urea cycle, producing TCA intermediates via reductive carboxylation and also inducing pyruvate production. CDK4/6 inhibition has also been reported to increase ATP levels and mitochondrial mass in multiple cell lines, which could provide another plausible explanation for the increased mitochondrial function in Palbociclib-treated prostate cells (Franco et al., 2016), although this hypothesis has not been further explored in this work. However, studies in metabolic reprogramming of RAS-driving non-small cell lung cancer (NSCLC) revealed that mitochondrial metabolism of pyruvate was essential for tumor formation *in vivo*. This finding suggests that pyruvate produced during glycolysis is not only oxidized in mitochondria but also converted to lactate in the cytosol and secreted (Davidson et al., 2016), in agreement with our results displaying greater TCA cycle flux, pyruvate production and overexpression of lactate/pyruvate transporter MCT4 (*SLC16A3*) after Palbociclib treatment. Bader et al. demonstrated that the TCA cycle in prostate adenocarcinoma is primarily fueled by pyruvate metabolism (Bader et al., 2019), by inducing the mitochondrial pyruvate carriers. Therefore, this metabolism represents an important metabolic vulnerability in AR+ prostate cancers. Our results indicate that AR- PC-3 cells also require pyruvate, according to the remarkable pyruvate production, however, our hypothesis sustains that Palbociclib-treated cells might supply pyruvate through increased glycolytic flux and reductive carboxylation. Pyruvate might nourish the TCA cycle to overcome mitochondrial inhibition imposed by ACO2 since pyruvate might be incorporated into the TCA cycle through the malic enzyme (ME) (Hsieh et al., 2023). Furthermore, the existence of a sub-compartmentalized version of the TCA cycle associated with cell state transitions such as cell differentiation has been recently reported (Arnold et al., 2022, Doan & Teitell, 2022). In this non-canonical TCA cycle, citrate is exported out of mitochondria using a citrate/malate antiporter (SLC25A1). The use of this citrate/malate shuttle could prevent the loss of carbons as CO_2 and produce acetyl-CoA in the cytosol, which becomes available for acetylation reactions, and lipogenesis. In this regard, we hypothesized that the increase of malate content observed after Palbociclib treatment, which can be metabolized through MDH2 since its codifying gene is overexpressed, might be derived from several sources, including the increased glycolytic flux, a potential non-canonical TCA cycle that internalizes malate to the mitochondria using a citrate antiporter, and reductive carboxylation fueling TCA cycle mediated by ME.

At the same time, despite no significant changes being found in the overall landscape of amino acid metabolism, metabolites and enzymes involved in the urea cycle are also important contributors to the metabolic reprogramming after Palbociclib treatment in PC-3 cells. Indeed, *ASL* overexpression catalyzes an essential step for detoxifying ammonia derived from increased glutamine metabolism and is also responsible for fumarate

production, which nourishes the TCA cycle. OTC increased activity boosts ornithine production toward citrulline formation, which serves for ASA production, arginine, and fumarate precursor, and also, through ODC overexpression, induces putrescine production and secretion. The increment in the urea cycle enzyme and polyamine metabolism requires an increased energy supply that may be sustained by the glycolytic flux and OxPhos and entails the participation of linked metabolic pathways such as one-carbon metabolism. Because polyamine metabolism is typically dysregulated in cancer, higher levels of polyamines are likely required for tumor development and transformation (Affronti et al., 2020, Seth Nanda et al., 2020, Zabala-Letona et al., 2017).

The significant metabolic increase induced by Palbociclib treatment is replicated by the GSMM reconstruction. This model identifies the primary driver of Palbociclib metabolic reprogramming, which involves the upregulation of central metabolic pathways, including glycolysis, TCA, and OxPhos, along with nucleotide metabolism. These adaptations support cell proliferation despite impaired cell cycle progression. Through the application of algorithms (qMTA and MOMA) to the GSMM, we identified metabolic vulnerabilities, highlighting potential targets to reverse or prevent the transition from the non-treated to the resistant Palbociclib phenotype. These targets are related to components of the electron transport chain (ETC), particularly cytochrome c oxidase and ATPase, which play crucial roles in oxidative phosphorylation and ATP production. Consequently, the model proposed the impairment of oxidative phosphorylation as a promising strategy to restore sensitivity to Palbociclib in metastatic prostate cells.

To impair OxPhos, this study proposes the utilization of the polyphenol Piceatannol, a natural compound that targets ATPase subunits and modulates PI3K, COX2, and apoptotic responses. Its antiproliferative activity stems from its multitarget effect, making it an effective anticancer agent (Banik et al., 2020, Çınar et al., 2022, Drug Bank database; Knox et al., 2024). The combination of Piceatannol with Palbociclib significantly reduces cell proliferation, demonstrating synergy after 96 hours of treatment. In this line, the combination of Palbociclib with either the antibiotic Tigecycline, a promising anticancer drug capable of altering mitochondrial respiration by targeting OxPhos (Dong et al., 2019), or Miconazole, an inhibitor of several cytochrome P450 proteins (Niwa et al., 2014, Piérard et al., 2012), demonstrated promising synergic antiproliferative results. Treatment resistance often arises from substantial alterations across the entire metabolic landscape, as observed in the case of prostate cancer after Palbociclib treatment. Antibiotics in cancer treatment offer the capacity to target multiple cell pathways simultaneously (Karp & Lyakhovich, 2022), therefore providing a comprehensive strategy to counteract the development of resistance to Palbociclib in this cell line. The mechanisms involved in the synergism exhibited after the combined treatment are not elucidated; however, these results highlight the efficacy of targeting OxPhos and cytochrome P450 proteins in Palbociclib-resistant cells, also evidencing the pivotal role of OxPhos in Palbociclib resistance acquisition, in agreement with other studies reporting this pathway as an important metabolic vulnerability in many types of aggressive cancer (Ashton et al., 2018, El-Botty et al., 2023).

Finally, the application of computational tools has proven highly successful in identifying metabolic targets and developing effective combination therapies. This approach exemplifies the power of GSMM reconstruction and predictions, greatly contributing to guiding the rational design of therapeutic strategies.

3.2.4. Materials and methods.

3.2.4.1. Cell culture.

The human metastatic prostate PC-3 (ATCC, Rockville, MD, USA) cell line isolated from a vertebra metastasis of a 62-year-old male with a castration-resistant adenocarcinoma, grade IV, was cultured in Roswell Park Memorial Institute (RPMI) 1640 medium (Avantor, PA, USA) containing 10 mM D-glucose and supplemented with 2 mM L-glutamine (Gibco, Thermo Fisher Scientific, MA, USA), 10% FBS (10270-106, Lot. 2058474, Gibco), and 1% Penicillin-Streptomycin (Gibco). Cultures were maintained at 37 ºC in a humidified atmosphere with 5 % CO_2.

3.2.4.2. Cell proliferation.

PC-3 cells were plated in 96- or 6-well plates (seeding 1.7×10^3/well, and 5×10^4/well respectively) and treated for 96 h with the specific treatments. Cell proliferation tests were assessed through manual counting using 0.2% Trypan Blue staining (Merck Life Sciences, Germany) and a Neubauer Chamber (Thermo Fisher Scientific) or automated counting using Countess II FL (Thermo Fisher Scientific). Cell confluence over time was monitored by live imaging with the Incucyte® (Sartorius, Germany) instrument. Additionally, indirect proliferation techniques were utilized with the fluorescent staining method Hoechst, using 4 µg/ml of bisBenzimide H 33342 trihydrochloride probe (Merck Life Sciences) in Hoechst stain buffer (1 M NaCl, 1 mM EDTA, 10 mM Tris pH 7.4) and measuring emitted fluorescence (460 nm) in a fluorescence plate reader (FLUOstar OPTIMA Microplate Reader, BMG LABTECH GmbH, Germany), and the CellTiter-Glo luminescent cell viability assay kit (Promega Corporation, Madison, Wi) to quantify the ATP by measuring the luminescent signal at 550 nm in a luminescent plate reader Mithras LB 940 (Berthold Technologies, Switzerland) .

Data were analyzed through dose-response curves with GraphPad Prism 9 (GraphPad Software, San Diego, CA, USA). Synergy analysis and quantification was performed using the CompuSyn software (Version 1.0) (ComboSyn, Inc., NJ, USA) and the Chou-Talalay method (Chou, 2010), based on the combination index (CI) where the combination displays synergistic (CI < 1), additive (CI = 1), or antagonist effect (CI > 1). The duplication time was determined by assessing the cell growth at different time points and applying the exponential growth equation:

$$Ln\left(\frac{N_f}{N_0}\right) = \mu \cdot t$$

where,

N_f is the number of final cells (million cells)
N_0 is the number of initial cells (million cells)
μ is the growth rate (h^{-1})
t is the time (h)

Assuming active proliferation, where cells undergo division, holding the following assumption $N_f = 2N_0$. The duplication time was calculated from the final equation:

$$\frac{Ln2}{\mu} = t$$

3.2.4.3. Chemicals and reagents.

Palbociclib was purchased from Selleckchem (Houston, TX, USA). Piceatannol was purchased from Cayman Chemical (Ann Arbor, MI, USA). Tigecycline was purchased from APExBIO (Houston, TX, USA). Miconazole nitrate was purchased from Selleck Chemicals (Houston, TX, USA).

Primary antibodies against CDK4 (sc-260), and CDK6 (sc-177) were purchased from Santa Cruz Biotechnology (Santa Cruz, CA, USA), and β-actin (#69100) from MP Biomedicals (Santa Ana, CA, USA). The anti-rabbit (NA934V) secondary antibody was purchased from Amersham Biosciences (GE Healthcare, Little Chalfont, UK).

3.2.4.4. Apoptosis analysis.

Adherent and floating cells in the medium were collected and incubated with Annexin V coupled with FITC, following the kit's instructions (Bender System MedSystem, Viena, Austria) for 30 minutes in binding buffer (10 mM Hepes/NaOH, pH 7.4, 140 mM NaCl, 2.5 mM $CaCl_2$). Propidium Iodide (PI) (MilliporeSigma, MA, USA) was added at the final concentration of 20 µg/ml minutes for the analysis in flow cytometry. The samples were measured by flow cytometry using Gallios™ Flow Cytometer (Beckman Coulter, CA, USA), and the results were analyzed using FlowJo version 7.6.1. This analysis revealed percentages of alive cells, cells presenting early apoptosis, and late apoptosis or necrosis.

3.2.4.5. Cell cycle analysis.

Cells were collected, fixed in cold 70% ethanol, and kept overnight at 4 °C. Cellular suspension was incubated for 1 h at 37 ºC with 0.2 mg/ml RNase (Roche Holding AG, Switzerland) in PBS. Propidium Iodide (PI) (MilliporeSigma) was added in a final concentration of 40 µg/ml minutes before the analysis in flow cytometry. The samples were measured by flow cytometry using Gallios™ Flow Cytometer (Beckman Coulter), and the results were analyzed using FlowJo version 7.6.1. and Mycycle software histograms were utilized to discern cell cycle phases by segregating populations based on their DNA content, where 2n and 4n represent G1/G0 and G2/M, respectively.

3.2.4.6. Protein extraction.

Protein extracts were obtained after 30 minutes of incubation with RIPA buffer (50mM Tris-HCl pH 8, 150mM NaCl, 1% Triton-X-100, 0.5% sodium deoxycholate, 0.1% SDS) supplemented with 1% phosphatase and protease cocktail inhibitors (MilliporeSigma), following the kit's instructions. Subsequently, cells were scraped and collected for quantification using the Pierce BCA Protein Assay Kit (Thermo Fisher Scientific).

3.2.4.7. Western blotting.

After protein extraction (section **3.2.4.6.**), lysates were denaturized for 5 minutes at 100 ºC with 5x loading buffer (250 mM Tris, pH 6.8, 50 mM DTT, 10% SDS, 50% glycerol, and 0.02% bromophenol blue). 15 µg of protein were loaded in an SDS-PAGE gel (staking gel: 5% acrylamide/bisacrylamide in 1M Tris pH 6.8, 1% SDS, 1% APS, and

0.08% TEMED, and resolving gel: 10% acrylamide/bisacrylamide in 1.5M Tris, pH 8.8, 1% SDS, 1% APS, and 0.08% TEMED). After electrophoresis and transference of proteins to polyvinylidene difluoride (PVDF) membranes (Immobilon®-P Membrane, 0.45 µm pore size, MilliporeSigma), the immunodetection was performed using the primary and secondary antibodies of interest incubated according to commercial specifications in 5% non-fat milk in PBS-0.1% Tween 20. The detection method is based on the horseradish peroxidase (HRP) enzyme whose chemiluminescent reaction was detected with photographic films detecting luminol produced. Films were processed in the Fujifilm FPM-100A and detected bands were semi-quantified through ImageJ 1.8.0 software (National Institute of Health, USA).

3.2.4.8. RNA extraction.

RNA purification was carried out using the Qiagen RNeasy kit (Qiagen, Hilden, Germany). Each sample provided 200 ng of total RNA in 50 µL of RNase–free water. Global transcriptomic profiling was accomplished through next-generation sequencing (NGS) of total RNA (see **Appendix II, Section II.1.** for further details of NGS experiments).

3.2.4.9. Transcriptomic pathway visualization.

Differentially expressed genes identified based on adjusted p-values < 0.05 following treatment were integrated and visualized in specific metabolic pathways using the Pathview software tool (Luo et al., 2017, Luo et al., 2013). This approach allowed the effective mapping and interpretation of the significant changes in gene expression within the context of metabolic pathways.

3.2.4.10. Respiratory assays.

After 72 hours of treatment, PC-3 cells were plated in XFe24-well plates (seeding 3 × 10^4/well) and incubated with the treatment for 24 hours to perform a total treatment of 96 hours. The Agilent Seahorse XF Cell Mito Stress Test was assessed following protocol instructions, measuring Oxygen Consumption and Extracellular Acidification Rates (OCR/ECAR) using a Seahorse XFe24 Analyzer (Agilent, Seahorse Bioscience, North Billerica, MA, USA) in the presence of metabolic substrates targeting different Electron Transport Chain (ETC) components at the following final concentrations; 1.5 µM of Oligomycin (ATP synthase (complex V)), Pyruvate (2 mM) added to 600 nM CCCP, and 2 µM of Rotenone + 2 µM of Antimycin A (Complex I and III, respectively) (Mito Stress test parameters are detailed in **Appendix III**). The final values were normalized by cell count, determined through automated counting using the Countess II FL Cell Counter (Thermo Fisher Scientific).

3.2.4.11. Mitochondrial activity.

PC-3 cells were plated in 12-well plates (seeding 2 × 10^4/well) and treated for 96 hours with the specific treatments. Half plate was processed for automated counting using the Countess II FL Cell Counter (Thermo Fisher Scientific) and the other half was stained with the staining colorimetric MTT assay, where the thiazolyl blue tetrazolium (3-(4,5-dimethylthiazol-2-yl)-2,5-diphenyltetrazolium) bromide dye (MTT) (PanReac

AppliCHem, Spain) was dissolved at 1 mg/ml in PBS and incubated 1:1 with serum-free medium for 1 h at 37 ºC 5% CO_2, avoiding light exposure. The colored formazan generated was dissolved in 100 µL of dimethyl sulfoxide (DMSO) and measured on an ELISA plate reader (Tecan Sunrise MR20-301, TECAN, Austria) at 550nm. Absorbance values were normalized by the number of cells.

3.2.4.12. Reactive Oxygen Species (ROS) analysis.

Cells were seeded in 6-well plates (seeding 5×10^4/well) and treated with Palbociclib or vehicle for 96h. Then, cells were incubated for 30 minutes with 5 µM of H2DCFDA probe (MilliporeSigma). After a quick trypsinization process (30 seconds), cells were collected and resuspended with 50 µM of H2DCFDA probe and 20 µg/ml of Propidium Iodide (PI) (MilliporeSigma). The fluorescence intensity proportional to H2DCFDA oxidated by all ROS were measured through Gallios™ Flow Cytometer (Beckman Coulter) and the results were analyzed using FlowJo version 7.6.1. Relative ROS levels were normalized with respect to the non-treated condition.

3.2.4.13. Metabolic experiments.

3.2.4.13.1. Quantification of extracellular metabolites using spectrophotometric enzymatic assays.

The consumption and production rates of glucose, glutamine, lactate, and glutamate were determined by assessing their concentrations in the extracellular media at different time points and comparing the final to the initial concentrations. Concentrations in the extracellular media were measured using a COBAS Mira Plus (Horiba ABX, France) automated spectrophotometric analyzer based on the measurable concentration of coenzyme NADH at 340 nm. For D-glucose, measurements involved two consecutive reactions: hexokinase, followed by D-glucose-6-phosphate dehydrogenase (G6PD), producing 6-phosphogluconate and NADH. Lactate concentrations were determined by employing lactate dehydrogenase (LDH). Measurements were conducted under pH=9 conditions in the presence of hydrazine to shift the reaction toward pyruvate and NADH formation, effectively preventing the reversible reaction. The reversible reaction of LDH was utilized to quantify the Pyruvate concentrations. Glutamate concentrations were measured after α-ketoglutarate conversion and NADH production by glutamate dehydrogenase (GLUD1), while glutamine was indirectly measured using the same method after glutamate conversion through glutaminase (GLS) reaction.

The calculation of the consumption/production rate for each metabolite was based on assuming exponential growth, with a constant growth rate during the incubation period. The results were subsequently normalized by the number of cells and expressed as a rate (µmol/(10^6 cell·h)).

$$Consumption/production\ rate\ = \left(\frac{\Delta M}{\Delta N}\right) \cdot \mu$$

where,

$\Delta M = M_f - M_0$ is the consumed/produced amount of each metabolite (µmol).

$\Delta N = N_f - N_0$ is the cell growth during the incubation time (million cells).

$\mu = Ln(N_f/N_0)/t$ is the growth rate constant (h^{-1}) for exponential growth

3.2.4.13.2. Mass spectrometry-based targeted metabolomics.

The metabolite profile was quantified using the Absolute IDQ p180 kit (20714, Biocrates Life Sciences AG, Innsbruck, Austria). This kit measures 180 endogenous metabolites across seven compound classes, including acylcarnitines, amino acids, biogenic amines, monosaccharides, phosphatidylcholines, and sphingolipids. The analysis of these small molecules and lipids was carried out using tandem mass spectrometry coupled with liquid chromatography (LC/MS/MS) on the MS/MS Sciex Triple Quad 6500 instrument (AB Sciex, Framingham, MA, USA). After quantification, extracellular concentrations were normalized and expressed as consumption/production rate (calculations detailed in section 3.2.4.13.1.), while intracellular concentrations were normalized based on cell protein content.

The obtained results were analyzed using the MetaboAnalyst 5.0 software (Pang et al., 2022), a comprehensive platform used for the statistical analysis of metabolomics data. This software offers a wide range of functions and tools, including the statistical methods employed in this study, such as heatmap analysis.

3.2.4.14. Stable isotope-resolved metabolomics (SIRM)

PC-3 cells were plated in 6-well plates (5× 10^4/well). After 72 hours of treatment, PC-3 cells were incubated with media with either 10 mM [1,2-$^{13}C_2$]-glucose and unlabeled 2 mM glutamine or unlabeled 10 mM glucose and 2 mM [U-$^{13}C_5$]-glutamine with and without treatment for 24 hours to perform a total treatment of 96 hours. Cells were collected and frozen for metabolite extractions.

The polar intracellular metabolites (detailed in **Table 3.2.2.**) were extracted by washing cells with ice-cold PBS and scrapped with 1:1 methanol:water solution, adding at this point 5 µl of the internal standard norvaline (1 mg/ml) for relative quantification. Samples were sonicated (3 cycles 5 seconds each) and resuspended in 2 ml of cold chloroform. After 30 minutes of incubation (gentle shaking at 4 ºC) samples were centrifuged (20.000 g, 15 minutes at 4 ºC) and the supernatant was dried under airflow. Metabolites extracted were derivatized resuspending pellet in 50 µl of methoxamine hydrochloride 2 % in pyridine for 90 minutes at 37 ºC, and incubating with N-tert-butyldimethylsilyl-N-methyltrifluoroacetamide (MTBSTFA) + 1 % tert-butyldimethylchlorosilane (TBDMCS) for 60 minutes at 55 ºC before GC-MS analysis.

Table 3.2.2. Intracellular metabolites measured by GC-MS. Intracellular metabolites were quantified according to their retention time and m/z clusters.

ID	Compound	Fragment	m/z cluster range	Retention time (min)
Mal-419	Malate	C1-C4	418.2-425.2	26.9
Asp-418 C1-C4	Aspartate	C1-C4	417.2-424.2	28
Glu-432 C1-C5	Glutamate	C1-C5	431.3-439.3	31.6
Cit-591	Citrate	C1-C6	590.4-599.4	37.3

The intracellular and extracellular analysis of ^{13}C-labelled metabolites for isotopologue distribution were performed using an Agilent 7890A gas chromatograph (Agilent) equipped with an HP-5 capillary column coupled to an Agilent 5975C mass spectrometer. Samples were injected (1 µl) adjusting 1 ml/min flow rate of the carrier helium gas. The GC-MS analysis was performed using the electron impact ionization method and the detector was run in single ion monitoring (SIM) mode. The oven temperature ramp was designed as follows: 100 ºC for 3 minutes, rising to 165ºC by increasing 10 ºC/min, rising to 225 ºC by increasing 2.5 ºC/min, rising to 265 ºC by increasing 25 ºC/min and finally rising to 300 ºC by increasing 7.5 ºC/min.

Raw mass spectrometry data was examined using MSD5975C Data Analysis (Agilent), which showed a spectral distribution of ions discerned by a mass-to-charge ratio (m/z) at each retention time. The specific ion clusters were used to determine the ^{13}C distribution at each carbon of the fragment. To quantify the contribution of each compound manual integration of peak areas was needed. The collected data was integrated through the software Ramid (Selivanov et al., 2020) for NetCDF files extraction containing the m/z raw time course to isotopologue distributions, and natural abundance of ^{13}C and Si isotopes incorporated during the derivatization processes that contributed to the mass isotope distribution were corrected through MIDcor software (Selivanov et al., 2020, Selivanov et al., 2017). The number of isotope substitutions was designated as m_i, being i the number of ^{13}C in the molecule (e.g. m0, m1, m2, etc). Direct isotopologue distribution was normalized by total ^{13}C enrichment ($\sum m = \sum_{i=1}^{i=n} m_i$), providing the mass isotopologue distribution for comparisons. The relative metabolite quantification was normalized with respect to norvaline internal standard and the number of cells.

3.2.4.15. Statistical analysis.

Statistical analysis was performed using jamovi software (Version 2.2) (The jamovi project, 2021). Group comparisons were evaluated using independent t-tests for pairwise comparisons, ensuring that the data met the assumptions of normality. The homogeneity of variances was assessed through Levene's test. When the assumption of homogeneity of variances was violated, Welch's correction was applied. Additionally, when the data did not meet the assumption of normality, the Mann-Whitney U test was employed. A significance level of $p < 0.05$ was used to determine statistical significance. Standard deviation was employed as a measure of dispersion in all statistical analyses.

3.3. Chapter 3. Targeting metabolic reprogramming after short-term treatment with the CDK4/6 inhibitor Palbociclib to forestall acquired resistance in metastatic colorectal cancer cells.

3.3.1. Introduction.

The search for alternative therapeutic strategies against drug resistance and tumor proliferation continues as a primary focus of scientific research. CDK4/6 inhibitors such as Palbociclib, approved in 2015 for the treatment of estrogen receptor-positive and human epidermal growth factor receptor 2-negative (ER+/HER2-) advanced breast cancer (U.S. Food and Drug Administration 2017), are novel therapeutic strategies targeting rapidly dividing cells by impairing cell cycle progression (Goel et al., 2017, Goel & Bergholz et al., 2022, Otto & Sicinski, 2017) that have proven effective in other cancer types, including colorectal cancer (Sorah et al., 2022, Zhang et al., 2017, Goel et al., 2017, Goel & Bergholz et al., 2022, Otto & Sicinski, 2017). However, resistance to CDK4/6 inhibitors frequently emerges (O'Leary et al., 2018). Specifically, Palbociclib impairs cell cycle progression and entails a significant increase in PI3K/AKT/mTOR signaling pathway, altering cellular metabolism in several cancer types such as breast, colon, and pancreatic cancer (Cretella et al., 2018, Franco et al., 2016, Lorito et al., 2020, Tarrado-Castellarnau et al., 2017). Alterations in cancer metabolism are recognized as a key determinant enabling the adaptability of cancer cells, allowing cell survival and promoting resistance to therapy (Hanahan & Weinberg, 2011, Pavlova & Thompson, 2016, Pavlova & Thompson, 2022).

Unveiling the metabolic reprogramming after drug treatment responsible for cell survival and drug resistance represents a powerful therapeutic opportunity (DeBerardinis & Chandel, 2016, Porporato et al., 2018, Seth Nanda et al., 2020, Stine et al., 2022) that can be addressed through combination therapies (Lee et al., 2018, Matthews et al., 2022, Otto & Sicinski, 2017, Wang et al., 2022, Liu et al., 2022). In previous studies, dependencies on glutamine, mTOR signaling, and compromised adaptation to hypoxia were successfully exploited through the inhibition of MYC downstream targets, with the combination of Palbociclib and a glutaminase (GLS1) inhibitor, sensitizing primary colorectal cancer cells to Palbociclib treatment (Tarrado-Castellarnau et al., 2017). Also, preceding results in this thesis (**Section 3.2.**, **Chapter 2**) indicate that metastatic prostate cells' survival after Palbociclib treatment depends on central metabolic pathways, such as glycolysis, glutaminolysis, TCA cycle, and oxidative phosphorylation (OxPhos), representing therapeutic opportunities. Indeed, our investigations revealed synergism following Palbociclib combination with Tigecycline, which exhibits an inhibitory effect on OxPhos, showing optimistic results in addressing Palbociclib resistance in the most aggressive model of advanced prostate cancer.

Building upon the success of preliminary works, in this chapter, we explore the same strategy by targeting Palbociclib-induced metabolic reprogramming in the SW620 cell line, bearing a positive-KRAS mutation ($KRAS^{G12V}$) and representing one of the most aggressive metastatic colorectal cancer types (Ahmed et al., 2013). This aggressive variant of colorectal cancer provides a suitable model for studying advanced disease stages and offers potential insights into the mechanisms of Palbociclib resistance and tumor recurrence in this advanced stage of the disease. In addition, our study is in line

with other research efforts that have explored promising combinations in KRAS-mutated cancers, such as the combination of CDK4/6 and MAPK inhibitors on pancreatic ductal adenocarcinoma (PDAC), which induce senescence mediated by RB and suppress tumor proliferation (Ruscetti et al., 2020).

Our results indicate that Palbociclib treatment leads to cell cycle arrest in the G1/G0 phase and promotes a significant alteration in the metabolic landscape. This metabolic reprogramming includes glutamine dependence, altered lipid and amino acid metabolism, and increased mitochondrial function to meet the higher oxygen and energetic demands required after Palbociclib treatment. These findings suggest a pivotal role of ROS signaling in driving the metabolic reprogramming triggered by Palbociclib short-term treatment. ROS modulation by EUK-134 treatment in combination with Palbociclib exhibits a promising synergism, depleting cellular metabolism and interacting with cell cycle regulation. This effective combination of Palbociclib and EUK-134 achieves promising results in other cell line models, such as the primary colorectal cancer cell line HCT116, and *in vivo* in NOD/SCID mice bearing SW620 tumors by significantly impairing cell proliferation and tumor growth. Therefore, our study proves that metabolic reprogramming characterization underlying short-term Palbociclib treatment is a potent strategy to identify metabolic vulnerabilities that can be exploited for the design of combination therapies in the field of cancer metabolism and drug response, and unveils a promising combined treatment able to impair cell progression both *in vitro* and *in vivo*.

3.3.2. Results.

3.3.2.1. Palbociclib impairs cell proliferation in metastatic colorectal cancer cells by arresting the cell cycle in G1/G0.

In order to evaluate the Palbociclib effect over the SW620 cell line, we tested the Palbociclib concentration required to reduce 50% of cell proliferation at 96 h (IC_{50}) on cell proliferation over time and on cell cycle and apoptosis after 96 h of treatment. First, we determined the IC_{50} by measuring the proliferation with increased concentrations of Palbociclib after 96 h of drug incubation (**Figure 3.3.1., A**). The results indicated that 40 nM of Palbociclib decreases cell proliferation at 50% at 96 h incubation compared to the control condition.

Cell cycle analysis after 96 h displayed an increment of 10% of SW620 cells arrested in the G1/G0 phase after Palbociclib treatment (**Figure 3.3.1., B**). These results indicated Palbociclib's impact on cell cycle progression, significantly increasing the cell population of the pre-replicative phase (G1/G0) and decreasing cell percentage in the replicative (S) and post-replicative (G2) phases. Furthermore, the treatment reduced the proliferative rate by a factor of 1.35, which translated to a significant augment of cell doubling time, shifting from 15.5 h in non-treated cells to 21 h in cells subjected to Palbociclib (**Figure 3.3.1., C**). While the impairment of cell cycle progression by Palbociclib promoted a considerable delay in cell proliferation, the apoptotic response to treatment was significant but relatively modest since less than 10% of the cell population displayed signs of early apoptosis (**Figure 3.3.1., D**), indicating that Palbociclib promotes either a senescent or quiescent state rather than apoptotic activation.

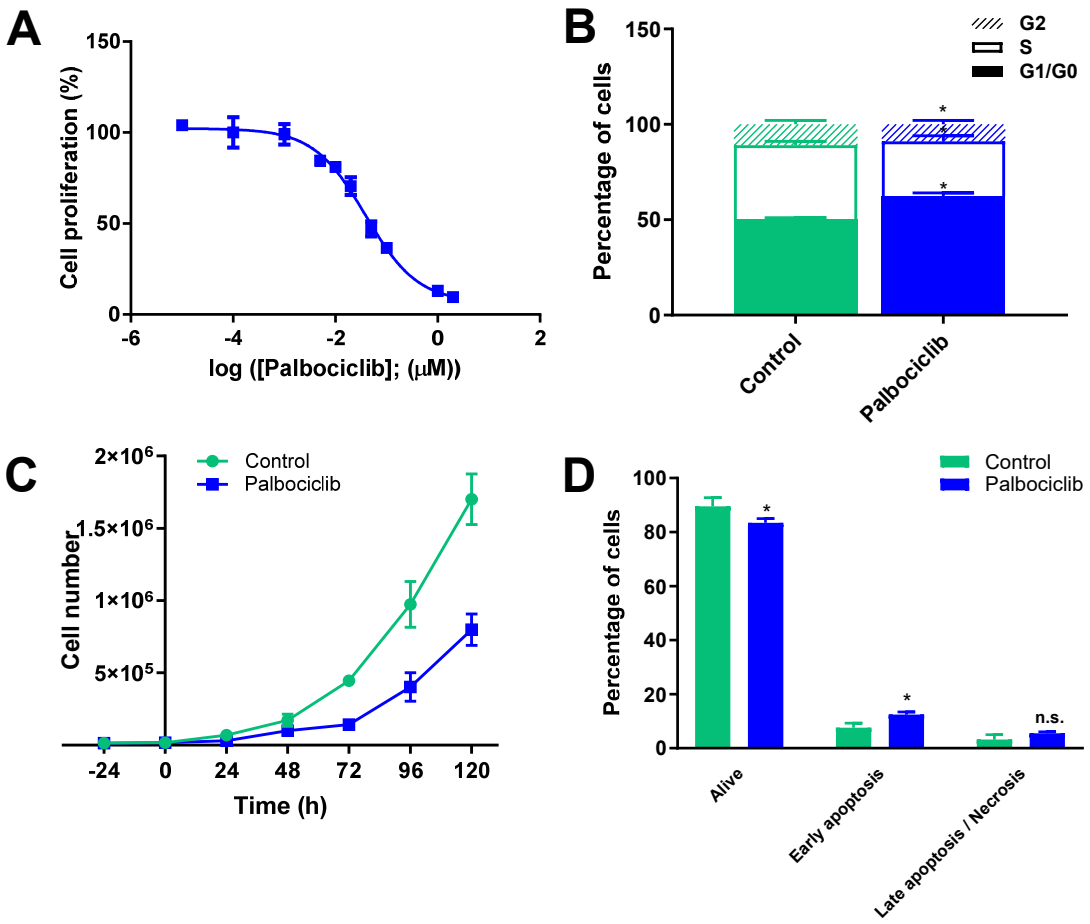

Figure 3.3.1. Palbociclib reduces SW620 cell proliferation by arresting the cell cycle in the G1/G0 phase. SW620 cells were incubated with and without Palbociclib for 96 h. A) Cell proliferation curve at increasing concentrations of Palbociclib to determine the IC_{50} at 96 h, B) Cell cycle analysis after DNA staining with propidium iodide (PI), indicating percentage distributed along the cell cycle phases; pre-replicative (G1/G0), synthesis (S), and post-replicative (G2) in control and Palbociclib-treated cells, C) Cell proliferation over time in control cells and cells treated with a fixed Palbociclib concentration (40 nM), and D) Apoptosis assay after Annexin V-FITC incubation discerning cells found alive, in early apoptosis and late apoptosis/necrosis in control and Palbociclib-treated cells. An independent sample t-test was applied for relative comparison between the two groups, * indicates significant differences ($p < 0.05$).

Thus, Palbociclib short-term treatment causes cell proliferation impairment in metastatic colorectal cancer cells by promoting cell cycle arrest in the G1/G0 phase. Since a high percentage of cells manage to overcome cell cycle impediments, other mechanisms must enable cells to survive and acquire resistance after short-term Palbociclib treatment.

3.3.2.2. Fatty acid metabolism dominates gene enrichment in Palbociclib-treated colorectal cells.

To understand the metabolic reprogramming involved in Palbociclib-treated cells, we first evaluated the differential expression analysis by employing a gene set enrichment analysis (GSEA) (Subramanian et al., 2005) focused on metabolic-related pathways defined by the Kyoto Encyclopedia of Genes and Genomes (KEGG) database using a combination of 2-4 letter code and 5 digit number (the unique KEGG-pathways identifiers and the genes included in each pathway are described in detail in https://www.kegg.jp/).

The gene set enrichment score indicated a significant (adjusted p-value < 0.05) positive enrichment in the 'hsa00600 sphingolipid metabolism' gene set (**Figure 3.3.2.**). Moreover, other fatty acid-related metabolic pathways were found to be upregulated (adjusted p-value < 0.25) together with amino acid metabolism and nucleotide synthesis-related processes, such as folate biosynthesis, after Palbociclib treatment in SW620 cells.

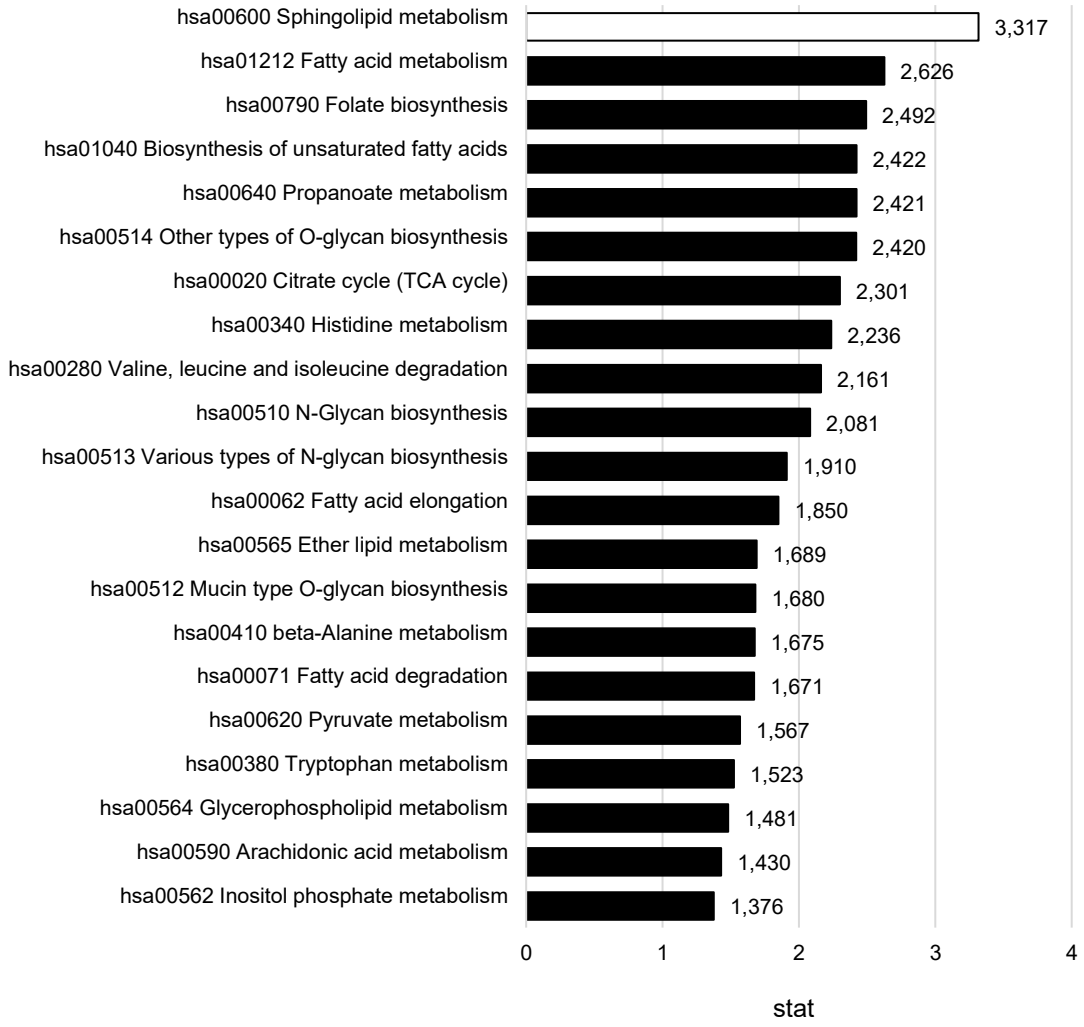

Figure 3.3.2. Gene set enrichment analysis (GSEA) according to KEGG pathways classification. Differential expression was analyzed after 96 h of treatment with Palbociclib in SW620 cells. Stat represents enrichment score, being positive when it increases or negative when it decreases. White-colored bars indicate significant differences with respect to non-treated cells (adjusted p-value < 0.05), and black-colored bars indicate patterns with adjusted p-value < 0.25.

Then, we employed the Pathview software (Luo et al., 2017, Luo et al., 2013). to visualize the sphingolipid metabolism and the sphingolipid signaling pathway filtering by the significantly differentially expressed genes in Palbociclib-treated SW620 cells. These pathway analyses highlighted a significant upregulation of genes participating in sphingolipid metabolism (**Figure 3.3.3.**) and sphingolipid signaling pathway, which is in line with the observed increase in sphingolipid metabolism (**Figure 3.3.4.**).

Therefore, the first insight into the metabolic profile of Palbociclib-treated cells shows a significant alteration of lipid metabolism and the induction of other metabolic pathways, which need further exploration to identify the major supporters of cell survival after Palbociclib treatment.

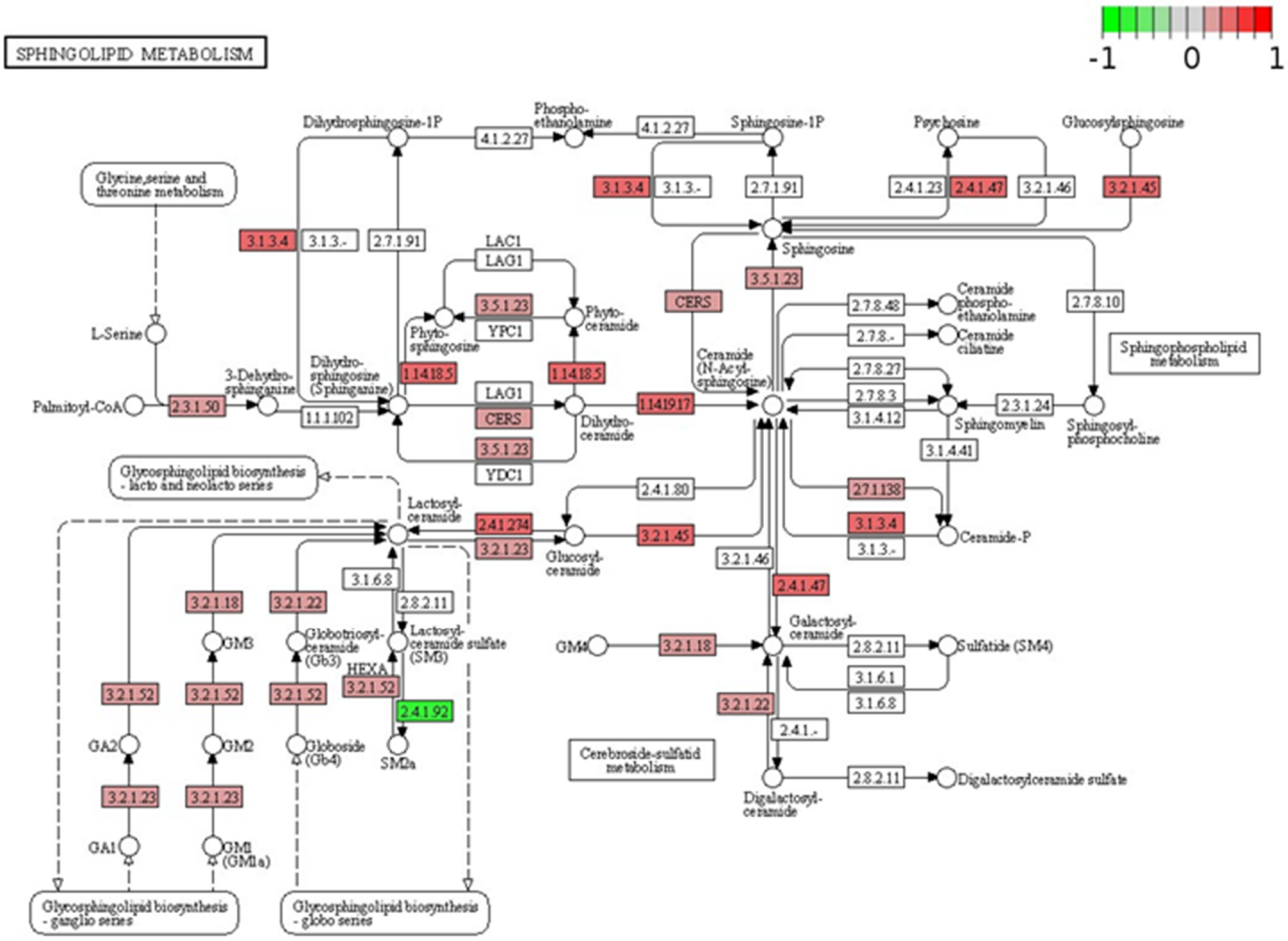

Figure 3.3.3. Sphingolipid metabolism increased after Palbociclib treatment in SW620 cells. Pathview map integrates genes involved in the 'sphingolipid metabolism' (KEGG) after 96 h of treatment with Palbociclib in SW620 cells. Colors refer to the expression level; green is downregulated and red is upregulated after Oxaliplatin treatment compared to control (Gene names associated with each reaction are available at https://www.genome.jp/kegg-bin/show_pathway?hsa00600). The figure was downloaded from the Pathview web server (www.pathview.uncc.edu).

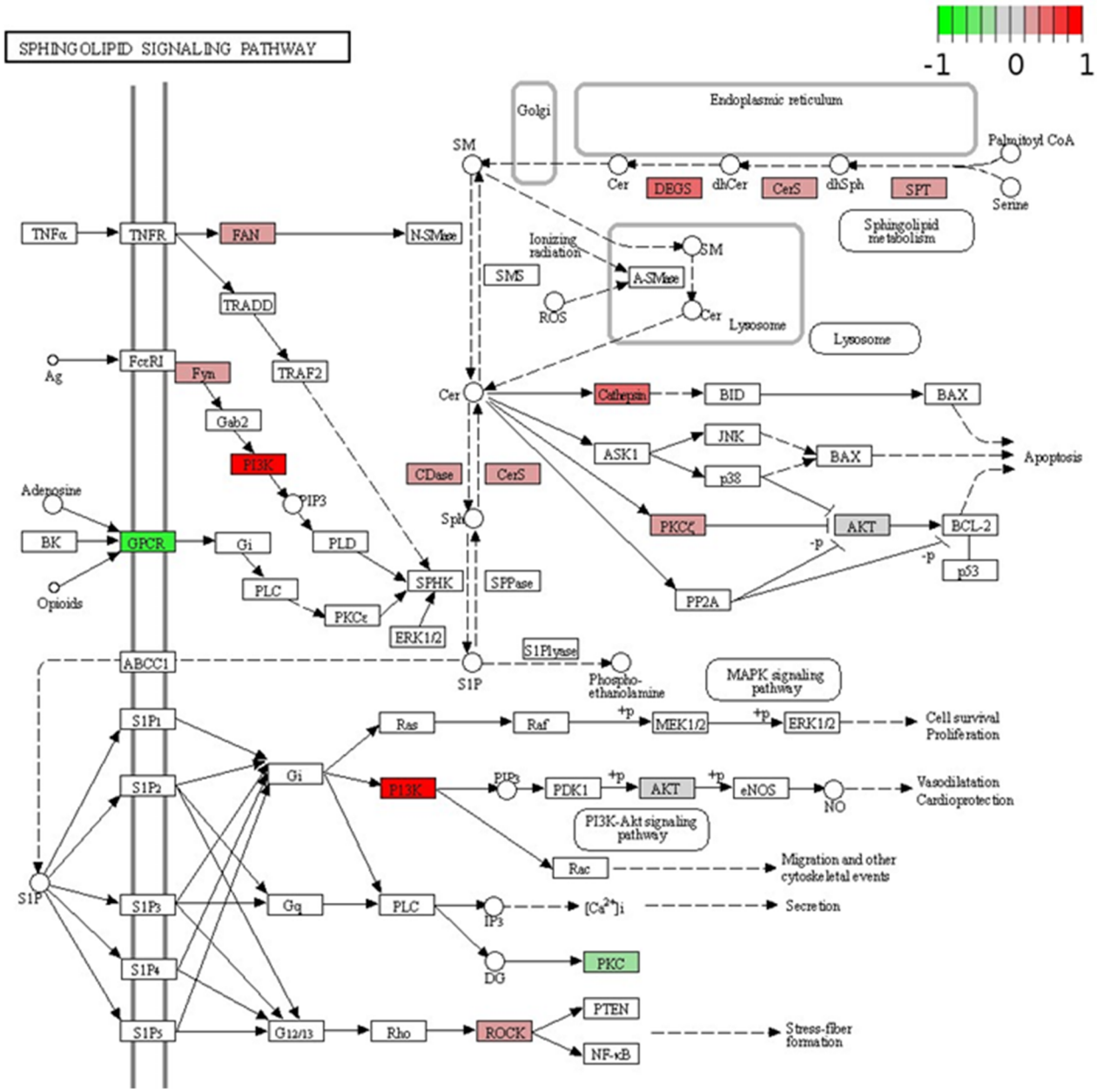

Figure 3.3.4. PI3K is upregulated in sphingolipid signaling pathway after Palbociclib treatment in SW620 cells. Pathview map integrates genes involved in the 'sphingolipid signaling pathway' (KEGG) after 96 h of treatment with Palbociclib in SW620 cells. Colors refer to the expression level; green is downregulated and red is upregulated after Oxaliplatin treatment compared to control (Gene names associated with each reaction are available at https://www.genome.jp/pathway/hsa04071). The figure was downloaded from the Pathview web server (www.pathview.uncc.edu).

3.3.2.3. Palbociclib treatment increases mitochondrial respiration in SW620 colorectal cells.

In order to obtain information about cell fitness and metabolic flexibility, we evaluated cellular respiration after Palbociclib treatment, as lipid metabolism can boost mitochondrial function by fueling the TCA cycle with acetyl-CoA. The respiratory capacity was measured using the Seahorse analyzer with the Mito Stress Test in SW620 cells with and without Palbociclib treatment. This assay provides information regarding the mitochondrial respiration parameters and the glycolytic function by measuring the

Oxygen Consumption Rate (OCR) and the Extracellular Acidification Rate (ECAR). The OCR results displayed a significant augment in basal respiration after Palbociclib treatment, indicating an increased oxygen demand (**Figure 3.3.5., A, B**). Furthermore, we observed a significant enhancement in all OCR-related parameters in Palbociclib-treated cells, including maximal respiration, non-ATP linked respiration (proton leak),

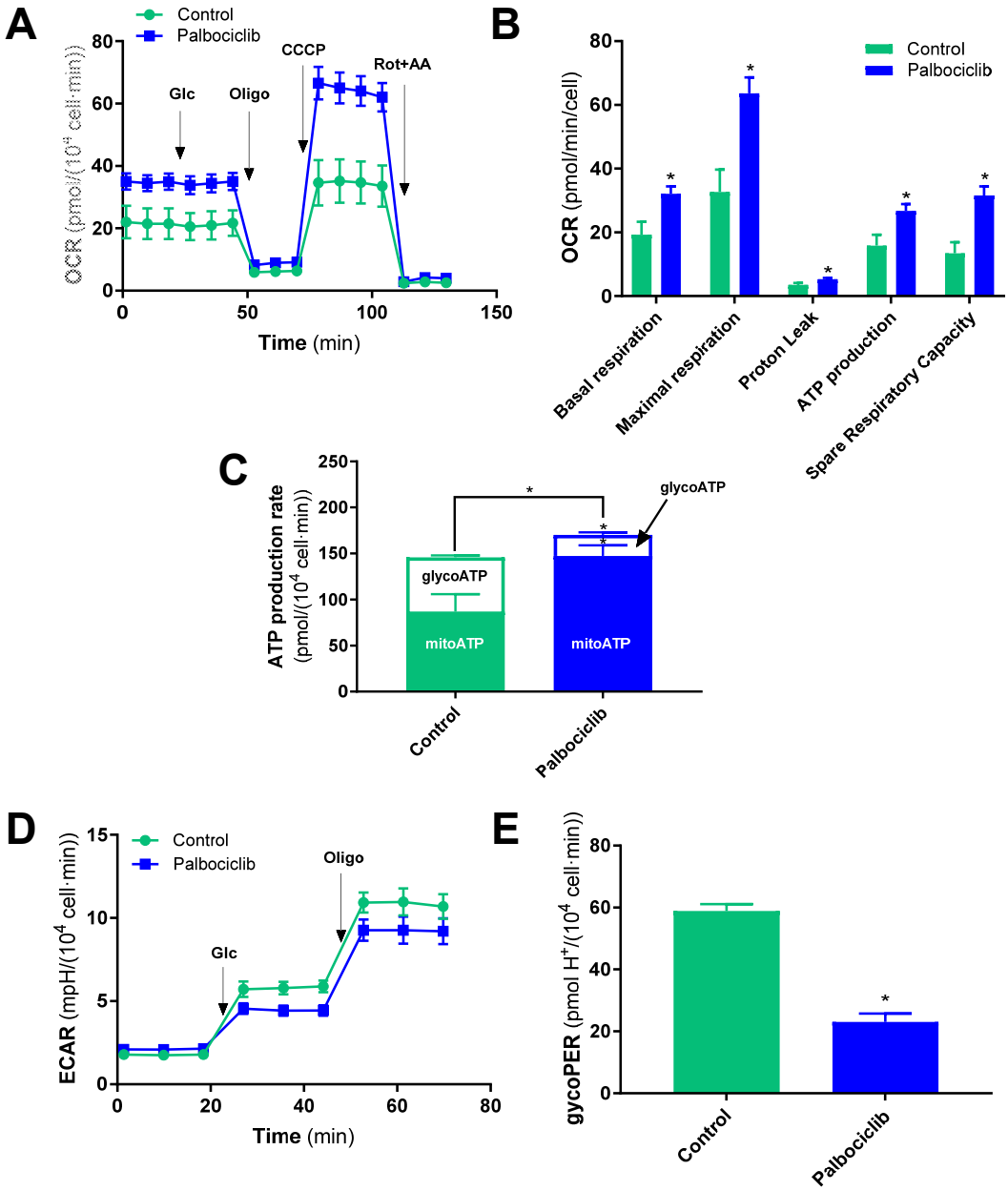

Figure 3.3.5. Palbociclib induces mitochondrial respiration in SW620 cells. Mito Stress Test performed in SW620 cells after 96 h with and without Palbociclib treatment (40 nM). A) Normalized monitored values of Oxygen Consumption Rate (OCR) over time. B) OCR-related parameters, including OCR basal respiration, maximal respiration, non-ATP linked respiration (proton leak), ATP production-associated respiration, and spare respiratory capacity. C) ATP production rate discerning mitochondrial ATP production (mitoATP) and glycolytic ATP production (glycoATP). D) Normalized monitored values of Extracellular Acidification Rate (ECAR) over time. E) Glycolytic Proton Efflux Rate (glycoPER). Mito Stress test was performed in Seahorse XFe medium supplemented with glutamine (2mM), with and without Palbociclib (depending on the condition) before the sequential injection of glucose (Glc, 12.5 mM), Oligomycin (1.5 µM), CCCP (600 nM), and Rotenone (Rot, 2 µM) + Antimycin (AA, 2 µM). An independent sample t-test was applied for relative comparison between the two groups, * indicates significant differences ($p < 0.05$).

ATP production-associated respiration, and spare respiratory capacity (**Figure 3.3.5., B**). Of note, the reported increment in ATP production-associated respiration was linked to augmented mitochondrial ATP production rate (**Figure 3.3.5., C**). In contrast, the rate of glycolytic ATP production displayed a significant decrease (**Figure 3.3.5., D**), in concordance with ECAR and glycolytic proton efflux rate (glycoPER) measurements, describing a reduction in the glycolytic function promoted by Palbociclib treatment (**Figure 3.3.5., E**).

Taking into account the inducing effect of Palbociclib on respiration and mitochondrial function, we assessed ROS production after 96 h of incubation in SW620 cells by flow cytometry. The results displayed a greater generation of ROS after Palbociclib treatment, showing an increment of 50% of fluorescent signal and, therefore, ROS accumulation with respect to the levels of control cells (**Figure 3.3.6.**), in correlation with the increased mitochondrial respiration observed after Palbociclib treatment.

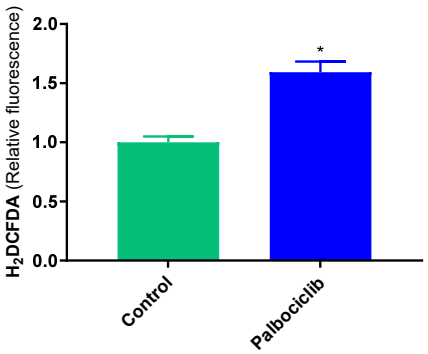

Figure 3.3.6. The palbociclib treatment causes an accumulation of reactive oxygen species (ROS) in SW620 cells. Intracellular ROS were measured upon incubation with an H_2DCFDA probe (5 µM) after 96 h of treatment with and without 40 nM of Palbociclib in SW620 cells. Fluorescence intensity values have been normalized with respect to the control condition. An independent sample t-test was applied for relative comparison between the two groups, ***** indicates significant differences ($p < 0.05$).

Altogether, our results indicate a metabolic shift towards oxidative phosphorylation (OxPhos) for energy production after Palbociclib treatment in SW620 cells, while the glycolytic function is either depleted or directed toward alternative metabolic routes instead of complete glucose oxidation for ATP production.

3.3.2.4. Metabolic reprogramming after Palbociclib treatment in SW620 cells.

Following the exploration of gene expression and the enhanced mitochondrial respiration observed after Palbociclib treatment, our next step was to explore the intracellular lipid profiling to understand the influence of the genetic alterations found in **section 3.3.2.2.** on lipid metabolism. With this aim, we used targeted metabolomics to determine the intracellular lipids concentration of sphingolipids (sphingomyelins), acylcarnitines, and glycerophospholipids after 96 h of Palbociclib treatment in SW620 cells.

We distributed the intracellular lipid concentrations in heatmaps by employing non-supervised clusterization. The three lipid categories clustered treated and non-treated conditions in two groups, indicating a significant alteration in the overall lipid profile after Palbociclib treatment in SW620 cells (**Figure 3.3.7.**, **Figure 3.3.8.**, and **Figure 3.3.9.**), correlating with the increased lipid metabolism revealed by the GSEA analysis (**Figure 3.3.2.**). The intracellular concentration of acylcarnitines was significantly decreased in

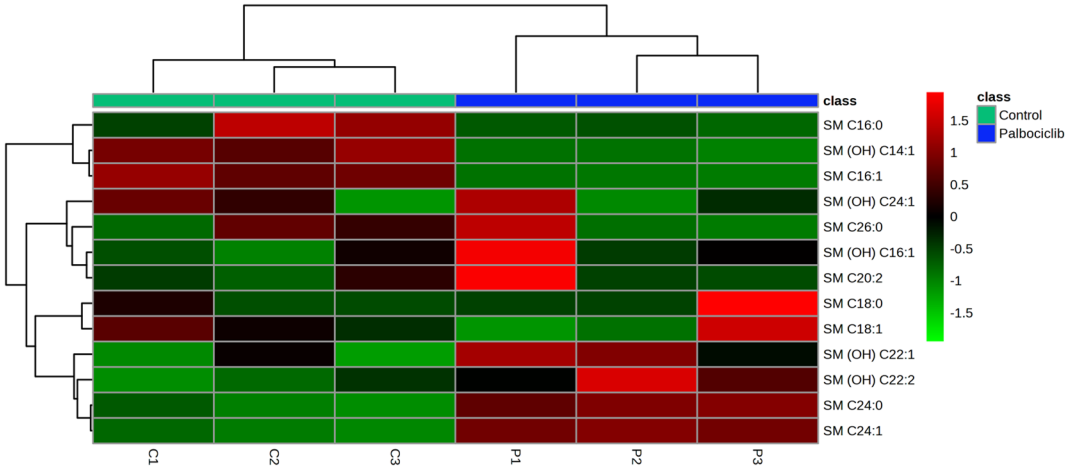

Figure 3.3.7. Sphingolipids profile in control and Palbociclib-treated SW620 cells. Heatmap distribution after non-supervised clusterization of the intracellular sphingomyelins (SM) in control and 96 h Palbociclib-treated (40 nM) SW620 cells. Results were normalized by sum applying Pareto data scaling using Metaboanalyst 5.0 software.

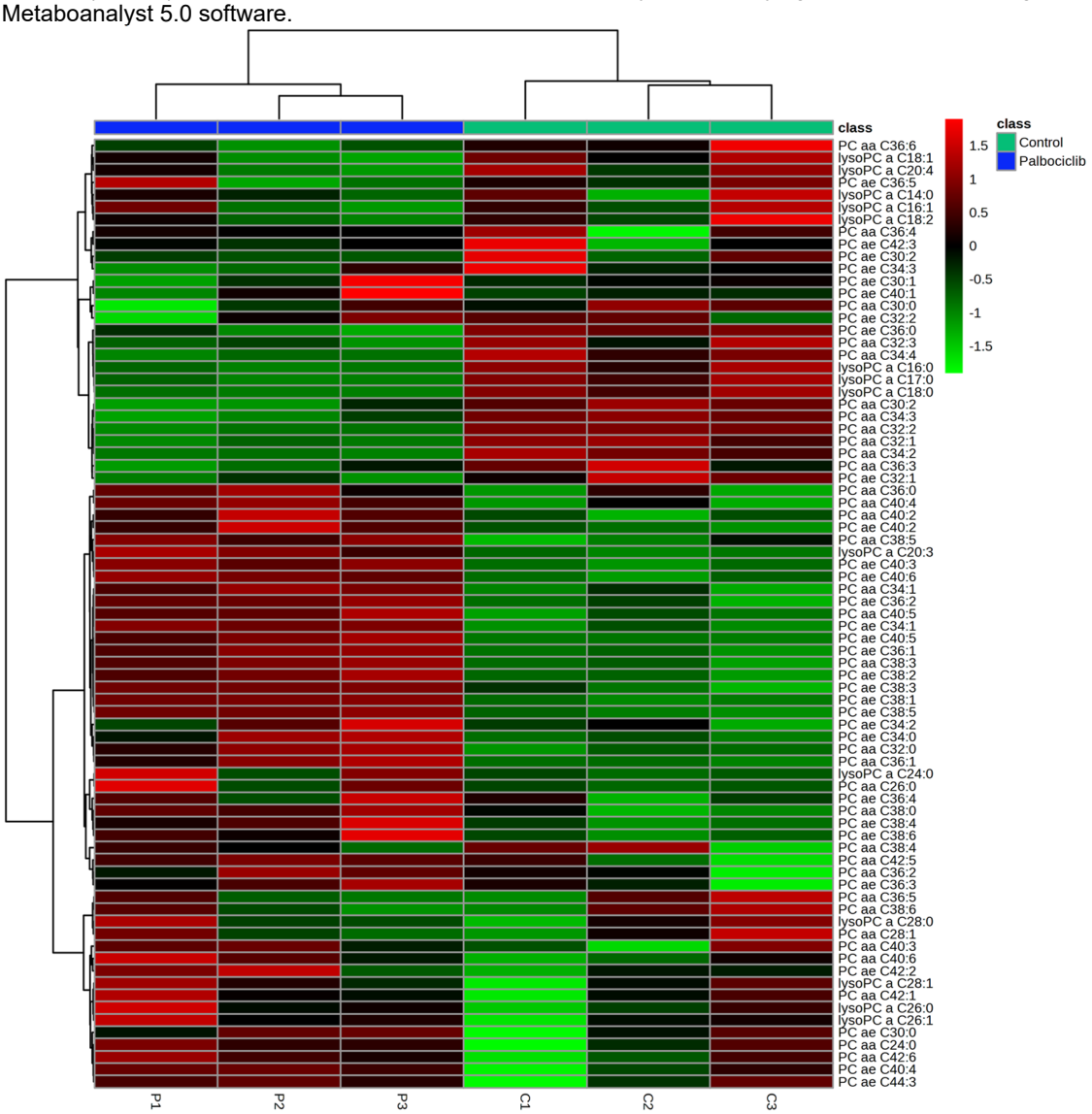

Figure 3.3.8. Glycerophospholipids profile in control and Palbociclib-treated SW620 cells. Heatmap distribution after non-supervised clusterization of the intracellular phosphatidylcholines in control and 96 h Palbociclib-treated (40 nM) SW620 cells. Results were normalized by sum applying Pareto data scaling using Metaboanalyst 5.0 software.

Palbociclib-treated cells compared to the non-treated condition (**Figure 3.3.9.**). Acylcarnitine formation is essential for fatty acid internalization across the mitochondrial membrane for subsequent β-oxidation. Therefore, we calculated the ratio of short-chain acylcarnitines to free carnitine, which is associated with overall ß-oxidation activity (Dossus & Kouloura et al., 2021). In this regard, our results showed no statistically significant changes (**Figure 3.3.9., B**).

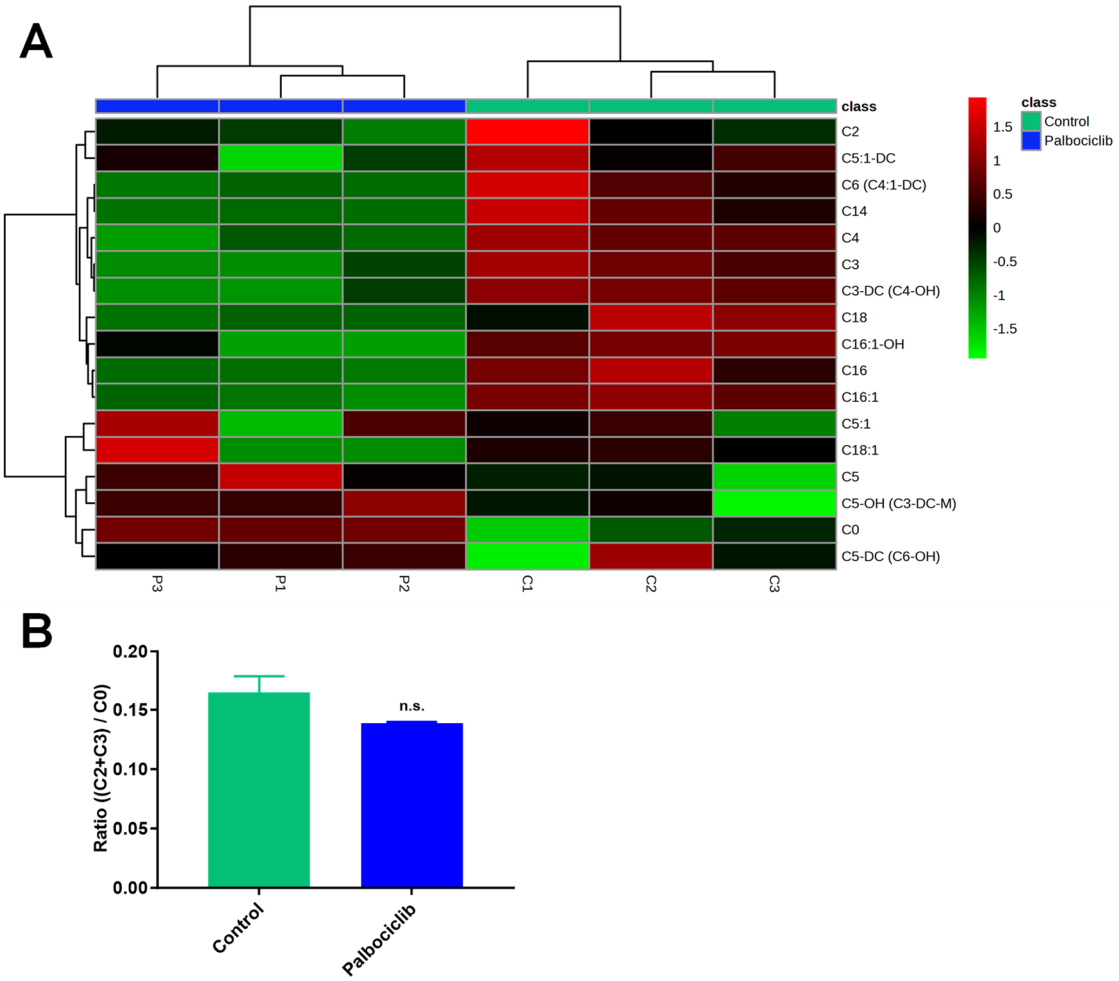

Figure 3.3.9. Acylcarnitines profile in control and Palbociclib-treated SW620 cells. A) Heatmap distribution after non-supervised clusterization of the intracellular acylcarnitines measured in control and 96 h Palbociclib-treated (40 nM) SW620 cells after 96 h of treatment with Palbociclib (40 nM) in the SW620 cell line. Results were normalized by sum applying Pareto data scaling using Metaboanalyst 5.0 software. B) Ratio of short-chain acylcarnitines to free carnitine ((C2+C3)/C0), which is a measure of overall β-oxidation activity. An independent sample t-test was applied for relative comparison between the two groups, n.s. indicates no significant differences ($p > 0.05$).

In order to get more insight into the potential balance between fatty acid synthesis (FAS) and fatty acid oxidation (FAO) exerted by Palbociclib treatment in SW620 cells, we evaluated the differential expression of crucial genes involved in fatty acids metabolism including both FAS and FAO. In particular, the rate-limiting enzyme in the fatty acid uptake for ß-oxidation is carnitine palmitoyl transferase 1 (CPT1), whose encoding gene was found significantly overexpressed log2FC(*CPT1A)*=(+)0.32±0.09 (adjusted p-value 0.01). At the same time, *ATP Citrate Lyase* log2FC(*ACLY)*=(+)0.23±0.06 (adjusted p-value 0.03) and *acetyl-CoA carboxylase* log2FC(*ACACA)*=(+)0.28±0.08 (adjusted p-value 0.005), both genes promoting lipogenesis, were found overexpressed after

Palbociclib treatment. Altogether, these observations also suggest an altered lipid metabolism following Palbociclib treatment in SW620 cells, involving greater activity in both synthesis and degradation processes.

To further explore the metabolic reprogramming underlying Palbociclib resistance and the major metabolic pathways contributing to the enhanced mitochondrial function beyond lipid metabolism, we evaluated the impact of Palbociclib treatment on the principal metabolic pathways. Since the respiratory results indicated a decrease in glycolytic function towards ATP production rate, we explored the effects of Palbociclib on glucose metabolism. With this aim, we measured the extracellular rates of glucose consumption and lactate production in comparison to control cells. Our findings showed no changes in the extracellular consumption rate of glucose, the lactate production rate, and the glucose commitment to lactate, suggesting that the Warburg effect was not altered after 96 h of Palbociclib treatment (**Figure 3.3.10., A, B**). These observations

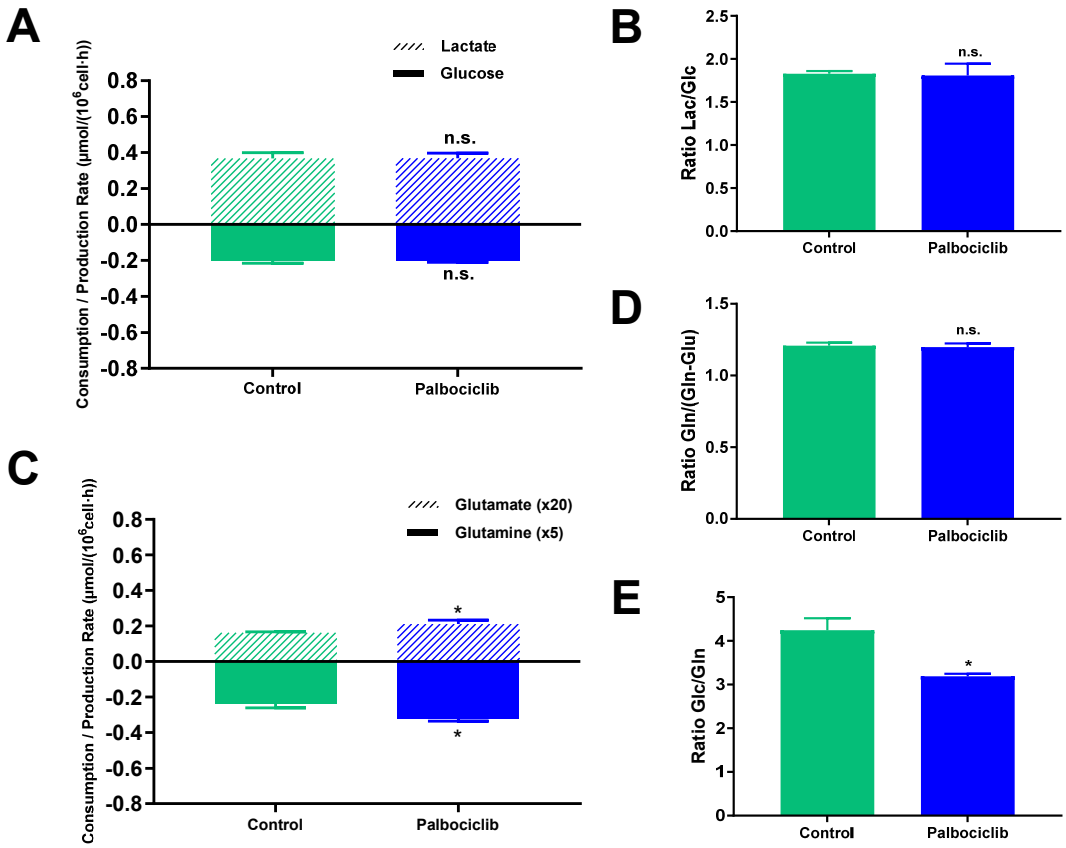

Figure 3.3.10. The Palbociclib effect over glycolysis and glutaminolysis in SW620 cells. A) Extracellular glucose consumption and lactate production rates measured in control and 96 h Palbociclib-treated (40 nM) SW620 cells, B) the lactate production with respect to glucose consumption, C) glutamine consumption and glutamate production rates measured in control and 96 h Palbociclib-treated (40 nM) SW620 cells, D) glutamine consumption with respect to glutamine not committed to glutamate production and E) the glucose with respect to glutamine utilization. An independent sample t-test was applied for relative comparison between the two groups, * indicates significant differences ($p < 0.05$).

indicate that Palbociclib-treated cells maintain glucose consumption despite the significant decrease in the glycolytic contribution to ATP production rate (**Figure 3.3.5., C**). In correlation with the glycolytic contribution, we observed reduced expression of *hexokinase 2 (HK2), 6-phosphofructo-2-kinase 3 and 4 (PFKFB3/4)*, and *enolase 1 and 2 (ENO1/2)* in the differential gene expression of the glycolysis metabolic pathway after

Palbociclib treatment (the comprehensive gene list is presented in **Appendix V**, **Table V.1.**). On the other hand, our findings elucidated an increase in glutamine consumption and glutamate production rates as a response to Palbociclib (**Figure 3.3.10., C**), while glutamine maintained the same fate in terms of glutamate production (estimated as Gln/(Gln-Glu)), indicating a rising demand for glutamine, being this latter the preferred carbon source after treatment (**Figure 3.3.10., D, E**).

Therefore, our observations suggest that Palbociclib treatment promotes an increased demand for alternative carbon sources to glucose to support enhanced mitochondrial function, respiration, and ATP production. In addition to the notable alteration in lipid profile and the maintenance of glucose consumption rate, our results reveal that glutamine is a major contributor to cell survival. In order to evaluate the contribution of other amino acids in Palbociclib metabolic reprogramming, we assessed targeted metabolomics to measure essential and non-essential amino acid cellular concentrations and extracellular fluxes after 96 h of incubation. Regarding essential amino acid (EAAs) fingerprint after Palbociclib treatment, we observed a significant decrease in their intracellular concentration, suggesting an increased essential amino acid metabolization (**Figure 3.3.11.**).

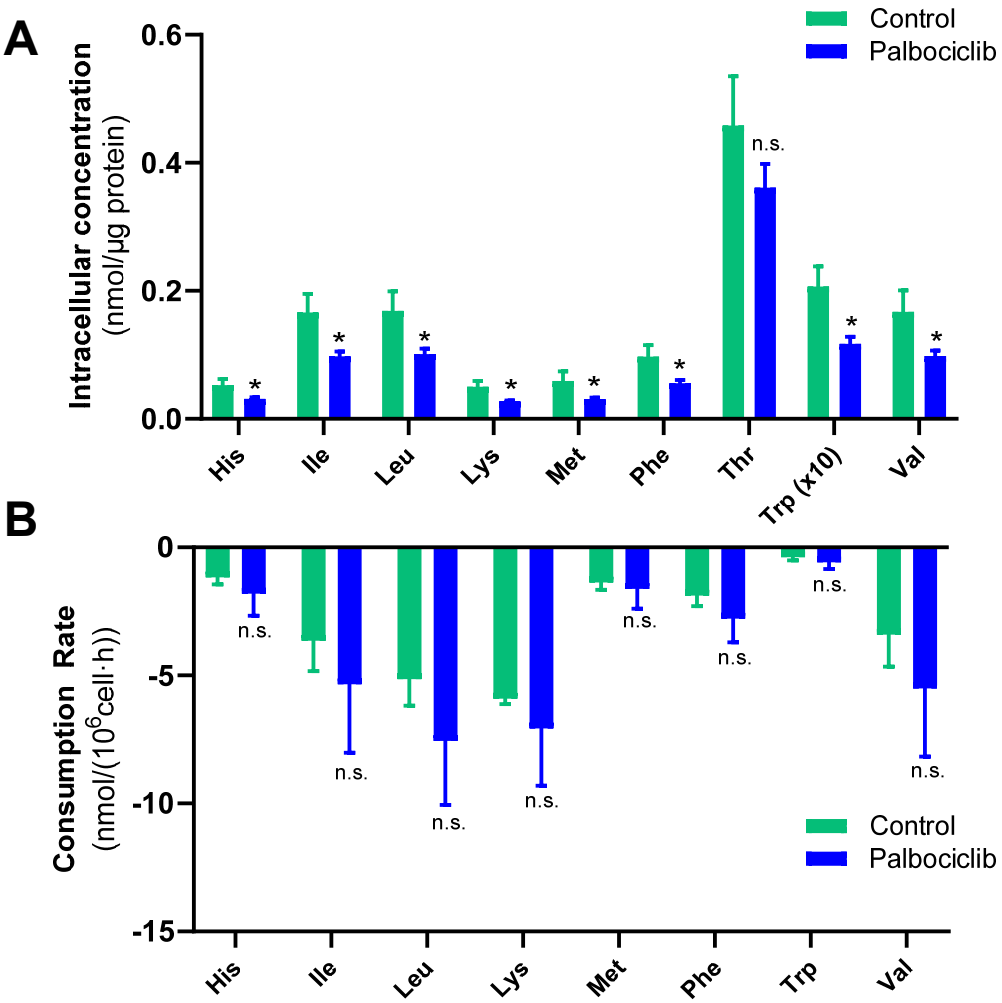

Figure 3.3.11. Essential amino acids (EAAs) profile after Palbociclib treatment in SW620 cells. A) Intracellular EAAs concentration, and B) extracellular EAAs consumption rates in control and 96 h Palbociclib-treated (40 nM) SW620 cells. An independent sample t-test was applied for relative comparison between the two groups, * indicates significant differences ($p < 0.05$).

Attending to non-essential amino acids (NEAAs), our analysis revealed a significant decrease in the intracellular concentrations of tyrosine, arginine, and citrulline (**Figure 3.3.12.**). Additionally, Palbociclib promoted a significant increase in the extracellular production rates of alanine, asparagine, aspartate, proline, ornithine, and glycine, together with an augmented serine consumption (**Figure 3.3.12.**).

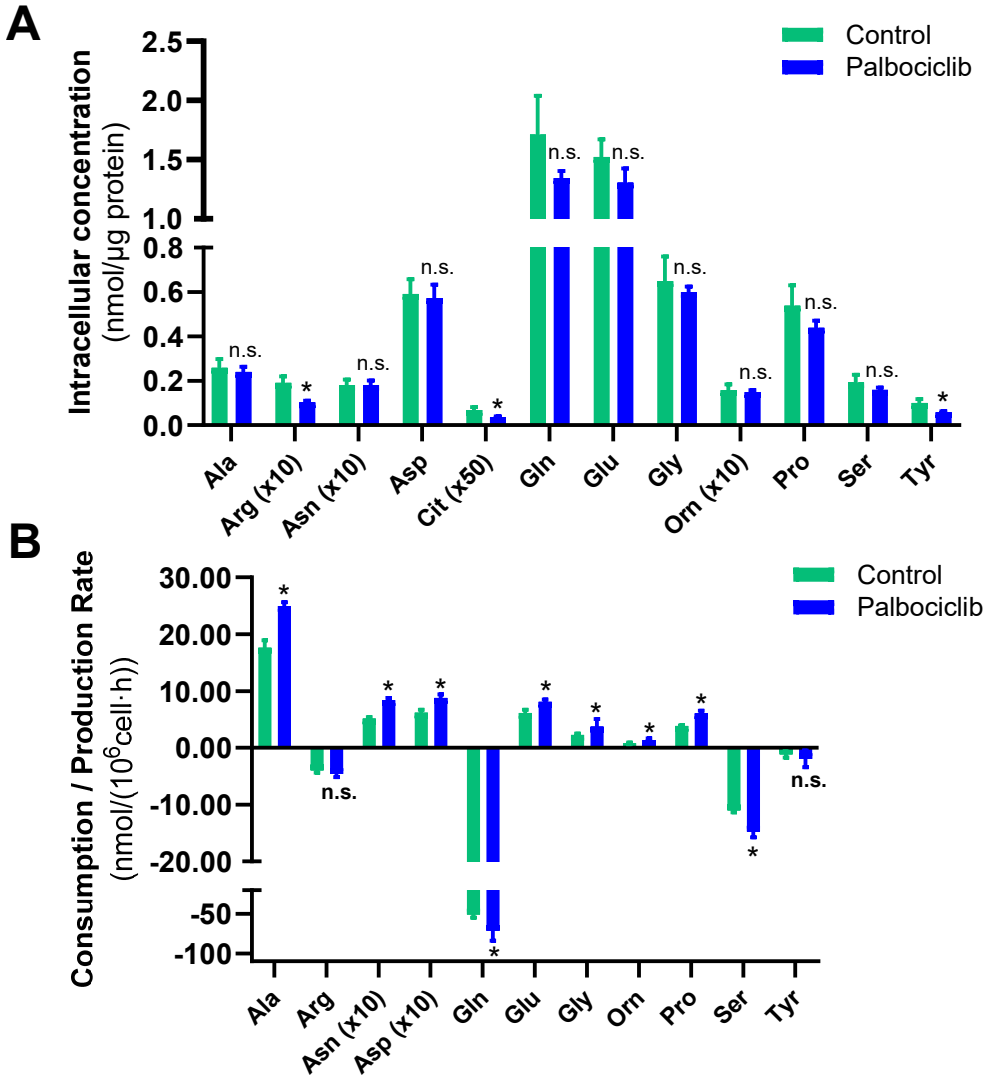

Figure 3.3.12. Non-essential amino acids (NEAAs) profile after Palbociclib treatment in SW620 cells. A) Intracellular NEAAs concentration, and B) extracellular NEAAs consumption and production rates in control and 96 h Palbociclib-treated (40 nM) SW620 cells. An independent sample t-test was applied for relative comparison between the two groups, * indicates significant differences ($p < 0.05$).

Together, these observations indicate a great impact on amino acid metabolism after Palbociclib treatment. These results correlate with increased glutamine metabolism, producing NEAAs and supporting the augmented activity of the TCA cycle. Furthermore, our results present altered metabolites involved in the urea cycle such as aspartate, arginine, citrulline, ornithine, and proline, prompting us to explore the metabolic indicators which are correlated to arginase (ARG), ornithine transcarbamylase (OTC) activity, and nitric oxide synthase (NOS) activity (Dossus & Kouloura et al., 2021).

Our study indicated an enhanced activity of arginase (ARG) (**Figure 3.3.13., A**) and a reduction in OTC activity (**Figure 3.3.13., B**), while the activity of NOS was preserved after Palbociclib treatment in SW620 cells (**Figure 3.3.13., C**).

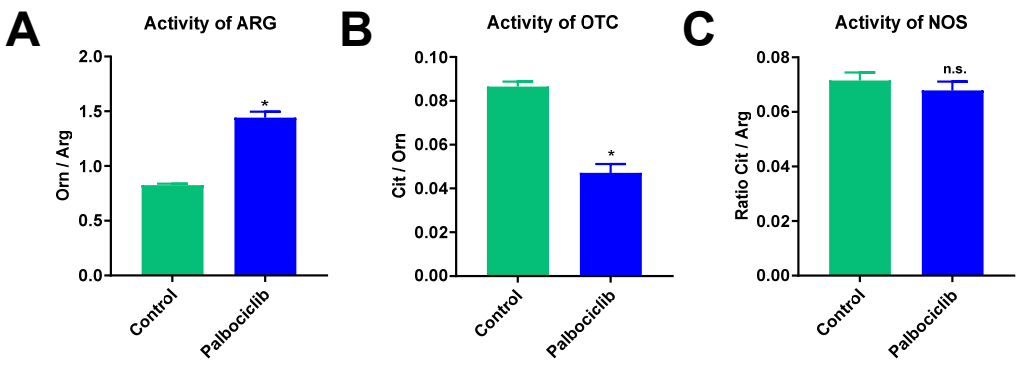

Figure 3.3.13. Activity indicators of key urea cycle enzymes after Palbociclib treatment. Ratios calculated from the intracellular amino acid concentration indicating A) activity of arginase (ARG) calculated from the ornithine/arginine ratio, B) activity of ornithine transcarbamylase (OTC) calculated from the citrulline/ornithine ratio, and C) activity of nitric oxide synthase (NOS) calculated from the ornithine/arginine ratio. An independent sample t-test was applied for relative comparison between the two groups, * indicates significant differences ($p < 0.05$).

These findings suggest that the increased arginine consumption rate is a commitment toward ornithine conversion, promoting ornithine production, which, in turn, serves as a precursor for polyamine synthesis, in agreement with the increased putrescine production observed after Palbociclib treatment (**Figure 3.3.14.**).

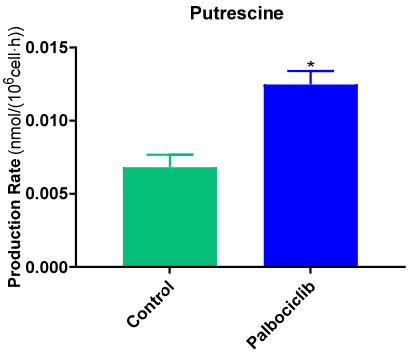

Figure 3.3.14. Putrescine augmented secretion after Palbociclib treatment in SW620 cells. Extracellular polyamine putrescine production rate measured after 96 h with and without Palbociclib treatment (40 nM) in SW620 cells. An independent sample t-test was applied for relative comparison between the two groups, * indicates significant differences ($p < 0.05$).

In brief, our study indicates that Palbociclib treatment induces significant metabolic reprogramming in SW620 cells, affecting lipid metabolism, enhancing cellular respiration, and altering amino acid utilization. This metabolic shift toward oxidative phosphorylation induces TCA anaplerosis despite there being no changes at the differential expression level of this metabolic pathway (differential gene expression is listed in **Appendix V, Table V.2.**), and the urea cycle enzyme activity boosting polyamine synthesis.

3.3.2.5. Targeting mitochondrial-derived ROS modulation synergizes with Palbociclib by impairing cell proliferation of SW620 cells.

The significant increment observed in mitochondrial respiration, mitochondrial ATP production, and TCA cycle anaplerosis in SW620 cells upon Palbociclib exposure, predict a strong reliance on mitochondrial metabolism, which represents an attractive

metabolic vulnerability, in agreement with previous results obtained following Palbociclib treatment in the PC-3 cells (**Section 3.2.**). Therefore, we assessed cell proliferation by targeting the mitochondrial metabolism in combination with Palbociclib using two different drugs attacking OxPhos, Tigecycline, which inhibits mitochondrial oxidative respiration, but also induces cell cycle arrest and oxidative stress in solid tumors (Dong et al., 2019). and VLX600, an iron-chelating OxPhos inhibitor (Reisbeck et al., 2023, Zhang et al., 2014). After 96 h of treatment with either Tigecycline or VLX600 on SW620 cell proliferation alone or in combination with Palbociclib, our results showed that Tigecycline inhibits cell proliferation at concentration values in the lower micromolar range. However, this combination did not display synergism, according to the combination index calculated through Compusyn software and the Chou-Talalay method (Chou, 2010) presenting combination index (CI) values upper to 1 (**Figure 3.3.15., A, B**). Regarding the combination of VLX600 with Palbociclib, our findings demonstrated moderate synergism according to the Chou-Talalay method (Chou, 2010) (**Figure 3.3.15., C, D**), representing a promising combination to overcome Palbociclib resistance.

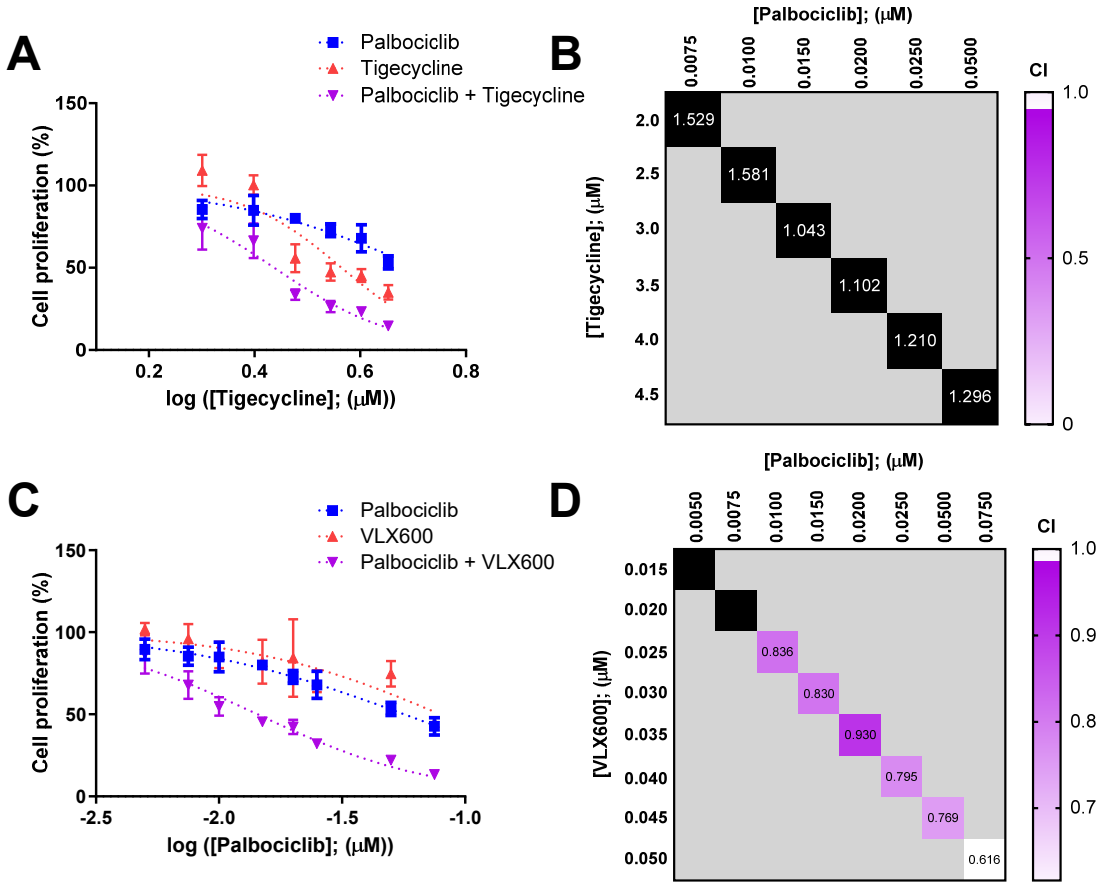

Figure 3.3.15. OxPhos inhibition in combination with Palbociclib in SW620 cells. A, C. Cell proliferation curves in the metastatic colorectal SW620 cell line after 96 h of treatment at increasing concentrations with A) Palbociclib (0.0075, 0.0100, 0.0150, 0.0200, 0.0250, 0.0500μM) and Tigecycline (2.0, 2.5, 3.0, 3.5, 4.0, 4.5μM) alone or in combination with a non-constant ratio, and C) Palbociclib (0.0050, 0.0075, 0.0100, 0.0150, 0.0200, 0.0250, 0.0500, 0.0750μM) and VLX600 (0.015, 0.020, 0.025, 0.030, 0.035, 0.040, 0.045, 0.050μM) alone or in combination with a non-constant ratio. B, D. Combination index (CI) values calculated with Compusyn software and Chou-Talalay method (black squares represent CI values > 1) for the combination B) Palbociclib and Tigecycline and, D) Palbociclib and VLX600.

Taking into account the promising effect of targeting OxPhos we also considered ROS as an opportunity for combined drug treatments, since complexes I and III of the ETC

are the major ROS producers in cancer cells (Sies & Jones, 2020, Hayes et al., 2020), which agree with the significant increment observed in ROS production after Palbociclib treatment in SW620 cells (**Figure 3.3.6.**). These results offer an interesting metabolic vulnerability since it has been extensively reported that this mitochondrial by-product plays a crucial role in cancer metabolic reprogramming, mediating different aspects of cell fate including diverse signaling pathways and cell death (Cheung & Vousden, 2022, Panieri & Santoro, 2016). However, it is difficult to predict the effect of drugs modulating intracellular ROS levels on cell proliferation due to the fact that responses are complex and multifactorial. Basal ROS levels are essential for cellular signaling. Increased ROS levels induce growth factors and oncogenes, modulating cell proliferation, migration, and survival. Conversely, aberrant ROS levels induce cellular stress promoting oxidative damage, altering nucleic acids, proteins, and lipids, and eventually promoting cell death (DeBerardinis & Chandel, 2016). Hence, ROS can confer advantages for cell proliferation but also lead to cell death. According to this dual behavior upon ROS modulation, we hypothesized that both, ROS inhibition and ROS detoxification impairment might alter cell proliferation in SW620 cells treated with Palbociclib.

With this aim, we conducted cell proliferation experiments targeting the most common ROS generated in the ETC, being superoxide radicals and oxygen peroxide using ATN-224, a superoxide dismutase 1 (SOD1) inhibitor (Juarez et al., 2006), and EUK-134, a superoxide dismutase mimetic drug with additional catalase function (Vincent et al., 2021), which is reported to protect from oxidative damage and has been successfully tested in cancer and healthy cells (Decraene & Smaers, et al., 2004, Gianello et al., 1996, Shah et al., 2015). Therefore, we assessed cell proliferation experiments on SW620 cells using ATN-224 or EUK-134 alone or in combination with Palbociclib after 96 h of treatment.

Our initial approach entailed the use of a SOD1 inhibitor, impairing superoxide detoxification. Nevertheless, the combination of ATN-224 with Palbociclib failed to reduce cell proliferation in a synergistic manner (**Figure 3.3.16.**).

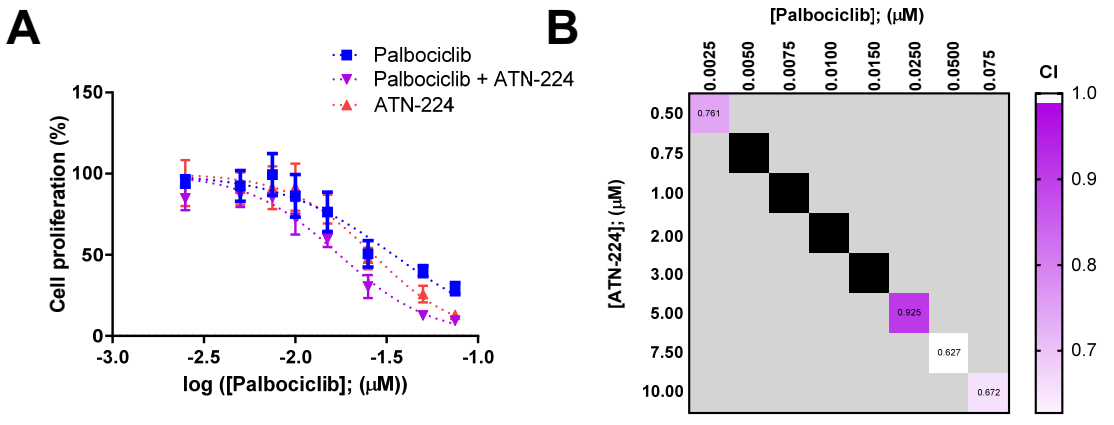

Figure 3.3.16. Effects of superoxide dismutase (SOD) inhibition in combination with Palbociclib in SW620 cells. A) **C**ell proliferation curves in the metastatic colorectal SW620 cell line after 96 h of treatment at increasing concentrations with Palbociclib (0.0025, 0.005, 0.0075, 0.0100, 0.0150, 0.0250, 0.0500, 0.0750μM) and ATN-224 (0.50, 0.75, 1.00, 2.00, 3.00, 5.00, 7.50, 10.00μM) alone or in combination with a non-constant ratio, B) Combination index (CI) value calculated with Compusyn software and Chou-Talalay method (black squares represent CI values > 1).

On the other hand, the alternative approach modulating ROS with this SOD-mimetic/catalase compound, EUK-134 in combination with Palbociclib displayed a significant reduction in SW620 cell proliferation after 96 h of treatment (**Figure 3.3.17.**), presenting synergism in almost every concentration tested.

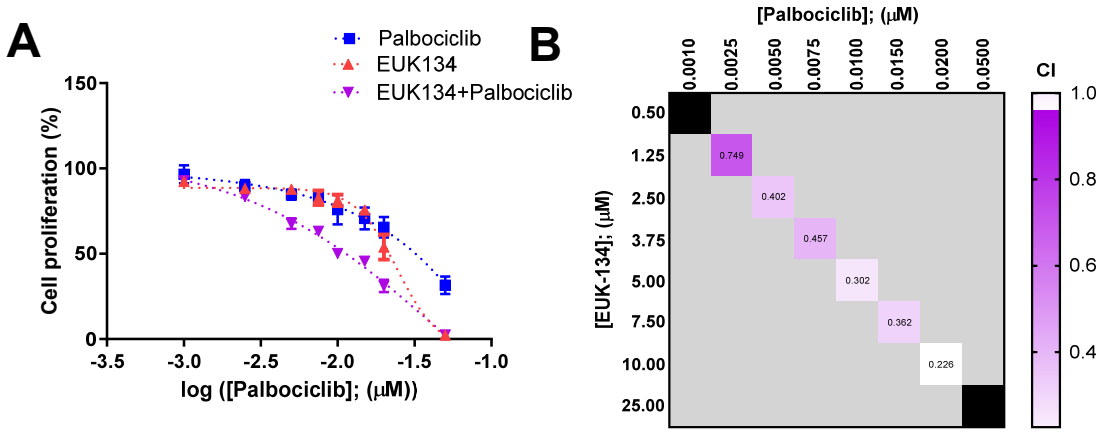

Figure 3.3.17. Effects of superoxide dismutase (SOD)-mimetic with catalase activity in combination with Palbociclib in SW620 cells. A) Cell proliferation curves in the metastatic colorectal SW620 cell line after 96 h of treatment at increasing concentrations with Palbociclib and EUK-134 alone or in combination with a constant ratio, (Palbociclib; EUK-134) [1:500]. B) Combination index (CI) value calculated with Compusyn software and Chou-Talalay method (black squares represent CI values > 1).

In summary, the most promising results were achieved following EUK-134 combination with Palbociclib, which significantly affected cell proliferation with a synergic effect, as opposed to SOD1, or mitochondrial respiration inhibitors. These findings provide a promising combination therapy to overcome Palbociclib resistance in SW620 cells and also identify ROS balance as a key player in mediating cell survival in this cell line of metastatic colorectal cancer.

3.3.2.6. Metabolic insights upon Palbociclib and EUK-134 combined treatment in SW620 cells.

EUK-134 is a salen-manganese compound reported as a superoxide dismutase mimetic that also presents catalase activity (Vincent et al., 2021). This compound can sensitize the Palbociclib effect after 96 h of treatment in SW620 cells as we demonstrated in the previous section. To study cell proliferation impairment, we evaluated cell proliferation over time, together with the impact on cell cycle progression and the apoptotic response of each treatment. Our results displayed a significant reduction in cell proliferation after 96 h in Palbociclib-treated (10 nM) SW620 cells (**Figure 3.3.18., A**), while the combination of Palbociclib with EUK-134 ([Palbociclib]= 10 nM + [EUK-134]=2.5 μM; Palbociclib+EUK-134 from now on) displayed a greater inhibition of cell proliferation than the additive effect of each individual drug. Cell cycle analysis confirmed the expected cell cycle arrest in the G1/G0 phase after Palbociclib treatment and revealed that the compound EUK-134 caused no alteration in the cell cycle in comparison to non-treated cells, either alone or in combination (**Figure 3.3.18., B**). These findings suggest that EUK-134 is either promoting cell cycle progression after cell cycle arrest or preventing cell cycle arrest triggered by Palbociclib.

The proliferative rate calculated through doubling time indicated that cells treated with Palbociclib+EUK-134 exhibited a slower duplication rate from 15 h in control to 19 h in the combination (**Figure 3.3.18., C**). On the other hand, the apoptotic response was not induced by EUK-134 alone, while there was an augmentation in early apoptosis with both Palbociclib and the combination after 96 h of treatment (**Figure 3.3.18., D**). However, none of the conditions that presented early apoptotic cells exceeded 10% of the total cell population despite the notable decrease observed in cell proliferation (**Figure 3.3.18., A**).

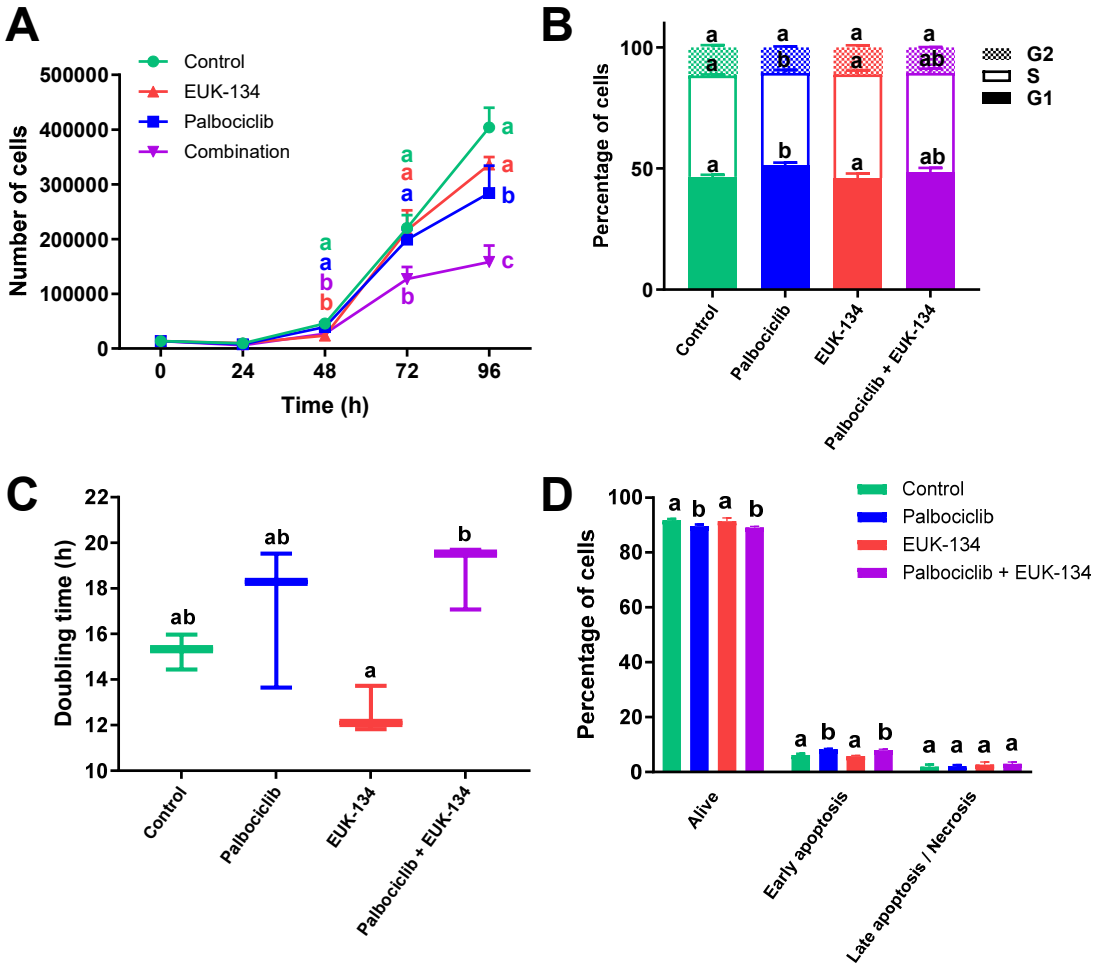

Figure 3.3.18. Palbociclib and EUK-134 combination effect over cell proliferation, cell cycle, and apoptosis in SW620 cells. SW620 cells were treated for 96 h with vehicle (Control), Palbociclib (10 nM), EUK-134 (2.5 µM), or their combination after 96 h. A) Cell proliferation over time. B) Doubling time calculated from cell proliferation. C) Cell cycle analysis after DNA staining with PI indicating the percentage of cells distributed along the pre-replicative (G1/G0), synthesis (S), and post-replicative (G2) cell cycle phases in control and Palbociclib-treated cells. D) Apoptosis assay after Annexin V-FITC incubation discerning cells found alive, in early apoptosis and late apoptosis/necrosis. An independent One-way ANOVA test was applied for relative comparison between groups, where a different letter indicates significant differences ($p < 0.05$).

Altogether, our results demonstrate the significant impairment of cell proliferation by Palbociclib and EUK-134 combination in SW620 cells after 96 h of treatment. Also, these findings suggest that EUK-134 overcomes cell cycle arrest induction by Palbociclib, leading to cell cycle progression while displaying the same apoptotic response as Palbociclib treatment alone. Therefore, the decrease of 50% in cell proliferation reported after Palbociclib and EUK-134 combination treatment can not only be explained through cell cycle arrest or apoptosis induction but also other mechanisms must be involved.

Since EUK-134 modulates ROS levels performing SOD-mimetic and catalase functions (Vincent et al., 2021), we hypothesized that cell proliferation impairment after Palbociclib and EUK-134 combination could be related to ROS balance, which may play an important role in Palbociclib resistance acquisition. Therefore, we measured the intracellular ROS produced after 96 h of treatment with Palbociclib, EUK-134, and the combination using an H_2DCFDA fluorescent probe to quantify the total reactive oxygen species (ROS) generated, and MitoSOX fluorescent probe to assess specifically the mitochondrial superoxide ($\cdot O_2^-$) species, which are directly scavenged by SOD. The intracellular total ROS (**Figure 3.3.19., A**) and mitochondrial superoxide species (**Figure 3.3.19., B**) were significantly increased after 96 h of incubation with the combined treatment. In contrast, another study in breast cancer using a 10-fold concentration of EUK-134 reported a reduction in superoxide and H_2O_2 levels but also a significant decrease in cell viability, indicating that ROS modulation and cytotoxicity are dependent on the concentration of EUK-134 (Shah et al., 2024). The obtained results in this work suggest that either the concentration of EUK-134 used is not able to reduce the total ROS and mitochondrial superoxide levels, or ROS accumulation is due to other non-mitochondrial ROS and superoxide anion sources, such as cytochrome P450 or NADPH oxidase (NOX) (Hayes et al., 2020).

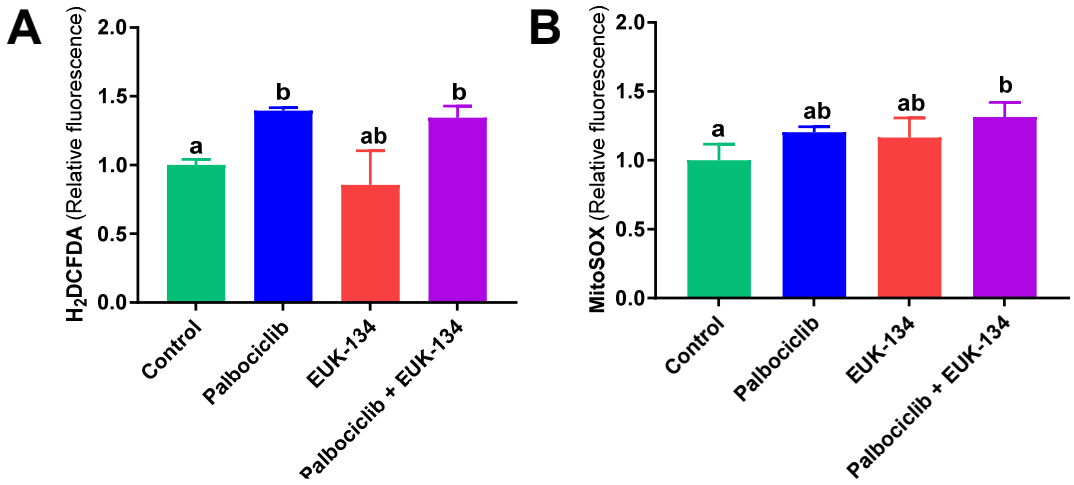

Figure 3.3.19. Palbociclib and EUK-134 combination causes an accumulation of reactive oxygen species (ROS) in SW620 cells. Intracellular ROS were measured in SW620 cells treated for 96 h with vehicle (Control), Palbociclib (10 nM), EUK-134 (2.5 µM), or their combination upon incubation with A) H_2DCFDA probe (5 µM) or B) MitoSOX probe (5 µM). Fluorescence intensity values were normalized with respect to the control condition. An independent One-way ANOVA test was applied for relative comparison between groups, where different letter indicates significant differences ($p < 0.05$).

Next, we studied the metabolic implications of Palbociclib and EUK-134 combination to reveal the altered metabolic pathways resulting from the combined treatment, which are correlated with the reduced cell proliferation and the synergistic response observed in SW620 cells. Given that ROS balance may be mediating Palbociclib adaptation and modulated by EUK-134, we evaluated the impact on the respirometry and mitochondrial function after 96 h in SW620 cells, since it was significantly enhanced after Palbociclib treatment.

The respiratory results displayed that EUK-134 promoted a significant OCR reduction, impairing the maximal respiration, the spare respiratory capacity, and the respiration associated with mitochondrial ATP production (**Figure 3.3.20., A, B, C**). The presence of EUK-134 in Palbociclib-treated cells caused a significant reduction of the respiratory

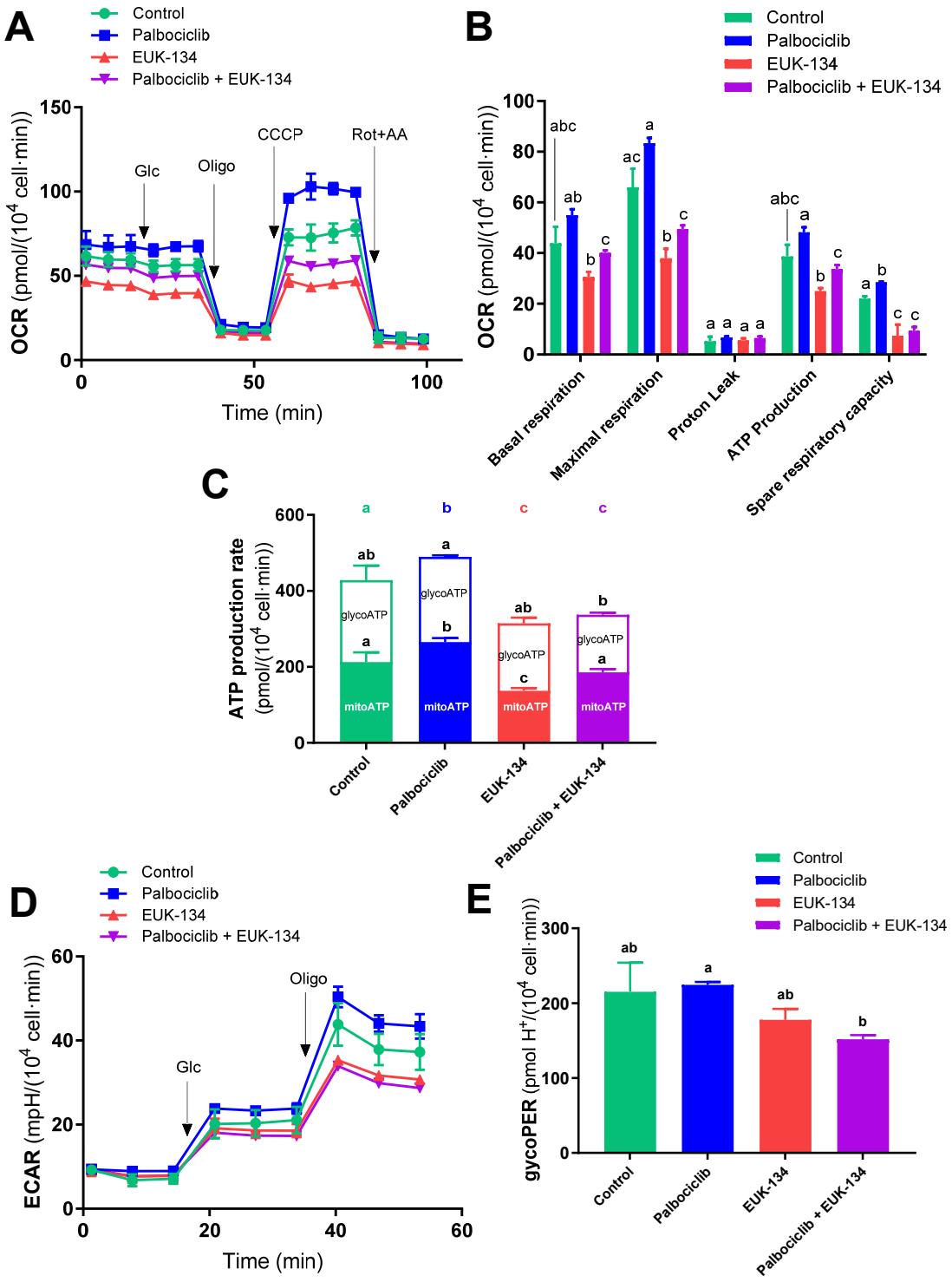

Figure 3.3.20. Mitochondrial respiration after Palbociclib and EUK-134 treatment in SW620 cells. Mito Stress Test performed in SW620 cells treated for 96 h with vehicle (Control), Palbociclib (10 nM), EUK-134 (2.5 μM), or their combination. A) Normalized monitored values of Oxygen Consumption Rate (OCR) over time, B) OCR-related parameters, including OCR basal respiration, maximal respiration, non-ATP linked respiration (proton leak), ATP production-associated respiration, and spare respiratory capacity. C) ATP production rate discerning mitochondrial ATP production (mitoATP) and glycolytic ATP production (glycoATP). D) Normalized monitored values of Extracellular Acidification Rate (ECAR) over time. E) Glycolytic Proton Efflux Rate (glycoPER). Mito Stress test was performed in Seahorse XFe medium supplemented with glutamine (2mM), with and without Palbociclib (depending on the condition) before the sequential injection of glucose (Glc, 12.5 mM), Oligomycin (1.5 μM), CCCP (600 nM), and Rotenone (Rot, 2 μM) + Antimycin (AA, 2 μM). An independent sample t-test was applied for relative comparison between the two groups, * indicates significant differences ($p < 0.05$).

response, reverting the OCR levels to those of control cells, and greatly depleting the spare respiratory capacity (**Figure 3.3.20., A, B**). These results also indicated that ROS accumulation observed after the combined treatment did not correlate with an increased mitochondrial function and respiration, suggesting that other non-mitochondrial ROS and superoxide anion sources may be induced by the combination treatment. Likewise, the combined treatment caused a significant reduction in the glucose oxidation towards ATP production and the glycolytic function compared to the Palbociclib single treatment (**Figure 3.3.20., D, E**). These results indicate that EUK-134 induces an impairment of mitochondrial function, affecting cell flexibility and decreasing the capacity to respond to the energetic demands, thus reverting the metabolic reprogramming prompted by Palbociclib treatment in SW620 cells. Therefore, this combination significantly disrupts cancer cell homeostasis since improved mitochondrial metabolism is an important supporter of Palbociclib resistance in SW620 cells.

To understand the scope of the mitochondrial function affectation observed in cells treated with the combination, we evaluated the metabolic fingerprint after 96 h of incubation with the vehicle, Palbociclib, EUK-134, or their combination. This assessment was primarily directed at the major carbon and nitrogenous sources within cells, thus we focused on the consumption rate of glucose and glutamine, and the production rate of lactate and glutamate. Palbociclib, EUK-134, and the combined treatment caused an increased glucose consumption rate, while a greater glutamine consumption was only displayed in Palbociclib-treated cells (**Figure 3.3.21., A**). The higher glucose uptake exhibited by Palbociclib treated cells was not observed in previous experiments performed with a 4-fold concentration of Palbociclib (**Figure 3.3.10., A**), which suggests that the glycolytic response depends on Palbociclib concentration. In the same manner, the ATP production rate from the glycolytic fraction from cells treated with 10 nM Palbociclib (**Figure 3.3.20., C**) was higher than that of those treated with 40 nM Palbociclib (**Figure 3.3.5., C**). On the other hand, glutamine dependence emerged after Palbociclib treatment, independent of drug concentration (**Figure 3.3.21., B**), contributing to the rise in the mitochondrial ATP production rate (**Figure 3.3.20., C**). The combined treatment counteracted the enhanced uptake of glutamine resulting from Palbociclib with increased glucose consumption instead (**Figure 3.3.21., A**), revealing an augmented demand and reliance on glucose utilization not committed to mitochondrial respiration, which may be associated with the mitochondrial impairment exhibited after the combined treatment. Glucose and glutamine commitment to lactate and glutamate production, respectively, remained constant, indicating that there were no significant changes in the fate of these carbon sources despite their different requirements (**Figure 3.3.21., C, D**).

Altogether, our results suggest that EUK-134 interferes with Palbociclib cell cycle regulation and impairs mitochondrial respiration, which is essential for metabolic flexibility and Palbociclib resistance. The decreased mitochondrial function observed in SW620 cells treated with the combination of Palbociclib and EUK-134 has a great metabolic impact, reducing glutamine consumption and inducing glucose uptake to meet the energetic and biosynthetic requirements.

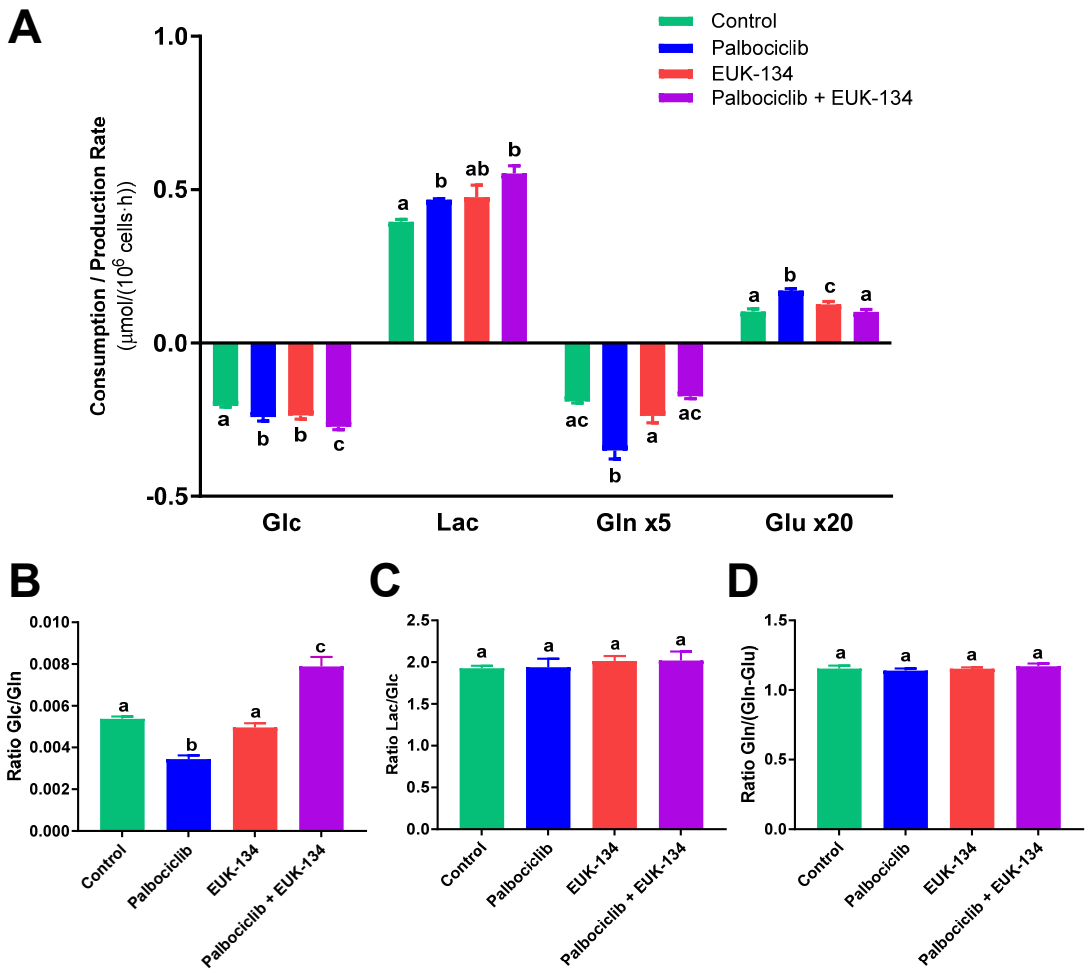

Figure 3.3.21. Palbociclib and EUK-134 effect over glycolysis and glutaminolysis in SW620 cells. A) Extracellular consumption rate of glucose and glutamine, and production rates of lactate and glutamate measured in SW620 cells treated for 96 h with vehicle (Control), Palbociclib (10 nM), EUK-134 (2.5 µM), or their combination. B-D. Ratios indicating B) the glucose with respect to glutamine utilization, C) the lactate production with respect to glucose consumption, and D) glutamine consumption with respect to glutamine not committed to glutamate production. An independent One-way ANOVA test was applied for relative comparison between groups, where different letter indicates significant differences ($p < 0.05$).

3.3.2.7. Palbociclib and EUK-134 combination treatment exhibit promising results in NOD/SCID mice xenotransplants.

The combination of Palbociclib and EUK-134 represents a promising strategy to address Palbociclib resistance in SW620 cells, impairing cell proliferation and reverting the metabolic adaptation to Palbociclib monotherapy. Therefore, we explored the potential impairment of tumor proliferation in a more intricate research model, by monitoring the effects of Palbociclib and EUK-134 combination treatment for 15 days in NOD/SCID mice bearing subcutaneous SW620 xenografts (**Figure 3.3.22.**).

The results demonstrated a significant reduction in tumor proliferation when the combination of Palbociclib and EUK-134 treatment was administered. This reduction had a great impact on tumor growth, which correlates with a significant decrease in tumor weight and volume. These findings suggest that Palbociclib in combination with EUK-134 is an effective therapeutic approach for restoring Palbociclib sensitivity that proves efficacy in studies *in vivo*.

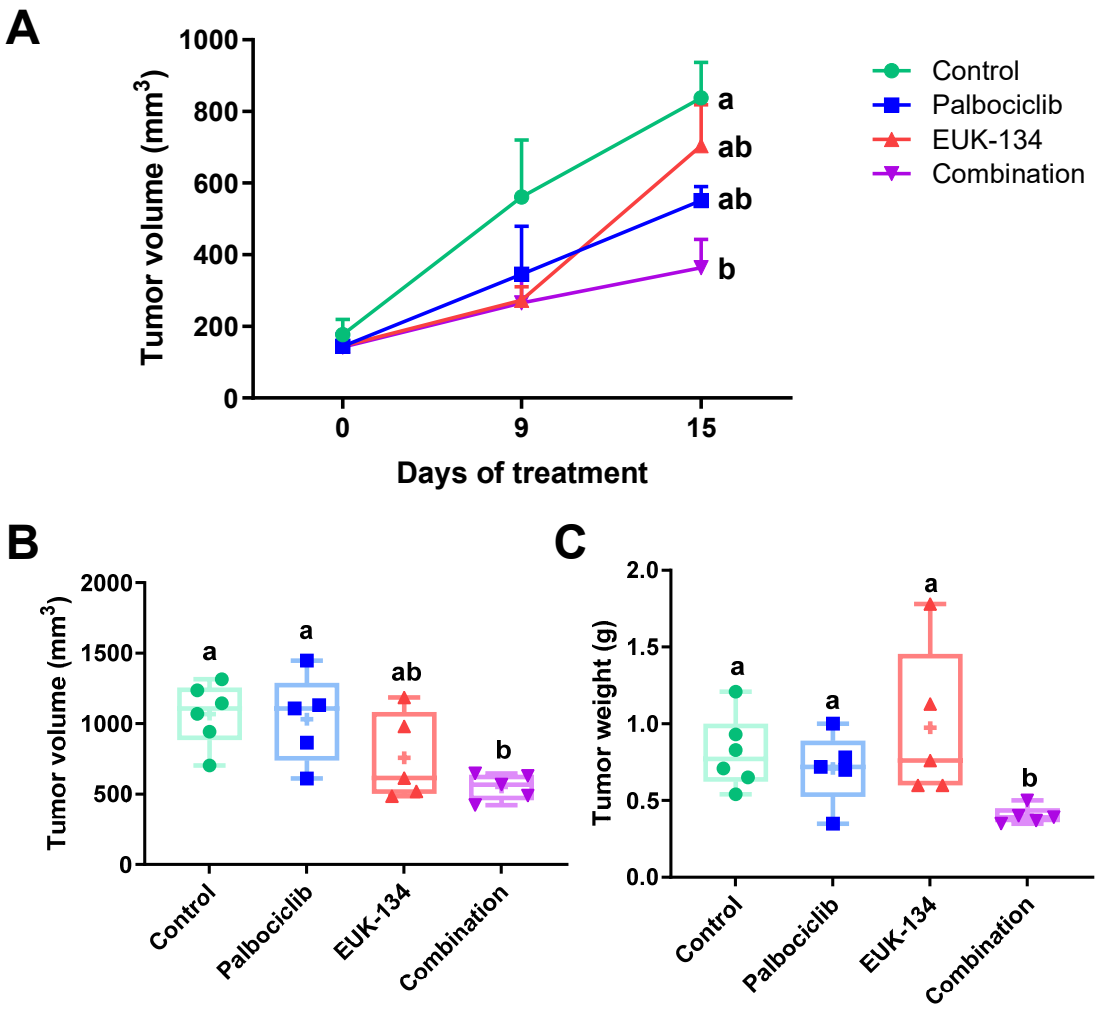

Figure 3.3.22. *In vivo* response of Palbociclib and EUK-134 combined therapy in NOD/SCID mice bearing subcutaneous SW620 xenografts. 10^6 SW620 cells were subcutaneously inoculated into 5-week-old NOD/SCID mice and tumors were grown for 15 days before starting with the treatments. Mice were administered with Vehicle, Palbociclib (25 mg/kg/day) EUK-134 (30 mg/kg/day), or their Combination by oral gavage was administered for 5 days each week, for a total of 3 weeks. A) Tumor volume evolution measured on days 0, 9, and 15 since treatment initiation. B) Tumor volume and C) tumor weight measured on tumor extraction on day 18 since treatment initiation (day 0). An independent One-way ANOVA test was applied for relative comparison between groups, where different letter indicates significant differences ($p < 0.05$).

3.3.2.8. Palbociclib and EUK-134 combination treatment exhibit promising results in primary tumor colorectal cancer cell line HCT116.

We next tested the promising combination of Palbociclib and EUK-134 in the primary tumor colorectal cell line HCT116, whose metabolic response upon 96 h of CDK4/6 depletion was already characterized by Tarrado-Castellarnau et al. (Tarrado-Castellarnau et al., 2017). They found that CDK4/6 inhibition enhances mitochondrial function in HCT116, presenting increased reliance on glutamine and amino acid metabolisms after 96 h of treatment, which is in agreement with our results in SW620 cells. Therefore, we evaluated the cell proliferation after 96 h of incubation with Palbociclib and EUK-134 combination in HCT116 cells. Results assessed in the primary tumor colorectal cell line model displayed a synergic effect when the combination was compared to the treatments alone (**Figure 3.3.23.**).

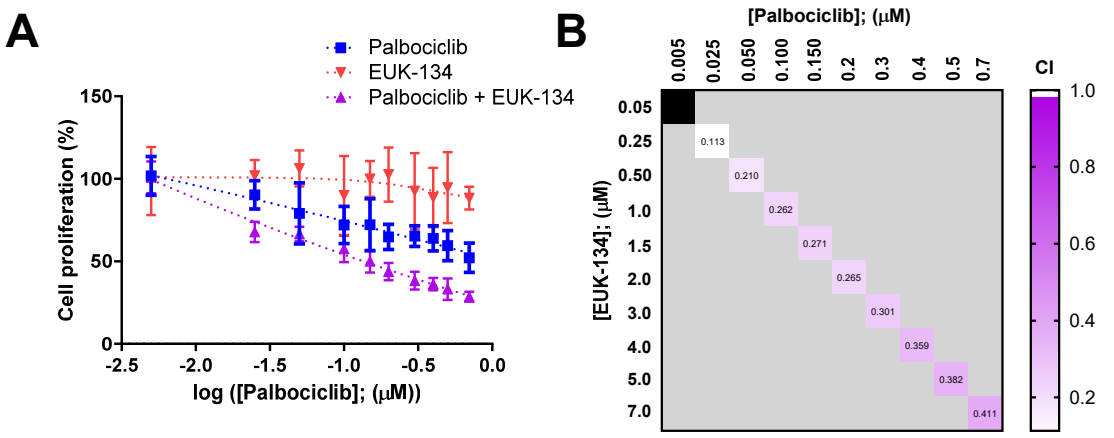

Figure 3.3.23. Palbociclib and EUK-134 effect in the primary colorectal HCT116 cells. A) **C**ell proliferation curves in the HCT116 cell line after 96 h of treatment at increasing concentrations with Palbociclib and EUK-134 alone or in combination with a constant ratio, (Palbociclib:EUK-134) [1:10]. B) Combination index (CI) value calculated with Compusyn software and Chou-Talalay method (black squares represent CI values > 1).

In summary, our findings indicate that the Palbociclib and EUK-134 combination displays promising results in a different colorectal cancer cell line with a similar metabolic reprogramming to CDK4/6 inhibition despite bearing different mutational burden (Ahmed et al., 2013). Therefore, these results demonstrate a successful approach that expands the potential of the application of this combined treatment across different colorectal cancer models, proving its capacity to sensitize tumor cells to Palbociclib treatment.

3.3.3. Discussion.

Palbociclib treatment has proven to induce important metabolic changes in other studies (Cretella et al., 2018, Franco et al., 2016) including primary tumor colorectal cells (Tarrado-Castellarnau et al., 2017), which exhibit metabolic vulnerabilities that can be addressed through combination therapies. In this work, we aimed to unveil metabolic reprogramming underlying Palbociclib treatment using the KRAS+ SW620 cell line, as the rational design to unveil combination therapies that lead to promising alternative therapeutic strategies to tackle Palbociclib resistance and tumor recurrence in the most advanced stage of colorectal cancer.

Cell growth impairment after CDK4/6 inhibitors treatment is observed in various cancer types (Franco et al., 2016, Goel & Bergholz et al., 2022, Goel et al., 2017, Tarrado-Castellarnanu et al., 2017, Tien & Sadar, 2022, Wang et al., 2022). This impairment is frequently associated with cell cycle arrest in the G1/G0 phase, preventing cell cycle progression (Cretella et al., 2018, Goel et al., 2017, Tarrado-Castellarnau et al., 2017, Whittaker et al., 2017). Cell cycle arrest mechanisms include a decrease in the proliferation rate of cancer cells, promoting cell cycle exit, either allowing cells to eventually re-enter the cell cycle and continue proliferating, staying in a quiescent state, or resulting in an irreversible state by promoting senescence or apoptosis (Matthews et al., 2022). Our results after Palbociclib treatment in SW620 metastatic colorectal cancer cells demonstrate a significant percentage of cells arrested in the G1/G0 phase, in agreement with reported studies (Franco et al., 2016, Goel & Bergholz et al., 2022, Goel et al., 2017, Tarrado-Castellarnanu et al., 2017, Tien & Sadar, 2022, Wang et al., 2022),

proving the effectiveness of Palbociclib treatment also in the advanced stage of the disease. However, it's worth noting that our results reveal only a moderate increase in apoptotic response upon Palbociclib treatment, suggesting that other mechanisms must be involved in the reported reduction of cell proliferation. In this regard, a significant percentage of cells are able to evade cell cycle arrest and continue proliferating while rewiring their metabolism to adapt to Palbociclib treatment.

This metabolic reprogramming includes a significant alteration in fatty acid and lipid metabolism, evidenced by differential expression results, GSEA, and intracellular lipid profiling. The alteration in lipid profiling after Palbociclib treatment is in agreement with other studies in the restructuration of sphingolipid composition induced by Palbociclib is associated with an important role in cell signaling modulation controlling cell survival or apoptotic response (Ogretmen, 2018). Our findings point to the existence of a dynamic balance in lipid metabolism, shifting fatty acid synthesis (FAS) and oxidation (FAO). The simultaneous activation of these pathways has been reported as a futile cycle in cancer cells that serves as an important ATP and NAD(P)H source upon fatty acid catabolism while triggering signaling pathways to modulate cell homeostasis and promote lipogenesis to meet the rapidly dividing cell requirements (Melone & Valentin et al. 2018). Furthermore, has been reported that drug resistance acquisition to Palbociclib in breast cancer is mediated by altered lipid metabolism and also is correlated to the hyperactivation of the PI3K/AKT/mTOR signaling pathway (Feng & Kurokawa, 2020), which has also been observed to contribute to the metabolic reprogramming of Palbociclib-resistant cells in different cancer types (Bonelli et al., 2017, Cretella et al., 2018, Franco et al., 2016, Tarrado-Castellarnau et al., 2017, Lorito et al., 2020).

Moreover, our results reveal a significant increment in OCR-related parameters such as basal and maximal respiration or spare respiration capacity, indicating an improved capacity to meet elevated energy and oxygen demands as well as metabolic flexibility after Palbociclib treatment. This increment in the mitochondrial function also leads to a significant production of ROS, which are accumulated after Palbociclib treatment. A recent study reported an increase in OxPhos dependence, accompanied by heightened TCA cycle, glutathione synthesis, and purine/pyrimidine metabolism, fueled by FAO on estrogen receptor-positive (ER+) breast cancers resistant to Palbociclib (El-Botty et al., 2023). The metabolic shift towards OxPhos is further evidenced in our work by a significant increase in glutamine consumption after Palbociclib treatment. Increased glutamine metabolism is associated with non-essential amino acid synthesis, TCA cycle replenishment, and redox homeostasis (Yoo, Yu & Sung et al., 2020). Our findings demonstrated an increased production of NEAAs following Palbociclib treatment in SW620 cells that might be correlated to altered one-carbon metabolism, the activity of some enzymes comprised in the Urea cycle, and polyamine synthesis. Increased glutamine dependence is a common signature in drug resistance observed in cancer cells (Yoo, Yu & Sung et al., 2020), which, together with increased mitochondrial metabolism, has been reported in colon, pancreatic, and lung cancer after CDK4/6 inhibition (Conroy et al., 2020, Franco et al., 2016, Tarrado-Castellarnau et al., 2017).

Our investigations also indicate a substantial decrease in the intracellular concentration of essential amino acids. Interestingly, BCAAs serve as alternative sources fueling the TCA cycle by generating succinyl-CoA and acetyl-CoA for further oxidation and lipogenesis (Lieu et al., 2020, Stine et al., 2022), also evidenced in a recent study

conducted by El-Botty et al., in which BCAAa replenish the TCA cycle contributing to ATP production following OxPhos is inhibition (El-Botty et al., 2023). Furthermore, increased carbon source requirements agree with decreased glycolytic function for ATP production. The glucose consumption remained constant after treatment while some important genes were found downregulated, suggesting a glycolytic flux impairment after Palbociclib treatment. Surprisingly, our results indicate that the effect on glycolysis is dependent on Palbociclib dose, since treatment with Palbociclib at low concentration enhanced glucose consumption. Observations made by Cretella et al. in Triple Negative Breast Cancer (TNBC) determine an inhibitory effect on glucose metabolism after Palbociclib treatment (Cretella et al., 2018), while in the study performed by Lorito et al., ER+ breast cancer cells achieve different degrees of glucose dependence based on human epidermal growth factor receptor 2 (HER2) presence, and Franco et al., and Tarrado-Castellarnau et al, reported increased glucose consumption rates after CDK4/6 inhibition (Franco et al., 2016, Tarrado-Castellarnau et al., 2017). Therefore, the metabolic response to Palbociclib treatment regarding glucose utilization varies depending on the model of study.

The significant increase in mitochondrial respiration, mitochondrial ATP production and TCA cycle anaplerosis after Palbociclib treatment, makes mitochondrial metabolism an attractive metabolic vulnerability that has been successfully addressed targeting oxidative phosphorylation through inhibition by VLX600 in SW620 cells, in agreement with previous results obtained following Palbociclib treatment in the PC-3 cells (**Section 3.2.**). The prevalent reliance on OxPhos has been reported in many types of aggressive cancer (Ashton et al., 2018, El-Botty et al., 2023). The excessive ROS production and relatively low apoptotic response suggest that these cells might improve cellular stress tolerance after Palbociclib treatment preventing cell death, and/or excessive ROS associated with increased mitochondrial metabolism might be playing a pivotal role underlying Palbociclib metabolic reprogramming, since it is described that ROS mediates different aspects of cell fate including diverse signaling pathways, metabolic reprogramming and cell death (Cheung & Vousden, 2022, Panieri & Santoro, 2016). Therefore, these results offer an interesting alternative combination treatment targeting ROS balance. Our findings demonstrate a significant impact on cell proliferation after EUK-134 treatment, a SOD-mimetic, in combination with Palbociclib in SW620 cells.

EUK-134 is known as SOD-mimetic with catalase activity, reported to mitigate oxidative stress and ameliorate neurotoxicity effects in different models (Decraene & Smaers 2004, Pong 2001, Rosenthal 2011, Shah 2015, Vincent et al., 2021). These beneficial effects displayed across different scenarios, make EUK-134 and Palbociclib combination an interesting strategy to address adaptation to Palbociclib in metastatic colorectal cells. Further exploration regarding the combination mechanisms to impair cell proliferation revealed that EUK-134 treatment reverts Palbociclib-induced metabolic adaptation by impairing mitochondrial function and promoting significant alterations in cellular metabolism, energy production, and cell survival. Our results indicate that the mitochondrial depletion promoted by EUK-134, when combined with Palbociclib promotes an increased demand for glucose consumption and utilization that is not fueling the TCA cycle but producing lactate from glycolysis. Supporting these findings, Zhang et al., reported mitochondrial dysfunction in colon cancer cells after treatment with the oxidative phosphorylation inhibitor VLX600 (Zhang et al., 2017). Since we reported that VLX600 displays synergism in combination with Palbociclib, mitochondrial dysfunction

may be the mechanism responsible for cell proliferation impairment after this combination treatment. On the other hand, ATN-224 inhibits SOD1, impairing superoxide scavenging in the cytosol and ETC (Che et al., 2016, Juarez et al., 2016) but does not affect cytochrome c oxidase function as demonstrated by Juarez et al., despite being a cupper chelator. SOD1 and SOD2 enzymes, despite presenting different functions and subcellular locations, may compensate for each other's depletion (Che et al., 2016), which may explain the lack of synergism of ATN-224 with Palbociclib. Also, the major product of SOD, H_2O_2, acts as a secondary messenger in metabolic processes and entails signaling functions in cancer cells (Boonstra & Post, 2004, Che et al., 2016), as well as the cytochrome c oxidase, whose target genes are also closely related to signaling events in cancer cells (Nývltová et al., 2022, Douiev et al., 2018). Therefore, we hypothesize that both the alteration in H_2O_2 balance and mitochondrial impairment are the mechanisms by which EUK-134 exerts the antiproliferative effect in Palbociclib-resistant cells in SW620 cells.

Alternatively, Palbociclib and EUK-134 combination restored cell cycle progression while reducing cell proliferation and increasing the apoptotic response compared to control cells. It has been reported that ROS modulation can also interfere with cell cycle progression via ubiquitination and phosphorylation (Boonstra & Post, 2004). ROS signaling is required to regulate cyclin D1 expression and induce cell cycle after quiescence state (Burch & Heintz, 2005), influencing the activation of essential proteins for the G1 to S phase and cell cycle progression (Menon et al., 2003). It also modulates the activity of CDK2 (Kirova et al., 2022), and additionally, higher cellular respiration, ROS levels, superoxide species, OxPhos, ATP production, and mitochondrial function are associated with an upregulation of CyclinB1/CDK1, which is essential for the G2/M transition (Wang & Fan et al., 2014). A study on human pluripotent cells demonstrated that ROS levels fluctuate throughout the cell cycle progression, reaching their peak during the S to G2/M transition (Ivanova et al., 2021). In correlation, colon cancer cells exhibit a higher dependence on mitochondrial respiration for ATP production during this G2/M phase (Bao et al., 2013). However, excessive or prolonged ROS exposure promote DNA damage, might induce cell cycle arrest, and ultimately lead to cell death (Boonstra & Post, 2004). Collectively, these studies indicate a crosstalk between ROS balance, cell metabolism, and cell cycle progression, since mechanisms regulating phase transition during the cell cycle also alter tumor metabolism (Fajas, 2013, Wang et al., 2022, Wu & Zhang et al., 2019). Hence, there is a possible connection between ROS modulation and EUK-134 treatment, that may contribute to the mechanism of action behind this successful therapeutic strategy, since our results reveal that EUK-134 treatment prevents the adaptation of cancer cells to Palbociclib by impairing their metabolic reprogramming and flexibility, altering cell cycle regulation, and compromising cell survival through interference in ROS-mediated processes.

Moreover, the promising results achieved with this combination in SW620 cells were replicated *in vivo* in immunodeficient NOD/SCID mice and *in vitro* in the primary tumor colorectal cell line HCT116, bearing different type of KRAS mutation ($KRAS^{G13D}$) and being a microsatellite instability (MSI) cell line, confirming that this combined treatment significantly compromised tumor progression and cell proliferation by overcoming Palbociclib adaptive resistance in different models, accounting for genetic heterogeneity and disease stage.

3.3.4. Materials and methods.

3.3.4.1. Cell culture.

The human metastatic colorectal SW620 (ATCC, Rockville, MD, USA) cell line isolated from the large intestine of a 51-year-old male Dukes C colorectal cancer patient, was cultured in Dulbecco's Modified Eagle Medium (DMEM) (Gibco, Thermo Fisher Scientific, MA, USA) containing 4 mM L-glutamine and supplemented with 12.5 mM D-glucose (Merck Life Sciences, Germany), 5% Fetal Bovine Serum (FBS, 10270-106, Lot. 2058474, Gibco), and 1% Penicillin-Streptomycin (10.000 U/ml, Gibco). The human colorectal carcinoma HCT116 cell line (ATCC) established from a primary tumor of a 54-year-old male patient was cultured in DMEM (Gibco) and Nutrient mixture HAM F12 (L0136-500, DDBIOLAB, Dutscher, France) (DMEM/F12, 1:1 mixture) supplemented with L-glutamine, 12.5 mM D-glucose, 10% FBS (10270-106, Lot. 2058474, Gibco) and 0.5% Penicillin-Streptomycin (10.000 U/ml, Gibco).

3.3.4.2. Cell proliferation.

SW620 cells were plated in 96-, 24-, or 6-well plates (seeding 2.3×10^3/well, 1.37×10^4/well, and 7×10^4/well respectively) and treated for 96 h with the specific treatments. HCT116 cells were plated in 96-well plates (seeding 1.5×10^3/well) and treated for 96h with the specific treatments Cell proliferation tests were assessed through manual counting using 0.2% Trypan Blue staining (Merck Life Sciences) and a Neubauer Chamber (Thermo Fisher Scientific) or automated counting using Countess II FL (Thermo Fisher Scientific). Additionally, indirect proliferation techniques were utilized with the fluorescent staining method Hoechst, using 4 µg/ml of bisBenzimide H 33342 trihydrochloride probe (Merck Life Sciences) in Hoechst stain buffer (1 M NaCl, 1 mM EDTA, 10 mM Tris pH 7.4) and measuring emitted fluorescence (460 nm) in a fluorescence plate reader (FLUOstar OPTIMA Microplate Reader, BMG LABTECH GmbH, Germany), and the CellTiter-Glo luminescent cell viability assay kit (Promega Corporation, Madison, Wi) to quantify the ATP by measuring the luminescent signal (550 nm) in a luminescent plate reader Mithras LB 940 (Berthold Technologies, Switzerland).

Data were analyzed through dose-response curves with GraphPad Prism 9 (GraphPad Software, San Diego, CA, USA). Synergy analysis and quantification was performed using the CompuSyn software (Version 1.0) (ComboSyn, Inc., NJ, USA) and the Chou-Talalay method (Chou, 2010), based on the combination index (CI) where the combination displays synergistic (CI < 1), additive (CI = 1), or antagonist effect (CI > 1). The duplication time was determined by assessing the cell growth at different time points and applying the exponential growth equation:

$$Ln\left(\frac{N_f}{N_0}\right) = \mu \cdot t$$

where,

N_f is the number of final cells (million cells)

N_0 is the number of initial cells (million cells)

μ is the growth rate (h^{-1})

t is the time (h)

Assuming active proliferation, where cells undergo division, holding the following assumption $N_f = 2N_0$. The duplication time was calculated from the final equation:

$$\frac{Ln2}{\mu} = t$$

3.3.4.3. Chemicals and reagents.

Palbociclib was purchased from Selleckchem (Houston, TX, USA), Tigecycline from APExBIO (Houston, TX, USA), VLX600 from Cayman Chemical (Ann Arbor, MI, USA), ATN-224 from TargetMol (Boston, MA, USA), and EUK-134 from Merck Life Sciences.

3.3.4.4. Cell cycle analysis.

Cells were collected, fixed in cold 70% ethanol, and kept overnight at 4 °C. Cellular suspension was incubated for 1 h at 37 ºC with 0.2 mg/ml RNase (Roche Holding AG, Switzerland) in PBS. Propidium Iodide (PI) (MilliporeSigma, MA, USA) was added in a final concentration of 40 µg/ml minutes before the analysis in flow cytometry. The samples were measured by flow cytometry using Gallios™ Flow Cytometer (Beckman Coulter, CA, USA), and the results were analyzed using FlowJo version 7.6.1. and Mycycle software histograms were utilized to discern cell cycle phases by segregating populations based on their DNA content, where 2n and 4n represent G1/G0 and G2/M, respectively.

3.3.4.5. Apoptosis analysis.

Adherent and floating cells in the medium were collected and incubated with Annexin V coupled with FITC, following the kit's instructions (Bender System MedSystem, Viena, Austria) for 30 minutes in binding buffer (10 mM Hepes/NaOH, pH 7.4, 140 mM NaCl, 2.5 mM $CaCl_2$). Propidium Iodide (PI) (MilliporeSigma) was added at the final concentration of 20 µg/ml minutes for the analysis in flow cytometry. The samples were measured by flow cytometry using Gallios™ Flow Cytometer (Beckman Coulter), and the results were analyzed using FlowJo version 7.6.1. This analysis revealed percentages of alive cells, cells presenting early apoptosis, and late apoptosis or necrosis.

3.3.4.6. RNA extraction.

RNA purification was carried out using the Qiagen RNeasy kit (Qiagen, Hilden, Germany). Each sample provided 200 ng of total RNA in 50 µl of RNase–free water. Global transcriptomic profiling was accomplished through next-generation sequencing (NGS) of total RNA (see **Appendix II, Section II.1.** for further details of NGS experiments).

3.3.4.7. Transcriptomic pathway visualization.

Differentially expressed genes identified based on adjusted p-values < 0.05 following treatment were integrated and visualized in specific metabolic pathways using the Pathview software tool (Luo et al., 2017, Luo et al., 2013). This approach allowed the

effective mapping and interpretation of the significant changes in gene expression within the context of metabolic pathways.

3.3.4.8. Respiratory assays.

After 24 hours of treatment, SW620 cells were plated in XFe96-, or XFe24-well plates (seeding 4.04 × 10^4/well, and 1× 10^5/well, respectively), and incubated with the treatment for 24 hours to perform a total treatment of 96 hours. The Agilent Seahorse XF Cell Mito Stress Test was assessed following protocol instructions, measuring Oxygen Consumption and Extracellular Acidification Rates (OCR/ECAR) using a Seahorse XFe24 Analyzer (Agilent, Seahorse Bioscience, North Billerica, MA, USA) in the presence of metabolic substrates targeting different Electron Transport Chain (ETC) components at the following final concentrations; 1.5 µM of Oligomycin (ATP synthase (complex V)), 600 nM of CCCP (Inner mitochondrial membrane), and 2 µM of Rotenone + 2 µM of Antimycin A (Complex I and III, respectively) (Mito Stress test parameters are detailed in **Appendix III**). The final values were normalized by cell count, determined through automated counting using the Countess II FL Cell Counter (Thermo Fisher Scientific) in the case of XFe24 plates or by measuring DNA content following fixation with 4% formaldehyde and DAPI probe measurement using the CellInsight CX7 platform (Thermo Fisher Scientific) in the case of XFe96 plates.

3.3.4.9. Reactive Oxygen Species (ROS) analysis.

Reactive Oxygen Species (ROS) quantification was determined with two different probes depending on the detectable ROS type.

3.3.4.9.1. Intracellular total ROS.

Cells were seeded in 6-well plates (seeding 5 × 10^4/well) and administered with treatment or vehicle for 96h. Then, cells were incubated for 30 minutes with 5 µM of H2DCFDA probe (MilliporeSigma). After a quick trypsinization process (30 seconds), cells are collected and resuspended with 50 µM of H2DCFDA probe and 20µg/ml of Propidium Iodide (PI) (MilliporeSigma). The fluorescence intensity proportional to H2DCFDA oxidated by all ROS were measured through Gallios™ Flow Cytometer (Beckman Coulter) and the results were analyzed using FlowJo version 7.6.1. Relative ROS levels were normalized with respect to the non-treated condition.

3.3.4.9.2. Intracellular mitochondrial superoxide species.

Cells were incubated according to the instructions specified in the MitoSOX kit (Invitrogen, Paisley, UK), a red mitochondrial superoxide ($\cdot O_2^-$) species indicator. Relative intensity levels were measured through Gallios™ Flow Cytometer (Beckman Coulter) and the results were analyzed using FlowJo version 7.6.1. Relative ROS levels were normalized with respect to non-treated the condition.

3.3.4.10. Metabolic experiments.

3.3.4.10.1. Quantification of extracellular metabolites using spectrophotometric enzymatic assays.

The consumption and production rates of glucose, glutamine, lactate, and glutamate were determined by assessing their concentrations in the extracellular media at different time points and comparing the final to the initial concentrations. Concentrations in the extracellular media were measured using a COBAS Mira Plus (Horiba ABX, France) automated spectrophotometric analyzer based on the measurable concentration of coenzyme NADH at 340 nm. For D-glucose, measurements involved two consecutive reactions: hexokinase, followed by D-glucose-6-phosphate dehydrogenase (G6PD), producing 6-phosphogluconate and NADH. Lactate concentrations were determined by employing lactate dehydrogenase (LDH). Measurements were conducted under pH=9 conditions in the presence of hydrazine to shift the reaction toward pyruvate and NADH formation, effectively preventing the reversible reaction. Glutamate concentrations were measured after α-ketoglutarate conversion and NADH production by glutamate dehydrogenase (GLUD1), while glutamine was indirectly measured using the same method after glutamate conversion through glutaminase (GLS) reaction.

The calculation of the consumption/production rate for each metabolite was based on assuming exponential growth, with a constant growth rate during the incubation period. The results were subsequently normalized by the number of cells and expressed as a rate (μmol/(10^6 cell·h).

$$Consumption/production\ rate\ = \left(\frac{\Delta M}{\Delta N}\right) \cdot \mu$$

where,

$\Delta M = M_f - M_0$ is the consumed/produced amount of each metabolite (μmol).

$\Delta N = N_f - N_0$ is the cell growth during the incubation time (million cells).

$\mu = Ln(N_f/N_0)/t$ is the growth rate constant (h^{-1}) for exponential growth.

3.3.4.10.2. Mass spectrometry-based targeted metabolomics.

The metabolite profile was quantified using the Absolute IDQ p180 kit (20714, Biocrates Life Sciences AG, Innsbruck, Austria). This kit measures 180 endogenous metabolites across seven compound classes, including acylcarnitines, amino acids, biogenic amines, monosaccharides, phosphatidylcholines, and sphingolipids. The analysis of these small molecules and lipids was carried out using tandem mass spectrometry coupled with liquid chromatography (LC/MS/MS) on the MS/MS Sciex Triple Quad 6500 instrument (AB Sciex, Framingham, MA, USA). After quantification, extracellular concentrations were normalized and expressed as consumption/production rate (calculations detailed in section 3.3.4.10.1.), while intracellular concentrations were normalized based on cell protein content.

The obtained results were analyzed using the MetaboAnalyst 5.0 software (Pang et al., 2022), a comprehensive platform used for the statistical analysis of metabolomics data. This software offers a wide range of functions and tools, including the statistical methods employed in this study, such as heatmap analysis.

3.3.4.11. Protein extraction.

Protein extracts were obtained after 30 minutes of incubation with RIPA buffer (50mM Tris-HCl pH 8, 150mM NaCl, 1% Triton-X-100, 0.5% sodium deoxycholate, 0.1% SDS) supplemented with 1% phosphatase and protease cocktail inhibitors (MilliporeSigma), following the kit's instructions. Subsequently, cells were scraped and collected for quantification using the Pierce BCA Protein Assay Kit (Thermo Fisher Scientific).

3.3.4.12. *In vivo* study and ethics.

A total of 10^6 SW620 cells in Matrigel (Fisher Scientific Waltham, MA, USA) were subcutaneously inoculated into 5-week-old NOD/SCID mice (strain: NOD.CB17-Prkdcscid/NCrHsd; West Lafayette, IN, USA) and tumors were grown for 15 days before starting with the treatments. Mice were administered with Vehicle (50 mM Sodium lactate buffer at pH 4), Palbociclib (25 mg/kg/day), EUK-134 (30 mg/kg/day), or their combination by oral gavage for 5 days each week, for a total of 3 weeks. Tumor volume evolution was monitored during the experiment and measured with a caliper on days 0, 9, and 15 since treatment initiation. Tumor volume and weight were measured on tumor extraction. This study protocol was approved by the Animal Experimentation Ethics Committee (CEEA) at the Department of Territory and Sustainability of the Generalitat de Catalunya. All procedures were conducted through an external service at the animal facility affiliated with the University of Barcelona located at the Bellvitge Hospital.

3.3.4.13. Statistical analysis.

Statistical analysis was performed using jamovi software (Version 2.2) (The jamovi project, 2021). Group comparisons were evaluated using independent t-tests for pairwise comparisons and one-way analysis of variance (ANOVA) for multiple groups, ensuring that the data met the assumptions of normality. The homogeneity of variances was assessed through Levene's test. When the assumption of homogeneity of variances was violated, Welch's correction was

applied. Additionally, when the data did not meet the assumption of normality, the Mann-Whitney U test was employed, and the non-parametric Kruskall-Wallis test was applied for Dwass-Steel-Critchlow-Fligner (DSCF) pairwise comparisons for multiple group comparisons. A significance level of $p < 0.05$ was used to determine statistical significance. Standard deviation was employed as a measure of dispersion in all statistical analyses unless otherwise specified.

4.

GENERAL DISCUSSION

4. GENERAL DISCUSSION

Colorectal and prostate cancer are among the most prevalent malignancies worldwide and constitute a significant cause of recurrence and mortality (Ferlay et al., 2020, Halabi et al., 2014). In the recent years, the emergence of resistance acquisition to standard therapies has led to the exploration of novel treatment strategies. This represents a formidable challenge for patients diagnosed with recurrent or *de novo* metastatic cancer who, regardless of the type of cancer, will pass away in five years (Ganesh & Massagué 2021). Genetic and epigenetic changes promoted by cancer therapy are heterogenic and therefore difficult to address. However, these events usually converge downstream in metabolic pathway alterations, whose impairment is a therapeutic opportunity to prevent the development of resistant phenotypes (Cruz-Bermúdez et al. 2019). For instance, Cruz-Bermúdez et al studied how Cisplatin-resistant non-small cell lung cancer (NSCLC) cells may result from a selection process after short-term Cisplatin treatment, supporting the idea of metabolic adaptations contributing to cell survival and the generation of long-resistant cell populations. In fact, metabolic reprogramming is considered a hallmark of cancer (Hanahan, 2022, Hanahan & Weinberg, 2011) that enables tumor cells to fulfill metabolic and energetic requirements for tumor survival and progression (Pavlova & Thompson, 2016). Therefore, metabolic reprogramming is a crucial contributor to any type of adaptative process, such as cancer initiation, metastatic progression, and drug resistance (La Vecchia & Sebastián, 2020). The study of the metabolic supporters contributing to drug resistance provides a therapeutic window to tackle the adaptation of cancer cells to chemotherapy through combination treatments, as has been demonstrated across many studies and cancer types (extensively reviewed in Seth Nanda et al., 2020, Stine et al., 2022).

In this work, we focus on the study of Oxaliplatin, a platinum-based chemotherapeutic agent that induces DNA damage and impairs DNA synthesis in rapidly dividing cells (Di Francesco et al., 2002, Huang et al., 2016, Kang et al., 2015, Kline & El-Deiry, 2013, Monneret, 2011). Oxaliplatin is an integral component of chemotherapeutic regimens applied in solid tumors (Meriggi & Zaniboni, 2010, Van Cutsem et al., 2016), and it is gaining attention for applications in prostate cancer (Lee et al., 2014, Marzo et al., 2022, Zhou et al., 2017), and Palbociclib, a cyclin-dependent kinase 4 and 6 (CDK4/6) inhibitor that prevents cell cycle proliferation by arresting cells in the pre-replicative phase of the cell cycle (Matthews et al., 2022), which exhibits effectiveness in several solid tumors (Goel et al., 2017, Goel & Bergholz et al., 2022, Otto & Sicinski, 2017, Schettini et al., 2018, Sorah et al., 2022, Zhang et al., 2017). Consequently, both Oxaliplatin and Palbociclib represent effective therapeutic anticancer molecules approved for their clinical use by the Food and Drug Administration (FDA) and authorized in the European Union. However, their use frequently leads to drug resistance and requires the development of rational combination therapies (Chen & Gong et al., 2022, Knudsen & Witkiewicz, 2017, Monneret, 2011, O'Leary et al., 2018, Rottenberg et al., 2021). Palbociclib, notably induces substantial metabolic alterations, as reported in several studies in breast, colon, pancreatic, and pleura cancer cells (Bonelli et al., 2017, Cretella et al., 2018, Franco et al., 2016, Tarrado-Castellarnau et al., 2017), activating PI3K/AKT/mTOR signaling, increasing glutamine dependence and mitochondrial metabolism. These metabolic adaptations represent vulnerabilities that can be targeted through therapeutic interventions. On the other hand, despite metabolic insights regarding Oxaliplatin-induced metabolism reprogramming that require further

elucidation, some studies obtained successful synergisms and sensitized cells to Oxaliplatin by targeting newly acquired metabolic vulnerabilities in colorectal and hepatocellular carcinoma cells (Li et al., 2021, Lin et al., 2022, Xu et al., 2020).

Our aim was to characterize the metabolic reprogramming underlying short-term treatment with either Oxaliplatin or Palbociclib in the most advanced stage of colorectal and prostate cancer. Colorectal cancer presents diverse genetic profiles, being metastatic tumors often the ones with the worst prognosis (Sveen et al., 2017, Van Cutsem et al., 2016), we selected the SW620 cell line, which harbors the KRAS mutation that is related to cell growth, differentiation, and survival, to represent one of the most aggressive variants of colorectal cancer (Huang, 2021, Luo & Song et al., 2022). On the other hand, prostate cancer is characterized by significant genetic heterogeneity and in the most advanced stage of the disease, tumors can progress even with androgen receptor (AR)-independent signaling, displaying continuous division, and thereby representing a major therapeutic challenge (Rebello & Oing et al., 2021). Considering this, we chose the established human PC-3 cell line to represent the most aggressive prostate cancer type (Germain & Lafront et al., 2023).

Comparing both cell lines, we found that SW620 cell line exhibited a greater sensitivity to both drugs, in agreement with other studies (Gaur et al., 2014, Yang et al., 2013). Our results determined that short-time drug incubation triggered substantial metabolic changes capable of altering the metabolic landscape in both cell types, shifting the main metabolic fuels and changing the bioenergetic requirements. These results revealed some common traits in both cancer types after drug exposition such as an increased glutamine utilization. Increased glutamine dependence is frequently observed in many cancer types, while enhanced glutamine use has been associated with drug resistance and explored in combinatory treatments as an interesting metabolic vulnerability, either by the inhibition of glutaminase (GLS) or glutamine transporters (Chen et al., 2021, Hudson et al., 2016, Tarrado-Castellarnau et al., 2017, Wang et al., 2015, Conroy et al., 2020). The increased glutamine uptake exhibited in cancer cells can be explained through its role serving as the primary carbon source for the tricarboxylic acid (TCA) cycle and the nitrogen source for protein, nucleotide, amino acid, and fatty acid synthesis (Yoo, Yu & Sung et al., 2020). Therefore, glutamine plays a pivotal role in providing metabolic flexibility for cell survival to cope with nutrient deprivation, increased energetic demands or replenishment of biosynthetic pathways, cell stress, and thus becoming essential in any adaptative process (Jin & Byun et al., 2023, Yoo, Yu & Sung et al., 2020). In this case, our findings indicated that greater glutamine utilization provides TCA cycle intermediates and non-essential amino acids, compensating for the NADPH depletion consequence of the glycolytic impairment after Oxaliplatin treatment, supports augmented oxidative phosphorylation (OxPhos) and TCA cycle in SW620 cells treated with Palbociclib, enhancing the mitochondrial function, and promotes reductive carboxylation for citrate production after Palbociclib treatment in the prostate cancer cells.

Beyond glutamine metabolism, urea cycle enzymes are found to be dysregulated after treatment with Oxaliplatin or Palbociclib. The urea cycle plays an important role in the detoxification of ammonia resulting from increased glutamine metabolism, also providing TCA intermediates, increasing the redirection of carbon and nitrogen to other biosynthetic routes such as one-carbon metabolism for nucleotide synthesis,

methylation, and redox homeostasis (Keshet et al., 2018, Newman & Maddocks, 2017), and boosting polyamine metabolism from ornithine, which is frequently dysregulated in cancer cells due to its involvement in cell signaling, antioxidant response, epigenetic regulation or apoptosis, thus sustaining rapid cell proliferation (Affronti et al., 2020, Casero & Stewart et al., 2018, Seth Nanda et al., 2020). Alternatively, glutamine-derived nitrogen can be recycled producing non-essential amino acids such as glutamate, proline, aspartate, and alanine in breast cancer cells (Spinelli et al., 2017), suggesting an alternative ammonium detoxification mechanism in cancer cells that could explain the eventual increment observed in these metabolites after Oxaliplatin or Palbociclib treatment.

Apart from shared metabolic responses, Palbociclib and Oxaliplatin promote different impacts on the overall metabolic landscape of the cell lines under study. The treatment with Oxaliplatin, both in PC-3 and SW620 cells, leads to significant perturbations in the whole cellular metabolism, in agreement with other platinum-resistant cancer cells (Cruz-Bermúdez et al., 2019, Tan & Li et al., 2022, Sriramkumar et al., 2022), resulting in a pronounced downregulation of numerous metabolic pathways. Conversely, Palbociclib induces a considerable enhancement of cellular metabolism, which is in agreement with the metabolic responses exerted in other cancer types (Cretella et al., 2018, Conroy et al., 2020, Franco et al., 2016, Lorito et al., 2020, Tarrado-Castellarnau et al., 2017), as evidenced by the upregulation of multiple gene set pathways after treatment, increasing demand for carbon and nitrogen sources, and improving mitochondrial metabolism in both cancer types.

In particular, the metabolic reprogramming in SW620 cells after Oxaliplatin treatment involves amino acid metabolism, and notably, glutamine catabolism as the major metabolic contributor to cell survival. Glutamine nourishes the TCA cycle and maintains mitochondrial function while stimulating polyamine synthesis for cell survival. Enhanced polyamine synthesis has previously been reported to prevent mitochondrial dysfunction and ROS-mediating apoptosis in neural stem cells (Sato et al., 2020). Furthermore, cancer cells require higher intracellular polyamine pools to maintain a high proliferative rate since they are involved in many cellular processes like gene regulation, cell death, and differentiation, and oncogenes such as *MYC, JUN, FOS, KRAS,* and *BRAF* that maintain these polyamine pools (Holbert et al., 2022) are frequently dysregulated in cancer cells after drug treatment, being involved in many metabolic processes (Dong et al., 2020, Hanahan & Weinberg, 2011). An example is the implication of MYC driving the metabolic reprogramming after Palbociclib treatment in HCT116 cells (Tarrado-Castellarnau et al., 2017). The cell line SW620 exhibits an induction of polyamine metabolism supported by *AMD1* and *ODC1* overexpression after Oxaliplatin treatment. Overexpression of these genes that encode rate-limiting enzymes of polyamine synthesis has also been observed in neuroblastoma cells (Hogarty et al., 2008) and associated with drug resistance in bladder cancer cells through MYC-mediating metabolic reprogramming (Zhu et al., 2022), as they are direct targets of *MYC* (Holbert et al., 2022). Hence, these findings suggest that MYC may be mediating the metabolic response after Oxaliplatin treatment in the colorectal cancer cell line.

Comparing the metabolic reprogramming after Oxaliplatin treatment in PC-3 and SW620 cells, our results demonstrated a different effect on the TCA cycle and fatty acid utilization, while sharing the notable glycolytic reduction. In this context, we hypothesize

that citrate might be involved in the TCA cycle, glycolysis, and fatty acid synthesis regulation, interfering in metabolic flexibility and adaptative responses (Porporato et al., 2018, Iacobazzi & Infantino, 2014, Williams & O'Neill, 2018). Prostate cancer cells treated with Oxaliplatin exhibit enhancement of fatty acid metabolism flux, fatty acid uptake through *CPT1C* overexpression, and mitochondrial respiration coupled with ATP production. Moreover, CS inhibition has been associated with enhanced production of aspartate and asparagine from OAA rather than further oxidation in the TCA cycle (Zhang et al., 2014). Increased fatty acid uptake and fatty acid oxidation (FAO) have been reported as a response for cell survival after glucose uptake impairment and oxidative stress induction in Cisplatin-resistant ovarian cancer cells (Tan & Li et al., 2022), and fatty acid uptake was also observed in pancreatic, lung, and breast cancer cell lines treated with Cisplatin in the same study reported by Tan & Li et al. However, SW620 cells exhibit *CS* and *PC* overexpression, indicating enhanced citrate production, and reduced overall β-oxidation activity. The distinct metabolic reprogramming observed in colorectal and prostate cancer cells after Oxaliplatin treatment may also be related to the induction of different processes for supplying the reducing potential required after the decrease in glucose utilization observed in both cancer types. Glycolytic depletion is frequently associated with a subsequent decrease in NADPH since an overall decrease in glycolysis reduces glucose flux to PPP, which is one of the main producers of NADPH in cancer cells (Ju & Lin et al., 2020). One-carbon and glutamine metabolisms in SW620 cells or FAO in prostate cancer cells are pathways reported to induce the antioxidant defense system for redox homeostasis in Oxaliplatin-treated gastric and colorectal cancer (Wang et al., 2020).

This glycolytic impairment following Oxaliplatin treatment observed in both types of cancer is in accordance with the metabolic impact reported after treatment with platinum compounds in other types of cancer such as NSCLC and ovarian cancer cell lines (Cruz-Bermúdez et al. 2019, Tan & Li et al., 2022). In this regard, we observed a decrease in the expression of the glycolytic orchestrator *PFKFB3* after short-term treatment with Oxaliplatin, which may drive the glycolytic decrease in SW620 and PC-3, as was observed in breast and endometrial cancer (O'Neal et al., 2016, Xiao et al., 2021).It is reported that *PFKFB3* also interacts with the cell cycle by direct interaction with CDK4, and the absence of this gene improves CDK4 inhibitors effectiveness in breast cancer cells (Jia et al., 2018). In this line, our findings demonstrate a synergism after Oxaliplatin and Palbociclib combination in both cell lines, SW620 and PC-3. These findings suggested that the different effects on cell cycle arrest induced by Oxaliplatin and Palbociclib may be responsible for the synergism observed. Indeed, Oxaliplatin-resistant cells exhibited cycle arrest in the G2/M phase in both cancer types, in agreement with cell cycle analysis in uterine and lung cancer cells after platinum treatment (Cruz-Bermúdez et al., 2019, Voland et al., 2006, William-Faltaos et al., 2007). On the contrary, Palbociclib induces cell cycle arrest in G1/G0. In the case of colorectal cancer cells, the synergism observed in Oxaliplatin treatment in combination with Cladribine, which is also reported to block the cell cycle in the G1/G0 phases (Ma et al., 2011, Xu & Jiao et al., 2020), suggests that this arrest is an alternative mechanism to nucleotide metabolism impairment to overcome Oxaliplatin resistance.

In the case of Palbociclib treatment, cell proliferation is effectively inhibited in metastatic prostate and colorectal cancer cells by blocking the cell cycle in the G1/G0 phase, in agreement with other studies in breast, pancreatic, and colorectal cancers (Cretella et

al., 2018, Franco et al., 2016, Goel et al., 2017, Tarrado-Castellarnau et al., 2017). In this regard, the absence of AR signaling in the PC-3 cell line may improve the effects of Palbociclib, since AR inhibition overcomes resistance to Palbociclib in breast cancer (Ji et al., 2019). Regarding the substantial metabolic alteration observed following Palbociclib treatment in both cell types, besides the augmented glutamine utilization, cells exhibit great reliability in mitochondrial metabolism and oxidative phosphorylation for cell survival. All the respiratory parameters, including basal oxygen consumption rate (OCR), ATP production, spare respiratory capacity, and maximum respiration, are enhanced and indicate improved metabolic flexibility and mitochondrial function associated with a Palbociclib-adaptive phenotype. The shift toward OxPhos as the primary energy source has been observed in several cancer types through mTOR signaling induction after Palbociclib treatment or CDK4/6 inhibition (Bonelli et al., 2017, Cretella et al., 2018, Franco et al., 2016, Tarrado-Castellarnau et al., 2017), increasing the overall central metabolism, including glycolysis, glutaminolysis, and, in turn, mitochondrial metabolism.

Prostate cancer cells induce core metabolic pathways after Palbociclib treatment, displaying higher glucose and glutamine consumption, and enhanced TCA cycle and OxPhos, which is reflected in augmented mitochondrial respiration and ATP production. OxPhos is identified as the major contributor to metabolic reprogramming in Palbociclib-treated PC-3 cells. Prostate cancer cells exhibit enhanced glycolytic activity, in agreement with other studies in pancreatic and colon cancer cell lines after CDK4/6 inhibition (Franco et al., 2016, Tarrado-Castellarnau et al., 2017), together with greater glutamine utilization funneled into reductive carboxylation, promoting citrate production and lipogenesis. Mitochondrial defective cells promoted higher glucose consumption and lactate production in response to defective OxPhos, and induced glutamine-dependent reductive carboxylation to generate 4-carbon TCA intermediates and greater citrate production to enhance lipogenesis, enabling cell growth in osteosarcoma and renal cancer cells (Mullen et al., 2011). Also, an impaired mitochondrial function might emerge by zinc transporters overexpression after Palbociclib treatment, since zinc accumulation is reported to promote ACO2 inhibition affecting the TCA cycle, as is described in normal prostate glycolytic cells (Bader et al., 2019). We hypothesized that Palbociclib-treated prostate cancer cells might display a truncated TCA cycle that is overcome by increasing anaplerotic routes, in agreement with the augmented mitochondrial function and OxPhos. In this regard, there is a substantial increase in pyruvate production, which is associated with fueling the TCA cycle in prostate adenocarcinoma, where pyruvate plays a major role (Bader et al., 2019). On the other hand, SW620 colorectal cancer cells after Palbociclib treatment support the increased mitochondrial function by amino acid metabolism, especially glutamine. Our results in this cell line indicated that there is a glycolytic impairment triggered by Palbociclib, in accordance with studies in Triple Negative Breast Cancer (TNBC) (Cretella et al. 2018), which is dependent on drug concentration, in agreement with studies reporting different responses regarding glucose metabolism after Palbociclib treatment (Lorito et al., 2020, Franco et al., 2016, Tarrado-Castellarnau et al., 2017). These findings evidenced that cancer cells mainly rely on glutamine, oxidative phosphorylation, and mitochondrial function to adapt and survive after Palbociclib treatment as a common trait.

On the other hand, Palbociclib also causes a substantial alteration in the intracellular lipid profile, increasing lipogenesis, similar to the response in prostate cancer cells.

However, our results also indicated an increase in fatty acid oxidation in colorectal cancer cells. The major differences are observed in the acylcarnitines profile, associated with the overall ß-oxidation activity (Dossus & Kouloura et al., 2021). The greater impact on fatty acid metabolism and the inhibition of glycolytic genes suggest that fatty acids are a preferred carbon source in SW620 cells after Palbociclib treatment. In this regard, our findings suggested the presence of a futile cycle in lipid metabolism, shifting fatty acid synthesis (FAS) and oxidation (FAO), which has also been described in several tumors (Melone & Valentin et al. 2018), serving as an important source of ATP and reducing potential upon fatty catabolism, while inducing signaling pathways to modulate cell homeostasis and promote lipogenesis to meet the rapidly dividing cell requirements. Altered lipid metabolism has also been associated with drug resistance acquisition upon hyperactivation of the PI3K/AKT/mTOR pathway (Feng & Kurokawa, 2020), which is reported to be altered after Palbociclib treatment in several studies (Bonelli et al., 2017, Cretella et al., 2018, Franco et al., 2016, Tarrado-Castellarnau et al., 2017, Lorito et al., 2020). Another remarkable difference between cell lines in response to Palbociclib is the major impact on amino acid metabolism. Essential amino acids display decreased intracellular concentration, while there is a substantial increase in the production of non-essential amino acids. Despite the increase in glutamine metabolism, amino acids also represent an alternative carbon source, especially branched-chain amino acids (BCAAs), providing acetyl Co-A and succinyl-Coa for lipogenesis and oxidation in TCA (Lieu et al., 2020, Stine et al., 2022). Together, these results suggest an increase in amino acid usage for cell survival and proliferation. Furthermore, increased glutamine metabolism provides non-essential amino acids such as asparagine and arginine, which, together with the BCAA leucine, are involved in the activation of mTORC1 (Yoo, Yu & Sung et al., 2020). This activation might be associated with maintaining glucose metabolism despite the presence of Palbociclib and the inhibition of glycolytic-related genes, since activation of mTORC1 induces protein synthesis and lipogenesis, but also aerobic glycolysis (Fan & Wu, 2021). Although signaling metabolic pathways have not been further studied in this work, our results suggest a possible alteration in the PI3K/AKT/mTOR signaling pathway, also considering its relationship in response to Palbociclib treatment observed in other types of cancer (Bonelli et al., 2017, Cretella et al., 2018, Franco et al., 2016, Tarrado-Castellarnau et al., 2017).

Different metabolic reprogramming studied in this thesis reveal a common metabolic vulnerability after Palbociclib treatment, converging to the identification of OxPhos and mitochondrial function as attractive targets for therapeutic interventions to sensitize cells to Palbociclib, which is consistent with numerous reports presenting oxidative phosphorylation as a major metabolic supporter in aggressive cancer types (Ashton et al., 2018, El-Botty et al., 2023). Indeed, Palbociclib combination with OxPhos inhibitors has proven to be a successful strategy in both types of cancer. The overall increase in cell metabolism triggered by Palbociclib in the prostate cancer cell line is addressed through a multitarget strategy using an antifungal or an antibiotic targeting OxPhos or cytochrome P450, which are promising anticancer therapy (Karp & Lyakhovich, 2022, Weng et al., 2023). The antibiotic Tigecycline targets cytochrome c oxidase, causing cell cycle arrest, apoptosis, autophagy, and oxidative stress induction on solid tumors (Dong et al., 2019), and the antifungal Miconazole, is reported to target cytochrome P450 proteins (Niwa et al., 2014, Piérard et al., 2012) but also to inhibit ATPase activity *in vitro* (Lax et al., 2002), blocking cell proliferation and promoting apoptosis in several types of

cancer (Jung et al., 2021, Yuan et al., 2017). Despite the promising efficacy of antifungal and antibiotics in Palbociclib-resistant prostate cancer cells, a growing body of research also suggests a negative impact on cancer treatment by promoting chronic inflammation, destroying the intestinal microbiota, interfering in the cellular metabolism of healthy cells, causing genotoxicity, and debilitating the immune system (Gao et al., 2020), thus, other strategies must be sought. In this sense, the promising results obtained after OxPhos inhibition by using the iron-chelating VLX600 in combination with Palbociclib, demonstrate that OxPhos impairment is an effective strategy to enhance Palbociclib effect.

However, the most interesting synergism in the colorectal cell line was exhibited upon EUK-134 combination with Palbociclib. EUK-134 is a superoxide dismutase (SOD)-mimetic with catalase activity (Vincent et al., 2021) that might modulate the major electron transport chain (ETC) by-product, ROS, and promotes mitochondrial depletion and glycolysis when combined with Palbociclib. Our findings indicate that ROS plays a pivotal role in Palbociclib metabolic reprogramming in SW620 cells since it is reported that ROS mediates metabolic processes and entails signaling functions in cancer cells (Boonstra & Post, 2004, Che et al., 2016). Therefore, we hypothesize that the alteration of ROS balance might result in an antiproliferative effect in Palbociclib-resistant SW620 cells. Altogether, EUK-134 treatment represented the most promising strategy to overcome Palbociclib resistance in the colorectal cell line by inducing mitochondrial function disruption, affecting the cellular metabolism, and altering the energetic supply, overall reverting the metabolic reprogramming associated with Palbociclib adaptation. Moreover, the use of moderate OxPhos inhibitors such as metformin, nitric oxide, arsenic trioxide, and atovaquone, exhibit better safety profiles than specific potent OxPhos inhibitors, which present higher toxicity in clinical trials (Machado et al., 2023).

Variations in ROS levels also interfere with cell cycle progression, since ROS levels fluctuate throughout the cell cycle progression in human pluripotent cells, displaying a peak during the S to G2/M transition (Ivanova et al., 2021). The redox state influences the activation of proteins required for the cycle initiation, cell cycle transition, and cell cycle exit (Boonstra & Post, 2004). Also, it is reported that higher ROS levels derived from an increased mitochondrial function are associated with CyclinB1/CDK1 upregulation, which is essential for the G2/M transition (Wang & Fan et al., 2014). Therefore, more evidence emerges indicating a crosstalk between cell cycle regulation and cellular metabolism, involving mechanisms that govern cell cycle phase transitions (Boonstra & Post, 2004, Fajas, 2013, Wang et al., 2022, Wu & Zhang et al., 2019) and suggesting a possible connection between ROS modulation and cell cycle regulation after EUK-134 treatment.

Altogether, we propose the mitochondrial impairment and the regulation of ROS and cell cycle as the mechanisms responsible for reverting the metabolic adaptation to Palbociclib, compromising cell survival and thus, overcoming Palbociclib short-term resistance in the SW620 colorectal cancer cells. We demonstrate EUK-134 and Palbociclib combination efficacy in preclinical models, significantly compromising tumor progression in NOD/SCID mice bearing colorectal cancer SW620 xenografts and cell proliferation in the primary tumor colorectal cancer cell line HCT116. These findings offer a successful approach that expands the potential of application to overcome Palbociclib resistance across different colorectal cancer models and represent a putative therapeutic

alternative to tackle the highly challenging and heterogeneous colorectal cancer (Sveen et al., 2017, Van Cutsem et al., 2016). Consistent with our investigation, another study proposes targeting ROS and mitochondrial function as a promising strategy in pancreatic ductal adenocarcinoma (PDA) models treated with CDK4/6 inhibitors (Franco et al., 2016). Moreover, this study demonstrated that only the knockdown of either hemeoxygenase 1 (HO-1) or catalase (CAT) caused a significant reduction in PDA cell growth, indicating that not all alterations of ROS signaling or regulating mechanisms cooperate with CDK4/6 inhibition.

Finally, in this thesis, we applied a computational approach through Genome-Scale Metabolic Modeling (GSMM) to simulate the resistant phenotypes by integrating multi-omics data to build each condition-specific GSMM. The use of GSMM to identify metabolic vulnerabilities proves to be a successful strategy for the rational design of combination therapies, according to the most promising combination found to overcome Oxaliplatin and Palbociclib short-term resistance. For instance, nucleotide metabolism impairment, which is addressed through Cladribine in this work, in combination with Oxaliplatin treatment is currently applied through the fluoropyrimidine 5-Fluorouracil and Folinic acid, targeting pyrimidine synthesis in combination with Oxaliplatin in FOLFOX therapy for metastatic colorectal cancer (Ser et al., 2016, Van Cutsem et al., 2016). Other therapeutic combinations proposed by the GSMM are also being applied for the treatment of solid malignancies such as Gemcitabine in combination with Oxaliplatin (GEMOX) (Chocry et al., 2022, Kim et al., 2012, Meriggi et al., 2010, Ziras et al., 2006). Gemcitabine is also a nucleoside analog that targets RRM1, thymidylate synthetase (TYMS), and cytidine/uridine monophosphate kinase 1 (CMPK1) (Wishart et al., 2018), impairing DNA synthesis and validating the GSMM predictions. On the other hand, targets proposed for the Palbociclib-surviving phenotype of PC-3 cells agree with the most representative metabolic changes described following Palbociclib treatment in several cancer types, such as OxPhos reliance and enhanced mitochondrial function (El-Botty et al., 2023, Evans et al., 2021, Franco et al., 2016, Tarrado-Castellarnau et al., 2017). Moreover, this strategy is based on drug repurposing, taking advantage of approved or investigational drugs, and therefore de-risked molecules, annotated in external databases such as DrugBank (Wishart et al., 2018) or Therapeutic Target Database (Chen et al., 2002), that could result in reduced overall development costs and shorter development times (Pushpakom et al., 2019).

Altogether, based on the metabolic reprogramming underlying Palbociclib and Oxaliplatin treatments, this thesis demonstrates that effective rational combination therapies can be predicted through the characterization of the metabolic reprogramming and also utilizing computational models, and that, in turn, the targeting of the identified metabolic vulnerabilities displays promising results in preclinical models. These findings provide alternative combination therapies that could be further explored to improve treatment outcomes and overcome drug resistance in advanced stages of prostate and colorectal cancers.

5.

CONCLUSIONS

5. CONCLUSIONS

- Oxaliplatin treatment impedes cell proliferation and induces a substantial decrease in the entire cellular metabolism, characterized by glycolytic impairment and increased glutamine reliance in advanced colorectal and prostate cancers.

- Oxaliplatin alters TCA intermediates and induces lipogenesis and polyamine synthesis in colorectal cancer cells, maintaining respiration and redox cell homeostasis through one-carbon metabolism, whereas in the prostate cancer cell line, Oxaliplatin induces respiration, fatty acid oxidation, and amino acid metabolism.

- Palbociclib inhibits cell proliferation by inducing cell cycle arrest in the G1/G0 phase and promotes an increase of the entire metabolic landscape in both cancer types, leading to greater glutamine utilization, enhanced mitochondrial function, respiration, and oxidative phosphorylation.

- Palbociclib induces glycolysis and pyruvate metabolism to support mitochondrial function and promotes glutamine-dependent reductive carboxylation in prostate cancer cells, whereas impacts lipid metabolism, raises essential amino acid demand, and increases non-essential amino acid production, indicating enhanced TCA cycle anaplerosis in colorectal cancer cells.

- Metabolic characterization and Genome-Scale Metabolic Models (GSMMs) proved to be useful tools for predicting metabolic drug targets that sensitize cancer cells to Oxaliplatin and Palbociclib.

- Oxaliplatin with Cladribine, which targets nucleotide metabolism, demonstrates a promising therapeutic effect in the colorectal cell line.

- Oxaliplatin-induced G2 phase cell cycle arrest represents a therapeutic opportunity in both cancer types that can be effectively addressed through combined therapies with drugs inducing cell cycle arrest in G1/G0 phases.

- Oxidative phosphorylation represents a major metabolic vulnerability in colorectal and prostate cancer cells that survive to Palbociclib treatment.

- The combination of Palbociclib with the superoxidase dismutase (SOD)-mimetic with catalase activity EUK-134 exhibits synergic effects by decreasing cell proliferation in both metastatic and primary tumor colorectal cell lines, and reducing tumor growth *in vivo* in NOD/SCID mice with SW620 xenografts.

6.

BIBLIOGRAPHY

6. BIBLIOGRAPHY

Adamo P, Ladomery MR. The oncogene ERG: a key factor in prostate cancer. Oncogene. 2016;35(4):403-414.

Affronti HC, Rowsam AM, Pellerite AJ, et al. Pharmacological polyamine catabolism upregulation with methionine salvage pathway inhibition as an effective prostate cancer therapy. Nat Commun. 2020;11(1):52.

Ahmad F, Cherukuri MK, Choyke PL. Metabolic reprogramming in prostate cancer. Br J Cancer. 2021;125(9):1185-1196.

Ahmed D, Eide PW, Eilertsen IA, Danielsen SA, Eknæs M, Hektoen M, Lind GE, Lothe RA. Epigenetic and genetic features of 24 colon cancer cell lines. Oncogenesis. 2013 Sep 16;2(9):e71.

Akamatsu K, Shibata MA, Ito Y, Sohma Y, Azuma H, Otsuki Y. Riluzole induces apoptotic cell death in human prostate cancer cells via endoplasmic reticulum stress. Anticancer Res. 2009;29(6):2195-2204.

Amin MB, Greene FL, Edge SB, et al. The Eighth Edition AJCC Cancer Staging Manual: Continuing to build a bridge from a population-based to a more "personalized" approach to cancer staging. CA Cancer J Clin. 2017;67(2):93-99.

Anand J, Chiou L, Sciandra C, Zhang X, Hong J, Wu D, Zhou P, Vaziri C. Roles of trans-lesion synthesis (TLS) DNA polymerases in tumorigenesis and cancer therapy. NAR Cancer. 2023 Feb 6;5(1):zcad005.

André T, Boni C, Navarro M, et al. Improved overall survival with oxaliplatin, fluorouracil, and leucovorin as adjuvant treatment in stage II or III colon cancer in the MOSAIC trial. J Clin Oncol. 2009;27(19):3109-3116

Arnold PK, Jackson BT, Paras KI, et al. A non-canonical tricarboxylic acid cycle underlies cellular identity. Nature. 2022;603(7901):477-481.

Ashton TM, McKenna WG, Kunz-Schughart LA, Higgins GS. Oxidative Phosphorylation as an Emerging Target in Cancer Therapy. Clin Cancer Res. 2018;24(11):2482-2490.

Aubrey BJ, Kelly GL, Janic A, Herold MJ, Strasser A. How does p53 induce apoptosis and how does this relate to p53-mediated tumour suppression?. Cell Death Differ. 2018;25(1):104-113.

Babbar N, Gerner EW. Targeting polyamines and inflammation for cancer prevention. Recent Results Cancer Res. 2011;188:49-64.

Bader DA, Hartig SM, Putluri V, et al. Mitochondrial pyruvate import is a metabolic vulnerability in androgen receptor-driven prostate cancer. Nat Metab. 2019;1(1):70-85.

Bader DA, McGuire SE. Tumour metabolism and its unique properties in prostate adenocarcinoma. Nat Rev Urol. 2020;17(4):214-231.

Banik K, Ranaware AM, Harsha C, et al. Piceatannol: A natural stilbene for the prevention and treatment of cancer. Pharmacol Res. 2020;153:104635.

Bansal A, Simon MC. Glutathione metabolism in cancer progression and treatment resistance. J Cell Biol. 2018;217(7):2291-2298.

Bao Y, Mukai K, Hishiki T, et al. Energy management by enhanced glycolysis in G1-phase in human colon cancer cells in vitro and in vivo. Mol Cancer Res. 2013;11(9):973-985.

Baquero JM, Benítez-Buelga C, Rajagopal V, et al. Small molecule inhibitor of OGG1 blocks oxidative DNA damage repair at telomeres and potentiates methotrexate anticancer effects. Sci Rep. 2021;11(1):3490. Published 2021 Feb 10.

Barker N, Ridgway RA, van Es JH, et al. Crypt stem cells as the cells-of-origin of intestinal cancer. Nature. 2009;457(7229):608-611.

Baudino TA. Targeted Cancer Therapy: The Next Generation of Cancer Treatment. Curr Drug Discov Technol. 2015;12(1):3-20.

Beale PJ, Rogers P, Boxall F, Sharp SY, Kelland LR. BCL-2 family protein expression and platinum drug resistance in ovarian carcinoma. Br J Cancer. 2000 Jan;82(2):436-40.

Biancur DE, Paulo JA, Małachowska B, et al. Compensatory metabolic networks in pancreatic cancers upon perturbation of glutamine metabolism. Nat Commun. 2017;8:15965.

Biller LH, Schrag D. Diagnosis and Treatment of Metastatic Colorectal Cancer: A Review. JAMA. 2021;325(7):669-685.

Bistulfi G, Affronti HC, Foster BA, et al. The essential role of methylthioadenosine phosphorylase in prostate cancer. Oncotarget. 2016;7(12):14380-14393.

Bohen S, J O'Connor M, Morgan M. DNA Damage Response – An Emerging Target for Groundbreaking Cancer Therapies. Eur Oncol Haematol. 2018; 14(Suppl 1):2–7

Boland PM, Yurgelun MB, Boland CR. Recent progress in Lynch syndrome and other familial colorectal cancer syndromes. CA Cancer J Clin. 2018;68(3):217-231.

Bonelli MA, Digiacomo G, Fumarola C, et al. Combined Inhibition of CDK4/6 and PI3K/AKT/mTOR Pathways Induces a Synergistic Anti-Tumor Effect in Malignant Pleural Mesothelioma Cells. Neoplasia. 2017;19(8):637-648.

Boonstra J, Post JA. Molecular events associated with reactive oxygen species and cell cycle progression in mammalian cells. Gene. 2004;337:1-13.

Bretones G, Delgado MD, León J. Myc and cell cycle control. Biochim Biophys Acta. 2015;1849(5):506-516.

Brown RE, Short SP, Williams CS. Colorectal Cancer and Metabolism. Curr Colorectal Cancer Rep. 2018 Dec;14(6):226-241.

Brunk E, Sahoo S, Zielinski DC, Altunkaya A, Dräger A, Mih N, Gatto F, Nilsson A, Preciat Gonzalez GA, Aurich MK, Prlić A, Sastry A, Danielsdottir AD, Heinken A, Noronha A, Rose PW, Burley SK, Fleming RMT, Nielsen J, Thiele I, Palsson BO. Recon3D enables a three-dimensional view of gene variation in human metabolism. Nat Biotechnol. 2018 Mar;36(3):272-281.

Brunner JS, Finley LWS. Metabolic determinants of tumour initiation. Nat Rev Endocrinol. 2023;19(3):134-150.

Bu P, Chen KY, Xiang K, et al. Aldolase B-Mediated Fructose Metabolism Drives Metabolic Reprogramming of Colon Cancer Liver Metastasis. Cell Metab. 2018;27(6):1249-1262.e4.

Burch PM, Heintz NH. Redox regulation of cell-cycle re-entry: cyclin D1 as a primary target for the mitogenic effects of reactive oxygen and nitrogen species. Antioxid Redox Signal. 2005 May-Jun;7(5-6):741-51.

Cancer Research UK: TNM staging for prostate cancer [Internet]. Cancer Research UK. 2022. [accessed in March 2023]. Available from: https://www.cancerresearchuk.org/about-cancer/prostate-cancer/stages/tnm-staging

Cancer Research UK: Types of cancer [Internet]. Last update 1 July 2020 [accessed in May 2023]. Available from: https://www.cancerresearchuk.org/what-is-cancer/how-cancer-starts/types-of-cancer

Cancer.Net: Prostate Cancer: Stages and Grades [Internet]. 2005-2023 American Society of Clinical Oncology (ASCO). 2023. [accessed in March 2023]. Available from: https://www.cancer.net/cancer-types/prostate-cancer/stages-and-grades

Cancer.Net: Types of cancer [Internet]. 2005-2023 American Society of Clinical Oncology (ASCO). 2023. [accessed in March 2023]. Available from: https://www.cancer.net/cancer-types

Casero RA Jr, Murray Stewart T, Pegg AE. Polyamine metabolism and cancer: treatments, challenges and opportunities. Nat Rev Cancer. 2018 Nov;18(11):681-695.

Chang HHY, Pannunzio NR, Adachi N, Lieber MR. Non-homologous DNA end joining and alternative pathways to double-strand break repair. Nat Rev Mol Cell Biol. 2017;18(8):495-506.

Chatterjee N, Walker GC. Mechanisms of DNA damage, repair, and mutagenesis. Environ Mol Mutagen. 2017;58(5):235-263.

Che M, Wang R, Li X, Wang HY, Zheng XFS. Expanding roles of superoxide dismutases in cell regulation and cancer. Drug Discov Today. 2016 Jan;21(1):143-149.

Chen G, Gong T, Wang Z, et al. Colorectal cancer organoid models uncover oxaliplatin-resistant mechanisms at single cell resolution [published correction appears in Cell Oncol (Dordr). 2022 Nov 24;:]. Cell Oncol (Dordr). 2022;45(6):1155-1167.

Chen J, Zhang Z, Ni J, et al. ENO3 promotes colorectal cancer progression by enhancing cell glycolysis. Med Oncol. 2022;39(5):80. Published 2022 Apr 28. doi:10.1007/s12032-022-01676-1

Chen P, Liu XQ, Lin X, Gao LY, Zhang S, Huang X. Targeting YTHDF1 effectively re-sensitizes cisplatin-resistant colon cancer cells by modulating GLS-mediated glutamine metabolism. Mol Ther Oncolytics. 2021;20:228-239.

Chen X, Ji ZL, Chen YZ. TTD: Therapeutic Target Database. Nucleic Acids Res. 2002 Jan 1;30(1):412-5.

Chen XZ, Guo R, Zhao C, Xu J, Song H, Yu H, Pilarsky C, Nainu F, Li JQ, Zhou XK, Zhang JY. A Novel Anti-Cancer Therapy: CRISPR/Cas9 Gene Editing. Front Pharmacol. 2022 Jul 22;13:939090.

Chen ZH, Yu YP, Zuo ZH, et al. Targeting genomic rearrangements in tumor cells through Cas9-mediated insertion of a suicide gene. Nat Biotechnol. 2017;35(6):543-550.

Cheung EC, Athineos D, Lee P, et al. TIGAR is required for efficient intestinal regeneration and tumorigenesis. Dev Cell. 2013;25(5):463-477.

Cheung EC, Vousden KH. The role of ROS in tumour development and progression. Nat Rev Cancer. 2022;22(5):280-297.

Cho ES, Cha YH, Kim HS, Kim NH, Yook JI. The Pentose Phosphate Pathway as a Potential Target for Cancer Therapy. Biomol Ther (Seoul). 2018 Jan 1;26(1):29-38.

Chocry M, Leloup L, Parat F, Messé M, Pagano A, Kovacic H. Gemcitabine: An Alternative Treatment for Oxaliplatin-Resistant Colorectal Cancer. Cancers (Basel). 2022 Nov 29;14(23):5894.

Chou TC, Martin N. CompuSyn software. CompuSyn for drug combinations: PC software and user's guide: a computer program for quantitation of synergism and antagonism in drug combinations, and the determination of IC50 and ED50 and LD50 values. ComboSyn Inc., Paramus, NJ. 2005. https://www.combosyn.com

Chou TC. Drug combination studies and their synergy quantification using the Chou-Talalay method. Cancer Res. 2010;70(2):440-446.

Çınar Ayan İ, Güçlü E, Vural H, Dursun HG. Piceatannol induces apoptotic cell death through activation of caspase-dependent pathway and upregulation of ROS-mediated mitochondrial dysfunction in pancreatic cancer cells. Mol Biol Rep. 2022;49(12):11947-11957.

Clem B, Telang S, Clem A, et al. Small-molecule inhibition of 6-phosphofructo-2-kinase activity suppresses glycolytic flux and tumor growth. Mol Cancer Ther. 2008;7(1):110-120.

Conroy LR, Lorkiewicz P, He L, Yin X, Zhang X, Rai SN, Clem BF. Palbociclib treatment alters nucleotide biosynthesis and glutamine dependency in A549 cells. Cancer Cell Int. 2020 Jul 1;20:280.

Conroy T, Desseigne F, Ychou M, et al. FOLFIRINOX versus gemcitabine for metastatic pancreatic cancer. N Engl J Med. 2011;364(19):1817-1825.

Corbin JM, Ruiz-Echevarría MJ. One-Carbon Metabolism in Prostate Cancer: The Role of Androgen Signaling. Int J Mol Sci. 2016 Jul 27;17(8):1208.

Cretella D, Ravelli A, Fumarola C, et al. The anti-tumor efficacy of CDK4/6 inhibition is enhanced by the combination with PI3K/AKT/mTOR inhibitors through impairment of glucose metabolism in TNBC cells. J Exp Clin Cancer Res. 2018;37(1):72.

Cruz-Bermúdez A, Laza-Briviesca R, Vicente-Blanco RJ, et al. Cisplatin resistance involves a metabolic reprogramming through ROS and PGC-1α in NSCLC which can be overcome by OXPHOS inhibition. Free Radic Biol Med. 2019;135:167-181.

Davidson SM, Papagiannakopoulos T, Olenchock BA, et al. Environment Impacts the Metabolic Dependencies of Ras-Driven Non-Small Cell Lung Cancer. Cell Metab. 2016;23(3):517-528.

DeBerardinis RJ, Chandel NS. Fundamentals of cancer metabolism. Sci Adv. 2016;2(5):e1600200.

Decraene D, Smaers K, Gan D, et al. A synthetic superoxide dismutase/catalase mimetic (EUK-134) inhibits membrane-damage-induced activation of mitogen-activated protein kinase pathways and reduces p53 accumulation in ultraviolet B-exposed primary human keratinocytes. J Invest Dermatol. 2004;122(2):484-491.

Desai K, McManus JM, Sharifi N. Hormonal Therapy for Prostate Cancer. Endocr Rev. 2021;42(3):354-373.

Di Francesco AM, Ruggiero A, Riccardi R. Cellular and molecular aspects of drugs of the future: oxaliplatin. Cell Mol Life Sci. 2002;59(11):1914-1927.

Di Gialleonardo V, Wilson DM, Keshari KR. The Potential of Metabolic Imaging. Semin Nucl Med. 2016 Jan;46(1):28-39.

Ding Q, Li R, Wang Q, Yu L, Zi F. A pan-cancer analysis of the role of argininosuccinate synthase 1 in human tumors. Front Oncol. 2023 Nov 20;13:1049147.

Doan MT, Teitell MA. Krebs and an alternative TCA cycle!. Cell Res. 2022;32(6):509-510.

Dong Y, Tu R, Liu H, Qing G. Regulation of cancer cell metabolism: oncogenic MYC in the driver's seat. Signal Transduct Target Ther. 2020;5(1):124.

Dong Z, Abbas MN, Kausar S, Yang J, Li L, Tan L, Cui H. Biological Functions and Molecular Mechanisms of Antibiotic Tigecycline in the Treatment of Cancers. Int J Mol Sci. 2019 Jul 22;20(14):3577.

Dorff TB, Tsao-Wei DD, Groshen S, et al. Efficacy of oxaliplatin plus pemetrexed in chemotherapy pretreated metastatic castration-resistant prostate cancer. Clin Genitourin Cancer. 2013;11(4):416-422.

Dossus L, Kouloura E, Biessy C, et al. Prospective analysis of circulating metabolites and endometrial cancer risk. Gynecol Oncol. 2021;162(2):475-481.

Douiev L, Abu-Libdeh B, Saada A. Cytochrome c oxidase deficiency, oxidative stress, possible antioxidant therapy and link to nuclear DNA damage. Eur J Hum Genet. 2018;26(4):579-581.

Droz JP, Muracciole X, Mottet N, Ould Kaci M, Vannetzel JM, Albin N, Culine S, Rodier JM, Misset JL, Mackenzie S, Cvitkovic E, Benoit G. Phase II study of oxaliplatin versus oxaliplatin combined with infusional 5-fluorouracil in hormone refractory metastatic prostate cancer patients. Ann Oncol. 2003 Aug;14(8):1291-8.

Ebrahim A, Lerman JA, Palsson BO, Hyduke DR. COBRApy: COnstraints-Based Reconstruction and Analysis for Python. BMC Syst Biol. 2013;7:74.

Eklöf V, Wikberg ML, Edin S, Dahlin AM, Jonsson BA, Öberg Å, Rutegård J, Palmqvist R. The prognostic role of KRAS, BRAF, PIK3CA and PTEN in colorectal cancer. Br J Cancer. 2013 May 28;108(10):2153-63.

El-Botty R, Morriset L, Montaudon E, et al. Oxidative phosphorylation is a metabolic vulnerability of endocrine therapy and palbociclib-resistant metastatic breast cancers. Nat Commun. 2023;14(1):4221.

El-Botty R, Morriset L, Montaudon E, et al. Oxidative phosphorylation is a metabolic vulnerability of endocrine therapy and palbociclib resistant metastatic breast cancers. Nat Commun. 2023;14(1):4221.

Elia I, Haigis MC. Metabolites and the tumour microenvironment: from cellular mechanisms to systemic metabolism. Nat Metab. 2021;3(1):21-32.

Erdem A, Marin S, Pereira-Martins DA, Geugien M, Cunningham A, Pruis MG, Weinhäuser I, Gerding A, Bakker BM, Wierenga ATJ, Rego EM, Huls G, Cascante M, Schuringa JJ. Inhibition of the succinyl

dehydrogenase complex in acute myeloid leukemia leads to a lactate-fuelled respiratory metabolic vulnerability. Nat Commun. 2022 Apr 19;13(1):2013.

European medicines agency; Palbociclib (IBRANCE) product information [Internet]. Last update: 16 July 2021 [accessed in November 2023]. Available from: https://www.ema.europa.eu/en/documents/product-information/ibrance-epar-product-information_en.pdf

Evan GI, Vousden KH. Proliferation, cell cycle and apoptosis in cancer. Nature. 2001;411(6835):342-348.

Evans KW, Yuca E, Scott SS, et al. Oxidative Phosphorylation Is a Metabolic Vulnerability in Chemotherapy-Resistant Triple-Negative Breast Cancer. Cancer Res. 2021;81(21):5572-5581.

Fadó R, Zagmutt S, Herrero L, et al. To be or not to be a fat burner, that is the question for cpt1c in cancer cells. Cell Death Dis. 2023;14(1):57.

Fajas L. Re-thinking cell cycle regulators: the cross-talk with metabolism. Front Oncol. 2013;3:4.

Fan H, Wu Y, Yu S, Li X, Wang A, Wang S, Chen W, Lu Y. Critical role of mTOR in regulating aerobic glycolysis in carcinogenesis (Review). Int J Oncol. 2021 Jan;58(1):9-19.

Fan J, Ye J, Kamphorst JJ, Shlomi T, Thompson CB, Rabinowitz JD. Quantitative flux analysis reveals folate-dependent NADPH production [published correction appears in Nature. 2014 Sep 25;513(7519):574]. Nature. 2014;510(7504):298-302.

Farber S, Diamond LK. Temporary remissions in acute leukemia in children produced by folic acid antagonist, 4-aminopteroyl-glutamic acid. N Engl J Med. 1948;238(23):787-793.

Felmlee MA, Jones RS, Rodriguez-Cruz V, Follman KE, Morris ME. Monocarboxylate Transporters (SLC16): Function, Regulation, and Role in Health and Disease. Pharmacol Rev. 2020;72(2):466-485.

Feng WW, Kurokawa M. Lipid metabolic reprogramming as an emerging mechanism of resistance to kinase inhibitors in breast cancer. Cancer Drug Resist. 2020 Spring;3(1):1–17.

Ferlay J, Ervik M, Lam F, Colombet M, Mery L, Piñeros M, et al. Global Cancer Observatory: Cancer Today. [Internet]. Lyon: International Agency for Research on Cancer; 2020 [accessed in March 2023]. Available from: https://gco.iarc.fr/today

Foguet C, Xu Y, Ritchie SC, et al. Genetically personalised organ-specific metabolic models in health and disease. Nat Commun. 2022;13(1):7356.

Fontana E, Eason K, Cervantes A, Salazar R, Sadanandam A. Context matters-consensus molecular subtypes of colorectal cancer as biomarkers for clinical trials. Ann Oncol. 2019;30(4):520-527.

Forman HJ, Zhang H, Rinna A. Glutathione: overview of its protective roles, measurement, and biosynthesis. Mol Aspects Med. 2009 Feb-Apr;30(1-2):1-12.

Franco J, Balaji U, Freinkman E, Witkiewicz AK, Knudsen ES. Metabolic Reprogramming of Pancreatic Cancer Mediated by CDK4/6 Inhibition Elicits Unique Vulnerabilities. Cell Rep. 2016 Feb 9;14(5):979-990. Erratum in: Cell Rep. 2020 Jul 7;32(1):107793. PMID: 26804906; PMCID: PMC4757440.

Franklin RB, Milon B, Feng P, Costello LC. Zinc and zinc transporters in normal prostate and the pathogenesis of prostate cancer. Front Biosci. 2005;10:2230-2239.

Fry DW, Harvey PJ, Keller PR, et al. Specific inhibition of cyclin-dependent kinase 4/6 by PD 0332991 and associated antitumor activity in human tumor xenografts. Mol Cancer Ther. 2004;3(11):1427-1438.

Gandaglia G, Abdollah F, Schiffmann J, Trudeau V, Shariat SF, Kim SP, Perrotte P, Montorsi F, Briganti A, Trinh QD, Karakiewicz PI, Sun M. Distribution of metastatic sites in patients with prostate cancer: A population-based analysis. Prostate. 2014, 74(2):210-6.

Ganesh K, Basnet H, Kaygusuz Y, et al. L1CAM defines the regenerative origin of metastasis-initiating cells in colorectal cancer [published correction appears in Nat Cancer. 2020 Nov;1(11):1128]. Nat Cancer. 2020;1(1):28-45.

Ganesh K, Massagué J. Targeting metastatic cancer. Nat Med. 2021;27(1):34-44.

Gao P, Tchernyshyov I, Chang TC, et al. c-Myc suppression of miR-23a/b enhances mitochondrial glutaminase expression and glutamine metabolism. Nature. 2009;458(7239):762-765.

Gao Y, Shang Q, Li W, et al. Antibiotics for cancer treatment: A double-edged sword. J Cancer. 2020;11(17):5135-5149. Published 2020 Jun 28. doi:10.7150/jca.47470

Germain L, Lafront C, Paquette V, et al. Preclinical models of prostate cancer - modelling androgen dependency and castration resistance in vitro, ex vivo and in vivo. Nat Rev Urol. 2023 Aug;20(8):480-493.

Gianello P, Saliez A, Bufkens X, et al. EUK-134, a synthetic superoxide dismutase and catalase mimetic, protects rat kidneys from ischemia-reperfusion-induced damage. Transplantation. 1996;62(11):1664-1666.

Giunchi F, Fiorentino M, Loda M. The Metabolic Landscape of Prostate Cancer. Eur Urol Oncol. 2019;2(1):28-36.

Goel S, Bergholz JS, Zhao JJ. Targeting CDK4 and CDK6 in cancer. Nat Rev Cancer. 2022;22(6):356-372.

Goel S, DeCristo MJ, Watt AC, et al. CDK4/6 inhibition triggers anti-tumour immunity. Nature. 2017;548(7668):471-475.

Goodman AM, Sokol ES, Frampton GM, Lippman SM, Kurzrock R. Microsatellite-Stable Tumors with High Mutational Burden Benefit from Immunotherapy. Cancer Immunol Res. 2019;7(10):1570-1573.

Greene J, Segaran A, Lord S. Targeting OXPHOS and the electron transport chain in cancer; Molecular and therapeutic implications. Semin Cancer Biol. 2022;86(Pt 2):851-859.

Grégoire V, Van NT, Stephens LC, Brock WA, Milas L, Plunkett W, Hittelman WN. The role of fludarabine-induced apoptosis and cell cycle synchronization in enhanced murine tumor radiation response in vivo. Cancer Res. 1994 Dec 1;54(23):6201-9. PMID: 7954467.

Gross MI, Demo SD, Dennison JB, et al. Antitumor activity of the glutaminase inhibitor CB-839 in triple-negative breast cancer. Mol Cancer Ther. 2014;13(4):890-901.

Guo T, Gu C, Li B, Xu C. Dual inhibition of FGFR4 and BCL-xL inhibits multi-resistant ovarian cancer with BCL2L1 gain. Aging (Albany NY). 2021;13(15):19750-19759.

Halabi S, Lin CY, Kelly WK, et al. Updated prognostic model for predicting overall survival in first-line chemotherapy for patients with metastatic castration-resistant prostate cancer [published correction appears in J Clin Oncol. 2014 May 1;32(13):1387]. J Clin Oncol. 2014;32(7):671-677.

Hamada N, Fujimichi Y, Iwasaki T, et al. Emerging issues in radiogenic cataracts and cardiovascular disease. J Radiat Res. 2014;55(5):831-846.

Han M, Lee D, Lee SH, Kim TH. Oxidative Stress and Antioxidant Pathway in Allergic Rhinitis. Antioxidants (Basel). 2021 Aug 9;10(8):1266.

Hanahan D, Weinberg RA. Hallmarks of cancer: the next generation. Cell. 2011;144(5):646-74.

Hanahan D, Weinberg RA. The hallmarks of cancer. Cell. 2000;100(1):57-70.

Hanahan D. Hallmarks of Cancer: New Dimensions. Cancer Discov. 2022;12(1):31-46.

Hatch SB, Swift LP, Caporali S, Carter R, Hill EJ, MacGregor TP, ''Atri S, Middleton MR, McHugh PJ, Sharma RA. XPF protein levels determine sensitivity of malignant melanoma cells to oxaliplatin chemotherapy: suitability as a biomarker for patient selection. Int J Cancer. 2014 Mar 15;134(6):1495-503.

Hayes JD, Dinkova-Kostova AT, Tew KD. Oxidative Stress in Cancer. Cancer Cell. 2020; 38(2):167-197.

Heo YJ, Hwa C, Lee GH, Park JM, An JY. Integrative Multi-Omics Approaches in Cancer Research: From Biological Networks to Clinical Subtypes. Mol Cells. 2021 Jul 31;44(7):433-443.

Hochegger H, Takeda S, Hunt T. Cyclin-dependent kinases and cell-cycle transitions: does one fit all?. Nat Rev Mol Cell Biol. 2008;9(11):910-916.

Hogarty MD, Norris MD, Davis K, et al. ODC1 is a critical determinant of MYCN oncogenesis and a therapeutic target in neuroblastoma. Cancer Res. 2008 Dec 1;68(23):9735-45.

Holbert CE, Cullen MT, Casero RA Jr, Stewart TM. Polyamines in cancer: integrating organismal metabolism and antitumour immunity. Nat Rev Cancer. 2022;22(8):467-480.

Hsieh JY, Chen KC, Wang CH, et al. Suppression of the human malic enzyme 2 modifies energy metabolism and inhibits cellular respiration. Commun Biol. 2023 May 22;6(1):548.

Huang H, He Q, Guo B, Xu X, Wu Y, Li X. Progress in Redirecting Antiparasitic Drugs for Cancer Treatment. Drug Des Devel Ther. 2021;15:2747-2767.

Huang J, Zhao Y, Xu Y, et al. Comparative effectiveness and safety between oxaliplatin-based and cisplatin-based therapy in advanced gastric cancer: A meta-analysis of randomized controlled trials. Oncotarget. 2016 Jun 7;7(23):34824-31.

Huang L, Guo Z, Wang F, Fu L. KRAS mutation: from undruggable to druggable in cancer. Signal Transduct Target Ther. 2021;6(1):386.

Huang R, Zhou PK. DNA damage repair: historical perspectives, mechanistic pathways and clinical translation for targeted cancer therapy. Signal Transduct Target Ther. 2021;6(1):254.

Hudson CD, Savadelis A, Nagaraj AB, et al. Altered glutamine metabolism in platinum resistant ovarian cancer. Oncotarget. 2016;7(27):41637-41649.

Huggins C, Hodges CV. Studies on prostatic cancer: I. The effect of castration, of estrogen and of androgen injection on serum phosphatases in metastatic carcinoma of the prostate. 1941. J Urol. 2002;168(1):9-12.

Hui S, Ghergurovich JM, Morscher RJ, et al. Glucose feeds the TCA cycle via circulating lactate. Nature. 2017;551(7678):115-118.

Iacobazzi V, Infantino V. Citrate--new functions for an old metabolite. Biol Chem. 2014;395(4):387-399.

Imyanitov EN, Kuligina ES, Sokolenko AP, et al. Hereditary cancer syndromes. World J Clin Oncol. 2023;14(2):40-68.

International Agency for Research on Cancer (IARC): IARC monographs on the identification of carcinogenic hazards to humans, Agents Classified by the IARC Monographs, Volumes 1–135 [Internet]. Last update 5 May 2023 [accessed in May 2023]. Available from: https://monographs.iarc.who.int/agents-classified-by-the-iarc/

Ivanova JS, Pugovkina NA, Neganova IE, Kozhukharova IV, Nikolsky NN, Lyublinskaya OG. Cell cycle-coupled changes in the level of reactive oxygen species support the proliferation of human pluripotent stem cells. Stem Cells. 2021;39(12):1671-1687.

Janiszewska M, Primi MC, Izard T. Cell adhesion in cancer: Beyond the migration of single cells. J Biol Chem. 2020 Feb 21;295(8):2495-2505.

Jeong J, Eide DJ. The SLC39 family of zinc transporters. Mol Aspects Med. 2013 Apr-Jun;34(2-3):612-9.

Ji W, Shi Y, Wang X, He W, Tang L, Tian S, Jiang H, Shu Y, Guan X. Combined Androgen receptor blockade overcomes the resistance of breast cancer cells to palbociclib. Int J Biol Sci. 2019 Jan 1;15(3):522-532.

Jia W, Zhao X, Zhao L, et al. Non-canonical roles of PFKFB3 in regulation of cell cycle through binding to CDK4. Oncogene. 2018;37(13):1685-1698.

Jin H, Wang L, Bernards R. Rational combinations of targeted cancer therapies: background, advances, and challenges. Nat Rev Drug Discov. 2023;22(3):213-234.

Jin J, Byun JK, Choi YK, Park KG. Targeting glutamine metabolism as a therapeutic strategy for cancer. Exp Mol Med. 2023;55(4):706-715.

Ju HQ, Lin JF, Tian T, Xie D, Xu RH. NADPH homeostasis in cancer: functions, mechanisms and therapeutic implications. Signal Transduct Target Ther. 2020;5(1):231.

Juarez JC, Betancourt O Jr, Pirie-Shepherd SR, et al. Copper binding by tetrathiomolybdate attenuates angiogenesis and tumor cell proliferation through the inhibition of superoxide dismutase 1. Clin Cancer Res. 2006;12(16):4974-4982.

Jung B, Staudacher JJ, Beauchamp D. Transforming Growth Factor β Superfamily Signaling in Development of Colorectal Cancer. Gastroenterology. 2017;152(1):36-52.

Jung HJ, Seo I, Jha BK, Suh SI, Baek WK. Miconazole induces autophagic death in glioblastoma cells via reactive oxygen species-mediated endoplasmic reticulum stress. Oncol Lett. 2021 Apr;21(4):335.

Kang X, Xiao HH, Song HQ, Jing XB, Yan LS, Qi RG. Advances in drug delivery system for platinum agents based combination therapy. Cancer Biol Med. 2015 Dec;12(4):362-74.

Karakitsou E, Foguet C, de Atauri P, Kultima K, Khoonsari PE, Martins dos Santos VAP, Saccenti E, Rosato A, Cascante M. Metabolomics in systems medicine: an overview of methods and applications. Curr. Opin. Syst. Biol. 2019; 15:91-99

Karp I, Lyakhovich A. Targeting cancer stem cells with antibiotics inducing mitochondrial dysfunction as an alternative anticancer therapy. Biochem Pharmacol. 2022;198:114966.

Kerk SA, Papagiannakopoulos T, Shah YM, Lyssiotis CA. Metabolic networks in mutant KRAS-driven tumours: tissue specificities and the microenvironment. Nat Rev Cancer. 2021;21(8):510-525.

Keshet R, Szlosarek P, Carracedo A, Erez A. Rewiring urea cycle metabolism in cancer to support anabolism. Nat Rev Cancer. 2018;18(10):634-645.

Kim SH, Shin SJ, Kim SY, et al. Combining capecitabine, oxaliplatin, and gemcitabine (XELOXGEM) for colorectal carcinoma patients pretreated with irinotecan: a multicenter phase I/II trial. Cancer Chemother Pharmacol. 2012;69(1):91-97.

Kirova DG, Judasova K, Vorhauser J, et al. A ROS-dependent mechanism promotes CDK2 phosphorylation to drive progression through the S phase. Dev Cell. 2022;57(14):1712-1727.e9.

Kitada M, Xu J, Ogura Y, Monno I, Koya D. Manganese Superoxide Dismutase Dysfunction and the Pathogenesis of Kidney Disease. Front Physiol. 2020;11:755.

Kline CL, El-Deiry WS. Personalizing colon cancer therapeutics: targeting old and new mechanisms of action. Pharmaceuticals (Basel). 2013;6(8):988-1038.

Knox C, Wilson M, Klinger CM, et al. DrugBank 6.0: the DrugBank Knowledgebase for 2024. Nucleic Acids Res. 2024 Jan 5;52(D1):D1265-D1275. Available from: https://go.drugbank.com/

Knudsen ES, Witkiewicz AK. The Strange Case of CDK4/6 Inhibitors: Mechanisms, Resistance, and Combination Strategies. Trends Cancer. 2017 Jan;3(1):39-55.

Kotowski K, Rosik J, Machaj F, Supplitt S, Wiczew D, Jabłońska K, Wiechec E, Ghavami S, Dzięgiel P. Role of PFKFB3 and PFKFB4 in Cancer: Genetic Basis, Impact on Disease Development/Progression, and Potential as Therapeutic Targets. Cancers (Basel). 2021 Feb 22;13(4):909.

Koundouros N, Poulogiannis G. Reprogramming of fatty acid metabolism in cancer. Br J Cancer. 2020;122(1):4-22.

Koutsoukos K, Andrikopoulou A, Dedes N, Zagouri F, Bamias A, Dimopoulos MA. Clinical Perspectives of ERCC1 in Bladder Cancer. Int J Mol Sci. 2020;21(22):8829.

Krausova M, Korinek V. Wnt signaling in adult intestinal stem cells and cancer. Cell Signal. 2014;26(3):570-579.

Kusakabe M, Onishi Y, Tada H, et al. Mechanism and regulation of DNA damage recognition in nucleotide excision repair. Genes Environ. 2019;41:2.

La Vecchia S, Sebastián C. Metabolic pathways regulating colorectal cancer initiation and progression. Semin Cell Dev Biol. 2020;98:63-70.

Lam C, Low JY, Tran PT, Wang H. The hexosamine biosynthetic pathway and cancer: Current knowledge and future therapeutic strategies. Cancer Lett. 2021 Apr 10;503:11-18.

Lax A, Soler F, Fernandez-Belda F. Inhibition of sarcoplasmic reticulum Ca2+-ATPase by miconazole. Am J Physiol Cell Physiol. 2002 Jul;283(1):C85-92.

Lee CK, Jeong SH, Jang C, et al. Tumor metastasis to lymph nodes requires YAP-dependent metabolic adaptation. Science. 2019;363(6427):644-649.

Lee JL, Ahn JH, Choi MK, et al. Gemcitabine-oxaliplatin plus prednisolone is active in patients with castration-resistant prostate cancer for whom docetaxel-based chemotherapy failed. Br J Cancer. 2014;110(10):2472-2478.

Lee YR, Chen M, Pandolfi PP. The functions and regulation of the PTEN tumour suppressor: new modes and prospects. Nat Rev Mol Cell Biol. 2018;19(9):547-562.

Lee YT, Tan YJ, Oon CE. Molecular targeted therapy: Treating cancer with specificity. Eur J Pharmacol. 2018;834:188-196.

Li H, Chen J, Liu J, Lai Y, Huang S, Zheng L, Fan N. CPT2 downregulation triggers stemness and oxaliplatin resistance in colorectal cancer via activating the ROS/Wnt/β-catenin-induced glycolytic metabolism. Exp Cell Res. 2021 Dec 1;409(1):112892.

Li J, Meng Y, Wu X, Sun Y. Polyamines and related signaling pathways in cancer. Cancer Cell Int. 2020;20(1):539.

Li J, Zheng W, Wu J, Zhang J, Lv B, Li W, Liu J, Zhang X, Huang T, Luo Z. CPT1C-mediated fatty acid oxidation facilitates colorectal cancer cell proliferation and metastasis. Acta Biochim Biophys Sin (Shanghai). 2023 Apr 20;55(8):1301-1309.

Li S, Gao D, Jiang Y. Function, Detection and Alteration of Acylcarnitine Metabolism in Hepatocellular Carcinoma. Metabolites. 2019 Feb 21;9(2):36.

Li XX, Wang ZJ, Zheng Y, et al. Nuclear Receptor Nur77 Facilitates Melanoma Cell Survival under Metabolic Stress by Protecting Fatty Acid Oxidation. Mol Cell. 2018;69(3):480-492.e7.

Lieu EL, Nguyen T, Rhyne S, Kim J. Amino acids in cancer. Exp Mol Med. 2020 Jan;52(1):15-30.

Lin JF, Hu PS, Wang YY, et al. Phosphorylated NFS1 weakens oxaliplatin-based chemosensitivity of colorectal cancer by preventing PANoptosis. Signal Transduct Target Ther. 2022;7(1):54. Published 2022 Feb 28.

Ling ZN, Jiang YF, Ru JN, Lu JH, Ding B, Wu J. Amino acid metabolism in health and disease. Signal Transduct Target Ther. 2023 Sep 13;8(1):345.

Linnekamp JF, Hooff SRV, Prasetyanti PR, et al. Consensus molecular subtypes of colorectal cancer are recapitulated in in vitro and in vivo models. Cell Death Differ. 2018;25(3):616-633.

Liu C, Huang Y, Qin T, et al. AZD5153 reverses palbociclib resistance in ovarian cancer by inhibiting cell cycle-related proteins and the MAPK/PI3K-AKT pathway. Cancer Lett. 2022;528:31-44.

Lorito N, Bacci M, Smiriglia A, et al. Glucose Metabolic Reprogramming of ER Breast Cancer in Acquired Resistance to the CDK4/6 Inhibitor Palbociclib. Cells. 2020;9(3):668.

Love MI, Huber W, Anders S. Moderated estimation of fold change and dispersion for RNA-seq data with DESeq2. Genome Biol. 2014;15(12):550.

Luo K, Song Y, Guan Z, et al. A KRAS-Associated Signature for Prognostic, Immune and Chemical Anti-Cancer Drug-Response Prediction in Colon Cancer. Front Pharmacol. 2022;13:899725. Published 2022 Jun 14.

Luo W, Brouwer C. Pathview: a R/Biocondutor package for pathway-based data integration and visualization. Bioinformatics, 2013, 29(14):1830-1831.

Luo W, Pant G, Bhavnasi YK, Blanchard SG Jr, Brouwer C. Pathview Web: user friendly pathway visualization and data integration. Nucleic Acids Res. 2017;45(W1):W501-W508.

Ma J, Wang S, Zhao M, et al. Therapeutic potential of cladribine in combination with STAT3 inhibitor against multiple myeloma. BMC Cancer. 2011;11:255.

Machado ND, Heather LC, Harris AL, Higgins GS. Targeting mitochondrial oxidative phosphorylation: lessons, advantages, and opportunities. Br J Cancer. 2023 Oct;129(6):897-899.

Majumdar S, Buckles E, Estrada J, Koochekpour S. Aberrant DNA methylation and prostate cancer. Curr Genomics. 2011 Nov;12(7):486-505.

Malumbres M, Sotillo R, Santamaría D, et al. Mammalian cells cycle without the D-type cyclin-dependent kinases Cdk4 and Cdk6. Cell. 2004;118(4):493-504.

Martinez-Balibrea E, Martínez-Cardús A, Ginés A, et al. Tumor-Related Molecular Mechanisms of Oxaliplatin Resistance. Mol Cancer Ther. 2015;14(8):1767-1776.

Martínez-Jiménez F, Movasati A, Brunner SR, et al. Pan-cancer whole-genome comparison of primary and metastatic solid tumours. Nature. 2023;618(7964):333-341.

Martínez-Reyes I, Chandel NS. Cancer metabolism: looking forward. Nat Rev Cancer. 2021, 21; 669–680.

Marzo T, Ferraro G, Cucci LM, Pratesi A, Hansson Ö, Satriano C, Merlino A, La Mendola D. Oxaliplatin inhibits angiogenin proliferative and cell migration effects in prostate cancer cells. J Inorg Biochem. 2022 Jan;226:111657.

Matthews HK, Bertoli C, de Bruin RAM. Cell cycle control in cancer. Nat Rev Mol Cell Biol. 2022;23(1):74-88.

Melone MAB, Valentino A, Margarucci S, Galderisi U, Giordano A, Peluso G. The carnitine system and cancer metabolic plasticity. Cell Death Dis. 2018;9(2):228.

Menon SG, Sarsour EH, Spitz DR, et al. Redox regulation of the G1 to S phase transition in the mouse embryo fibroblast cell cycle. Cancer Res. 2003;63(9):2109-2117.

Menter DG, Davis JS, Broom BM, Overman MJ, Morris J, Kopetz S. Back to the Colorectal Cancer Consensus Molecular Subtype Future. Curr Gastroenterol Rep. 2019;21(2):5.

Meriggi F, Zaniboni A. Gemox: a widely useful therapy against solid tumors-review and personal experience. J Chemother. 2010;22(5):298-303.

Metallo CM, Gameiro PA, Bell EL, Mattaini KR, Yang J, Hiller K, Jewell CM, Johnson ZR, Irvine DJ, Guarente L, Kelleher JK, Vander Heiden MG, Iliopoulos O, Stephanopoulos G. Reductive glutamine metabolism by IDH1 mediates lipogenesis under hypoxia. Nature. 2011 Nov 20;481(7381):380-4.

Mondul AM, Moore SC, Weinstein SJ, Karoly ED, Sampson JN, Albanes D. Metabolomic analysis of prostate cancer risk in a prospective cohort: The alpha-tocolpherol, beta-carotene cancer prevention (ATBC) study. Int J Cancer. 2015 Nov 1;137(9):2124-32.

Monneret C. Platinum anticancer drugs. From serendipity to rational design. Ann Pharm Fr. 2011;69(6):286-295.

Morgan MA, Lawrence TS. Molecular Pathways: Overcoming Radiation Resistance by Targeting DNA Damage Response Pathways. Clin Cancer Res. 2015 Jul 1;21(13):2898-904.

Moser T, Ziemssen T, Sellner J. Real-world evidence for cladribine tablets in multiple sclerosis: further insights into efficacy and safety. Wien Med Wochenschr. 2022;172(15-16):365-372.

Mota-Martorell N, Jové M, Borrás C, et al. Methionine transsulfuration pathway is upregulated in long-lived humans. Free Radic Biol Med. 2021;162:38-52.

Mughal MJ, Bhadresha K, Kwok HF. CDK inhibitors from past to present: A new wave of cancer therapy. Semin Cancer Biol. 2023;88:106-122.

Mullen AR, Hu Z, Shi X, Jiang L, Boroughs LK, Kovacs Z, Boriack R, Rakheja D, Sullivan LB, Linehan WM, Chandel NS, DeBerardinis RJ. Oxidation of alpha-ketoglutarate is required for reductive carboxylation in cancer cells with mitochondrial defects. Cell Rep. 2014 Jun 12;7(5):1679-1690.

Mullen AR, Wheaton WW, Jin ES, et al. Reductive carboxylation supports growth in tumour cells with defective mitochondria. Nature. 2011;481(7381):385-388.

Mullen NJ, Singh PK. Nucleotide metabolism: a pan-cancer metabolic dependency. Nat Rev Cancer. 2023 May;23(5):275-294.

Murray-Stewart TR, Woster PM, Casero RA Jr. Targeting polyamine metabolism for cancer therapy and prevention. Biochem J. 2016;473(19):2937-2953.

Muzio G, Maggiora M, Paiuzzi E, Oraldi M, Canuto RA. Aldehyde dehydrogenases and cell proliferation. Free Radic Biol Med. 2012;52(4):735-746.

Myant KB, Cammareri P, McGhee EJ, Ridgway RA, Huels DJ, Cordero JB, Schwitalla S, Kalna G, Ogg EL, Athineos D, Timpson P, Vidal M, Murray GI, Greten FR, Anderson KI, Sansom OJ. ROS production and NF-κB activation triggered by RAC1 facilitate WNT-driven intestinal stem cell proliferation and colorectal cancer initiation. Cell Stem Cell. 2013 Jun 6;12(6):761-73.

Nakamura H, Takada K. Reactive oxygen species in cancer: Current findings and future directions. Cancer Sci. 2021 Oct;112(10):3945-3952.

National Cancer Institute: Cancer types [Internet]. National Cancer Institute at the National Institutes of Health (NIH). 2023. [accessed in March 2023]. Available from: https://www.cancer.gov/types

National Cancer Institute: Types of Cancer Treatment [Internet]. National Cancer Institute at the National Institutes of Health (NIH). [accessed in March 2023]. Available from: https://www.cancer.gov/about-cancer/treatment/types

Newman AC, Maddocks ODK. One-carbon metabolism in cancer. Br J Cancer. 2017;116(12):1499-1504.

Niwa T, Imagawa Y, Yamazaki H. Drug interactions between nine antifungal agents and drugs metabolized by human cytochromes P450. Curr Drug Metab. 2014;15(7):651-679.

Noronha A, Daníelsdóttir AD, Gawron P, Jóhannsson F, Jónsdóttir S, Jarlsson S, Gunnarsson JP, Brynjólfsson S, Schneider R, Thiele I, Fleming RM. ReconMap: an interactive visualization of human metabolism. Bioinformatics. 2017 Feb 15;33(4):605-607.

Novellasdemunt L, Antas P, Li VS. Targeting Wnt signaling in colorectal cancer. A Review in the Theme: Cell Signaling: Proteins, Pathways and Mechanisms. Am J Physiol Cell Physiol. 2015;309(8):C511-C521.

Nývltová E, Dietz JV, Seravalli J, Khalimonchuk O, Barrientos A. Coordination of metal center biogenesis in human cytochrome c oxidase. Nat Commun. 2022;13(1):3615.

Ogretmen B. Sphingolipid metabolism in cancer signalling and therapy. Nat Rev Cancer. 2018;18(1):33-50.

Oki E, Ando K, Nakanishi R, Sugiyama M, Nakashima Y, Kubo N, Kudou K, Saeki H, Nozoe T, Emi Y, Maehara Y. Recent advances in treatment for colorectal liver metastasis. Ann Gastroenterol Surg. 2018 Apr 17;2(3):167-175.

O'Leary B, Cutts RJ, Liu Y, et al. The Genetic Landscape and Clonal Evolution of Breast Cancer Resistance to Palbociclib plus Fulvestrant in the PALOMA-3 Trial. Cancer Discov. 2018;8(11):1390-1403. doi:10.1158/2159-8290.CD-18-0264

O'Neal J, Clem A, Reynolds L, et al. Inhibition of 6-phosphofructo-2-kinase (PFKFB3) suppresses glucose metabolism and the growth of HER2+ breast cancer. Breast Cancer Res Treat. 2016;160(1):29-40.

Otto T, Sicinski P. Cell cycle proteins as promising targets in cancer therapy. Nat Rev Cancer. 2017;17(2):93-115.

Pal R, Wei N, Song N, et al. Molecular subtypes of colorectal cancer in pre-clinical models show differential response to targeted therapies: Treatment implications beyond KRAS mutations. pLoS One. 2018;13(8):e0200836.

Pandit B, Royzen M. Recent Development of Prodrugs of Gemcitabine. Genes (Basel). 2022 Mar 5;13(3):466.

Pang Z, Zhou G, Ewald J, et al. Using MetaboAnalyst 5.0 for LC-HRMS spectra processing, multi-omics integration and covariate adjustment of global metabolomics data. Nat Protoc. 2022;17(8):1735-1761.

Panieri E, Santoro MM. ROS homeostasis and metabolism: a dangerous liason in cancer cells. Cell Death Dis. 2016;7(6):e2253.

Park H, Youk J, Kim I, et al. Comparison of cladribine- and fludarabine-based induction chemotherapy in relapsed or refractory acute myeloid leukaemia. Ann Hematol. 2016;95(11):1777-1786.

Park SH, Lim DH, Sohn TS, et al. A randomized phase III trial comparing adjuvant single-agent S1, S-1 with oxaliplatin, and postoperative chemoradiation with S-1 and oxaliplatin in patients with node-positive gastric cancer after D2 resection: the ARTIST 2 trial☆. Ann Oncol. 2021;32(3):368-374.

Parker C, Castro E, Fizazi K, Heidenreich A, Ost P, Procopio G, Tombal B, Gillessen S; Prostate cancer: ESMO Clinical Practice Guidelines for diagnosis, treatment, and follow-up. Ann Oncol. 2020, 31(9):1119-1134.

Pavlova NN, Hui S, Ghergurovich JM, et al. As Extracellular Glutamine Levels Decline, Asparagine Becomes an Essential Amino Acid. Cell Metab. 2018;27(2):428-438.e5.

Pavlova NN, Thompson CB. The Emerging Hallmarks of Cancer Metabolism. Cell Metab. 2016 Jan 12;23(1):27-47.

Pavlova NN, Zhu J, Thompson CB. The hallmarks of cancer metabolism: Still emerging. Cell Metab. 2022;34(3):355-377.

Pfeuffer S, Rolfes L, Hackert J, et al. Effectiveness and safety of cladribine in MS: Real-world experience from two tertiary centres. Mult Scler. 2022;28(2):257-268.

Phillips CM, Zatarain JR, Nicholls ME, et al. Upregulation of Cystathionine-β-Synthase in Colonic Epithelia Reprograms Metabolism and Promotes Carcinogenesis. Cancer Res. 2017 Nov 1;77(21):5741-5754.

Piérard GE, Hermanns-Lê T, Delvenne P, Piérard-Franchimont C. Miconazole, a pharmacological barrier to skin fungal infections. Expert Opin Pharmacother. 2012;13(8):1187-1194.

Pinho SS, Reis CA. Glycosylation in cancer: mechanisms and clinical implications. Nat Rev Cancer. 2015;15(9):540-555.

Pong K, Doctrow SR, Huffman K, Adinolfi CA, Baudry M. Attenuation of staurosporine-induced apoptosis, oxidative stress, and mitochondrial dysfunction by synthetic superoxide dismutase and catalase mimetics, in cultured cortical neurons. Exp Neurol. 2001;171(1):84-97.

Porporato PE, Filigheddu N, Pedro JMB, Kroemer G, Galluzzi L. Mitochondrial metabolism and cancer. Cell Res. 2018;28(3):265-280.

Poupon L, Lamoine S, Pereira V, et al. Targeting the TREK-1 potassium channel via riluzole to eliminate the neuropathic and depressive-like effects of oxaliplatin. Neuropharmacology. 2018;140:43-61. Doi:10.1016/j.neuropharm.2018.07.026

Pushpakom S, Iorio F, Eyers PA, Escott KJ, Hopper S, Wells A, Doig A, Guilliams T, Latimer J, McNamee C, Norris A, Sanseau P, Cavalla D, Pirmohamed M. Drug repurposing: progress, challenges and recommendations. Nat Rev Drug Discov. 2019 Jan;18(1):41-58.

Qasrawi A, Bahaj W, Qasrawi L, Abughanimeh O, Foxworth J, Gaur R. Cladribine in the remission induction of adult acute myeloid leukemia: where do we stand?. Ann Hematol. 2019;98(3):561-579.

Qu Q, Zeng F, Liu X, Wang QJ, Deng F. Fatty acid oxidation and carnitine palmitoyltransferase I: emerging therapeutic targets in cancer. Cell Death Dis. 2016 May 19;7(5):e2226. doi: 10.1038/cddis.2016.132. PMID: 27195673; PMCID: PMC4917665.

Rebello RJ, Oing C, Knudsen KE et al. Prostate cancer. Nat Rev Dis Primers. 2021, 7:9.

Reimers AM, Reimers AC. The steady-state assumption in oscillating and growing systems. J Theor Biol. 2016;406:176-186.

Reisbeck L, Linder B, Tascher G, et al. The iron chelator and OXPHOS inhibitor VLX600 induces mitophagy and an autophagy-dependent type of cell death in glioblastoma cells. Am J Physiol Cell Physiol. 2023;325(6):C1451-C1469.

Reya T, Clevers H. Wnt signaling in stem cells and cancer. Nature. 2005;434(7035):843-850.

Romero N, Rogers G, Neilson A, and Dranka BP. Quantifying Cellular ATP Production Rate Using Agilent Seahorse XF Technology. [White paper]. Printed in the USA, April 12, 2018.

Romero N, Swain P, Neilson A, and Dranka BP. Improving Quantification of Cellular Glycolytic Rate Using Agilent Seahorse XF Technology [White paper]. Printed in the USA, February 18, 2021.

Rosenberg B, Vancamp L, Krigas T. Inhibition of cell division in escherichia coli by electrolysis products from a platinum electrode. Nature. 1965;205:698-699.

Rosenthal RA, Fish B, Hill RP, et al. Salen Mn complexes mitigate radiation injury in normal tissues. Anticancer Agents Med Chem. 2011;11(4):359-372.

Rottenberg S, Disler C, Perego P. The rediscovery of platinum-based cancer therapy. Nat Rev Cancer. 2021;21(1):37-50.

Ruscetti M, Morris JP 4th, Mezzadra R, Russell J, Leibold J, Romesser PB, Simon J, Kulick A, Ho YJ, Fennell M, Li J, Norgard RJ, Wilkinson JE, Alonso-Curbelo D, Sridharan R, Heller DA, de Stanchina E, Stanger BZ, Sherr CJ, Lowe SW. Senescence-Induced Vascular Remodeling Creates Therapeutic Vulnerabilities in Pancreas Cancer. Cell. 2020 Apr 16;181(2):424-441.e21.

Sabharwal A, Middleton MR. Exploiting the role of O6-methylguanine-DNA-methyltransferase (MGMT) in cancer therapy. Curr Opin Pharmacol. 2006;6(4):355-363.

Sanderson SM, Gao X, Dai Z, Locasale JW. Methionine metabolism in health and cancer: a nexus of diet and precision medicine. Nat Rev Cancer. 2019;19(11):625-637.

Santamaría D, Barrière C, Cerqueira A, et al. Cdk1 is sufficient to drive the mammalian cell cycle. Nature. 2007;448(7155):811-815.

Sato M, Toyama T, Kim MS, et al. Increased putrescine levels due to ODC1 overexpression prevents mitochondrial dysfunction-related apoptosis induced by methylmercury. Life Sci. 2020;256:118031.

Sawers L, Ferguson MJ, Ihrig BR, Young HC, Chakravarty P, Wolf CR, Smith G. Glutathione S-transferase P1 (GSTP1) directly influences platinum drug chemosensitivity in ovarian tumour cell lines. Br J Cancer. 2014 Sep 9;111(6):1150-8.

Schettini F, De Santo I, Rea CG, et al. CDK 4/6 Inhibitors as Single Agent in Advanced Solid Tumors. Front Oncol. 2018;8:608. Published 2018 Dec 12.

Schmidt BJ, Ebrahim A, Metz TO, Adkins JN, Palsson BØ, Hyduke DR. GIM3E: condition-specific models of cellular metabolism developed from metabolomics and expression data. Bioinformatics. 2013;29(22):2900-2908.

SEER*Explorer: An interactive website for SEER cancer statistics [Internet]. Surveillance Research Program, National Cancer Institute; 2023 Apr 19. Available from: https://seer.cancer.gov/statistics-network/explorer/

Segrè D, Vitkup D, Church GM. Analysis of optimality in natural and perturbed metabolic networks. Proc Natl Acad Sci U S A. 2002;99(23):15112-15117.

Seidel JA, Otsuka A, Kabashima K. Anti-PD-1 and Anti-CTLA-4 Therapies in Cancer: Mechanisms of Action, Efficacy, and Limitations. Front Oncol. 2018;8:86.

Selivanov VA, Benito A, Miranda A, et al. MIDcor, an R-program for deciphering mass interferences in mass spectra of metabolites enriched in stable isotopes. BMC Bioinformatics. 2017;18(1):88. Published 2017 Feb 3.

Selivanov VA, Marin S, Tarragó-Celada J, et al. Software Supporting a Workflow of Quantitative Dynamic Flux Maps Estimation in Central Metabolism from SIRM Experimental Data. Methods Mol Biol. 2020;2088:271-298.

Ser Z, Gao X, Johnson C, et al. Targeting One Carbon Metabolism with an Antimetabolite Disrupts Pyrimidine Homeostasis and Induces Nucleotide Overflow. Cell Rep. 2016;15(11):2367-2376.

Seth Nanda C, Venkateswaran SV, Patani N, Yuneva M. Defining a metabolic landscape of tumours: genome meets metabolism. Br J Cancer. 2020;122(2):136-149.

Shah MA, Rogoff HA. Implications of reactive oxygen species on cancer formation and its treatment. Semin. Oncol. 2021, 48(3):238-245.

Shah MH, Liu GS, Thompson EW, Dusting GJ, Peshavariya HM. Differential effects of superoxide dismutase and superoxide dismutase/catalase mimetics on human breast cancer cells. Breast Cancer Res Treat. 2015;150(3):523-534.

Shen W, Gao C, Cueto R, Liu L, Fu H, Shao Y, Yang WY, Fang P, Choi ET, Wu Q, Yang X, Wang H. Homocysteine-methionine cycle is a metabolic sensor system controlling methylation-regulated pathological signaling. Redox Biol. 2020 Jan;28:101322.

Shi L, Pan H, Liu Z, Xie J, Han W. Roles of PFKFB3 in cancer. Signal Transduct Target Ther. 2017;2:17044.

Siegel RL, Miller KD, Wagle NS, Jemal A. Cancer statistics, 2023. CA Cancer J Clin. 2023;73(1):17-48.

Sies H, Jones DP. Reactive oxygen species (ROS) as pleiotropic physiological signalling agents. Nat Rev Mol Cell Biol. 2020, 21(7):363-383.

Singh MP, Rai S, Pandey A, Singh NK, Srivastava S. Molecular subtypes of colorectal cancer: An emerging therapeutic opportunity for personalized medicine. Genes Dis. 2019;8(2):133-145.

Sonveaux P, Végran F, Schroeder T, et al. Targeting lactate-fueled respiration selectively kills hypoxic tumor cells in mice. J Clin Invest. 2008;118(12):3930-3942.

Sorah JD, Moore DT, Reilley MJ, et al. Phase II Single-Arm Study of Palbociclib and Cetuximab Rechallenge in Patients with KRAS/NRAS/BRAF Wild-Type Colorectal Cancer. Oncologist. 2022;27(12):1006-e930.

Spinelli JB, Yoon H, Ringel AE, Jeanfavre S, Clish CB, Haigis MC. Metabolic recycling of ammonia via glutamate dehydrogenase supports breast cancer biomass. Science. 2017;358(6365):941-946.

Sriramkumar S, Sood R, , et al. Platinum-induced mitochondrial OXPHOS contributes to cancer stem cell enrichment in ovarian cancer. J Transl Med. 2022; 20: 246

Stine ZE, Schug ZT, Salvino JM, Dang CV. Targeting cancer metabolism in the era of precision oncology. Nat Rev Drug Discov. 2022;21(2):141-162.

Stordal B, Pavlakis N, Davey R. Oxaliplatin for the treatment of cisplatin-resistant cancer: a systematic review. Cancer Treat Rev. 2007;33(4):347-357.

Subramanian A, Tamayo P, Mootha VK, et al. Gene set enrichment analysis: a knowledge-based approach for interpreting genome-wide expression profiles. Proc Natl Acad Sci U S A. 2005;102(43):15545-15550.

Suppramote O, Prasopporn S, Aroonpruksakul S, Ponvilawan B, Makjaroen J, Suntiparpluacha M, Korphaisarn K, Charngkaew K, Chanwat R, Pisitkun T, Okada S, Sampattavanich S, Jirawatnotai S. The Acquired Vulnerability Caused by CDK4/6 Inhibition Promotes Drug Synergism Between Oxaliplatin and Palbociclib in Cholangiocarcinoma. Front Oncol. 2022 May 17;12:877194.

Sveen A, Bruun J, Eide PW, et al. Colorectal Cancer Consensus Molecular Subtypes Translated to Preclinical Models Uncover Potentially Targetable Cancer Cell Dependencies. Clin Cancer Res. 2018;24(4):794-806.

Tajan M, Vousden KH. Dietary Approaches to Cancer Therapy. Cancer Cell. 2020;37(6):767-785.

Tan Y, Li J, Zhao G, et al. Metabolic reprogramming from glycolysis to fatty acid uptake and beta-oxidation in platinum-resistant cancer cells. Nat Commun. 2022;13(1):4554.

Taniguchi K, Sakai M, Sugito N, et al. PKM1 is involved in resistance to anti-cancer drugs. Biochem Biophys Res Commun. 2016;473(1):174-180.

Tarrado-Castellarnau M, de Atauri P, Tarragó-Celada J, et al. De novo MYC addiction as an adaptive response of cancer cells to CDK4/6 inhibition. Mol Syst Biol. 2017;13(10):940.

Tarragó-Celada J, Cascante M. Targeting the Metabolic Adaptation of Metastatic Cancer. Cancers (Basel). 2021;13(7):1641.

Tarragó-Celada J, Foguet C, Tarrado-Castellarnau M, et al. Cysteine and Folate Metabolism Are Targetable Vulnerabilities of Metastatic Colorectal Cancer. Cancers (Basel). 2021;13(3):425. Published 2021 Jan 23.

Tedeschi PM, Markert EK, Gounder M, et al. Contribution of serine, folate and glycine metabolism to the ATP, NADPH and purine requirements of cancer cells. Cell Death Dis. 2013;4(10):e877. Published 2013 Oct 24.

The jamovi project (2021). jamovi. (Version 2.2) [Computer Software]. Retrieved from: https://www.jamovi.org

Tien AH, Sadar MD. Cyclin-dependent Kinase 4/6 Inhibitor Palbociclib in Combination with Ralaniten Analogs for the Treatment of Androgen Receptor-positive Prostate and Breast Cancers. Mol Cancer Ther. 2022;21(2):294-309.

Tocris Bioscience; Cancer Research Product Guide. [Internet]. Edition 3. 2016. Available from: https://www.tocris.com/literature/product-guides/cancer

U.S. Food and Drug Administration; Postmarket Drug Safety Information for Patients and Providers: Eloxatin Information. [Internet]. U.S. Food and Drug Administration (FDA). Last update: 10 May 2015 [accessed in March 2023]. Available from: https://www.fda.gov/drugs/postmarket-drug-safety-information-patients-and-providers/eloxatin-information

U.S. Food and Drug Administration; Postmarket Drug Safety Information for Patients and Providers: Palbociclib (IBRANCE) Information. [Internet]. U.S. Food and Drug Administration (FDA). Last update: 31 March 2017 [accessed in March 2023]. Available from: https://www.fda.gov/drugs/resources-information-approved-drugs/palbociclib-ibrance

Unno J, Itaya A, Taoka M, et al. FANCD2 binds CtIP and regulates DNA-end resection during DNA interstrand crosslink repair. Cell Rep. 2014;7(4):1039-1047.

Valcárcel LV, Torrano V, Tobalina L, Carracedo A, Planes FJ. rMTA: robust metabolic transformation analysis. Bioinformatics. 2019;35(21):4350-4355.

Van Cutsem E, Cervantes A, Adam R, et al. ESMO consensus guidelines for the management of patients with metastatic colorectal cancer. Ann Oncol. 2016;27(8):1386-1422.

Van der Veen JN, Kennelly JP, Wan S, Vance JE, Vance DE, Jacobs RL. The critical role of phosphatidylcholine and phosphatidylethanolamine metabolism in health and disease. Biochim Biophys Acta Biomembr. 2017;1859(9 Pt B):1558-1572.

Vincent A, Thauvin M, Quévrain E, et al. Evaluation of the compounds commonly known as superoxide dismutase and catalase mimics in cellular models. J Inorg Biochem. 2021;219:111431.

Visentin M, Zhao R, Goldman ID. The antifolates. Hematol Oncol Clin North Am. 2012 Jun;26(3):629-48, ix.

Vodenkova S, Buchler T, Cervena K, Veskrnova V, Vodicka P, Vymetalkova V. 5-fluorouracil and other fluoropyrimidines in colorectal cancer: Past, present and future. Pharmacol Ther. 2020;206:107447.

Voland C, Bord A, Péleraux A, et al. Repression of cell cycle-related proteins by oxaliplatin but not cisplatin in human colon cancer cells. Mol Cancer Ther. 2006;5(9):2149-2157.

Wadosky KM, Shourideh M, Goodrich DW, Koochekpour S. Riluzole induces AR degradation via endoplasmic reticulum stress pathway in androgen-dependent and castration-resistant prostate cancer cells. *Prostate*. 2019;79(2):140-150. doi:10.1002/pros.23719

Wagener, C., Stocking, C., & Müller, O. Cancer Signaling: from molecular biology to targeted therapy. John Wiley & Sons. 2016

Wang A, Fang M, Jiang H, et al. Palbociclib promotes the antitumor activity of Venetoclax plus Azacitidine against acute myeloid leukemia. Biomed Pharmacother. 2022;153:113527.

Wang G, Zhao D, Spring DJ, DePinho RA. Genetics and biology of prostate cancer. Genes Dev. 2018;32(17-18):1105-1140.

Wang H, Nicolay BN, Chick JM, Gao X, Geng Y, Ren H, Gao H, Yang G, Williams JA, Suski JM, Keibler MA, Sicinska E, Gerdemann U, Haining WN, Roberts TM, Polyak K, Gygi SP, Dyson NJ, Sicinski P. The metabolic function of cyclin D3-CDK6 kinase in cancer cell survival. Nature. 2017 Jun 15;546(7658):426-430.

Wang Q, Hardie RA, Hoy AJ, et al. Targeting ASCT2-mediated glutamine uptake blocks prostate cancer growth and tumour development. J Pathol. 2015;236(3):278-289.

Wang Y, Lu JH, Wang F, et al. Inhibition of fatty acid catabolism augments the efficacy of oxaliplatin-based chemotherapy in gastrointestinal cancers. Cancer Lett. 2020;473:74-89.

Wang YN, Zeng ZL, Lu J, et al. CPT1A-mediated fatty acid oxidation promotes colorectal cancer cell metastasis by inhibiting anoikis. Oncogene. 2018;37(46):6025-6040.

Wang Z, Fan M, Candas D, Zhang TQ, Qin L, Eldridge A, Wachsmann-Hogiu S, Ahmed KM, Chromy BA, Nantajit D, Duru N, He F, Chen M, Finkel T, Weinstein LS, Li JJ. Cyclin B1/Cdk1 coordinates mitochondrial respiration for cell-cycle G2/M progression. Dev Cell. 2014 Apr 28;29(2):217-32.

Wang Z. Cell Cycle Progression and Synchronization: An Overview. Methods Mol Biol. 2022;2579:3-23.

Warburg O. Über den Stoffwechsel der Carcinomzelle. Naturwissenschaften. 1924;12:1131–1137.

Warnke C, Wiendl H, Hartung HP, Stüve O, Kieseier BC. Identification of targets and new developments in the treatment of multiple sclerosis--focus on cladribine. Drug Des Devel Ther. 2010 Jul 21;4:117-26.

Wei Z, Liu X, Cheng C, Yu W, Yi P. Metabolism of Amino Acids in Cancer. Front Cell Dev Biol. 2021 Jan 12;8:603837.

Weng N, Zhang Z, Tan Y, Zhang X, Wei X, Zhu Q. Repurposing antifungal drugs for cancer therapy. J Adv Res. 2023 Jun;48:259-273.

Whittaker SR, Mallinger A, Workman P, Clarke PA. Inhibitors of cyclin-dependent kinases as cancer therapeutics. Pharmacol Ther. 2017;173:83-105.

William-Faltaos S, Rouillard D, Lechat P, Bastian G. Cell cycle arrest by oxaliplatin on cancer cells. Fundam Clin Pharmacol. 2007;21(2):165-172.

Williams NC, O'Neill LAJ. A Role for the Krebs Cycle Intermediate Citrate in Metabolic Reprogramming in Innate Immunity and Inflammation. Front Immunol. 2018;9:141.

Wu HL, Gong Y, Ji P, Xie YF, Jiang YZ, Liu GY. Targeting nucleotide metabolism: a promising approach to enhance cancer immunotherapy. J Hematol Oncol. 2022;15(1):45. Published 2022 Apr 27.

Wu Q, Zhang W, Xue L, et al. APC/C-CDH1-Regulated IDH3β Coordinates with the Cell Cycle to Promote Cell Proliferation. Cancer Res. 2019;79(13):3281-3293.

Wu Y, Zhang D, Wu B, et al. Synergistic Activity of an Antimetabolite Drug and Tyrosine Kinase Inhibitors against Breast Cancer Cells. Chem Pharm Bull (Tokyo). 2017;65(8):768-775.

Xiao Y, Jin L, Deng C, et al. Inhibition of PFKFB3 induces cell death and synergistically enhances chemosensitivity in endometrial cancer. Oncogene. 2021;40(8):1409-1424.

Xie YH, Chen YX, Fang JY. Comprehensive review of targeted therapy for colorectal cancer. Signal Transduct Target Ther. 2020 Mar 20;5(1):22.

Xu H, He Y, Ma J, et al. Inhibition of pyruvate dehydrogenase kinase-1 by dicoumarol enhances the sensitivity of hepatocellular carcinoma cells to oxaliplatin via metabolic reprogramming. Int J Oncol. 2020;57(3):733-742.

Xu L, Jiao J, Sun X, Sang W, Gao X, Yang P, Yan D, Song X, Sun C, Liu M, Qin Y, Tian Y, Zhu F, Zeng L, Li Z, Xu K. Cladribine Induces ATF4 Mediated Apoptosis and Synergizes with SAHA in Diffuse Large B-Cell Lymphoma Cells. Int J Med Sci. 2020 May 30;17(10):1375-1384.

Yang L, Venneti S, Nagrath D. Glutaminolysis: A Hallmark of Cancer Metabolism. Annu Rev Biomed Eng. 2017 Jun 21;19:163-194.

Yang W, Soares J, Greninger P, Edelman EJ, Lightfoot H, Forbes S, Bindal N, Beare D, Smith JA, Thompson IR, Ramaswamy S, Futreal PA, Haber DA, Stratton MR, Benes C, McDermott U, Garnett MJ. Genomics of Drug Sensitivity in Cancer (GDSC): a resource for therapeutic biomarker discovery in cancer cells. Nucleic Acids Res. 2013 Jan;41(Database issue):D955-61.

Yi M, Ban Y, Tan Y, Xiong W, Li G, Xiang B. 6-Phosphofructo-2-kinase/fructose-2,6-biphosphatase 3 and 4: A pair of valves for fine-tuning of glucose metabolism in human cancer. Mol Metab. 2019 Feb;20:1-13.

Yin M, Yan J, Martinez-Balibrea E, Graziano F, Lenz HJ, Kim HJ, Robert J, Im SA, Wang WS, Etienne-Grimaldi MC, Wei Q. ERCC1 and ERCC2 polymorphisms predict clinical outcomes of oxaliplatin-based chemotherapies in gastric and colorectal cancer: a systemic review and meta-analysis. Clin Cancer Res. 2011 Mar 15;17(6):1632-40.

Yoo HC, Yu YC, Sung Y, Han JM. Glutamine reliance in cell metabolism. Exp Mol Med. 2020;52(9):1496-1516.

Yoon H, Lee S. Fatty Acid Metabolism in Ovarian Cancer: Therapeutic Implications. Int J Mol Sci. 2022 Feb 16;23(4):2170.

Yuan SY, Shiau MY, Ou YC, et al. Miconazole induces apoptosis via the death receptor 5-dependent and mitochondrial-mediated pathways in human bladder cancer cells. Oncol Rep. 2017;37(6):3606-3616.

Zabala-Letona A, Arruabarrena-Aristorena A, Martín-Martín N, et al. mTORC1-dependent AMD1 regulation sustains polyamine metabolism in prostate cancer. Nature. 2017;547(7661):109-113.Cutruzzolà F, Giardina G, Marani M, et al. Glucose Metabolism in the Progression of Prostate Cancer. Front Physiol. 2017;8:97.

Zamboni N, Saghatelian A, Patti GJ. Defining the metabolome: size, flux, and regulation. Mol Cell. 2015 May 21;58(4):699-706.

Zaugg K, Yao Y, Reilly PT, Kannan K, Kiarash R, Mason J, Huang P, Sawyer SK, Fuerth B, Faubert B, Kalliomäki T, Elia A, Luo X, Nadeem V, Bungard D, Yalavarthi S, Growney JD, Wakeham A, Moolani Y, Silvester J, Ten AY, Bakker W, Tsuchihara K, Berger SL, Hill RP, Jones RG, Tsao M, Robinson MO, Thompson CB, Pan G, Mak TW. Carnitine palmitoyltransferase 1C promotes cell survival and tumor growth under conditions of metabolic stress. Genes Dev. 2011 May 15;25(10):1041-51.

Zhan T, Rindtorff N, Boutros M. Wnt signaling in cancer. Oncogene. 2017;36(11):1461-1473.

Zhang C, Xu C, Gao X, Yao Q. Platinum-based drugs for cancer therapy and anti-tumor strategies. Theranostics. 2022 Feb 7;12(5):2115-2132.

Zhang J, Fan J, Venneti S, Cross JR, Takagi T, Bhinder B, Djaballah H, Kanai M, Cheng EH, Judkins AR, Pawel B, Baggs J, Cherry S, Rabinowitz JD, Thompson CB. Asparagine plays a critical role in regulating cellular adaptation to glutamine depletion. Mol Cell. 2014 Oct 23;56(2):205-218.

Zhang J, Zhou L, Zhao S, Dicker DT, El-Deiry WS. The CDK4/6 inhibitor palbociclib synergizes with irinotecan to promote colorectal cancer cell death under hypoxia. Cell Cycle. 2017 Jun 18;16(12):1193-1200.

Zhang L, Shay JW. Multiple Roles of APC and its Therapeutic Implications in Colorectal Cancer. J Natl Cancer Inst. 2017 Aug 1;109(8):djw332.

Zhang M, Raveche ES. Apoptosis induction in fludarabine resistant malignant B-1 cells by G2-M cell cycle arrest. Oncol Rep. 1998;5(1):23-30.

Zhang N, Fu JN, Chou TC. Synergistic combination of microtubule targeting anticancer fludelone with cytoprotective panaxytriol derived from panax ginseng against MX-1 cells in vitro: experimental design and data analysis using the combination index method. Am J Cancer Res. 2015;6(1):97-104.

Zhang X, Fryknäs M, Hernlund E, Fayad W, De Milito A, Olofsson MH, Gogvadze V, Dang L, Påhlman S, Schughart LA, Rickardson L, D'Arcy P, Gullbo J, Nygren P, Larsson R, Linder S. Induction of mitochondrial dysfunction as a strategy for targeting tumour cells in metabolically compromised microenvironments. Nat Commun. 2014;5:3295.

Zhang Z, Liu R, Shuai Y, et al. ASCT2 (SLC1A5)-dependent glutamine uptake is involved in the progression of head and neck squamous cell carcinoma. Br J Cancer. 2020;122(1):82-93.

Zhao Q, Wu ZE, Li B, Li F. Recent advances in metabolism and toxicity of tyrosine kinase inhibitors. Pharmacol Ther. 2022;237:108256.

Zheng J, Ramirez VD. Piceatannol, a stilbene phytochemical, inhibits mitochondrial F0F1-ATPase activity by targeting the F1 complex. Biochem Biophys Res Commun. 1999 Aug 2;261(2):499-503.

Zhou H, Liu Z, Wang Y, et al. Colorectal liver metastasis: molecular mechanism and interventional therapy. Signal Transduct Target Ther. 2022;7(1):70.

Zhou J, Kang Y, Chen L, Wang H, Liu J, Zeng S, Yu L. The Drug-Resistance Mechanisms of Five Platinum-Based Antitumor Agents. Front Pharmacol. 2020 Mar 20;11:343.

Zhou J, Yang T, Liu L, Lu B. Chemotherapy oxaliplatin sensitizes prostate cancer to immune checkpoint blockade therapies via stimulating tumor immunogenicity. Mol Med Rep. 2017 Sep;16(3):2868-2874.

Zhou Y, Bollu LR, Tozzi F, et al. ATP citrate lyase mediates resistance of colorectal cancer cells to SN38. Mol Cancer Ther. 2013;12(12):2782-2791.

Zhou Y, Tao L, Zhou X, et al. DHODH and cancer: promising prospects to be explored. Cancer Metab. 2021;9(1):22.

Zhu Y, Piao C, Zhang Z, Jiang Y, Kong C. The potential role of c-MYC and polyamine metabolism in multiple drug resistance in bladder cancer investigated by metabonomics. Genomics. 2022;114(1):125-137.

Zhu Z, Turner NC, Loi S, et al. Comparative biomarker analysis of PALOMA-2/3 trials for palbociclib. NPJ Precis Oncol. 2022;6(1):56.

Ziras N, Potamianou A, Varthalitis I, et al. Multicenter phase II study of gemcitabine and oxaliplatin (GEMOX) as second-line chemotherapy in colorectal cancer patients pretreated with 5-fluorouracil plus irinotecan. Oncology. 2006;70(2):106-114.

Zou Z, Hu X, Luo T, Ming Z, Chen X, Xia L, Luo W, Li J, Xu N, Chen L, Cao D, Wen M, Kong F, Peng K, Xie Y, Li X, Ma D, Yang C, Chen C, Yi W, Liu O, Liu S, Luo J, Luo Z. Naturally-occurring spinosyn A and its derivatives function as argininosuccinate synthase activator and tumor inhibitor. Nat Commun. 2021 Apr 15;12(1):2263.

APPENDIX

APPENDIX I

I.1. Essential amino acids (EAAs) measured in SW620 cells after Oxaliplatin treatment.

Extracellular consumption and production rates of essential amino acids (EAAs) displayed no significant differences in the production or consumption from the medium and after Oxaliplatin treatment in the colorectal cell line SW620 (**Figure I.1.**).

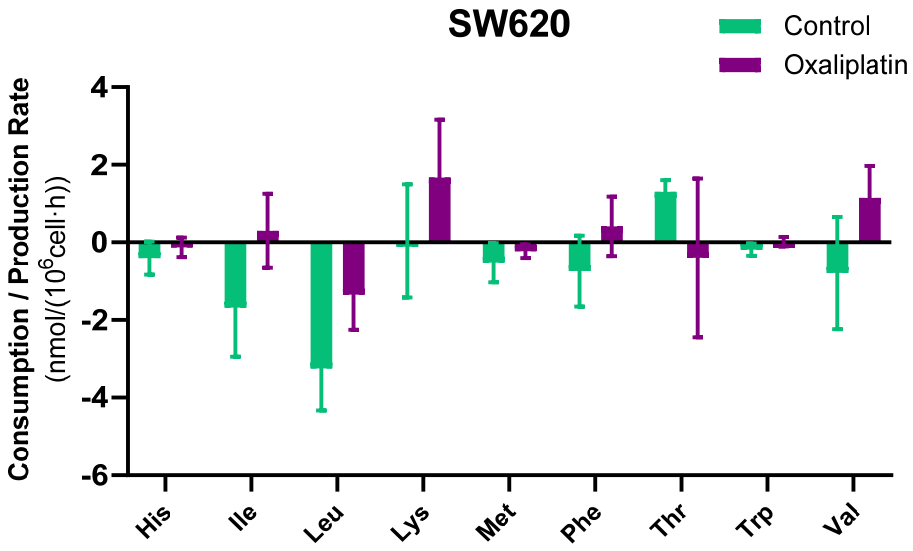

Figure I.1. Extracellular consumption and production rates of essential amino acids in SW620 cells. Extracellular consumption and production rates of EAAs measured after 48 h in control and Oxaliplatin-treated (0.25 μM) SW620 cells. Amino acids that were not significantly produced or consumed from the medium are also shown. An independent sample t-test was applied for relative comparison between the two groups. No significant differences were found ($p > 0.05$).

I.2. Differential expression of genes associated with detailed pathways after Oxaliplatin treatment in SW620 and PC-3 cells.

Table I.1. Differential expression of genes encoding for the most important enzymes in the serine biosynthesis, folate cycle, methionine cycle, methionine salvage pathway, polyamine metabolism, and urea cycle. Differential gene expression in terms of Log 2 fold-change (Log2FC) after 48 h of treatment with Oxaliplatin regarding the principal encoding genes of the indicated metabolic pathways in SW620 and PC-3. * Indicates adjusted p-value < 0.05. NA (not-assigned) indicates not gene expression.

Gene	Encoding protein	Log2FC SW620	Log2FC PC-3
Serine biosynthesis			
PHGDH	*phosphoglycerate dehydrogenase*	-0.32	-0.92 *
PSAT1	*phosphoserine aminotransferase 1*	-0.31	-0.55 *
PSPH	*phosphoserine phosphatase*	-0.39 *	-0.18
Folate cycle			
SHMT1	*serine hydroxymethyltransferase 1*	+0.19	-0.14
SHMT2	*serine hydroxymethyltransferase 2*	-0.58 *	-0.53 *
MTHFD1	*methylenetetrahydrofolate dehydrogenase*	+0.27 *	-0.17
MTHFD1L	*methylenetetrahydrofolate dehydrogenase (NADP+ dependent) 1 like*	-0.19 *	-0.66 *
MTHFD2	*methylenetetrahydrofolate dehydrogenase (NADP+ dependent) 2*	-0.53 *	-0.05
MTHFD2L	*methylenetetrahydrofolate dehydrogenase (NADP+ dependent) 2 like*	+0.33	+1.27 *
MTHFR	*methylenetetrahydrofolate reductase*	+0.26	+0.43
DHFR	*dihydrofolate reductase*	+0.07	-0.11
Methionine cycle			
MTR	*5-methyltetrahydrofolate-homocysteine methyltransferase*	+0.01	-0.41 *
AHCY	*adenosylhomocysteinase*	-0.23 *	-0.27 *
Methionine salvage pathway			
MTAP	*methylthioadenosine phosphorylase*	-0.02	-0.52 *
AMD1	*adenosylmethionine decarboxylase 1*	+0.27 *	-0.28
Polyamine metabolism			
ODC1	*ornithine decarboxylase 1*	+0.44 *	-0.74 *
SRM	*spermidine synthase*	+0.28	-0.38 *
SMS	*spermine synthase*	-0.31	-0.53 *
SAT1	*spermidine/spermine N1-acetyltransferase 1*	-0.46 *	+1.52 *
SMOX	*spermine oxidase*	-0.02	+1.07 *
PAOX	*polyamine oxidase*	-1.95	-2.3
Urea cycle			
OTC	*ornithine transcarbamylase*	-1.37	NA
ASS1	*argininosuccinate synthase 1*	-0.73 *	+0.74
NOS1	*nitric oxide synthase 1*	+0.55	-3.76 *
ASL	*argininosuccinate lyase*	+0.06	+0.21
ARG1	*arginase 1*	NA	NA
ARG2	*arginase 2*	+0.01	-0.28

APPENDIX II

NGS experiments were performed in the Genomics Unit of the CNIC. RNA sequencing analysis data, gene sets enrichment analysis (GSEA), computational multi-omics data integration, Genome-Scale Metabolic Modeling (GSMM) reconstruction of SW620 and PC-3 cell lines, metabolic flux analysis distribution, and predictions of metabolic inhibitors were performed by Dr Carles Foguet, from the computational team within our research group.

II.1. Transcriptomics

RNA sequencing library preparation, sequencing, and generation of FastQ files were performed in an external service as indicated above, from data extracted and collected using Qiagen RNeasy kit (Qiagen, Hilden, Germany) (data extraction is detailed in **Materials and methods**). Total RNA (200 ng) was used to generate barcoded RNA-seq libraries using the NEBNext Ultra II Directional RNA Library preparation kit (New England Biolabs) according to manufacturer's instructions. First, poly A+ RNA was purified using poly-T oligo- attached magnetic beads followed by fragmentation and first and second cDNA strand synthesis. Next, cDNA ends were repaired and adenylated. The NEBNext adaptor was then ligated followed by second strand removal, uracil excision from the adaptor and PCR amplification. The size of the libraries was checked using the Agilent 2100 Bioanalyzer and the concentration was determined using the Qubit® fluorometer (ThermoFisher). Libraries were sequenced on a HiSeq 2500 (Illumina) and processed with RTA v1.18.66.3. FastQ files for each sample were obtained using bcl2fastq v2.20.0.422 software (Illumina). RNA-sequencing data normalization of read counts per gene for differential analysis of count data was performed through DESeq2 method (Love et al., 2014).

II.2. Metabolic modeling and target identification

The human genome-scale metabolic model (GSMMs) Recon3D (Brunk et al., 2018) was used as a framework to integrate multiple layers of data collected from non-treated and treated cells to build cell line-specific genome-scale maps and predict putative targets in the four conditions, including SW620 treated with Oxaliplatin, PC-3 treated with Oxaliplatin, and PC-3 treated with Palbociclib (**Figure II.1.**).

Data obtained from targeted metabolomics, metabolites consumption and production rates, and the respiratory assay parameters related to oxygen consumption rate (OCR) was used as input in several steps of the analysis. Metabolite consumption and production rates were normalized by cell count and growth rate as described in *Equation 1* and mapped to exchange reactions in the model.

Eq. 1

$$Consumption/production\ rate = \frac{\Delta M}{\Delta N} \cdot \mu$$

where,

$\Delta M = M_f - M_0$ is the consumed/produced amount of each metabolite (µmol).

$\Delta N = N_f - N_0$ is the cell growth during the incubation time (million cells).

$\mu = \frac{ln\left(\frac{N_f}{N_0}\right)}{t_f}$ is the growth rate constant (h^{-1})

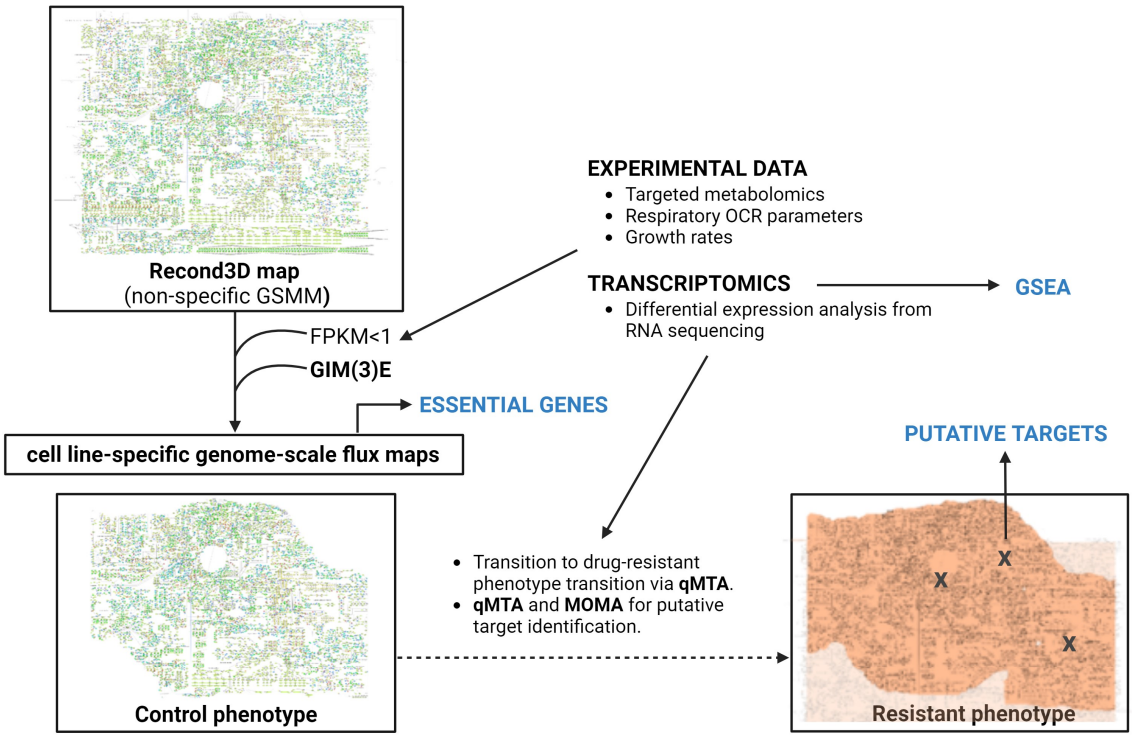

Figure II.1. Computational workflow for metabolic modeling and target prediction through muti-omics data integration. Figure adapted from Noronha et al. 2017 and created with https://www.biorender.com/ (2023).

Metabolomics measured in the cellular pellet were integrated with the proliferation rate to account for the dilution associated with proliferation. They were mapped to sink reactions that removed the respective metabolites from the models (*Equation 2*), representing the requirements of metabolite synthesis to maintain the concentration of metabolites while proliferating (Reimers & Reimers, 2016).

Eq. 2

$$Sink\ reaction\ rate = \frac{M}{N_f} \cdot \mu$$

Recon3D includes all possible reactions from the human genome; however, at any given condition, only subset of enzymes and reactions are active. In order to build GSMMs specific to the enzymes active in each cell line, reactions associated with lowly expressed enzymes in each condition were pruned from the model unless they were necessary for either 1) simulating the experimental measurement or 2) proliferation (10% of theoretical max proliferation value). A gene was considered lowly expressed if its expression was under 1Fragments Per Kilobase of transcript per Million mapped reads (FPKM).

Next, we computed a control flux distribution for each cell line by integrating the experimental measurements and transcriptomics from the control condition running the GIM(3)E algorithm (Schmidt et al., 2013) in the condition-specific model defined above. Briefly, GIM(3)E (*Equation 3*) runs a weighed minimization of total flux by assigning a minimization weight to each reaction inversely proportional to the expression of the enzymes mapped to it.

Eq. 3

$$\min \sum_i (v_i \cdot w_i)$$

$$w_i = max(0, ge_{max} - ge_i)$$

subjected to:

$$s \cdot v = 0, \qquad lb < v < ub$$

$$v_{biomass} \geq v_{biomass}^{opt} \cdot 0.95$$

where,

v_i	is the simulated flux distribution.
w_i	is weight given to the minimization of flux vi .
ge_{max}	is the maximum gene expression found in metabolic genes ($log_2(FPKM)$).
ge_i	is the gene expression assigned to reaction i ($log_2(FPKM)$).
s	is the stoichiometric matrix. Its product by the vector of flux solutions is set to 0 to constraint the model to a steady state (i.e. all input and output reactions must be balanced for each metabolite).
lb	lower bound defined for metabolic fluxes.
ub	upper bound defined for metabolic fluxes.
$v_{biomass}$	is the flux through the biomass reaction.
$v_{biomass}^{opt}$	is the optimal biomass production before applying GIM(3)E.

A representative flux distribution within 99% of the GIME3 optimal solution is obtained by sequentially applying flux variability analysis, sampling the resulting flux solution space using the Artificially Centering hit-and-run algorithm implemented into COBRApy, and computing the average flux value for each reaction (Ebrahim et al., 2013).

We use the quadratic metabolic transformation algorithm (qMTA) to simulate the metabolic transition from the control phenotype to resistant phenotype (Foguet et al., 2022). Briefly, starting from the control flux distribution, this algorithm seeks to find the flux transition most consistent with the measured differential gene expression, respiratory assay parameters, metabolomics and metabolite consumption and production rates. This was achieved by minimizing an objective function with three separate terms: the first term minimizes the difference between the flux fold changes and gene fold changes for differentially expressed genes, the second minimizes the differences between simulated fluxes and the other experimental measurements, and the last term minimizes variations to reactions not mapped to experimental fluxes or differentially expressed genes (***Equation 4***).

Eq. 4

$$\min \quad \left(G \sum_{g \in Ge} W_g \sum_{\mathrm{i} \in \mathrm{R}g} \frac{\left(v_i^{target} - v_i^{res,MTA}\right)^2}{\left(v_i^{target} - v_i^{ref}\right)^2} + E \sum_{i \in \mathrm{Re}} \left(\frac{E_j - v_i^{res,MTA}}{\sigma_i} \right)^2 + U \sum_{i \in Ru} \frac{\left(v_i^{ref} - v_i^{res,MTA}\right)^2}{v_i^{ref}} + \right)$$

$$W_g = \max\left(-LOG10\left(p_g\right), 0\right)$$

$$v_g^{target} = v_i^{ref} \cdot FoldChange_g$$

subjected to:

$$s \cdot v^{res,MTA} = 0, \qquad lb < v^{res,MTA} < ub$$

where,

$G, E\ U$ is the weight given to each minimization term. For this analysis we used G=0.05, $E = 0.9$ and U=0.05 .

Ge are the set of differentially expressed genes.

$\mathrm{R}g$ are the reactions mapped to gene g .

$\mathrm{R}e$ are the reactions mapped to measured metabolomics, consumption and production rates or respiration parameters.

$\mathrm{R}e$ are the reactions not mapped to neither differential gene expression or experimental measurements.

E_j is the experimental mean for measure j in the treated condition.

σ_j is the experimental standard deviation for measure j in the treated condition.

v_i^{ref} is the flux distribution or reference belonging to the non-treated condition computed with GIM(3)E.

v^{MTA} is the flux distribution simulated with qMTA, it represents the flux distribution in the treated condition.

v_g^{target} is the expected reaction flux target based on gene expression (is defined as the product of the reference flux value and the gene expression fold change mapped to the reaction ($FoldChange_g$).

W_g is the weight given to each gene. It is used to give more weight to genes with a more statistically significant differential gene expression.

p_{th} is the p-value threshold used to define a fold change in gene as differentially expressed. The threshold was defined as 0.25 FDR-adjusted p-value.

p_g is the FDR-adjusted p-value for measure g for the fold change between the condition under study and the control.

The metabolic reprogramming driving the adaptation to the treatment-induced stress can be quantified by comparing the reaction flux values simulated in each treatment ($v_i^{res,MTA}$) to those in control (v_i^{ref}). Reactions fluxes were grouped into metabolic pathways based on KEGG annotations to facilitate results understanding and the fold variations of total flux values through each pathway in comparison to the control were then computed.

Finally, this framework was used to identify putative metabolic inhibitors to prevent the transition to the resistant phenotype. Metabolic inhibitors from DrugBank (Knox et al., 2024) or Therapeutic Target Database (Chen et al., 2002) were assessed as well as putative inhibitors targeting individual enzymes. The potential of a given metabolic inhibitor to impede the drug-associated metabolic transformation was evaluated by sequentially reducing the maximum flux (*ub*) of the reactions inhibited by each inhibitor reactions to half of the flux value in the control condition (v_i^{ref}) and running qMTA. In parallel, the capacity of metabolic inhibitor to switch from the drug-adapted state to the control state (Valcárcel et al., 2019) was tested, by running the minimization of metabolic adjustment (MOMA) algorithm while reducing the maximum flux (*ub*) of the reactions inhibited by a given metabolic inhibitor to half of the flux value in the drug-adapted state ($v_i^{res,MTA}$) (Segrè et al., 2002) (**Figure II.2.**).

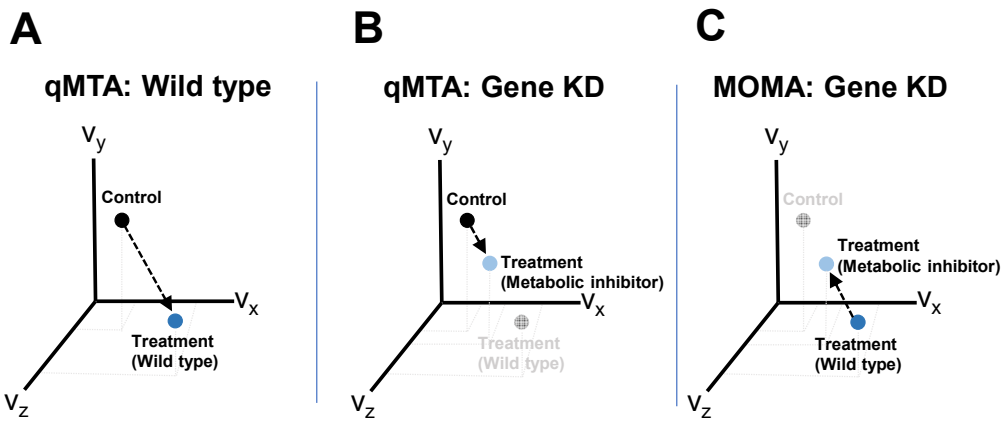

Figure II.2. A, B. Characterization of the metabolic adaptation to the resistant phenotypes and target identification. The three axes represent hypothetical reaction fluxes where is illustrated A) the characterization of the metabolic transition to resistant phenotype. B, C. the `potential targets identification after running B) qMTA simulating the capacity of a metabolic inhibitor to prevent the transition from control to resistant phenotype and C) MOMA to simulate the capacity of a metabolic inhibitor to revert the resistant phenotype to the control.

For each of these tests, a transformation score (TS) is computed as follows:

Eq. 5

$$TS = \sum_{m \in E}^{\cdot} \left(W_m \cdot sign\left(Log\left(FC_m\right)\right) \sum_{i \in R_m}^{\cdot} |v_i^{res}| - |v_i^{ref}| \right)$$

where,

v_i^{res} is the resulting flux distribution after either running qMTA with no additional metabolic inhibitors, running qMTA with a metabolic inhibitor or running MOMA with a metabolic inhibitor.

E is the set of all experimental measurements mapped to reactions (transcriptomics, metabolomics, metabolite uptake and secretion and respiration parameters) and Rm the reactions mapped to these measurements.

A metabolic inhibitor would be a candidate to target the drug induced adaptation if it impairs the metabolic transformation from the non-treated to the resistant phenotype while also reversing the resistant state towards the non-treated phenotype. This is measured with the difference between the base TS (i.e., computed when running qMTA without any additional metabolic inhibitors) and the TS when running qMTA with or MOMA with additional metabolic inhibitors.

$$Dif_I^{qMTA} = \left(TS_{qMTA}^{base} - TS_{qMTA}^{I}\right)$$
$$Dif_I^{MOMA} = \left(TS_{qMTA}^{base} - TS_{MOMA}^{I}\right)$$

where,

TS_{qMTA}^{base} is the TS score when running qMTA from the control to the drug adapted state.

TS^{I}_{qMTA} is the TS score when running qMTA from the control to the drug adapted state with metabolic inhibitor I.

TS^{I}_{MOMA} is the TS score when simulating the effect of metabolic inhibitor I starting from $v^{res,MTA}$.

A putative promising metabolic inhibitor would be one that both TS^{I}_{qMTA} and TS^{I}_{MOMA} are lower than TS^{base}_{qMTA} ($Dif_I^{qMTA} > 0$ and $Dif_I^{MOMA} > 0$). Hence, target score (S_I) for each metabolic inhibitor was finally computed as follows:

Eq. 6

$$S_I = \left|Dif_I^{qMTA} \cdot Dif_I^{MOMA}\right| \cdot \min\left(sign\left(Dif_I^{qMTA}\right), sign\left(Dif_I^{MOMA}\right)\right)$$

Aggregate score value was normalized (S_I) with respect to the quadratic value of TS score base, when running qMTA from the control to the drug adapted state (TS^{base}_{qMTA}).

Eq. 7

$$S_I = 1000\frac{AggregateScore}{\left(TS^{base}_{qMTA}\right)^2}$$

$$= 1000\frac{\left|Dif_g^{qMTA} \cdot Dif_g^{MOMA}\right|}{\left(TS^{base}_{qMTA}\right)^2} \cdot \min\left(sign\left(Dif_g^{qMTA}\right), sign\left(Dif_g^{MOMA}\right)\right)$$

APPENDIX III

III.1. Respiratory parameters in Mito Stress Seahorse assay.

The parameters calculated from the Mito Stress Seahorse assay provide valuable insights into the mitochondrial function. **Figure III.1.** illustrates the oxygen consumption rate (OCR) response to four key injections: Glucose (Acute injection), Oligomycin (Oligo), CCCP, and Rotenone/Antimycin (Rot+AA). These sequential injections are essential to calculate the respiratory parameters, including basal respiration, non-mitochondrial respiration, ATP production-associated respiration, maximal respiratory capacity, spare respiratory capacity, and non-ATP-linked oxygen consumption (proton leak).

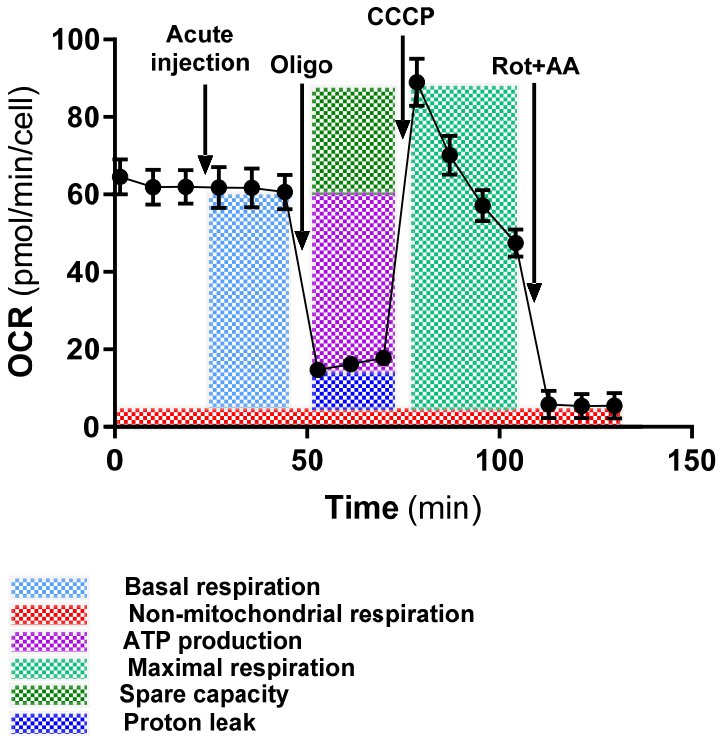

Figure III.1. Mito Stress Seahorse parameters. The Oxygen Consumption Rate (OCR) response over time after the four injections (Acute injection, Oligomycin (Oligo), CCCP, and Rot+AA (Rotenone and Antimycin A)) are depicted. Calculations for the respiratory parameters: Basal respiration (light blue), non-mitochondrial respiration (red), ATP production-associated respiration (pink), Maximal respiratory capacity (light green), Spare respiratory capacity (dark green), and non-ATP-linked oxygen consumption or H+ (Proton) leak (dark blue), are highlighted in the indicated colors.

APPENDIX IV

IV.1. Differential expression gene values.

Differential expression of genes associated with detailed pathways after Palbociclib treatment in PC-3 cells.

Table IV.1. Differential expression of genes encoding for the most important enzymes in the urea cycle and polyamine metabolism. Differential gene expression in terms of Log 2 fold-change (Log2FC) after 96 h of treatment with Palbociclib regarding the principal encoding genes of the indicated metabolic pathways in PC-3.
* Indicates adjusted p-value < 0.05. NA (not-assigned) indicates not gene expression.

Gene	**Encoding protein**	**Log2FC**
Methionine cycle and methionine salvage pathway		
MTR	*5-methyltetrahydrofolate-homocysteine methyltransferase*	- 0.30
AHCY	*adenosylhomocysteinase*	+0.24
MTAP	*methylthioadenosine phosphorylase*	- 0.34
AMD1	*adenosylmethionine decarboxylase 1*	- 0.02
Urea cycle		
ASS1	*argininosuccinate synthase 1*	+0.44
NOS1	*nitric oxide synthase 1*	- 0.61
ASL	*argininosuccinate lyase*	+0.59 *
ARG1	*arginase*	NA
ARG2	*arginase 2*	+0.65
Polyamine metabolism		
Gene	**Encoding protein**	**Log2FC**
ODC1	*ornithine decarboxylase 1*	+0.48 *
SRM	*spermidine synthase*	+0.28
SMS	*spermine synthase*	- 0.17
SAT1	*spermidine/spermine N1-acetyltransferase 1*	+0.84 *
SMOX	*spermine oxidase*	+0.45
PAOX	*polyamine oxidase*	+1.01

IV.2. Mass isotopomer distribution.

Complete isotopologue distribution after incubation with 10 mM of [1,2-$^{13}C_2$]-glucose or 2 mM of [U-$^{13}C_5$]-glutamine.

Table IV.2. Complete isotopologue distribution for [1,2-$^{13}C_2$]-glucose. Polar intracellular metabolites measured by GC-MS in control and Palbociclib-treated PC-3 cells. mn indicates the number of ^{13}C in the molecule.

ID	mn	Mean	SD	Mean	SD
Asp-418 C1-C4	m0	0.81756667	0.00926517	0.8063	0.01445095
	m1	0.0402	0.00578878	0.0514	0.00991363
	m2	0.11443333	0.00470142	0.11713333	0.00839305
	m3	0.0239	0.00630238	0.02216667	0.00411015
	m4	0.00433333	0.00230072	2.83E-03	0.00112398
Cit-591	m0	0.49103333	0.00527668	0.51516667	0.01066505
	m1	0.05466667	0.00656836	0.05036667	0.00837397
	m2	0.3524	0.00680368	0.336	0.00075498
	m3	0.03603333	0.00309246	0.0363	0.00208087
	m4	0.0521	0.00419047	0.05033333	0.00450814
	m5	0.01246667	0.00049329	0.00943333	0.00089629
Glu-432 C1-C5	m0	0.75986667	0.00450814	0.7657	0.00255343
	m1	0.04233333	0.00170098	0.04253333	0.00447698
	m2	0.15746667	0.00329292	0.1534	0.00175214
	m3	0.02333333	0.00115036	0.0202	0.00157162
	m4	0.015	0.00156205	0.01666667	0.00156312
	m5	0.0016	0.00045826	0.00136667	0.00060277
Mal-419	m0	0.77776667	0.01120818	0.7851	0.009755
	m1	0.0505	0.00493862	0.05283333	0.00567656
	m2	0.14076667	0.00418609	0.13596667	0.00680906
	m3	0.02556667	0.00047258	0.02183333	0.00281129
	m4	0.00436667	0.00172143	2.80E-03	0.00327414

Table IV.3. Complete isotopologue distribution for [U-$^{13}C_5$]-glutamine. Polar intracellular metabolites measured by GC-MS in control and Palbociclib-treated PC-3 cells. mn indicates the number of ^{13}C in the molecule.

ID	mn	Mean	SD	Mean	SD
Asp-418 C1-C4	m0	0.30236667	0.02133784	0.2747	0.01522465
	m1	0.09993333	0.00734461	0.09366667	0.0044658
	m2	0.17896667	0.01841367	0.1798	0.00315753
	m3	0.04563333	0.00588246	0.0588	0.0022
	m4	0.36963333	0.00635715	0.39046667	0.01769416
Cit-591	m0	0.23953333	0.01524347	0.22443333	0.00791033
	m1	0.10846667	0.00515493	0.1108	0.00373229
	m2	0.18036667	0.00483356	0.17336667	0.00265016
	m3	0.06523333	0.00482113	0.07393333	0.00228983
	m4	0.36906667	0.0146739	0.36063333	0.00708684
	m5	0.02593333	0.00055076	0.04476667	0.00381357

Glu-432 C1-C5	m0	0.1899	0.0037	0.1777	0.00926661
	m1	0.07973333	0.00215716	0.07876667	0.00261024
	m2	0.05976667	0.00020817	0.06143333	0.00077675
	m3	0.19073333	0.00217332	0.19076667	0.00190351
	m4	0.02253333	0.0009609	0.02293333	0.00041633
	m5	0.44813333	0.0063343	0.4616	0.01444403
Mal-419	m0	0.235	0.01638994	0.22183333	0.00440038
	m1	0.1021	0.00304467	0.09843333	0.00313741
	m2	0.18666667	0.00125033	0.18323333	0.00417892
	m3	0.05303333	0.00073711	0.069	0.00415812
	m4	0.42206667	0.01587272	0.4264	0.00802994

APPENDIX V

V.1. Differential expression gene values.

Differential expression of genes associated with detailed pathways after Palbociclib treatment in SW620 cells.

Table V.1. Differential expression of genes encoding for the most important enzymes in glycolysis and PPP. Differential expression in terms of Log2foldchange (Log2FC) after 96 h of treatment with Palbociclib (40 nM) in SW620. * Indicates adjusted p-value < 0.05.

Gene	Encoding protein	Log2FC
Glycolysis		
HK1	*hexokinase 1*	+0.03
HK2	*hexokinase 2*	- 0.41 *
GPI	*glucose-6-phosphate isomerase*	- 0.12
PFKFB2	*6-phosphofructo-2-kinase/fructose-2,6-biphosphatase 2*	+0.13
PFKFB3	*6-phosphofructo-2-kinase/fructose-2,6-biphosphatase 3*	- 0.66 *
PFKFB4	*6-phosphofructo-2-kinase/fructose-2,6-biphosphatase 4*	- 0.92 *
PFKL	*phosphofructokinase, liver type*	- 0.17
PFKM	*phosphofructokinase, muscle*	+0.37 *
PFKP	*phosphofructokinase, platelet*	- 0.13
ALDOA	*aldolase, fructose-bisphosphate A*	- 0.47
ALDOC	*aldolase, fructose-bisphosphate C*	- 1.12
TPI1	*triosephosphate isomerase 1*	- 0.23
GAPDH	*glyceraldehyde-3-phosphate dehydrogenase*	- 0.21
PGK1	*phosphoglycerate kinase 1*	- 0.34
PGAM1	*phosphoglycerate mutase 1*	- 0.04
ENO1	*enolase 1*	- 0.26 *
ENO2	*enolase 2*	- 1.03 *
ENO3	*enolase 3*	+0.01
PKM	*pyruvate kinase M1/2*	- 0.04
LDHA	*lactate dehydrogenase A*	- 0.38
LDHB	*lactate dehydrogenase B*	+0.15
Pentose phosphate pathway (PPP)		
Gene	**Encoding protein**	**Log2FC**
G6PD	*glucose-6-phosphate dehydrogenase*	- 0.10
H6PD	*hexose-6-phosphate dehydrogenase/glucose 1-dehydrogenase*	+0.06
PGD	*phosphogluconate dehydrogenase*	+0.01
TKT	*transketolase*	- 0.06
TALDO1	*transaldolase 1*	- 0.02
RPIA	*ribose 5-phosphate isomerase A*	- 0.10
RPE	*ribulose-5-phosphate-3-epimerase*	+0.09

Table V.2. Differential expression of genes encoding for the most important enzymes in the TCA cycle. Differential expression in terms of Log2foldchange (Log2FC) after 96 h of treatment with Palbociclib (40 nM) in SW620.

Gene	Encoding protein	Log2FC
Tricarboxylic acid cycle (TCA) cycle		
ACO1	*aconitase 1*	+0.22
ACO2	*aconitase 2*	+0.06
CS	*citrate synthase*	+0.06
DLST	*dihydrolipoamide S-succinyltransferase*	+0.10
FH	*fumarate hydratase*	+0.10
IDH1	*isocitrate dehydrogenase (NADP(+)) 1*	+0.08
IDH2	*isocitrate dehydrogenase (NADP(+)) 2*	+0.06
IDH3A	*isocitrate dehydrogenase (NAD(+)) 3 catalytic subunit alpha*	+0.19
IDH3B	*isocitrate dehydrogenase (NAD(+)) 3 non-catalytic subunit beta*	+0.11
IDH3G	*isocitrate dehydrogenase (NAD(+)) 3 non-catalytic subunit gamma*	- 0.01
MDH1	*malate dehydrogenase 1*	+0.11
MDH2	*malate dehydrogenase 2*	+0.03
OGDH	*oxoglutarate dehydrogenase*	- 0.02
OGDHL	*oxoglutarate dehydrogenase like*	+0.09
PC	*pyruvate carboxylase*	- 0.09
SDHA	*succinate dehydrogenase complex flavoprotein subunit A*	+0.14
SDHB	*succinate dehydrogenase complex iron sulfur subunit B*	- 0.08
SDHC	*succinate dehydrogenase complex subunit C*	+0.08
SDHD	*succinate dehydrogenase complex subunit D*	+0.12
SUCLA2	*succinate-CoA ligase ADP-forming subunit beta*	+0.18
SUCLG1	*succinate-CoA ligase GDP/ADP-forming subunit alpha*	- 0.01
SUCLG2	*succinate-CoA ligase GDP-forming subunit beta*	+0.12

APPENDIX VI

Throughout the course of this thesis, one original article has been published.

Title: Glutamine Modulates Expression and Function of Glucose 6-Phosphate Dehydrogenase via NRF2 in Colon Cancer Cells

Authors: Ibrahim H. Polat, Míriam Tarrado-Castellarnau, Adrian Benito, **Claudia Hernandez-Carro**, Josep Centelles, Silvia Marin, and Marta Cascante.

Abstract: Nucleotide pools need to be constantly replenished in cancer cells to support cell proliferation. The synthesis of nucleotides requires glutamine and 5-phosphoribosyl-1-pyrophosphate produced from ribose-5-phosphate via the oxidative branch of the pentose phosphate pathway (ox-PPP). Both PPP and glutamine also play a key role in maintaining the redox status of cancer cells. Enhanced glutamine metabolism and increased glucose 6-phosphate dehydrogenase (G6PD) expression have been related to a malignant phenotype in tumors. However, the association between G6PD overexpression and glutamine consumption in cancer cell proliferation is still incompletely understood. In this study, we demonstrated that both inhibition of G6PD and glutamine deprivation decrease the proliferation of colon cancer cells and induce cell cycle arrest and apoptosis. Moreover, we unveiled that glutamine deprivation induce an increase of G6PD expression that is mediated through the activation of the nuclear factor (erythroid-derived 2)-like 2 (NRF2). This crosstalk between G6PD and glutamine points out the potential of combined therapies targeting oxidative PPP enzymes and glutamine catabolism to combat colon cancer.